ESRF HIGHLIGHTS 2013

ESRF
The European Synchrotron

ESRF
The European Synchrotron

ESRF HIGHLIGHTS 2013

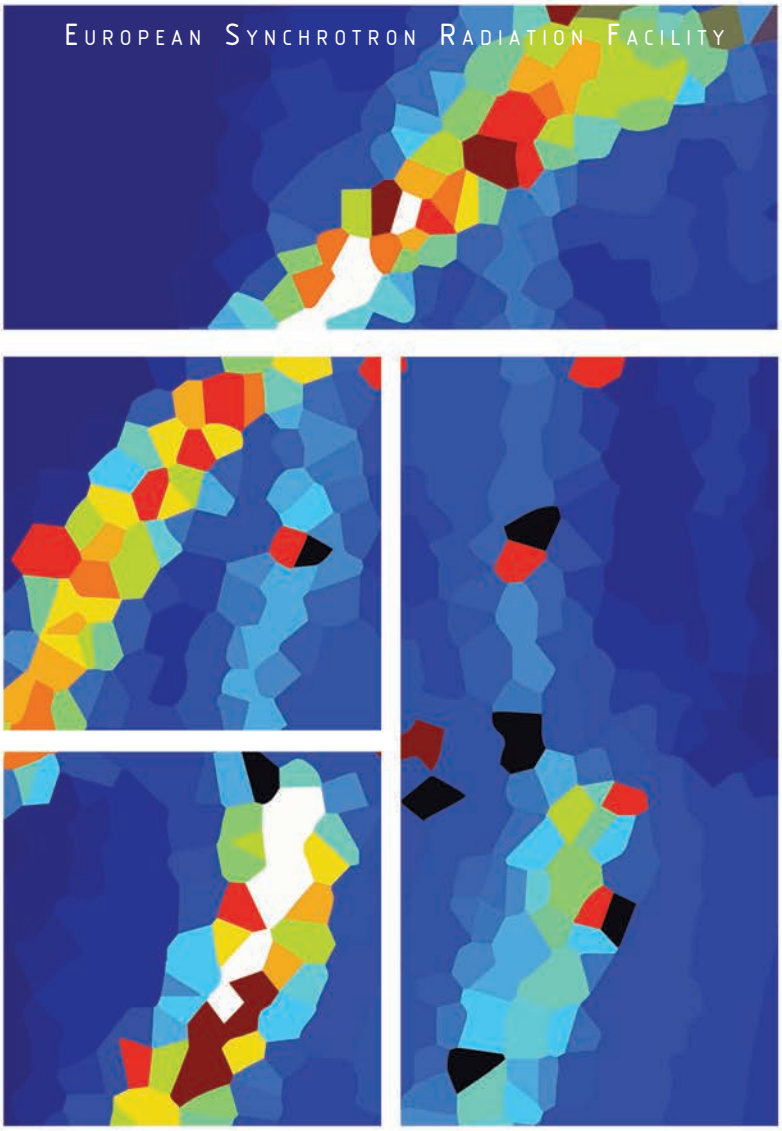

DEAR READER

Francesco Sette

The ESRF storage ring returned to full User Service Mode (USM) operation for 2013, delivering 5544 hours of beamtime, with enhanced performance and many new features. Excellent day-to-day facility operation is indeed a key element to ensure that the scientific productivity of the ESRF continues to be very high. Our users, working closely with ESRF staff, have again achieved many world-class scientific results. The scientific output, with about 1800 scientific publications, including the most prestigious journals, is as high as in previous years and our beamlines continue to be overbooked, in many cases very heavily.

An extensive programme of new buildings has been completed

In parallel to the routine operation of the facility, construction of three more upgrade beamlines began as part of the first phase of the ESRF Upgrade Programme. This programme continues to progress according to plan. Another major milestone of the upgrade in 2013 was the successful completion of the EX2 project, with the delivery of two new large experimental halls, laboratories and offices, the ESRF visitor centre, and amenities to enhance the quality of the daily life of ESRF users and staff. In both new experimental halls, the construction of the upgrade beamlines started on the very day they were handed over to the ESRF. The EX2 project included numerous challenges, not least a very tight schedule and budget. Both were met in addition to strict technical specifications, in particular for the long-term and vibrational stability of the concrete floor.

A project to improve the building infrastructure of the European Photon and Neutron (EPN) science campus, which the ESRF shares with the ILL and the EMBL, has been brought very close to completion. Early in 2014, a new site entrance will be inaugurated along with a renovated and enlarged canteen in the Common Building. The new Science Building close to the road bridge across the ESRF storage ring will be inaugurated in February. This building will host joint ESRF-ILL activities in soft matter science, business development with industrial users, the joint library and the Theory Group. It will also provide joint support laboratories for the benefit of users, staff and collaborators. In March 2014, it will be connected to the Experimental Hall via a dedicated foot bridge.

The EPN science campus is steadily improving its visibility, creating many new opportunities, particularly for young scientists. This is also possible thanks to the efforts of, and enhanced collaboration with, our colleagues at the ILL, the EMBL, and the Institut de Biologie Structurale (IBS). The IBS has just recently moved into its new premises on the campus. Thanks to the new site infrastructure buildings and the vegetation and landscaping plan to be concluded in spring 2014, the campus is gradually becoming a more beautiful place in which to work.

Three years of building activities, both on our site and in the surrounding areas, have not always been easy to deal with, and I thank both users and staff for their continuous engagement to cope with this exceptional situation.

Support from Members and Associates continues to motivate the ESRF

The global economic context, including the situation throughout Europe, has not changed over the past twelve months, and probably will not qualitatively improve in 2014. Despite the difficult scenario, we were very pleased to welcome the Republic of South Africa in May 2013, which joined the ESRF on a five-year arrangement. We also applauded the decision of Israel to renew its Scientific Association with the ESRF at an increased value, just as the Republic of Austria did last year. We are also very pleased that Portugal has renewed its agreement and that Centralsync should follow shortly. Exceptional measures with respect to our funding have had to be prolonged until the end of 2014, although at a slightly improved level, and by the end of 2014 we hope to be able to reach a secure and stable financial context in the medium term, possibly with a return to our full level of funding.

New opportunities for scientific discovery thanks to new and improved beamlines

Many of the scientific results presented in the following pages would not have been possible a few years ago. The performance of synchrotron beamlines continues to increase steadily on a global scale. Experiments, and discoveries that were thought impossible not long ago are now becoming reality. The pages of these 2013 Highlights are mainly focussed on providing the reader with a synthesis of the science enabled by these new opportunities.

The ESRF beamline portfolio comprised important improvements in 2013, notably in the existing experimental hall. The new Inelastic X-ray Scattering Upgrade Beamline ID20 started user operation with world-breaking performance. The Upgrade Beamline NINA on ID16 is being commissioned and is close to starting full user

operation mode. Several other major refurbishments have come on line such as the new optics for ID19, and the installation of large-area-pixel-detector systems at several diffraction beamlines. These improvements often have a twofold impact: they enable a higher throughput and experiments that were not possible before.

One of the biggest upgrade beamline projects is the "Village" for Structural Biology around ID30, where the next generation of automation is being developed. In 2013, the final technological choices were made, and tested for fully automated screening of crystals. The first station using this new very demanding technology should come on line for users in the summer of 2014.

Machine, beamlines and instrumentation are maintained at world-class level

Throughout 2013, the accelerators and X-ray source have continued to provide a very stable and reliable operation, with the final run of 2013 coming very close to 100% delivery. Important improvements in view to securing world-class levels of performance and reliability continued throughout the year. The storage ring now houses three novel design prototypes of radio-frequency (RF) cavities, fed by state-of-the-art semiconductor RF amplifiers, which perform fully according to specifications. The replacement of the existing cavities with the new ones will continue in the coming years, as these new cavities are of key importance for future storage ring improvements: indeed, these upgrades are an early investment in view of the second phase of the Upgrade Programme.

In 2013, the machine was for the first time operated in top-up mode during several days of machine dedicated time. These tests included delivery of beam to several beamlines hosting users, and they were a complete success. A detailed analysis of the results is now under way, so that the possibility of introducing top-up mode operation at the ESRF can be discussed in 2014 with the SAC and the users.

Preparations for the Upgrade Programme Phase II are in full swing

Last but not least, and indeed of primary importance for our future, is the work started during the last few years to prepare the second phase of the ESRF Upgrade Programme. The cornerstone of the second phase is the construction and commissioning of a new storage ring lattice with qualitatively improved features in terms of X-ray beam brightness and coherence, and with reduced environmental impact. This will enhance the ESRF's leadership in synchrotron science and keep the laboratory at the forefront for many years to come. The objective of the ESRF is to prepare this phase until mid-2014 through a detailed technical design report to be submitted for critical scrutiny to the ESRF Science Advisory Committee (SAC), Accelerator Programme Advisory Committee (APAC), Administrative and Finance Committee (AFC), and Council. According to the present planning, the implementation of Phase II should be launched in January 2015 with the objective to deliver USM with the renewed storage ring by 2020. With the help of these committees, the work on the scientific programme of Phase II saw good progress in 2013, as well as the critical analysis of the technologies to be developed to ensure the optimal use of the new source; particular attention is being devoted to new detector technologies and data handling strategies. Similarly, the technical and implementation aspects of the new storage ring are under study and are greatly advancing. The new accelerator lattice concept developed at the ESRF, which greatly reflects the Long Term Strategic Mission of the ESRF reviewed by the Council in 2012, has been validated by international benchmarking and is now being adopted by many other world-leading synchrotron facilities. The Phase II of the Upgrade Programme is a new and exciting challenge for everybody at the ESRF, in addition to the operation of the facility and the completion of Upgrade Phase I.

The Council endorsed and supported the progress and the strategic path developed by the ESRF on the long-term vision of our laboratory at its meeting in November 2013. We hope, therefore, that today's efforts are preparing the ground for a positive decision in 2014 on the launch of the Upgrade Programme Phase II with its new storage ring project.

The ESRF is a major player in society and synchrotron science

The ESRF returns a lot to society. This includes, of course, the advancement of scientific knowledge, but also contributions towards major societal challenges, such as education and training of the next generation, and contributing to industrial innovation. A recently published brochure highlights the impact of the ESRF Upgrade Programme which has only been possible thanks to the expertise, commitment and motivation of the ESRF staff, its users and the scientific community. We are proud to present these results to the governments of our Member and Scientific Associate Countries, and we thank them for their continued support.

In parallel, the ESRF is also playing an important role in the global synchrotron landscape. It continues to be seen as a role model for efficient operation and global leadership, and numerous delegations from existing and future facilities visited Grenoble in 2013 to learn more. This leadership role also has a technical side, covering, for example, coordination of detector developments across Europe and developing beamline control software to be shared with other synchrotrons. We are therefore honoured that the European Commission has entrusted the ESRF with the management of the 17 Million Euro CRISP programme, where 11 European research infrastructures jointly study key technologies for tomorrow's accelerators, instrumentation and data processing.

At its meeting in November 2013, the ESRF Council elected Bertrand Girard and Miguel Ángel García Aranda as its new Chair and Vice-Chair for the period 2014-2016. Their predecessors,

Jean Moulin as Chair and Michel van der Rest as Vice-Chair, have, over the past three years, played pivotal roles in ensuring continued support to the ESRF by its Members and Associates, and in widening the circle of countries that contribute to our activities. I personally wish to thank them for their engagement and support, and welcome B. Girard and M.A. García Aranda.

I wish to conclude this introduction by thanking everybody who has contributed to the progress made in 2013, and to the many successes. In particular, I wish to thank the members of the scientific, technical, administrative, and financial committees for their help and advice, and the Council delegates for their guidance and continued support. The ESRF users have performed wonderful scientific work and in parallel given important support and critical advice to the ESRF. All my colleagues at the ESRF have worked extremely hard to deliver simultaneously world-class operation of the facility while building the future of the ESRF through its upgrade programme.

Thanks to all of you and I hope you enjoy reading these 2013 Highlights!

FRANCESCO SETTE,
ESRF Director General

STATUS OF THE UPGRADE PROGRAMME

After two years of work on our ambitious construction programme, 2013 has seen the delivery of the new buildings that change not only the visual appearance of the site but more importantly create new opportunities for the science programme at the ESRF. Immediately after the delivery of the new buildings (ID16 satellite, Chartreuse and Belledonne halls), work on new beamlines commenced with many beamlines now under construction. 2014 will see the inauguration of many new beamlines with unprecedented scientific capabilities offered to our user community. The upgrade of the accelerator complex is heading towards a successful conclusion with the first encouraging tests on top-up operation during machine dedicated time. We are now eagerly awaiting the full implementation of top-up operation in 2015 for the timing modes. We thank our staff for all of these achievements, delivered while the facility was kept in full user operation.

Fig. 1: Inauguration ceremony of the new experimental halls, 24 June 2013.

EX2 – Signing off

Eight years after the inception of the ambitious EX2 construction project, we are now ready to sign off. The last phase, which consists in finalising the accounts of the project, is going ahead and will hopefully be concluded early 2014.

The climax of the first half of 2013 was the completion of one of the major technical challenges: the high quality slab. The technical design choice was the fruit of a thorough analysis and scrutiny by an international panel of experts to meet stringent requirements in terms of stability and vibration, critical for the construction of highly demanding nanofocussing beamlines. The last layer of the multilayered slab, consisting of densely steel-reinforced concrete, was poured in two distinct operations during the month of April. For the Belledonne hall, 800 m^3 of concrete had to be brought in and was poured in one go, whereas the smaller Chartreuse hall required "only" 525 m^3.

On 24 June an official ribbon cutting ceremony was held to commemorate the inauguration of the halls (**Figure 1**), attended by Council delegates and observers, ESRF Directors, and key contributors in the realisation of EX2.

Beamline construction started immediately after the delivery of the

new halls with ID30 in Chartreuse and ID32 in Belledonne.

The occupation of the new premises began in the fourth quarter of 2013 with the delivery of the last part of the building programme, the Laboratory and Office Building in front of the Belledone hall extension (**Figure 2**).

Logistics require the careful orchestration of moves affecting a large fraction of the ESRF staff over the next 12 months.

The penultimate phase of the project is settling the accounts with the contractors. At the time of writing, this chapter of the project is still under way and we are confident that the project will be concluded within budget.

Fig. 2: The finished Laboratory and Office Building in front of the Belledonne hall extension.

Upgrade of the source

The upgrade of the accelerator system is progressing well and as planned. The extension of the ID23 straight section to 7 metres has been completed. This change in magnet configuration had the consequence of breaking the symmetry of the lattice but these significant changes to the optics had no negative effects on machine performance. In fact, beam parameters are even better than previously thanks to improved tuning techniques.

The 7-metre section enabled tests of low-β optics, which were carried out with success, paving the way for the possible development and installation of shorter-period, smaller-gap undulators. Upon completion of these tests, three new HOM-damped RF cavities were installed and are currently operating in active mode, powered by the new SSA amplifiers.

The storage ring top-up operation project is advancing well. The hardware related activities necessary to complete the project are under development. Very encouraging tests have been carried out, so far mostly in machine dedicated time. Further tests with users will be scheduled in 2014 in order to prepare the final top-up delivery during user operation in 2015.

The technical design study for the Phase II upgrade based on a 7-bend achromat lattice is progressing well. The project was received with enthusiasm by the Accelerator Project Advisory Committee (APAC) in September, who then produced a very positive official report.

Renewal of beamlines

Activities within the Instrumentation and Development Division (ISDD) and the Experiments Division (ExpD) for the construction of new upgrade beamlines (UPBLs) have reached their peak with the delivery of the experimental hall extensions. A total of 10 beamlines is currently under construction with most of them to return to user operation in 2014. In addition, significant financial and human resources have been invested in the continuous refurbishment and further development of the remaining beamlines.

The main projects for beamline renewal are as follows:

UPBL1 – Diffraction for nano-analysis
Most of the optical components, including the white beam mirrors and multilayer monochromator, double crystal monochromator and transfocator are currently in the manufacturing or procurement phase. The SAXS/GISAXS end-station is in

Fig. 3: CAD picture of UPBL1 SAXS and GISAXS end station.

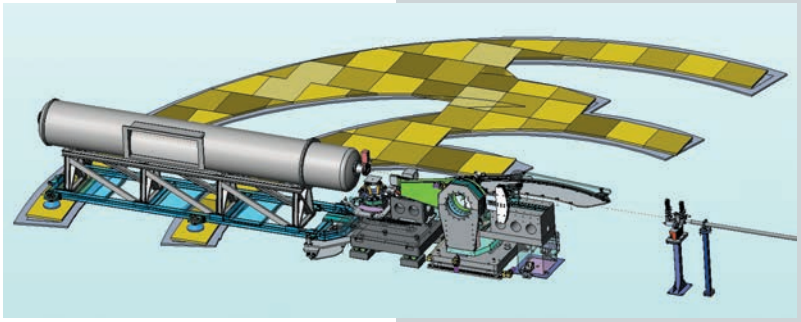

the final phase of design (Figure 3). The prototype for the ultra-long-working-distance microscope has been finalised.

UPBL2 – High energies for interfaces and materials processing

The design of the multilayer device (based on ESRF generic mechanical systems for mirrors) is near to completion. The outline of the beamline layout is finalised and the contracts for the construction of the infrastructure have been signed. The procurement of multilayer monochromator substrates has been initiated, and the evaluation of commercial flat panel detectors completed.

UPBL4 – Nano-imaging and nano-analysis

Overall the project is progressing well. The optics hutch was completed in June 2013 and all optics hutch components have now been installed, with first commissioning results proving satisfactory. There is still a significant effort to be devoted to control software.

NI- nanotomography endstation: The pre-focusing multilayer monochromator is now installed and the medium energy (17 keV) nanofocusing mirror substrate is in the manufacturing phase. The piezo hexapod is operating correctly, thus making it possible to compensate the errors of the sample rotation. The production of the main components for a composite device combining customised Maxipix modules and two 16 Mpixel imaging detectors, including a FReLoN camera, with specially designed lenses has been completed and the instrument is in the assembly phase. Figure 4 shows the nanotomography sample stage.

NA- nano-analysis endstation: The white-beam double mirror system has been installed. A Ge solid-state detector for high energy fluorescence measurements and two multi-element SDD detectors have been purchased.

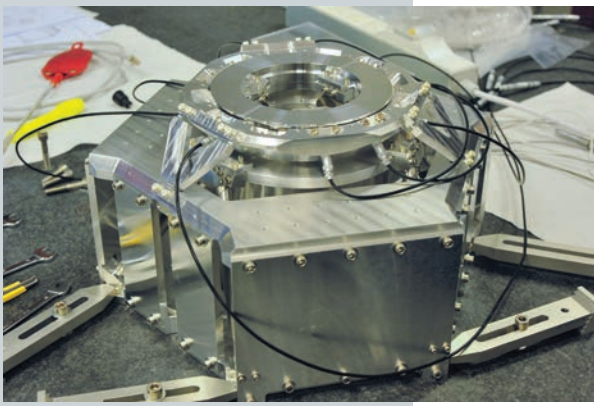

Fig. 4: UPBL4 NI nanotomography end station sample stage.

UPBL6 – Hard X-ray spectroscopy (RIXS & XRS)

The assembly of both spectrometers has been completed and successful commissioning results have been obtained. Maxipix and APD detectors have been delivered and two on-line diamond BPMs were installed. Target energy resolution has been slightly surpassed and first scheduled user experiments on the RIXS and NIXS spectrometer have been successful.

UPBL7 – Soft X-ray spectroscopy (RIXS & XMCD)

All mirror mechanical devices have been assembled, and are now awaiting the integration of the mirror substrates. Entrance and exit slits have been delivered and tested. Spherical grating substrates were delivered to the ESRF for intermediate metrology tests prior to the final manufacturing phase. The plane grating monochromator has been delivered and the liquid nitrogen cooled grating pre-mirror assembly will be integrated soon. Finally, the installation of the 11 m long RIXS spectrometer arm is under way.

UPBL9a – Time-resolved ultra-small-angle scattering

The mechanical assembly of the double mirror device has been completed, and is now waiting for mirror substrates. The 32 m long SAXS tube and associated equipment are in the manufacturing phase and will be delivered early 2014. The SAXS and WAXS detectors have been purchased, while a specially designed new high-sensitivity FReLoN detector for USAXS applications has been manufactured.

UPBL9b – Pump-probe and time-resolved experiments

The TDR has been validated and a new high heat-load beam chopper has been ordered.

UPBL10 – Automated crystallographic evaluation

Following the installation and commissioning of all major optical devices, the beam has been delivered to the three end-stations. An order

has been placed for the new Pilatus 6M detector. The MxCube V2 control software, which was successfully used to take the first data at the end of September 2013, is now complete. It was decided to delay the start of user operation on ID30A-1 and ID30A-3 to prepare the installation of the new high capacity dewar and the new robot system for fast sample transfer and goniometry.

UPBL11 – Time-resolved and extreme conditions XAS

A first series of on-site acceptance tests of the XH Ge microstrip detector for time-resolved EDXAS have been carried out and the Lima drivers were developed by the STFC with the help of the ESRF. The acquisition sequences were prepared with the XH simulator from the STFC. This allowed the XH detector to be integrated into the beamline before it arrived.

ID22 refurbishment

The TDR for the move and complete refurbishment of the powder diffraction beamline from ID31 to ID22 has been completed and validated. The infrastructure for the new beamline has been prepared and installation of the new components in the optics and experimental hutches is progressing well.

Other activities in the ISDD have continued to focus on UPBLs and related beamline instrumentation, although reflection has begun on the instrumentation programme for Phase II and, more particularly, on future detector developments.

Several developments were driven by the very challenging specifications of optical components for UPBLs. A special effort has been made to enhance optical metrology capabilities, including protocols for measurement of sub-nm figure errors on short radius and highly aspheric reflective optics, precise measurement techniques for variable line spacing diffraction grating characterisation and improved instrumentation for stitching interferometry methods. As in previous years, special efforts were put into establishing generic engineering solutions to minimise the resource investment required for their integration into customised systems. A large number of standard XBPMs and beam viewers were produced and installed on about 15 different beamlines (**Figure 5**). A new, very compact transfocator has also been developed and commissioned for integration into the limited space typically available around sample environments (**Figure 6**).

Fig. 5: Monochromatic beam viewer.

Moving into the later phases of the remaining UPBLs, the Detector & Electronics Group has dedicated significant resources to the selection, installation and integration of high performance detector instrumentation. This has been facilitated by earlier efforts to identify standard solutions based on commercial devices, which can be tailored to specific beamline needs. R&D activities include definition of the readout architecture and successful testing of Medipix3 chips at the 350 MHz clock frequency for the SMARTPIX project; the development of new high efficiency semitransparent scintillating screens; progressing in the construction of the first full 1 kpixel XNAP detector prototype based on pixelated APD sensors; and continuation of the HiZPAD2 project (CALIPSO Joint Research Activity) for high energy pixel detectors.

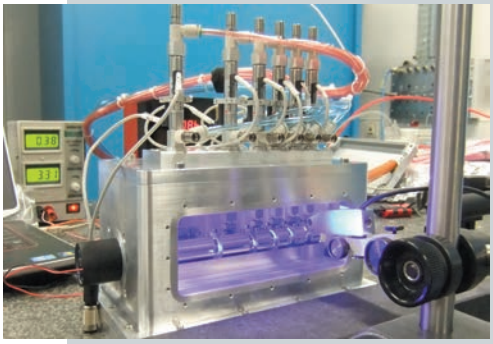

Fig. 6: Compact transfocator undergoing tests.

The modernisation of the control system is on-going, following two directions: on one hand the generalisation of the standard motion controller, IcePAP, on both beamlines and the accelerator, is being pursued. On the other hand, the first elements of the R&D programme for new control software have been put in place.

Finally, in 2013, the strengthening of commercial & outreach activities took place for several European partnerships, and included the supply of a number of optical components and detectors to other facilities, collaborations with E-XFEL for the design of one endstation at DESY, and the Solar Innovation collaboration with the CEA.

B. DIJKSTRA, R. DIMPER, H. REICHERT, P. RAIMONDI AND J. SUSINI

X-RAY IMAGING

The articles presented in this chapter illustrate the broad range of scientific topics covered by the X-ray imaging beamlines at the ESRF, from medicine and life science to palaeontology and historical artefacts. All the examples share a common property: the heterogeneity (and often complexity) of the samples. They usually differ in terms of size, composition and structure: from the 30 cm long burrow cast in the article by Fernandez *et al.* to 300 nm wide nanowires (**Figure 8**, below). The X-ray imaging beamlines offer our users a very wide range of accessible lateral resolution and corollary sample size, and an extended set of imaging and analytical tools.

Ultimate nanometric resolution will soon be accessible through the NINA project (nano-imaging and nano-analysis, ESRF Upgrade Programme UPBL4). NINA will provide two new beamlines, ID16A and ID16B (**Figure 7**), designed following the experience gained on the ID22 Nano-imaging End-station, which is now closed. It has been a very busy year for those involved in this flagship project: installation of the common optics hutch was completed in October, successful radiation tests of the experimental hutches were carried out in early November. Now our efforts are focused on the installation of the end-stations, with the aim of putting into operation the nano-analysis beamline ID16B for user experiments in Spring 2014. The Nano-imaging Beamline ID16A will be optimised for ultimate hard X-ray focusing of a beam with a large energy bandwidth (1%) at specific energies (17 keV or 33.6 keV). It will address problems in biology, biomedicine and nanotechnology using X-ray fluorescence microscopy and nanotomography. The kind of research that could benefit from beamline ID16A is illustrated by two highlight articles, the investigation of the subtissue metal distributions within *Daphnia magna* and the study of copper pathology in vulnerable brain regions in Parkinson's disease. Cryogenic sample preservation, which is fundamental for such biological samples, will be available by the end of 2014. New coherent imaging techniques, such as near-field ptychography, will also be an interesting capability of the beamline. The article by Stockmar *et al.* in the chapter Enabling Technology illustrates this area of research. The main focus of the Nano-analysis Beamline ID16B is analytical capabilities exploiting a tuneable monochromatic nanobeam (spatial resolution 50 nm^{-1} µm), in particular for X-ray absorption spectroscopy and X-ray diffraction. These techniques will be complemented by fluorescence nanoscopy and nanotomography. Different operation modes will be available (monochromatic and pink beam) over a wide and continuous energy range (5-65 keV). Flexibility in terms of sample environments, especially interesting for *in situ* and *in operando* analyses, will also be a feature of ID16B. The nano-XAS study performed by Chu *et al.* on single Co-implanted ZnO nanowires, illustrated in **Figure 8**, is a typical example of future research activities at ID16B. This study combines both the nanoscale resolution and the chemical information offered by a set of complementary X-ray techniques.

At an intermediate submicrometric scale, the spectromicroscopy beamline ID21 also offers new instrumental capabilities, with the so-called "full-field XANES set-up", which combines 2D imaging with spectroscopic characterisation. This instrument is very efficient for the large scale microspectroscopic study of concentrated elements, as illustrated in the article by Meirer *et al.* on the analysis of Fe speciation in ancient ceramics. The full-field XANES set-up complements well the scanning X-ray microscope that offers micro-spectroscopy in X-ray fluorescence mode for more diluted elements.

Finally, at the opposite end of the beam size scale, the paleontology facility project aims at improving X-ray coherent imaging capabilities for large samples. The diversity of the highlights related to paleontology reflects the intense activity of this community at the ESRF. Important instrumental developments are under way at ID17 and ID19 to improve simultaneously the field of view and the lateral resolution. A transfocator has already been installed in the ID19 optics hutch and a new monochromator will follow shortly. Further developments in optics and detectors are planned for 2014 to further increase the field of view, and more generally the versatility of the different imaging configurations, in particular, the capabilities in rapid *in situ* imaging.

M. COTTE

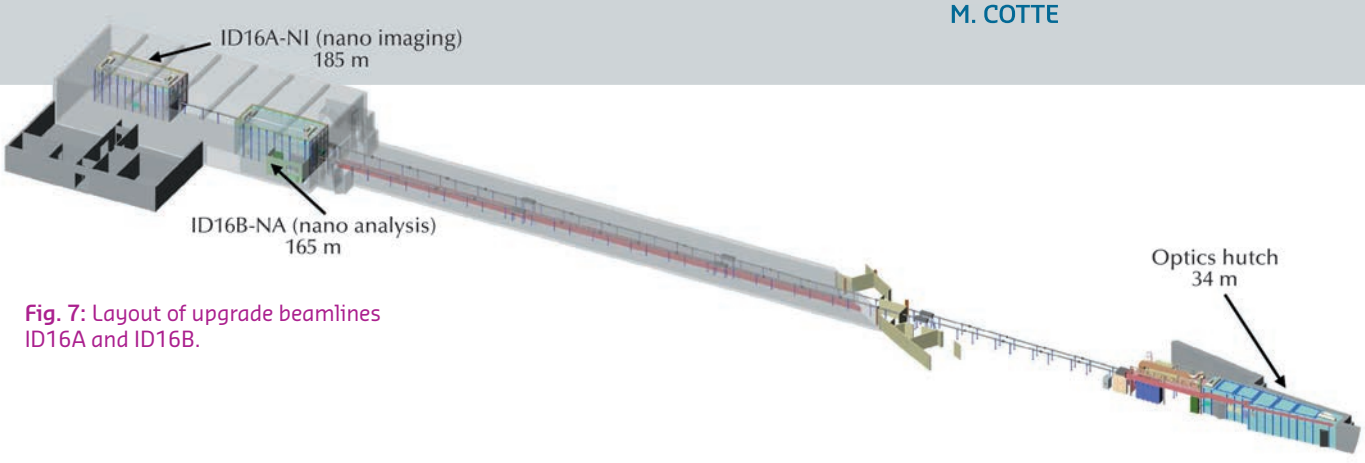

Fig. 7: Layout of upgrade beamlines ID16A and ID16B.

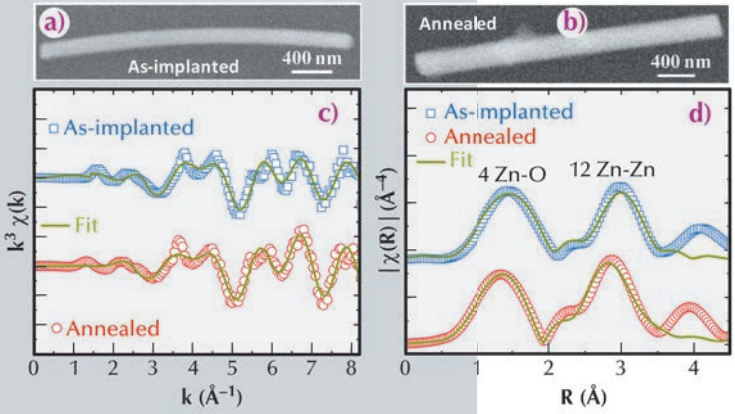

Fig. 8: Nano-EXAFS study of as-implanted (a) and annealed (b) Co:ZnO nanowires. Data and best fit of Zn K-edge EXAFS oscillation functions $k^3\chi(k)$ (c) and magnitude of the Fourier-transformed (d). The spectra reveal an elongation of the first two nearest interatomic distances for the as-implanted nanowire compared to the annealed one. It indicates an expansion of the lattice along the as-implanted nanowire. The similar interatomic distances between the annealed nanowire and bulk ZnO (1.95 ±0.02 and 3.23 ±0.02 Å) suggest a good recovery of the implantation-induced damage through a thermal annealing process (From Chu *et al.* [1]).

References
[1] M.H. Chu, G. Martínez-Criado, J. Segura-Ruiz, S. Geburt and C. Ronning, *Appl. Phys. Lett.* **103**, 141911 (2013).

DEVELOPMENT OF NEW TREATMENTS FOR EPILEPSY USING SYNCHROTRON RADIATION

Epilepsy is the most common neurological disorder with an incidence reaching 0.5% of the population. About one third of the patients with epilepsy are affected by medically refractory seizures. These patients are exposed to the risk of severe traumatic, metabolic and neuropsychological sequelae and can die as a consequence of uncontrolled seizures. Epilepsy surgery aiming to resect the epileptic focus can provide seizure freedom to selected patients but there is a high risk of neurological complications when the focus involves the eloquent cortex, such as the language and motor areas, or the dominant hippocampus, a structure located in the mesial part of the temporal lobe exerting a crucial role in the genesis of new memories. For refractory epilepsy located in brain regions unattainable with conventional surgery, multiple subpial transections (MST) and stereotactic radiosurgery (SRS) are the most attractive [1] of the non-resective surgical approaches. MST is a microsurgical procedure placing vertical incisions through the epileptic cortex in order to cut the horizontal axons responsible for the propagation of seizures while preserving the vertical columns acting as the basic unit of cortical function. Seizure spread is arrested by the parcellisation and disconnection of the ictal focus. The cortical columns subserving eloquent and non-eloquent neurological functions are not injured by MST, allowing the treatment of epileptic foci located over sensorimotor or language cortex not amenable to surgical resection.

Focal irradiation of an epilepsy focus through SRS is an emerging treatment for medically refractory seizures, providing a non-invasive approach which is mainly limited by the delay of efficacy and side effects (several months are required to obtain seizure relief). However, current LINAC- or cobalt-based technologies do not allow high doses to to be delivered to cortical slices of millimetric size, thus replicating the exquisite cortical incisions generated by MST.

We have investigated a novel and exciting approach combining the advantages of SRS and MST at beamline **ID17**, where arrays of microplanar beams were used to generate cortical transections equivalent to MST in a non-invasive, bloodless way. These microscopic arrays of X-ray beams

Principal publication and authors
P. Romanelli (a,b), E. Fardone (b), G. Battaglia (c), E. Bräuer-Krisch (b), Y. Prezado (b), H. Requardt (b), G. Le Duc (b), C. Nemoz (b), D.J. Anschel (d), J. Spiga (e) and A. Bravin (b), *PLoS ONE* 8, e53549 (2013).
(a) Brain Radiosurgery,Cyberknife Center,CDI, Milan (Italy)
(b) ESRF
(c) Istituto Di Ricovero e Cura a Carattere Scientifico Neuromed, Località Camerelle, Pozzilli (Italy)
(d) Comprehensive Epilepsy Center of Long Island, St. Charles Hospital, Port Jefferson, New York (USA)
(e) Department of Physics, University of Cagliari and Istituto Nazionale di Fisica Nucleare, Monserrato (Italy)

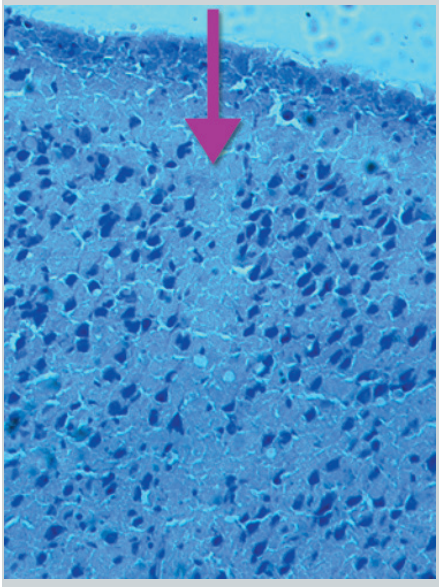

Fig. 9: Synchrotron-generated sensorimotor cortex transection.

(microbeams) originating from a synchrotron source were used to generate neocortical or hippocampal transections by delivering very high doses of radiation to tissue slices of microscopic thickness. Neurons, glia and axons along the penetration path were ablated, leaving a path equivalent to that of a microsurgical incision (**Figure 9**). The adjacent tissue was exposed to much lower valley doses (less than 5 Gy) unable to induce histologically evident tissue damage [2]. In essence, synchrotron-generated cortical transections provide a microradiosurgical equivalent of MST. Compared to MST, which require an invasive procedure involving all the risks related to open surgery, microbeam transections are performed in a non-invasive way and the size and spacing of the transections can be modified by the surgeon according to the needs. We have also shown that microbeam transection of the primary motor cortex, a highly challenging target, is well tolerated. No sign of motor deficit was found after prolonged observation and periodic rotarod testing. Convulsive seizures originating from this region disappeared almost immediately after microbeam transections.

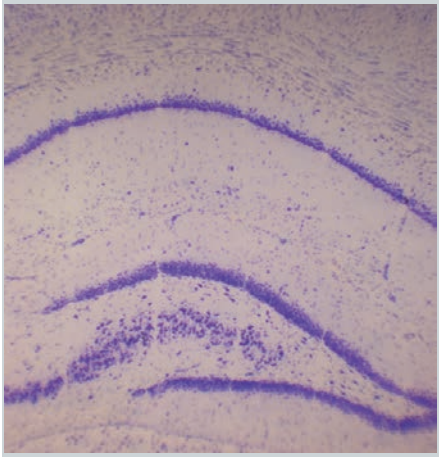

Fig. 10: Synchrotron-generated hippocampal transections.

Seizure control and preservation of motor function after sensorimotor cortex transection are an exciting new application of synchrotron-generated microbeams, opening the way to the application of this new concept to the most common source of medically-refractory seizures, the hippocampus. We have investigated hippocampal transections in a rat model (**Figure 10**) and further studies are ongoing to characterise the ability of hippocampal transections to control seizures originating from this region.

Microbeam transections hold a great potential to modulate cortical function and to treat focal epilepsy. Microbeam transections, either placed over neocortical seizure foci or through the hippocampus, could prove to be an excellent tool to be added to the current techniques used to control seizures. The development of devices delivering submillimetric beams able to generate cortical transections might add a powerful new tool to the clinical treatment of epilepsy and, more generally, to modulate cortical functions in a wide variety of neuropsychiatric disorders.

References
[1] P. Romanelli, P. Striano, M. Barbarisi, G. Coppola and D.J. Anschel, *Epilepsy Res.* **99**, 193-201 (2012).
[2] P. Romanelli and A. Bravin, *Neurol Res.* **33**, 825-31 (2011).

OLDEST KNOWN PRIMATE SKELETON CASTING A NEW LIGHT ON THE ORIGIN OF ANTHROPOIDS

Principal publication and authors
X. Ni (a,d), D.L. Gebo (b), M. Dagosto (c), J. Meng (d), P. Tafforeau (e), J.J. Flynn (d) and K.C. Beard (f), *Nature* **498**, 60-64 (2013).
(a) Chinese Academy of Sciences (China)
(b) Northern Illinois University (USA)
(c) Northwestern University (USA)
(d) American Museum of Natural History (USA)
(e) ESRF
(f) Carnegie Museum of Natural History (USA)

Primates is a mammalian order that includes lemurs, tarsiers, monkeys, apes and human beings. The oldest known undoubted fossil primates are about 55 million years old [1]. Fossils from this era are extremely rare. Only bone fragments and isolated teeth of these earliest primates are previously known. We have discovered the world's oldest known fossil primate skeleton representing a previously unknown genus and species named *Archicebus achilles*.

The fossil was unearthed from sedimentary rock strata that were deposited in an ancient lake roughly 55 million years ago, during the early part of the Eocene epoch, in central China's Hubei Province, near the course of the

modern Yangtze River. It is about 7 million years older than the oldest fossil primate skeletons known previously, which include *Darwinius* from Messel in Germany and *Notharctus* from the Bridger Basin in Wyoming.

Like most other fossils recovered from ancient lake strata, the skeleton of *Archicebus* was found by splitting apart the thin layers of rock containing the fossil. As a result, the skeleton of *Archicebus* is now preserved in two complementary pieces called a "part" and a "counterpart", each of which contains elements of the actual skeleton as well as impressions of bones from the other side.

In order to study the entire fossil, we scanned the specimen at beamlines **ID17** and **ID19**. We used a specific technology developed at the ESRF to examine those parts of the fossil that are still buried in the rock at a level of detail that is unique in the world. Three-dimensional digital reconstruction of the fossil using the synchrotron scans allowed us to study the tiny, fragile skeleton of *Archicebus* in intricate detail (**Figure 11**).

Archicebus marks the first time that we have a reasonably complete picture of a primate close to the divergence between tarsiers and anthropoids. It represents a big step forward in our efforts to chart the course of the earliest phases of primate and human evolution.

Archicebus differs radically from any other primate, living or fossil, known to science. It looks like an odd hybrid with the feet of a small monkey, the arms, legs and teeth of a very primitive primate, and a primitive skull bearing surprisingly small eyes. Therefore in addition to being the oldest known example of an early primate skeleton, the new fossil is crucial for shedding light on a pivotal event in primate and human evolution.

The evolutionary relationships among primates and their potential relatives, and among the major lineages within the primate order have been debated intensively for many years **[1,2]**. To test the different hypotheses and determine the phylogenetic position of the new primate, we carried out cladistic analysis based on a huge database that includes both molecular and morphological information. The results of our analysis indicate that *Archicebus* belongs to an entirely separate branch of the primate evolutionary tree that lies much closer to the lineage leading to modern monkeys, apes and humans (**Figure 12**). *Darwinius* and *Notharctus*, on the other hand, are adapiform primates that are early relatives of living lemurs, the most distant branch of the primate family tree with respect to humans and other anthropoids.

Even though *Archicebus* appears to be a very basal member of the tarsier lineage, it resembles early anthropoids in several features, including its small eyes and monkey-like feet. This suggests that the common ancestor of tarsiers and anthropoids was in some ways more similar than most scientists have thought.

Statistical analyses aimed at reconstructing how much an adult *Archicebus* would have weighed and what kind of activity pattern the animal would have had in life show that it was active during daytime and slightly smaller than the smallest living primates, which are pygmy mouse lemurs from Madagascar. The very basal evolutionary position of *Archicebus* supports the idea that the common ancestor of tarsiers and anthropoids was diurnal and miniscule. This overturns earlier ideas suggesting that the earliest members of primates were nocturnal and quite large.

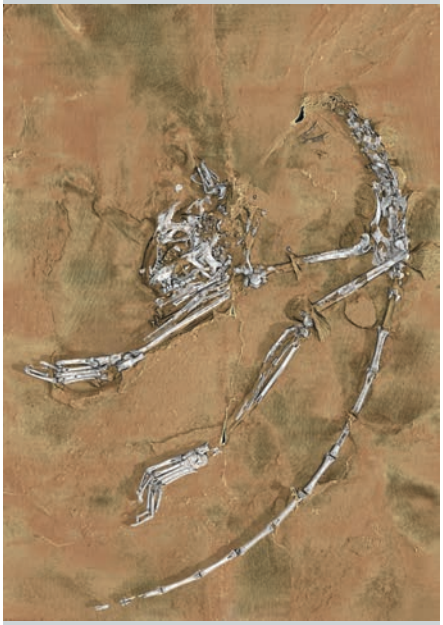

Fig. 11: Three-dimensional reconstruction of the type specimen (IVPP V18618) of *Archicebus Achilles*, images acquired at ID17.

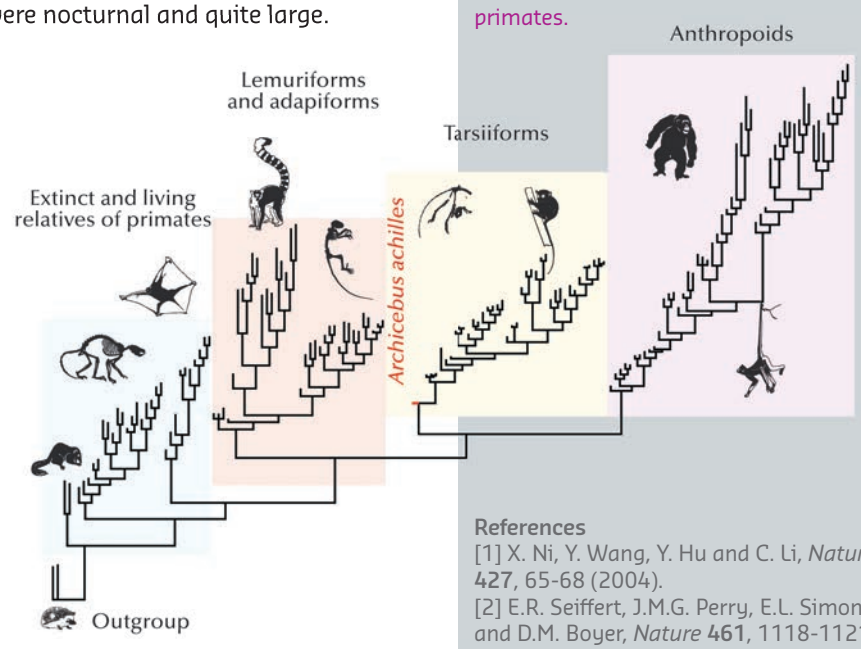

Fig. 12: Summary phylogenetic tree showing *Archicebus achilles* as the most basal taxa of tarsiiform primates.

References
[1] X. Ni, Y. Wang, Y. Hu and C. Li, *Nature* **427**, 65-68 (2004).
[2] E.R. Seiffert, J.M.G. Perry, E.L. Simons and D.M. Boyer, *Nature* **461**, 1118-1121 (2009).

HIDDEN ANATOMICAL FEATURES OF AN EARLY TETRAPOD REVEALED BY PPC-SRμCT

Principal publication and authors
S.E. Pierce (a,b), P.E. Ahlberg (c), J.L. Molnar (b), S. Sanchez (c,d), P. Tafforeau (d), J.R. Hutchinson (b) and J.A. Clack (a). *Nature* **494**, 226–229 (2013).
(a) University Museum of Zoology, Department of Zoology, University of Cambridge (UK)
(b) Department of Comparative Biomedical Sciences and Structure & Motion Laboratory, The Royal Veterinary College, Hatfield (UK)
(c) Subdepartment of Evolution and Development, Department of Organismal Biology, Evolutionary Biology Centre, Uppsala University (Sweden)
(d) ESRF

One of the most significant events in Earth's evolutionary history was that which produced terrestrial vertebrates (tetrapods) from water bound fish. Transformation of fins into limbs (with fingers and toes) is usually considered the most crucial step in tetrapod evolution; however, modifications of the vertebral column (and ribs) are of equal importance as the 'backbone' helps to both stabilise and mobilise the body during movement. The exact anatomical construction of the vertebral column in the earliest tetrapods has, however, been a point of discussion for over a century, primarily because vertebral elements remain trapped within rock matrix obscuring critical anatomical detail.

Recently, the three-dimensional skeletal anatomy of the 360 million year old stem tetrapod *Ichthyostega* (**Figure 13a**) was recreated from microcomputed tomography (μCT) scans **[1]**. The μCT data exposed all elements within the vertebral column and indicated the presence of new and exciting anatomical features, as well as an unexpected vertebral configuration. However, the resolution of the images was quite low, making the vertebral structures look somewhat blurry. Moreover, beam-hardening artefacts, due to the bright-white oxide inclusions within the inner spongiosa that absorbed a high proportion of the dynamic range, made the outer layer of the bone (cortex) indiscernible (**Figure 13b**). The resulting three-dimensional rendering of the vertebral column was of poor quality and missing detailed anatomical features necessary to make confident evolutionary inferences.

To overcome this limitation, key fossil specimens were subjected to propagation phase-contrast X-ray synchrotron microtomography (PPC-SRμCT) at beamline **ID19** using a specially developed attenuation protocol for imaging large, dense fossils with metallic oxide inclusions. The attenuation protocol, detailed by Sanchez *et al.* **[2]**, involves immersing fossil samples in a tube filled with aluminium or glass balls, and placing a U-shaped aluminium profiler between the beam and the sample. The net effect normalises the absorption profile by increasing the relative ratio of photons going through the densest parts of the sample, thereby providing access to a larger dynamic range of the detector. The combination of PPC-SRμCT, a polychromatic beam and the attenuation protocol, produced superior quality images as compared to traditional μCT, including substantially greater contrast and crisp anatomical details (**Figure 13c**).

High resolution three-dimensional rendering of the PPC-SRμCT data led to the discovery of hitherto undocumented anatomical features within the vertebral column of *Ichthyostega* (**Figure 14**). These include: (1) a change in neural spine and transverse process orientation along the column, indicating specialisation of axial musculature; (2) the first evolutionary appearance of a sternum, which would

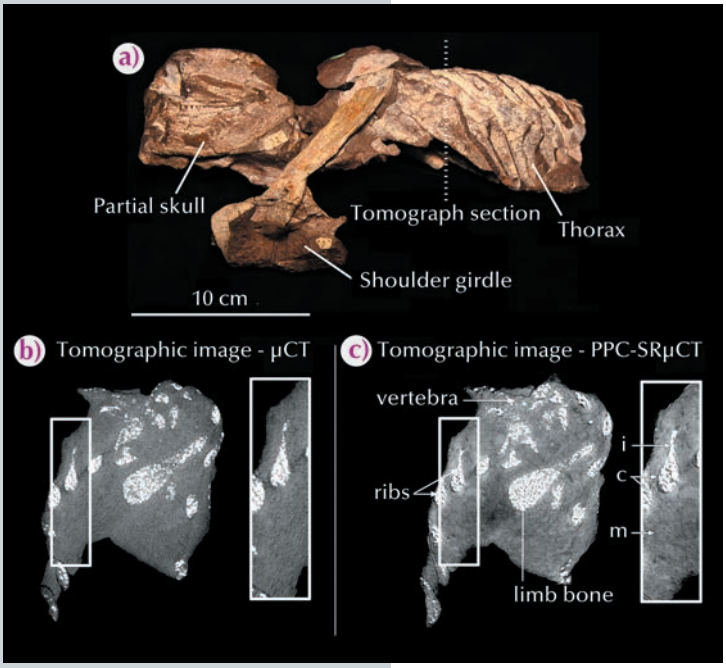

Fig. 13: (a) Photograph of *Ichthyostega* fossil material (MGUH VP 6115) showing region of the comparative tomographic slice; (b) μCT image showing a section through the thorax of *Ichthyostega* embedded in rock matrix, m. Notice the bright, white metallic oxide inclusions in the spongiosa, i, prevent the cortical surfaces, c, of the bones from being resolved; (c) Image at the same location as (b) obtained with PPC-SRμCT and the attenuation protocol. The image reveals improved contrast and sharp anatomical structures, with the exact cortical surfaces of the bones resolved.

have strengthened the ventral region of the ribcage perhaps permitting the animal to balance its body weight on its chest; (3) an unusual posterior-to-anterior ossification sequence, a pattern in opposition to *Hox* gene expression patterns and a developmental trend previously only documented in fish; (4) a complete rearrangement of the bones within each vertebral unit, a significant evolutionary result which culminated in a redefinition of the tetrapod plesiomorphic state.

Overall, this collaborative project added new and valuable anatomical data that has helped to redefine and elucidate the fish-tetrapod evolutionary transition. It also advanced fossil imaging techniques, opening the possibility for future groundbreaking discoveries.

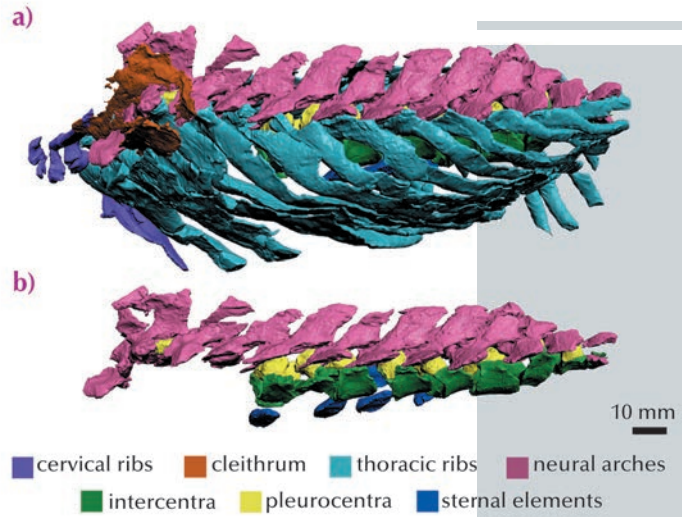

Fig. 14: Thorax region of *Ichthyostega* (MGUH VP 6115) rendered from PPC-SRμCT data. (a) Lateral view of whole specimens; (b) Lateral view of vertebral elements only. Rock matrix removed to highlight bony structures. Anterior towards left. Scale bar, 10 mm.

References
[1] S.E. Pierce, J.A. Clack and J.R. Hutchinson. *Nature* **486**, 523–526 (2012).
[2] S. Sanchez, V. Fernandez, S.E. Pierce and P. Tafforeau, *Nat. Protocols* **8**, 1708–1717 (2013).

ODDEST COUPLE EVER FOUND

Principal publication and authors
V. Fernandez (a), F. Abdala (a), K.J. Carlson (a,b), D. Collins Cook (b), B.S. Rubidge (a), A. Yates (a,c) and P. Tafforeau (d), *PLoS ONE* **8**, e64978 (2013).
(a) Evolutionary Studies Institute, University of the Witwatersrand (South Africa)
(b) Department of Anthropology, Indiana University (USA)
(c) Museum of Central Australia, Alice Springs (Australia)
(d) ESRF

Burrowing is a widespread activity in the animal kingdom that is used for a great variety of reasons such as predator protection or food hoarding. In hostile environments, adaptation to a fossorial lifestyle is crucial as it provides a more stable environment throughout the year. The numerous fossilised burrow casts from the Permo-Triassic period (~ 252 Million years ago) of South Africa are viewed as a response by terrestrial tetrapods in order to survive the harsh climatic conditions following the mass extinction event that occurred at the end of the Permian period. A few therapsids (forerunners of mammals) have been discovered in fossilised burrow casts, documenting the importance of fossorial lifestyles in this lineage for overcoming harsh climatic conditions. However, while hundreds of fossilised burrow casts have been reported from these rocks, relatively few studies have been undertaken on them as the information required is hidden within rock. The traditional protocol, until now, has consisted of cracking open the burrow casts and, if fossilised skeletal material was preserved, removing the rock of the cast to expose the encased bony elements.

The use of X-ray tomography as an alternative non-destructive extraction protocol for these types of studies is a solution that enables the investigation of the entire burrow cast. A sample investigation performed using laboratory X-ray sources, however, was limited by the lack of contrast between sediment and fossilised bones (**Figure 15**). Propagation phase contrast synchrotron microtomography has overcome this problem and made it possible to visualise the contents of a burrow cast as large as 18 cm in diameter. We used the microtomography set-up at beamline **ID17** which produced a wide and highly energetic monochromatic beam with a long propagation distance. In addition, we used attenuation and half-acquisition protocols **[1,2]**.

The first experiment of this kind on a fossilised burrow cast revealed the skeletons of the fox-sized mammal-like reptile *Thrinaxodon* and temnospondyl amphibian *Broomistega* (**Figure 16**). Full segmentation of both skeletons showed

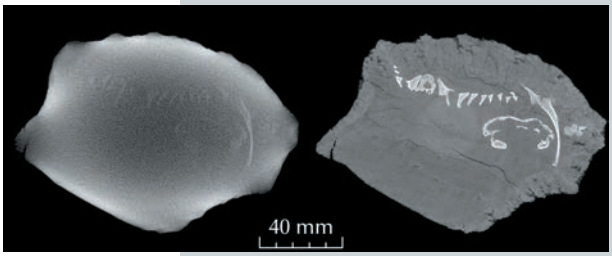

Fig. 15: Comparison of a virtual transverse section of the burrow cast obtained from a laboratory micro-CT (left) and from the ID17 beamline (right). Fossilised bones appear in white.

Fig. 16: Three-dimensional rendering of the *Thrinaxodon* (light brown) and the *Broomistega* (green) enclosed in the burrow cast.

References
[1] K.J. Carlson, D. Stout, T. Jashashvili, D.J. De Ruiter, P. Tafforeau, K. Carlson, L.R. Berger, *Science* **333**, 1402-1407 (2011).
[2] S. Sanchez, V. Fernandez, S.E. Pierce, P. Tafforeau, *Nature Protocols* **8**, 1708–1717 (2013).

that the two animals were buried together at the terminal end of the burrow. The study of the sedimentological pattern indicated that the two animals most likely died from a series of rapid flood events that filled the burrow. It appeared that neither animal was flushed into the burrow by the flooding event, rather they were both present before the flood.

We investigated possible reasons for such an odd cohabitation of two animals with a similar diet and similar body size. Close examination of the skeleton of the *Broomistega* showed a series of seven broken ribs on the right side of the animal. As some of these fractures were healed or healing, it was clear that this trauma occurred before the flooding event and was not directly related to the death of the animal. As *Broomistega* was primarily an aquatic creature, we concluded that it probably used the burrow as a temporary shelter because its injury would not have permitted rapid escape from predators while on land.

Comparison with examples of modern burrow-sharing of different species led to the conclusion that tolerance of the visitor by the host was driven by exceptional conditions. As several *Thrinaxodon* specimens have previously been discovered in curled-up positions and also preserved within burrow casts, it was hypothesised that this animal was aestivating in burrows during arid parts of the year. Experiencing deep torpor may explain why so many individuals of this species have been buried in such a resting posture. Discovery of this exceptional cohabitation corroborates this hypothesis, documenting how our very distant ancestors may have adapted to harsh climatic conditions and lack of food and water resources, successfully surviving the most calamitous mass extinction event in the history of life on Earth.

HEARING BY WORD OF MOUTH

Principal publication and authors
R. Boistel (a,b,c), T. Aubin (a,b), P. Cloetens (d), F. Peyrin (d,e), T. Scotti (f), P. Herzog (f), J. Gerlach (g), N. Pollet (h), and J.-F. Aubry (i), *Proc Natl Acad Sci U S A*. **110**, 15360-15364 (2013).
(a) Centre de Neurosciences Paris-Sud (CNPS), Centre National de la Recherche Scientifique (CNRS) Unité Mixte de Recherche (UMR) 8195, Université Paris XI, Orsay (France)
(b) Université Paris Sud, Orsay (France)
(c) Institut International de Paléoprimatologie et de Paléontologie Humaine (IPHEP), CNRS UMR 7262, Université de Poitiers (France)
(d) ESRF
(e) Centre de Recherche en Acquisition et Traitement de l'Image pour la Santé, CNRS UMR 5515, Institut national des sciences appliquées de Lyon, Villeurbanne (France)
(f) Laboratoire de Mécanique et d'Acoustique (LMA), CNRS UPR 7051, Marseille (France)
(g) Nature Protection Trust of Seychelles, Victoria, Mahé (Seychelles)
(h) Institute of Systems and Synthetic Biology, Genopole, CNRS, Université d'Evry Val d'Essonne (France)
(i) Institut Langevin, CNRS UMR 7587, École supérieure de physique et de chimie industrielles de la ville de Paris ParisTech (France)

X-rays enabled the discovery of a new hearing mechanism for animals lacking an ear. Using X-ray synchrotron holotomography, the biomechanical properties of ear tissues have been measured and a model of the acoustic propagation and resonator mode generated from these measurements.

The mechanism of sound perception is globally well understood. We know that the outer ear receives sound waves and that the tympanic or middle ear transmits these waves to the eardrum. The sound waves make the eardrum vibrate, and the eardrum delivers these vibrations to the inner ear using one or several ossicles. Finally specialised nerve cells of the inner ear translate the vibrations into nervous pulses sent to the brain.

Vertebrates such as mammals, birds, crocodylids, turtles and squamatas use this mechanism. However, we know that the middle ear evolved independently many times in terrestrial tetrapods [1]. The functional anatomy of hearing in frogs differs from that of other terrestrial tetrapods. Most frogs have only a tympanum at the head surface, even though two species use ultrasound call and are equipped with a tympanic cavity [2,3,4]. Moreover, several species are "earless" in the sense that they lack a tympanic middle ear. Indeed, we know that approximately three hundred frog species lack a tympanic middle ear.

Gardiner's frogs (*Sechellophryne gardineri*) from the Seychelles are one of the smallest frogs in the world with a length of about 10 mm (**Figure 17**). They do not possess a middle ear with an eardrum yet they produce acoustic signals. These frogs are members of the *Sooglossidae* family and they evolved in isolation on the Seychelles Archipelago over the last 47–65 My. We sought to understand how these frogs perceive sound without a middle ear and eardrum, and how they perceive

sound when 99.9% of any sound wave reaching an animal is reflected at the surface of its skin.

To investigate whether Gardiner frog's use sound to communicate with each other, we set up loudspeakers in their natural habitat to broadcast an array of pre-recorded mating calls. This caused male frogs present in the rainforest to answer. Therefore we established that Gardiner frogs are able to hear and that they use acoustic communication. The next step was to understand the hearing mechanism used by this species of apparently deaf frogs, from an anatomical point of view.

Various mechanisms have been proposed for other frogs without a middle ear: an extra-tympanic pathway through the lungs, muscles connected to the inner ear, and bone conduction. We used X-ray tomographic techniques at beamline **ID19**, including holotomography, to scan Gardiner's frogs and related frogs equipped with a middle ear (**Figure 18**). We then constructed 3D models of these frogs to analyse the head's functional anatomy in detail. We established that neither the pulmonary system nor the muscles could contribute significantly to the transmission of sound to the inner ears.

We then used numerical simulations to investigate the possibility that the sound was received through the frog's head (**Figure 18**). These simulations highlighted the key role played by the mouth which acts as a resonator, or amplifier, for the frequencies emitted by this species (**Figure 18**). X-ray imaging of different species showed that the transmission of the sound from the oral cavity to the inner ear has been optimised by two evolutionary adaptations located between the mouth and the inner ear, a reduction in thickness of the tissue and a smaller number of tissue layers. Our conclusion is that sound perception in Gardiner's frogs is without use of a tympanic middle ear and occurs by the unique combination of a resonating mouth cavity and bone conduction (**Figure 18**).

Fig. 17: Gardiner's frog in natura and volume rendering obtained by a holotomography scan.

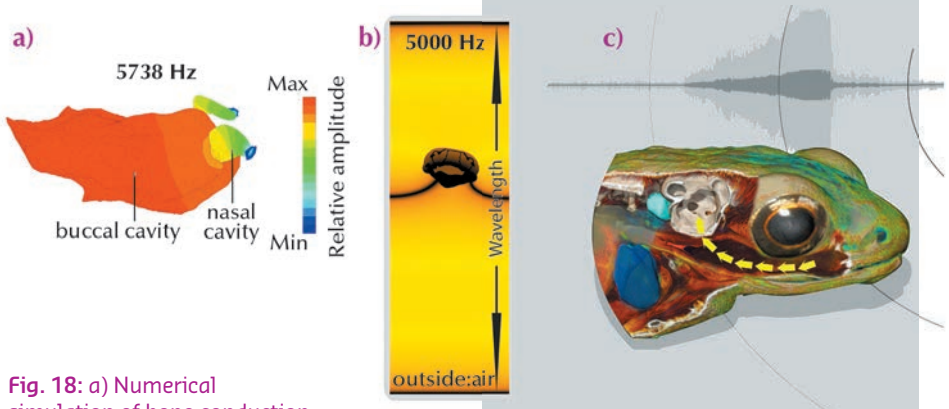

Fig. 18: a) Numerical simulation of bone conduction and mouth cavity (resonator). b) Volume rendering of head illustrating the sound transmission in to inner ear. c) Illustration of the Gardiner's frog hearing mechanism: the mouth acts as a resonating cavity for the frequencies of the frog's song, amplifying the amplitude of the sound in the mouth. The body tissue between the buccal cavity and the inner ear is specially adapted to transmit these sound waves to the inner ear.

References
[1] J.W.H. Schnupp and C.E. Carr, *Nat Neurosci* **12**, 692–697 (2009).
[2] A.S. Feng, P.M. Narins, C.H. Xu, W.Y. Lin, Z.L. Yu, Q. Qiu, Z.M. Xu and J.X. Shen, *Nature* **440**, 333-6 (2006).
[3] V.S. Arch, T.U. Grafe, M. Gridi-Papp and P.M. Narins, *PLoS One* **4**, e5413 (2009);
[4] R. Boistel *et al. PLoS One* **6**, e22080 (2011).

THE INTERACTION OF ASBESTOS AND IRON IN LUNG TISSUE REVEALED BY SYNCHROTRON-BASED SCANNING X-RAY MICROSCOPY

Asbestos is a potent carcinogen associated with malignant mesothelioma and lung cancer but its carcinogenic mechanisms are still poorly understood. Asbestos toxicity is ascribed to its particular physico-chemical characteristics including the presence of the fibres and their ability to adsorb iron, which may cause an alteration of the homeostasis

Principal publication and authors
L. Pascolo (a), A. Gianoncelli (b), G. Schneider (c), M. Salomé (d), M. Schneider (e), C. Calligaro (f), M. Kiskinova (b), M. Melato (a) and C. Rizzardi (c), *Scientific Reports* **3**,1123 (2013).
(a) Institute for Maternal and Child Health, IRCCS Burlo Garofolo, Trieste (Italy)
(b) Elettra - Sincrotrone Trieste S.C.p.a., Trieste (Italy)
(c) Department of Anatomical Pathology, University of Trieste (Italy)
(d) ESRF
(e) Hospital of Monfalcone, Monfalcone (Italy)
(f) Servizio Diagnostica Veterinaria, University of Udine (Italy)

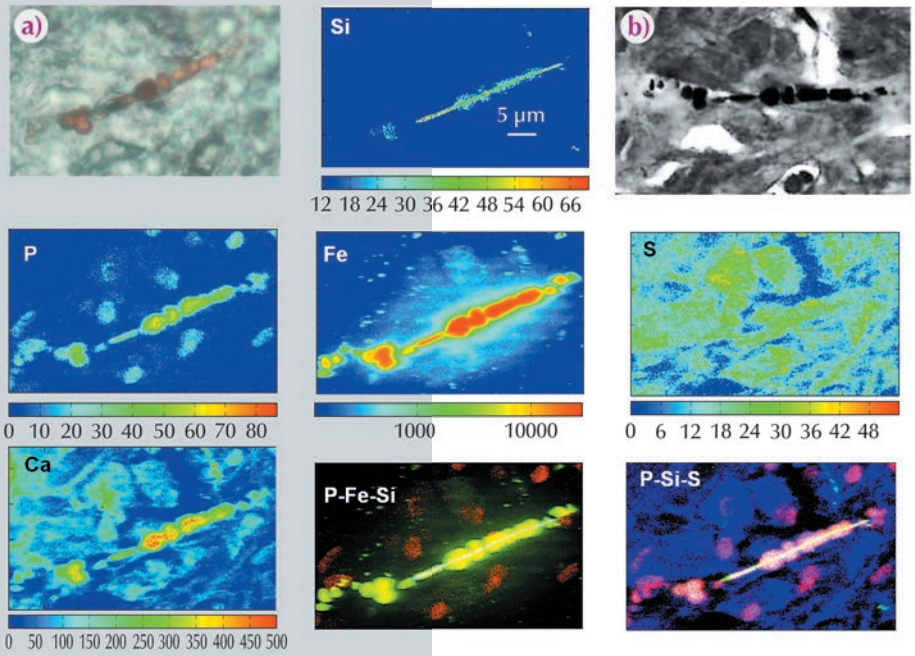

Fig. 19: Micro-XRF and X-ray microscopy of lung tissue containing asbestos. (a) Visible light image; (b) X-ray microscopy absorption image (TwinMic beamline, 0.9 keV) and the corresponding Si, Ca, P, S and Fe XRF maps (ID21, 7.3 keV).

of this element in the tissue. When asbestos fibres are inhaled, they may get trapped within the lung and remain indefinitely in the body locked inside biostructures called "asbestos bodies" which are the result of a complex biomineralisation process. Using a combination of advanced synchrotron-based X-ray imaging and microspectroscopic methods, we studied representative lung tissue samples from ten patients exposed to asbestos (from shipyard workers in Monfalcone, Italy). We obtained important correlative morphological and chemical information on the chemistry of asbestos body formation and other changes in the surrounding lung tissue. The iron concentration, distribution and speciation in diseased human lungs were analysed for the first time thanks to the high elemental and chemical sensitivity of synchrotron XRF spectro-imaging and micro-XANES available at beamline **ID21**. Our results contribute to an explanation of iron mobilisation while asbestos is present in lung tissue. Fe XRF maps (**Figure 19**, Fe panel) clearly demonstrate how the asbestos fibres and bodies can cause high mobilisation of iron into the surrounding cells (mainly alveolar macrophages) and tissue. The results suggest both continuous deposition of Fe-containing species (ferritin) around the asbestos fibres and metal release due to asbestos body degradation. Confirming and expanding on previous studies **[1]**, the results showed that, along with iron, other chemical elements, including phosphorus, calcium and magnesium, participate in the formation of asbestos bodies and are also indicative of calcification processes. In **Figure 19** the asbestos body is identified by light microscopy (panel a) as an orange-brown formation, while the X-ray absorption image in panel (b) (obtained at TwinMic beamline, Elettra Synchrotron) allows better definition of the features of the body. The XRF elemental maps allow identification of the original silicate fibre (Si map), from which the asbestos body originated. The coating is best represented by P and Fe maps. The Fe map clearly shows accumulation of Fe in the vicinity of the asbestos bodies, both as a diffuse signal and as bright spots resembling intracellular vesicles or siderosomes. Interestingly, P and S maps reveal cell structures: S seems to be a good marker of cell substance and useful to delineate cytoplasmic borders, while P seems to pinpoint the cell nuclei where the content of this element is high. When merging the P, Si and Fe maps (P-Fe-Si) or P, Si and S maps (P-Si-S), it appears that both the majority of iron diffuse signal and the vesicular spots, are mainly related to the presence of macrophage-like cells. The calcium distribution (Ca) appears to correlate with cell and tissue architecture but it is much more abundant in the coating of the asbestos body.

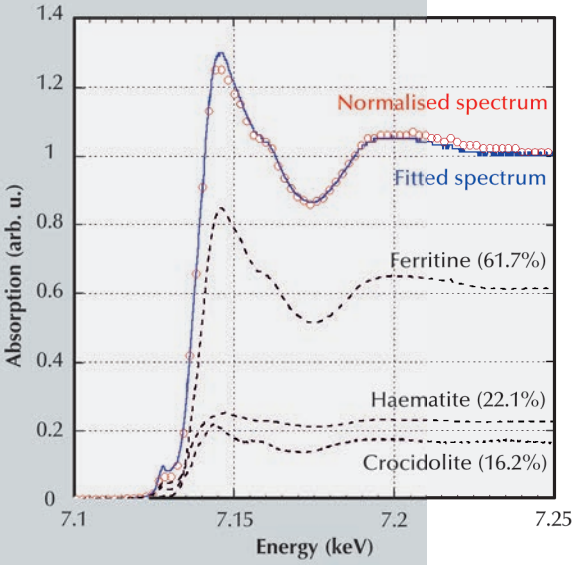

Fig. 20: Micro-XANES analyses of asbestos bodies. An example of a deconvoluted micro-XANES spectrum of an asbestos body measured with a microprobe of 1 µm^2 at ID21.

Since the oxidation state of Fe could provide important information on the processes involved in the asbestos body formation, Fe K-edge XANES spectra

were collected in selected ~1 μm^2 spots from the Fe maps at beamline ID21 (**Figure 20**). The measures confirm that most of the iron detected around asbestos fibres (coating and ferruginous bodies) is compatible with the presence of ferritin and the Fe^{3+} oxidation state of iron. In addition, micro-XANES analyses demonstrate their potential to discriminate the fate of iron-containing fibres from iron-free asbestos in lung tissues. However, the most novel and intriguing result of micro-XANES analyses was the detection of significant percentages of haematite in the asbestos bodies. We suppose that this is the result of ferritin transformation occurring during the prolonged residence time in the asbestos bodies in the lung tissues.

References
[1] L. Pascolo, A. Gianoncelli, B. Kaulich, C. Rizzardi, M. Schneider, C. Bottin, M. Polentarutti, M. Kiskinova, A. Longoni and M. Melato, *Part Fibre Toxicol.* **8**, 7 (2011).

RECOVERING THE FIRING PROTOCOL OF ANCIENT CERAMICS THROUGH IRON PHASE DISTRIBUTION ANALYSIS USING FULL-FIELD XANES IMAGING

Principal publication and authors
F. Meirer (a), Y. Liu (b), E. Pouyet (c), B. Fayard (c), M. Cotte (c, d), C. Sanchez (e), J.C. Andrews (b), A. Mehta (b) and P. Sciau (f), *J. Anal. At. Spectrom.* **28**, 1870-1883 (2013).
(a) Debye Institute for Nanomaterials Science, Utrecht (Netherlands)
(b) SSRL-SLAC, Menlo Park (USA)
(c) ESRF
(d) Laboratoire d'Archéologie Moléculaire et Structurale, CNRS, Ivry-sur-Seine (France)
(e) Archéologie des Sociétés Méditerranéennes, CNRS, Lattes (France)
(f) CEMES-CNRS, Toulouse (France)

Fine ceramics with black high gloss slip on red bodies, manufactured in the Mediterranean basin from 6th c. BCE to 1st c. CE, were a benchmark of technological innovation in high temperature redox chemistry [1]. This technology, first developed in Corinth and Athens (6th c. BCE), slowly moved west to central and northern Italy (4th c. BCE) and finally to southern Roman Gaul where it vanished in the early decades of the 1st century CE. Although several tens of thousands of ceramic fragments have survived, a detailed technological protocol on how they were produced is almost entirely lost. Here, using two black gloss sherds from the Roman period, we show that by probing their mineralogical variation and distribution we can reconstruct some of this lost technology. Our results also indicate that although the basic Fe redox chemistry remained unchanged for over 600 years, significant changes in firing protocol took place even over a span of less than 100 years [2].

Because the minerals that reveal the lost processing conditions are often very heterogeneously distributed and confined to near surface and interfacial regions between the ceramic body and the slip, a probe with high spatial resolution, large field of view and high sensitivity to mineralogy is required to map them.

A new full-field spectromicroscopy technique at beamline **ID21** [3] that combines XANES and full-field imaging allowed us to map the Fe-phases in a Campanian ceramic (1st c. BCE, Italy), see **Figure 21**, and a similar microscope at BL 6-2 SSRL [4] allowed us to correlate Fe mineralogy with 3D porosity for another fragment from the same sherd. The phase maps show that dense zones (slip and some body regions) are hercynite (Fe^{2+}, green in **Figure 21**), while more oxygen permeable regions were predominantly maghemite (Fe^{3+}, blue in **Figure 21**).

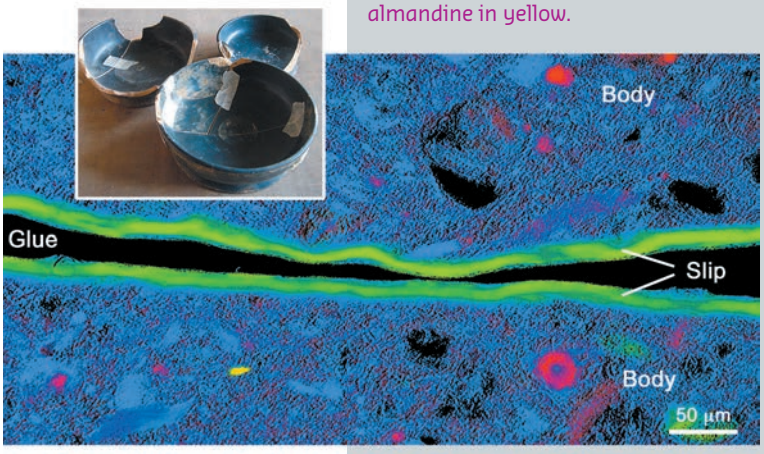

Fig. 21: Campanian ceramics (1st c. BCE) and Fe phase map of the cross-section of a sample. Hercynite is shown in green, maghemite in blue, hematite in red and almandine in yellow.

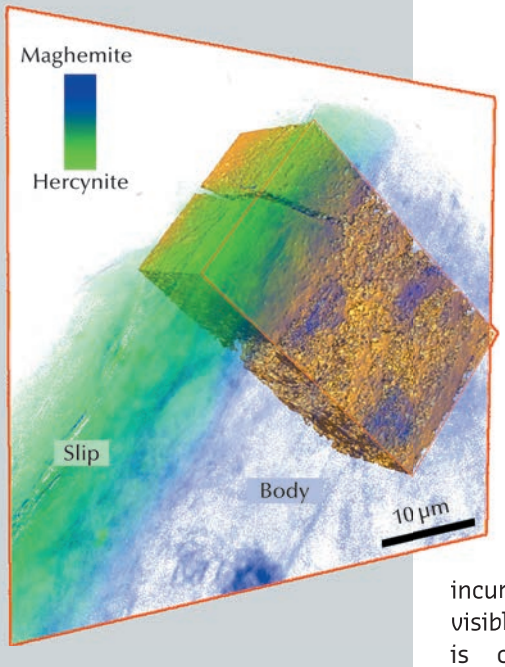

Fig. 22: Registration of the 3D tomographic data with the 2D mosaic phase map of the cross-section Campanian sample.

References

[1] J.V. Noble, *The techniques of painted Attic pottery*, New York (1965).
[2] P. Sciau, Y. Leon, P. Goudeau, S.C. Fakra, S. Webb and A. Mehta, *J. Anal. At. Spectrom.* **26**, 969 (2011).
[3] B. Fayard, E. Pouyet, G. Berruyer, D. Bugnazet, C. Cornu, M. Cotte, V. De Andrade, F. Di Chiaro, O. Hignette, J. Kieffer, T. Martin, E. Papillon, M. Salomé and V. A. Sole, *Journal of Physics: Conference Series* **425**, 192001 (2013).
[4] F. Meirer, J. Cabana, Y.J. Liu, A. Mehta, J.C. Andrews and P. Pianetta, *Journal of Synchrotron Radiation* **18**, 773 (2011).

Similar phase maps, not shown, were obtained for a Pre-sigillata ceramic (1st c. CE, Roman France). The mineralogical maps from the two sherds show subtle but significant differences.

The presence and distribution of maghemite, an intermediate Fe^{+3} mineral formed during re-oxidation of hercynite, is the key to some of the firing protocols. Occurrences of maghemite at the outside surface and the interface between slip and body, and especially the tendril like incursion from oxidised to reduced areas visible in **Figure 22**, in both ceramics is compelling and very pictorial evidence that these vessels were once reduced and then partially re-oxidised. Furthermore, a relatively uniform hercynite slip and nearly absent re-oxidation layer on the surface indicates a successful firing protocol that allowed the body to re-oxidise while preventing most of the slip from doing so. This remarkable achievement, that would be difficult even in modern replications, suggests possession of great skill in controlling the redox chemistry through sophisticated manipulation of clay chemistry and morphology and kiln firing conditions.

Differences in maghemite/hematite distribution in the two sherds, on the other hand, point to differences in firing protocol by highlighting two critical differences. The first critical difference is the very patchy and, when present, very thin oxidation layer on the surface of the Campanian slip in contrast to a thicker and more uniform layer on the Pre-sigillata slip. The second is the absence of hematite, except for a few small islands centred on embedded crystals, in the body of Campanian sherd as opposed to mostly hematite body of the Pre-sigillata sherd. These two distinctions, when combined with the presence of patches of un-oxidised Fe^{+2} minerals in the body (Almandine particle, and small patches of hercynite) suggests that the final re-oxidation step (in the three phase firing protocol, first outlined by Noble [1]) for the Campanian ceramic must have occurred at significantly lower temperature and/or shorter duration than that for the Pre-sigillata ceramic.

Full-field XANES microscopy should have a profound impact on the recovery of lost ancient ceramic technology. Its versatility should also lead to a deeper understanding of the functioning of other complex, hierarchically heterogeneous systems, such as heterogeneous catalysis and energy storage systems.

SYNCHROTRON X-RAY FLUORESCENCE SHOWS REDUCED NEURONAL COPPER IN VULNERABLE BRAIN REGIONS IN PARKINSON'S DISEASE

Principal publication and authors

K.M. Davies (a), S. Bohic (b), A. Carmona (c), R. Ortega (c), V. Cottama (a), D.J. Hare (d), J.P.M. Finberg (d), S. Reyes (a), G.M. Halliday (a), J.F.B. Mercer (f) and K.L. Double (a), *Neurobiology of Aging* **35**, 858-866 (2014).

(a) Sydney Medical School, University of Sydney (Australia)
(b) Inserm U836, Grenoble (France)
(c) CENBG - CNRS, Gradignan (France)
(d) Melbourne University (Australia)
(e) Faculty of Medicine, Technion, Haifa (Israel)
(f) Deakin University, Melbourne (Australia)

Neurodegenerative cascades in Parkinson's disease (PD) involve protein aggregation and oxidative stress. Although the triggers for these events are unknown, changes in biometals have long been suspected to play a role [1]. Copper is an important biometal in the brain, as exemplified by Menkes' and Wilson's diseases, which are serious neurological disorders of

Cu dyshomeostasis. Furthermore, the complexing of Cu with the PD-associated protein α-synuclein increases aggregation and toxicity of this protein, possibly via stimulation of free radical production [2]. But Cu is also an essential cofactor in a range of cuproproteins, including the key protective cellular antioxidant superoxide dismutase 1 (SOD1).

A major obstacle for the investigation of metals in neurodegenerative disease, however, has been the absence of suitable methods to study intracellular changes in the location and levels of metals and the broader regional distribution of metals in the postmortem human brain. Synchrotron radiation X-ray fluorescence microscopy (SRXFM) is ideal for highly sensitive, high resolution quantitative investigations of metals at the cellular level in the brain [3], as exemplified in **Figure 23**. We used SRXFM at beamline **ID22** (now closed and transferred to ID16) to investigate metals in individual surviving pigmented neurons within the degenerating substantia nigra pars compacta (SN) and locus coeruleus (LC), as well as in the non-degenerating occipital cortex, in the brains of cases with PD, incidental Lewy body's disease (ILBD) or Alzheimer's disease (AD), and compared with controls. Results from these single cell SRXFM studies were confirmed using microparticle induced X-ray emission (μPIXE) at the AIFIRA facility, CNBG, France, to quantify regional tissue metal levels. Copper (Cu) levels from non-degenerating tissues of the occipital cortex were similar in all cases. In contrast, Cu was significantly reduced within individual pigmented neurons of the degenerating SN and LC in PD and in ILBD, a disorder suggested as representing a preclinical stage of PD [4].

Quantitative analysis of fixed sections by SRXFM revealed a decrease up to 45% in neuromelanin (NM)-associated Cu in the SN from PD and ILBD cases with respect to both age-matched controls and AD cases. Our finding of decreased NM-associated Cu levels in the PD SN was confirmed in fresh frozen tissue sections. μPIXE analysis of NM-containing neurons confirmed a decrease in Cu-associated NM in PD and ILBD compared with controls. Similarly, Cu decrease was observed for NM from LC neurons in PD compared with controls, while no differences were seen in the grey matter of the occipital cortex. This data confirms a specific reduction in Cu within remaining NM-pigmented neurons in PD and shows that this deficit occurs in cases with ILBD and limited cell loss, suggesting an early deficit that precedes cell death and clinical symptoms. As Cu levels were not altered in the degenerating LC in AD, it is unlikely that the reduction in Cu observed in these regions in PD results simply from neurodegeneration *per se*. Furthermore, as Cu levels were unchanged in regions that do not degenerate in PD, it appears that this early decrease is specific to regions vulnerable to neuronal cell loss in this disorder.

We therefore examined the distribution and cellular localisation of Cu transport proteins, and activity of the protective antioxidant, and cuproprotein, superoxide dismutase 1 (SOD1), in

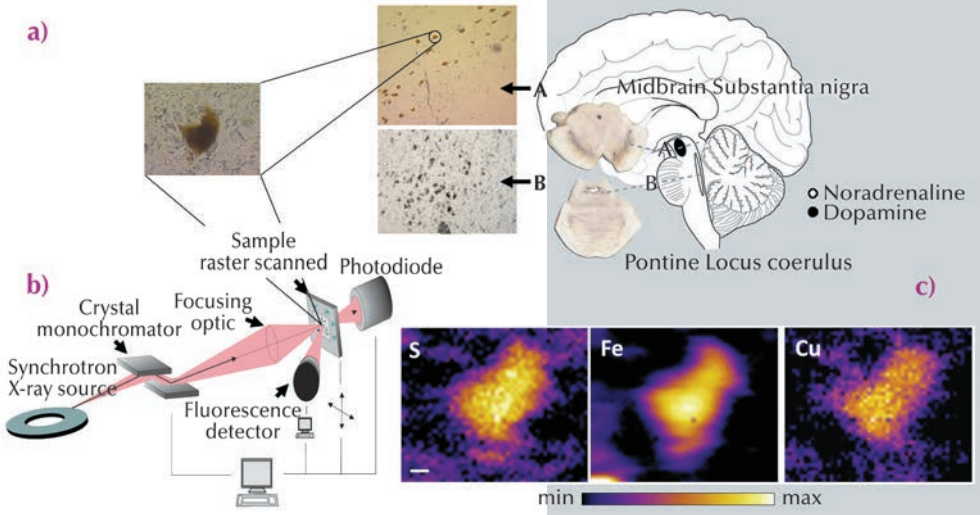

Fig. 23: (a) Anatomical location of the human brain nuclei studied. Typical section from the locus coeruleus (LC), substantia nigra pars compacta (SN) and a magnified view of typical neuromelanin (NM)-containing neurons from healthy human brain analysed by synchrotron radiation X-ray fluorescence microscopy (SRXFM) (b) Experimental set-up for SRXFM. (c) shows representative SRXRF maps for selected elements in a single intact NM-containing neuron of the SN shown in (a). Sulfur (S), iron (Fe) and copper (Cu). Scale bar 5 μm.

References
[1] S. Bolognin, L. Messori and P. Zatta, *Neuromolecular Med.* **11**, 223-238 (2009).
[2] X. Wang, D. Moualla, J.A. Wright and D.R. Brown, *J Neurochem.* **113**, 704-714 (2010).
[3] S. Bohic, K. Murphy, W. Paulus *et al., Anal Chem.* **80**, 9557-9566 (2008).
[4] D.W. Dickson, H. Braak, J.E. Duda *et al., Lancet Neurol.* **8**:1150-7 (2009).

post-mortem human brains with a pathological diagnosis of PD, compared with controls, using inductively coupled plasma-mass spectrometry, western blot, and immunofluorescence. We identified a marked reduction in neuronal Cu transport protein 1 (Ctr1) immunoreactivity in the SN in PD. Further, in the PD SN, neuron-associated Ctr1 levels were significantly correlated with Cu levels. In these same PD cases, in brain regions displaying α-synuclein pathology, SOD1 specific activity was altered to reflect the pattern of cell loss. The reductions in cellular Ctr1 and Cu would compromise the ability of these neurons to defend themselves against high levels of oxidative stress, consistent with the severity of cell loss observed in these PD-vulnerable brain regions. Further investigation of cupropathology in PD may identify novel targets for the development of protective therapies for this disorder.

HARD X-RAY NANOPROBE INVESTIGATIONS OF THE SUB-TISSUE METAL DISTRIBUTIONS WITHIN DAPHNIA MAGNA

Principal publication and authors
B. De Samber (a), K.A.C. De Schamphelaere (b), C.R. Janssen (b), B. Vekemans (a), R. De Rycke (c), G. Martinez-Criado (d), R. Tucoulou (d), P. Cloetens (d) and L. Vincze (a), *Anal. Bioanal. Chem.* **405**, 6061-6068 (2013).
(a) Department of Analytical Chemistry, Ghent University (Belgium)
(b) Laboratory of environmental toxicology and Applied Ecology, Department of Applied Ecology and Environmental Biology, Ghent University (Belgium)
(c) Department of Molecular Biomedical Research, Flanders Institute for Biotechnology (VIB), Belgium and Department of Biomedical Molecular Biology, Ghent University (Belgium)
(d) ESRF

The freshwater crustacean *Daphnia magna* is an important and frequently used model organism to investigate toxicity, uptake, elimination and detoxification processes associated with the exposure to transition metals (*e.g.* Cu, Zn, Ni) [1-2]. Since biological effects due to metals are initiated by metal bioaccumulation, the fundamental processes underlying bioaccumulation will lead to an improved capacity to evaluate the impact of metals on aquatic organisms [3]. Aquatic biota regulate their internal concentrations of essential metals through active regulation, storage/detoxification or a combination of both. To fully understand these processes, advanced trace level elemental imaging techniques are necessary as conventional bulk elemental analysis methods lack the ability to distinguish the accumulation in critical tissues from whole body accumulation [3]. Since our ultimate aim was to clarify some of the regulation processes by which metals influence the aquatic biota, the metal intoxication needs to be characterised by studying the tissue specific distribution of metals and also by determining their distribution at the sub-tissue level.

We performed exploratory experiments to study the tissue specific distribution of metals on the sub-micrometre scale using the intense nanometre sized hard X-ray beam at the XRF-nanoprobe of beamline **ID22NI**. Elemental distributions of trace concentration levels could be determined with unprecedented spatial resolution by scanning nano-XRF techniques, which can be translated into the quantitative distribution of metals and metalloids at the sub-microscopic level. With the aim of shifting the ecotoxicological research on *D. magna* from the microscopic tissue scales towards a (sub) cellular field of view, thin tissue sections of the crustacean *D. magna* were then analysed. Since nano-XRF has never been performed on Daphnia thin-sections, our measurements are the first to shed light on the sub-tissue metal distributions within these organisms, cultured under controlled exposure conditions. The laboratory clone juveniles (0-48h) of *Daphnia magna Straus* (clone K6), used in all our experiments, was originally collected from a pond in Kiel (Antwerp, Belgium) and has been successfully cultured under controlled laboratory conditions for more than

10 years. The basis exposure medium consisted of 0.077 mmol/L $NaHCO_3$, 0.078 mmol/L KCl, 0.5 mmol/L $MgSO_4$. The experiment was designed to investigate the accumulation of Zn at a concentration level of 1 mg/L, which caused a 50% mortality of the population after 48 hours of exposure.

Figure 24 shows an optical microscope image (a) of an unstained thin section (thickness 2 µm) of the osmoregulatory gill tissue of *Daphnia magna*, together with several scanning nano-XRF maps associated with the indicated sub-regions (z1, z2, z3), corresponding to the sub-tissue elemental distributions of Ca, Fe, Zn and Cl. **Figure 24b** and **c** show colour-coded (RGB) representations of the exopodite and filter plate regions with the conjoint presence of Ca (red), Zn (green) and Cl (blue). Interestingly, a cross section of an epipodite was present within this dorsoventral section, allowing the investigation of the distribution of cations and anions within this osmoregulatory gill tissue. **Figure 24d** shows an RGB representation of the conjoint presence of Ca, Zn and Fe within the epipodite. The marked presence of Fe confirms the haemolymph flowing through this tissue. This iron rich 'vesicle' is enclosed by respectively the Ca containing exoskeleton and a thin Zn rich layer in the micrometre range. These observations corroborate previous ecotoxicological research in which the accumulation of Zn within the exoskeleton was suggested [1]. The elevated levels of Zn could be clearly detected and quantified in the analysed regions, corresponding to concentration levels up-to 2500 ng/cm^2. The fast-scanning nano-XRF technique (typical acquisition time/pixel was 100-200 ms, pixel size 100-200 nm) was well-suited to trace level bio-imaging, demonstrating the potential of providing new insights in the cellular detoxification processes within these types of biological model organisms. Our results also illustrate that trace level chemical imaging using scanning X-ray fluorescence analysis is progressing towards the nanoscopic scales, advancing our understanding concerning the role of metals in ecotoxicology.

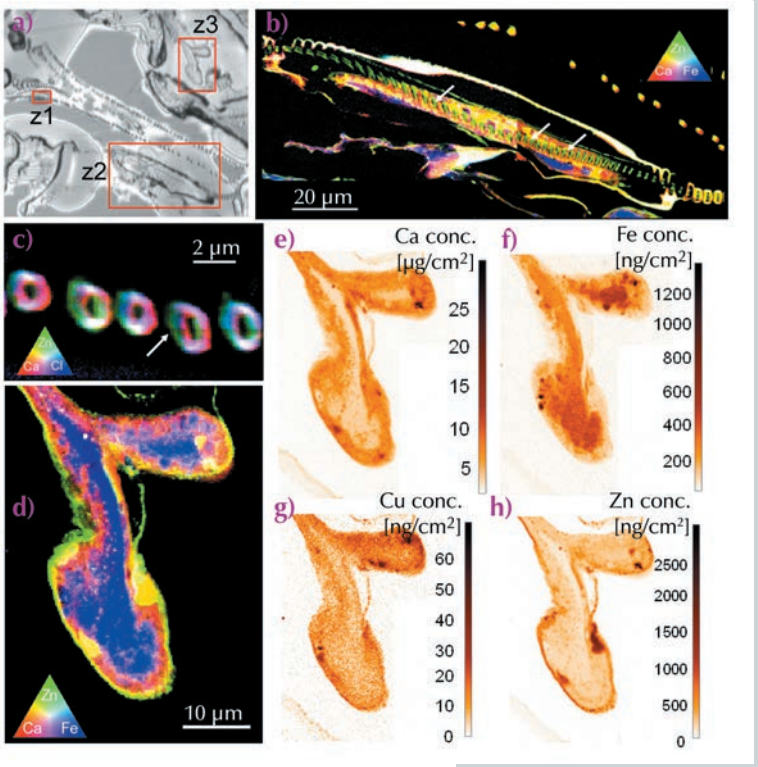

Fig. 24: a) Optical image of an unstained thin section (2 µm) of gill tissue of *D. magna;*
b) elemental distribution maps of Ca, Fe and Zn in the exopodite (region z2);
c) Ca, Zn and Cl distributions within the filter-plate (region z1);
d) Ca, Zn and Fe distributions within the epipodite (region z3);
e-h) areal concentration maps of Ca, Fe, Cu and Zn detected within the epipodite (region z3).

References
[1] B. Muyssen and C. Janssen, *Arch. Environ. Contam. Toxicol.* **43**, 492-496 (2002).
[2] K. De Schamphelaere and C. Janssen, *Environ. Sci. Technol.* **38**, 6201-6209 (2004).
[3] B. De Samber, G. Silversmit, K. De Schamphelaere, R. Evens, T. Schoonjans, B. Vekemans, C. Janssen, B. Masschaele, L. Van Hoorebeke, I. Szaloki, F. Vanhaecke, K. Rickers, G. Falkenberg and L. Vincze, *J. Anal. At. Spectrom.* **25**, 544-553 (2010).

DYNAMICS AND EXTREME CONDITIONS

As in previous years, the selected highlights can only give a flavour of the scientific accomplishments of the users of the Dynamics and Extreme Conditions group of beamlines. Their work resulted in about 100 publications in peer reviewed journals with 19 papers in high-impact journals. In this chapter we invite you to travel from Earth's crust through the mantle into the core before taking off to other planets of our solar system. This chapter also comprises a selection of studies on functional materials, including superconductors, before concluding with a fundamental study on the validity of the reciprocity principle.

March 2013 has seen a slight re-organisation of the group structure with beamline ID26 leaving to the Electronic Structure and Magnetism group, and the techniques and instrumentation test part of beamline ID06 joining our group. This station, currently reserved for in-house technical developments, provided, in 2013, the test bed for pulsed magnetic field studies, the development of X-ray phase plates and a compact, portable transfocator, as well as a prototype diffraction X-ray microscopy set-up.

The large volume press (LVP at ID06) continued to operate at 30% of the standard allocation time for an ESRF beamline. Experiments included ultrasonic measurements combined with diffraction; phase diagram determination and *in situ* synthesis of materials, and deformation studies reaching total strains up to 25%. Furthermore, new detection and data acquisition schemes were investigated and implemented.

At the Nuclear Resonance Beamline, ID18, the synchrotron Mössbauer source (SMS) was made available for the users programme. It provides a tuneable X-ray beam (typically +/- 1 μeV around the iron Mössbauer resonance at 14.4 keV) with an energy resolution of about 10 neV and 10 kHz "resonant" γ-quanta.

The official inauguration of the new inelastic X-ray scattering beamline, ID20 (ESRF Upgrade Programme UPBL6), took place on 30 May on the occasion of the spring meeting of the Science Advisory Committee. Official user experiments started in June 2013. The beamline has reached its target performance and is now fully operational.

The high-pressure beamlines ID09A and ID27 can again look back on a very productive year. Using novel approaches, new high pressure records up to 6.7 Mbar at ambient temperature could be set. Work on the Technical Design Report for the move of ID09A to ID15 has started and shall be completed by summer 2014; while the move of ID09A is foreseen for 2015.

External funding has become a significant complement to the investment capacity of the group. ID06LVP profited from the ANR Mantle Rheology project, which developed research techniques for the measurement and modelling of deformation mechanisms of mantle materials in collaboration with partners from Lille and Paris. A BMBF (German ministry for education and research) grant under the leadership of the group of L. Dubrovinsky (Bayerisches Geoinstitut Bayreuth) led to the installation of a double-side laser-heating setup at beamline ID18. The follow-up grant aims at developing a high-pressure sample environment for the characterisation of time-dependent processes in materials at extreme conditions. A further BMBF grant supports the installation of a high-throughput diffractometer for diffuse scattering studies as a side-station to beamline ID28, led by the group of B. Winkler (University of Frankfurt). Further support is received in the framework of the Helmholtz Russia Joint Research Group ("Sapphire ultra optics for synchrotron radiation"; R. Hermann, FZ Jülich) and the XNAP collaboration for the development of a two-dimensional counting pixel X-ray detector based on silicon avalanche photodiodes.

This year's achievements would not have been possible without a vibrant user community and the continuous support and effort of all the other ESRF divisions. The prospect of a possible Upgrade Phase II is a further motivation to jointly pave the way to new science and technology and maintain the group's beamlines at the forefront of cutting edge research.

M. KRISCH

EARTH AND PLANETARY SCIENCE

THE EARTH'S CENTRE IS 1000 DEGREES HOTTER THAN PREVIOUSLY THOUGHT

The interior of the Earth constitutes an enormous engine whose operation relies on the available heat. This heat is constrained by the temperature profile inside the Earth. We have determined the temperature near the Earth's centre to be 5500 K, 1000 degrees hotter than in a previous experiment run 20 years ago.

The interior of the Earth can be divided into the crust, the mantle and the core. The core is further divided into an external portion made of liquid iron, alloyed with lighter elements, while the inner part - the inner core - is solid due to the intense pressure. Analysis of earthquake-triggered seismic waves passing through the Earth, tells us the thickness of the Earth's layers, and even how the pressure increases with depth. However, these waves do not provide information on temperature. The temperature in the core has an important influence on the movement of material within the liquid core, creating the Earth's magnetic field, and the solid mantle above [1], underpinning geophysical models that explain the creation of hot-spot volcanoes like the Hawaiian Islands or La Réunion.

At the border between liquid outer core and solid inner core, at 330 GPa (3.3 million atmospheres), the temperature is close to the melting temperature of iron. The melting curve of iron under extreme pressure thus allows a determination of the temperature in the Earth's core.

Speck-sized samples of iron have been compressed to pressures reaching several million atmospheres using a diamond anvil cell (Figure 25). Powerful laser beams were used to heat the samples up to around 5000 K. At the same time, the sample was probed by X-ray diffraction at beamline **ID27** to determine whether it was solid or liquid. This was done on a second timescale, sufficiently short to keep pressure and temperature constant in the sample. We have measured melting of iron to 5100 K and 2.2 million atmospheres pressure, and then used an extrapolation method to determine the melting temperature of pure iron at a pressure equivalent to that of the border between the liquid and solid core, finding a temperature of 6230 +/- 500 K (Figure 26). This extrapolated value could change slightly if iron undergoes an unknown phase transition between the measured and the extrapolated values. Taking into account a depression of the liquidus due to the presence of light elements in the core, estimated to be 700 K ± 200 K [2], our measurements yield a temperature around 5500 K at the inner core boundary.

Fast X-ray diffraction observations made in this work also allows an explanation for the underestimation of the melting temperature in earlier studies [3]. Several hundreds of degrees below melting, recrystallisation effects appear in iron samples, leading to dynamic changes of the solid iron's texture. The experiment twenty years ago used an optical technique to determine whether the samples were solid or molten, and it was probably the observation of recrystallisation at the surface that was interpreted as melting.

Principal publication and authors
S. Anzellini (a), A. Dewaele (a), M. Mezouar (b), P. Loubeyre (a) and G. Morard (c), *Science* **340**, 464-466 (2013).
(a) Commissariat à l'Énergie Atomique, Direction des Applications Militaires Île de France Arpajon (France)
(b) ESRF
(c) Institut de Minéralogie et de Physique des Milieux Condensés, Université Pierre et Marie Curie, Paris (France)

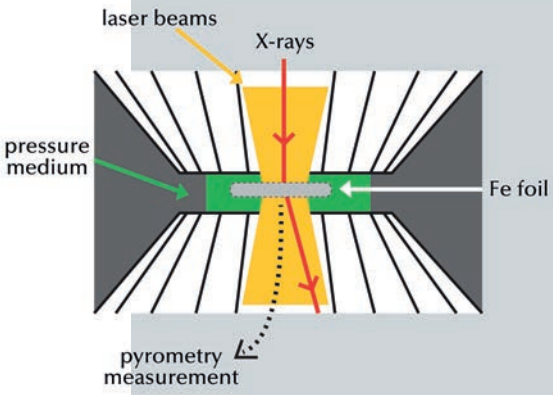

Fig. 25: Principle of the experiment. The sample is compressed in a diamond anvil cell and laser heated. Monochromatic X-ray diffraction is used to detect the phase of iron.

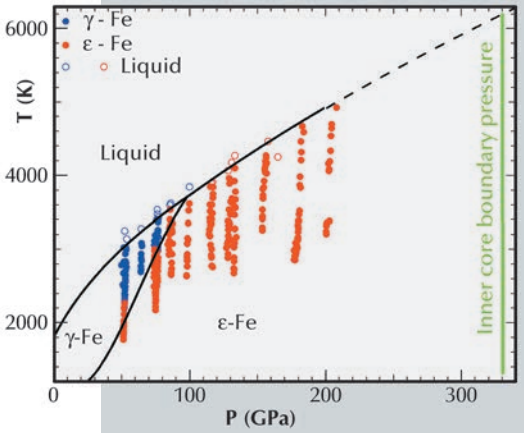

Fig. 26: High pressure-high temperature (P-T) phase diagram of iron. The pressure-temperature conditions at which X-ray diffraction patterns have been collected are indicated by symbols. The phase boundaries between γ-Fe, ε-Fe and liquid Fe are based on these measurements.

References
[1] T. Lay, J. Hernlund and B.A. Buffett, *Nat. Geosci.* **1**, 25-32 (2008).
[2] D. Alfè, M.J. Gillan and G.D. Price, *Contemp. Phys.* **48**, 63-80 (2007).
[3] R. Boehler, *Nature* **363**, 534-536 (1993).

IRON ELECTRONIC STATE AND THE ELECTRICAL CONDUCTIVITY OF THE EARTH'S LOWER MANTLE

Principal publication and authors
V. Potapkin (a,b), C. McCammon (b), K. Glazyrin (b), A. Kantor (a,b), I. Kupenko (a,b), C. Prescher (b), R. Sinmyo (b), G.V. Smirnov (c), A.I. Chumakov (a,c), R. Rüffer (a) and L. Dubrovinsky (b), *Nature Communications* **4**, 1427 (2013).
(a) ESRF
(b) Universität Bayreuth, Bayreuth (Germany)
(c) National Research Center 'Kurchatov Institute', Moscow (Russia)

Much of our knowledge of the Earth's interior comes from comparison of laboratory measurements of physical properties of mantle minerals with data from bulk geophysical methods. Traditionally, seismology has provided the best constraints on the internal structure of the Earth, however, electromagnetic methods can be used to construct electrical conductivity profiles, which are more sensitive to temperature and composition variations.

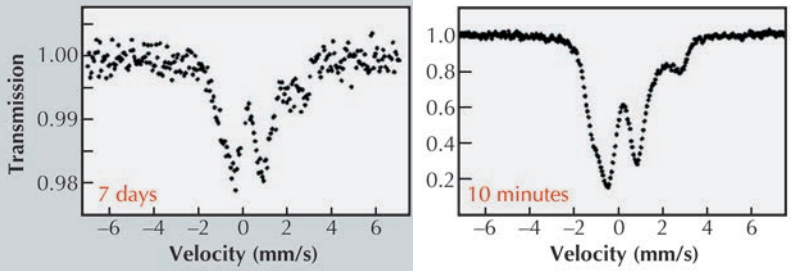

Fig. 27: Comparison of room temperature Mössbauer spectra of $(Mg,Fe)(Si,Al)O_3$ perovskite at 93 GPa in a diamond anvil cell collected over the indicated time periods using a radioactive source (left) with one collected using the new synchrotron Mössbauer source (right).

Iron is the most abundant element inside the Earth and variations in pressure or temperature can cause changes in the number of electrons (oxidation state) or in the distribution of electrons (spin state), which can affect electrical conductivity. The iron atoms in the Earth's most abundant phase, $(Mg,Fe)(Si,Al)O_3$ perovskite, are known to exist in two different oxidation states (ferrous iron and ferric iron), and both oxidation states have the possibility of undergoing a spin state transition at high pressure. Deducing the nature of iron spin transitions in $(Mg,Fe)(Si,Al)O_3$ perovskite is challenging due to the numerous combinations of oxidation and spin state in the two crystallographic sites of its crystal structure.

To solve such problems we have developed a novel setup on **ID18**: a synchrotron Mössbauer source (SMS) [1] that offers a number of advantages over conventional Mössbauer spectroscopy. It has high brilliance and a nearly fully resonant emitted beam that can be focused to a spot of only a few micrometres diameter, leading to a vast improvement in signal quality for small samples (< 50 μm) (**Figure 27**).

In this study, we used SMS spectroscopy to study the effect of pressure on the hyperfine interactions of $(Mg,Fe)(Si,Al)O_3$ perovskite compressed and heated using a laser-heated diamond anvil cell up to pressures of 122 GPa. A representative set of SMS spectra is shown in **Figure 28a**. We found that no spin transition occurs in ferric iron (Fe^{3+}) at lower mantle conditions, contrary to previous claims. Instead, ferrous iron (Fe^{2+}) likely undergoes a partial spin transition to an intermediate spin state, suggesting that the previously observed sharp drop in electrical conductivity of $(Mg,Fe)(Si,Al)O_3$ perovskite [2] is due to a spin transition of ferrous iron. To test this hypothesis, we measured the high-pressure high-temperature electrical conductivity of $(Mg,Fe)(Si,Al)O_3$

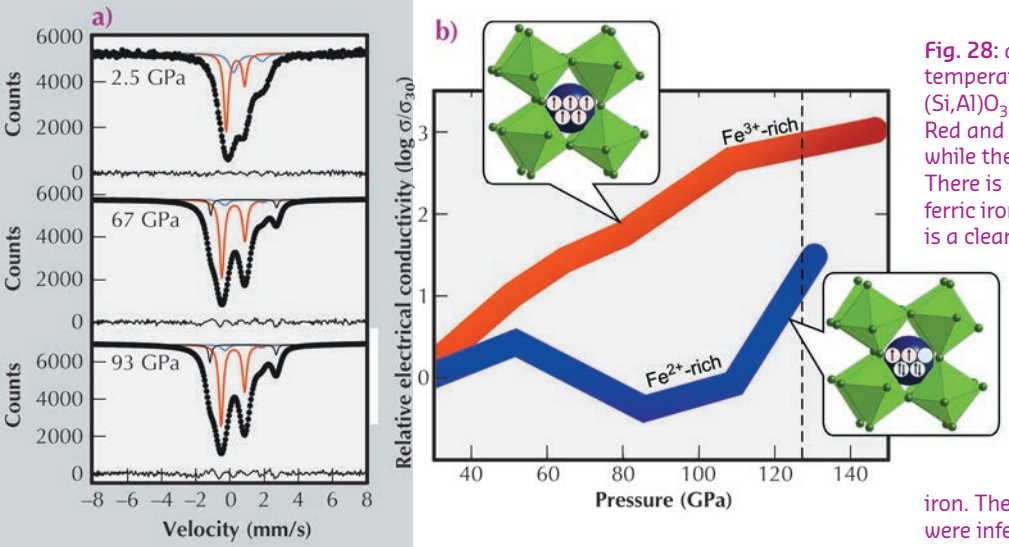

Fig. 28: a) Representative room temperature Mössbauer spectra of $(Mg,Fe)(Si,Al)O_3$ perovskite at increasing pressure. Red and blue curves are fits to the exp data, while the bottom black line is the residual. There is no evidence of a spin transition in ferric iron (Fe^{3+}) (red doublet), whereas there is a clear pressure evolution of the signal associated with ferrous iron (Fe^{2+}) (blue curve). b) Influence of pressure on the high-temperature electrical conductivity of $(Mg,Fe)(Si,Al)O_3$ perovskite (red: our data; blue: ref [2]). The large drop in conductivity of the Fe^{2+}-rich material is likely due to a partial spin transition in Fe^{2+} (ferrous) iron. The sketched electron configurations were inferred from the SMS spectra.

perovskite containing predominantly ferric iron, and observed no drop in electrical conductivity (**Figure 28b**).

Temperature and total iron content have previously been considered to have the greatest influence on lower-mantle electrical conductivity profiles, but our data show that the ferric to ferrous iron ratio can also affect conductivity significantly at pressures corresponding to the middle part of the lower mantle. Electrical conductivity is strongly influenced by iron oxidation and spin state and provides one more example of how small changes in electronic structure can cause large changes in physical properties, bringing us one step closer to understanding how the Earth's internal engine works.

References
[1] V. Potapkin, A.I. Chumakov, G. V. Smirnov, J.-P. Celse, R. Rüffer, C. McCammon and L. Dubrovinsky The ^{57}Fe synchrotron Mössbauer source at the ESRF, *J. Synchrotron Radiat.* **19**, 559 (2012).
[2] K. Ohta, K. Hirose, M. Ichiki, K.Shimizu, N.Sata and Y. Ohishi, *Earth Planet. Sci. Lett.* **289**, 497 (2010).

PROSPECTING FOR DEEP WATER WITH X-RAYS

Principal publication and authors
A.D. Rosa (a), C. Sanchez-Valle (a), C. Nisr (b), S.R. Evans (c), R. Debord (d) and S. Merkel (b), *Earth and Planetary Science Letters* **377–378**, 13–22 (2013).
(a) Institute for Geochemistry and Petrology, ETH Zurich (Switzerland)
(b) Unité Matériaux et Transformations, CNRS, Université de Lille (France)
(c) ESRF
(d) Institut Lumière Matière, UMR5306 CNRS – UCBL Lyon 1, Villeurbanne (France)

The Earth's interior could contain more than three times the amount of water present at its surface, water that is incorporated into the structure of high pressure crystalline silicates **[1]**. This "water" plays a critical role in deep geological processes that shape the inner (and surface) evolution of the Earth. Indeed, minute amounts of hydrous components in silicates have major effects on mantle convection and melting, fuel plate tectonics and influence catastrophic events, such as earthquakes and volcanic eruptions.

Exchanges between the Earth's surface and its interior recycle water over geological timescales of millions of years. Water is reintroduced into the deep Earth by hydrated oceanic tectonic plates in subduction zones. Even if much of the water is released at shallow depths (< 200 km) and returns to the surface by volcanism, a large fraction is retained in the slab and could travel beyond 400 km in depth. However, the extent of water recycling in volcanic arcs and the degree of hydration of subducted plates descending below the transition zone (TZ, > 700 km depth), remain uncertain **[2]**.

Constraints on the deep water cycle thus rely upon the interpretation of remote geophysical observations. Seismic studies **[3]** show regions of negative velocity anomalies (~3%) and high shear-wave V_S anisotropy (0.9 ± 0.3%) in the Tonga slab below the TZ that may be associated with the presence of hydrous phases. Phase D, (Mg,Fe,Al) $Si_2H_2O_6$, is the stable water carrier in the subducted hydrated mantle (peridotite) below the TZ and a plausible candidate to explain these anomalies due to its high water content (10-18 wt% H_2O) and large intrinsic anisotropy **[4]**. A better knowledge of the elasticity and deformation mechanism of phase D is therefore seminal for the quantitative interpretation of these seismic anomalies in terms of hydration.

We conducted experiments at beamline **ID09A** to determine the deformation mechanisms and lattice preferred orientations (LPO) of phase D at pressures relevant for slabs penetrating below the TZ. Powdered samples of phase D were deformed non-hydrostatically in uniaxial compression up to 48 GPa in a diamond anvil cell. X-ray diffraction patterns were collected in radial geometry to monitor the lattice strain and the development of texture in the sample under pressure (**Figure 29**).

At low strains, the layered structure of phase D displays strong 0001 texture, where the stacking fault axis (c-axis) preferentially aligns parallel to the compression axis. A subsidiary 10-10 texture develops at pressures

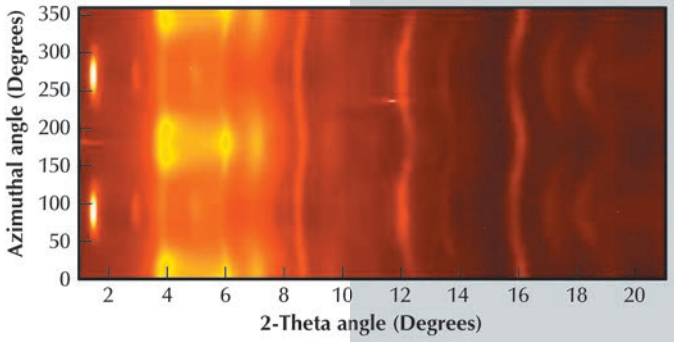

Fig. 29: Unrolled X-ray diffraction image of phase D collected at 48 GPa. Changes in the intensity with the azimuth angle and the strong modulations of the diffraction lines upon compression are indicative of strong textures and high lattice strain.

References
[1] A.B. Thompson, *Nature* **358**, 295 (1992)
[2] H.W. Green II, W.P. Chen and M.R. Brudzinski, *Nature* **467**, 828 (2010).
[3] W.P. Chen and M.R. Brudzinski, *Geophys Res Lett* **30**, 1682 (2003).
[4] A.D. Rosa, C. Sanchez-Valle and S. Ghosh, *Geophys Res Lett* **39**, L06304 (2012).

above 19 GPa (**Figure 30a**). Plasticity simulations in polycrystalline aggregates using a viscoplastic self-consistent model showed that the LPO of phase D at the uppermost lower mantle (23-35 GPa, 700 – 1200 km depth) are mainly consistent with dominant easy glide on basal planes and with the harder first order pyramidal slip, respectively (**Figure 30b**). Furthermore, phase D displays the lowest strength among phases in hydrous peridotite in this region (**Figure 30c**). Phase D might thus accommodate most of the strain and might develop strong textures upon slab deformation, being a major source of shear anisotropy below the TZ.

The effect of textured phase D on the seismic velocity structure and shear anisotropy of deformed hydrous peridotite could be modelled thanks to these results coupled with elasticity data from Brillouin scattering studies [4], allow modelling. On the basis of these calculations, our results show that 16 vol.% of phase D in subducted hydrous peridotite explains all seismic anomalies reported in the Tonga subduction below the TZ [3]. The seismic observations thus place constraints on the degree of hydration of the Tonga slab beyond the transition zone, leading to the requirement that a minimum of 1.2 wt.% H_2O is retained in the slab by hydrous peridotite below 700 km depth. The implications of these results are far reaching because they provide evidence for substantial hydration of subducting plates penetrating below the TZ, in contrast with previous views [2].

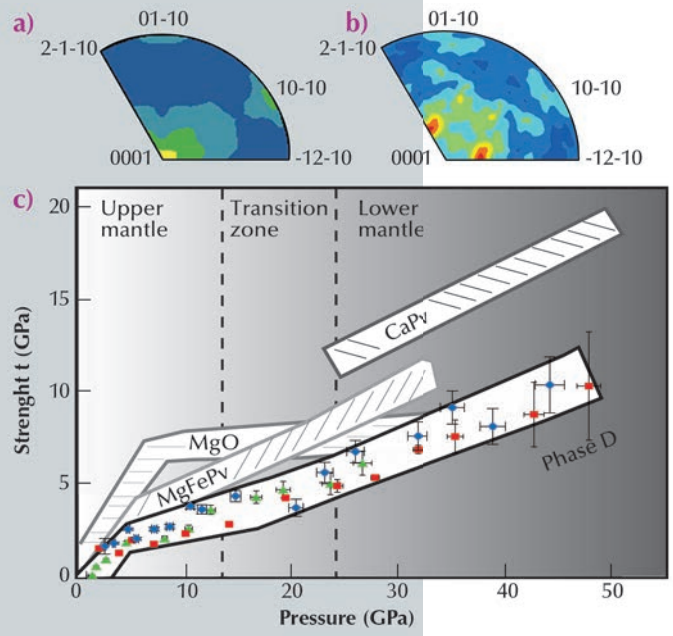

Fig. 30: a) Experimental and b) simulated inverse pole figures of phase D at 48 GPa showing the orientation distribution density of the compression axis within the trigonal lattice frame of Phase D crystallites in the sample. Strong 0001 texture and a subsidiary 10-10 texture are observed. c) Strength of phases coexisting in the hydrated mantle within subducting slabs at lower mantle pressures. Symbols are data for Phase D: red, Mg-bearing; blue, Fe-bearing; green, Al-Fe-bearing Phase D. [MgFePv, $(Mg_{0.9}Fe_{0.1})SiO_3$ perovskite; CaPv, $CaSiO_3$ perovskite; MgO, periclase].

Principal publication and authors
C.J. Sahle (a,b), C. Sternemann (a), C. Schmidt (c), S. Lehtola (b), S. Jahn (c), L. Simonelli (d), S. Huotari (b), M. Hakala (b), T. Pylkkänen (b), A. Nyrow (a), K. Mende (a), M. Tolan (a), K. Hämäläinen (b) and M. Wilke (c), *Proc. Natl. Acad. Sci. USA* **110**, 6301 (2013).
(a) Fakultät Physik/Dortmund Electron Accelerator, Technische Universität Dortmund (Germany)
(b) Department of Physics, University of Helsinki (Finland)
(c) Section 3.3, Deutsches GeoForschungsZentrum GFZ, Potsdam (Germany)
(d) ESRF

MICROSCOPIC STRUCTURE OF WATER UNDER CONDITIONS OF THE EARTH'S CRUST AND MANTLE

The detailed structure of liquid water on a molecular scale remains a mystery even after more than a century of research [1]. The explanation for the unusual structure and dynamics of water is still under debate. For example, there is an intense discussion about whether the microscopic structure of water in the liquid phase can be described by a continuum model or a mixture of two components, one with a highly polymerised (fully hydrogen-bonded) network, *i.e.* closely related to the structure of low-density amorphous ice, and one closely related to high density amorphous ice.

Detailed knowledge of the microscopic topology of water at high temperatures and pressures is also valuable, *e.g.* for the geosciences. This knowledge might help to better understand the geochemical processes in the crust and upper mantle. Supercritical water is thought to play an important role in heat and mass transfer as well

as element fractionation processes in the Earth's lithosphere. Many geochemical processes and reactions, *e.g.* the formation of hydrothermal ore and petroleum deposits and even contributions to the origin of life, have been linked to the unique properties of supercritical water [2]. Apart from this fundamental interest in the atomic structure of water under different pressure and temperature conditions, supercritical water is also interesting for many chemical processes where it is used as an inexpensive reaction medium for chemical and material synthesis, waste destruction, plastics recycling, and biomass processing.

For the present study, we used X-ray Raman scattering (XRS) at the inelastic X-ray scattering beamline **ID16** to probe the oxygen K-edge of water contained in a hydrothermal diamond anvil cell (HDAC). With this setup, we were able to produce simultaneously high pressure and high temperature conditions. Using the hard X-rays from ID16 and the XRS technique, we were able to measure the oxygen K-edge, which lies in the soft X-ray regime at *ca.* 535 eV, from within the HDAC. The measured data is shown in **Figure 31a** and exhibits a continuous evolution from a water-like spectrum at room temperature and atmospheric pressure to a more gas-like spectrum at the highest temperatures and pressures investigated.

We compared the experimental spectra to those computed using density functional theory and structural snapshots obtained from *ab initio* molecular dynamics (MD) simulations. The results of these simulations are shown in **Figure 31b**. Because we find good match between the simulated and measured spectra, we could investigate the atomic structures of the MD simulations to learn more about the details of the molecular arrangements in water. Specifically, we studied the evolution of hydrogen bonds and number of nearest neighbours as a function of temperature and pressure. These results are presented in **Figure 32**.

A detailed analysis of the MD simulation snapshots suggests that at ambient conditions, molecules with four H-bonds and five oxygen neighbours within a distance of 3.6 Å dominate. With temperature and pressure increasing along the vapour pressure curve, the number of H-bonds per molecule decreases to 0.6 at T = 600°C and P = 134 MPa, implying a dramatic increase of distortions of the hydrogen-bond network. For all measured state points, we were able to identify typical local structural environments with specific spectral fingerprints, which describe water at different pressure/temperature conditions. A spatial statistical analysis of the MD simulation boxes suggests that the structure of water at the probed high temperature and pressure conditions can be understood in terms of a homogeneous microscopic structure.

Our experimental findings provide an unprecedented benchmark for new theoretical models, both in terms of simulations of the atomic structures and the calculation of XRS spectra from the models.

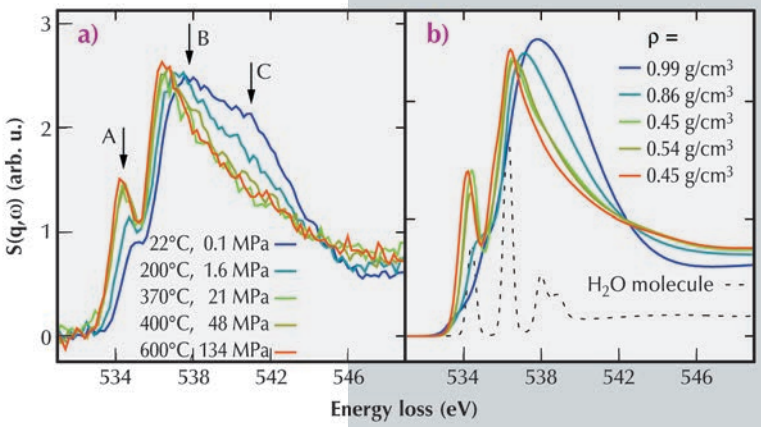

Fig. 31: a) Spectra of the oxygen K-edge of water measured at different temperatures and pressures along the liquid-gas coexistence curve. The pre-, main-, and post-edge are indicated by A, B, and C, respectively. b) Calculated spectra for similar temperatures and densities as in (a), as well as a spectrum of a water monomer. The experimental densities are indicated in the figure, and the colour code corresponds to the colour of the respective spectrum also in part (a) of the figure.

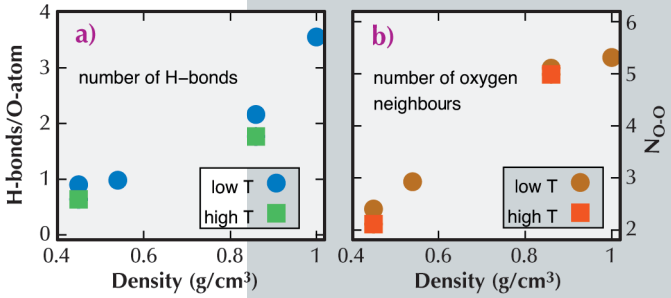

Fig. 32: Number of H-bonds per H_2O molecule (a) and number of nearest neighbours (b) as a function of density extracted from the MD simulation snapshots. The terms "high T" and "low T" refer to values determined for p/T points at equal density but different temperature.

References
[1] P. Ball, *Nature* **452**, 291–292 (2008).
[2] N. Akiya and P.E. Savage, *Chem. Rev.* **102**, 2725–2750 (2002).

REACTIVITY OF XENON WITH ICE UNDER PLANETARY CONDITIONS

Principal publication and authors
C. Sanloup (a,b), S.A. Bonev (c,d), M. Hochlaf (e), and H.E. Maynard-Casely (f), *Phys. Rev. Lett.* **110**, 265501 (2013).
(a) Institut des Sciences de la Terre Paris, UPMC Univ Paris 06, Paris (France)
(b) School of Physics, University of Edinburgh, Edinburgh (UK)
(c) Lawrence Livermore National Laboratory, Livermore (USA)
(d) Department of Physics, Dalhousie University, Halifax (Canada)
(e) Laboratoire Modélisation et Simulation Multiéchelle, Université Paris-Est, Marne-la-Vallée (France)
(f) Bragg Institute, Australian Nuclear Science and Technology Organisation, Lucas Heights, (Australia)

Noble gases are characterised by their high chemical stability. It is both interesting and challenging to force them into bonding with other atoms because of their lack of reactivity. Furthermore, the chemical bonds they form are highly energetic. This has fuelled the search for high-energy noble gas compounds, and, since Neil Bartlett made the first xenon compound ($Xe^+[PtF_6]^-$) in 1962, over 100 noble gas compounds have been synthesised, the vast majority involving xenon. One of the most recently discovered compounds is the HXeOXeH molecule [1], in which two xenon atoms are inserted into a water molecule. It was synthesised by the reaction between water and xenon, driven by UV light at low temperatures (below 70 K). Instead of using very low temperature, another way to make unstable molecules exist for longer periods is to create them under very high pressure. For xenon, there is a large deficiency in the atmospheres of Earth, Mars [2] and Jupiter, the only planets for which noble gas content has been measured. This is the so-called 'missing Xe paradox', which suggests that xenon is retained inside the planets, *i.e.* under high pressure conditions.

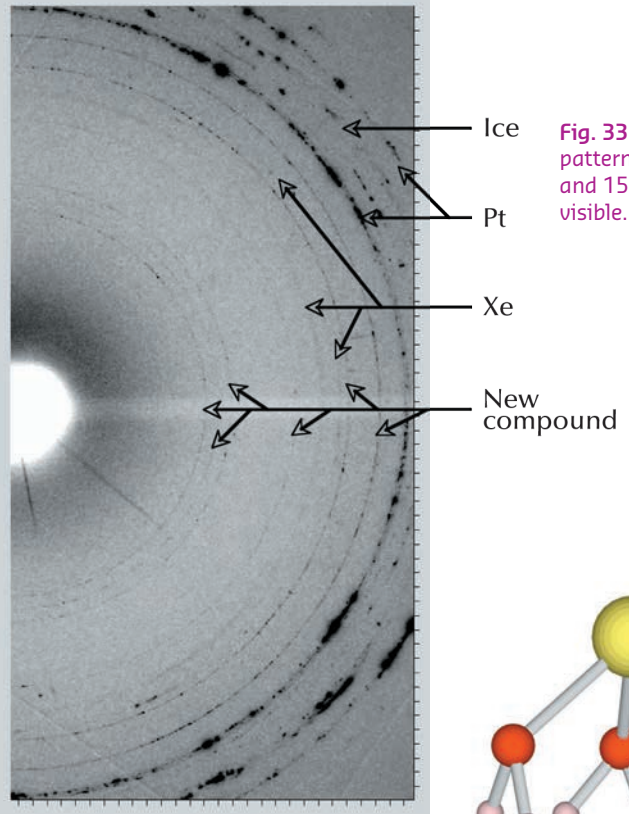

Fig. 33: 2-D diffraction pattern obtained at 58 GPa and 1500 K, new rings are visible.

Using laser-heated diamond anvil cells at beamline **ID27**, we have discovered that xenon reacts with water ice at pressures above 50 GPa and temperatures of 1500 K (**Figure 33**) – conditions found in the interiors of Uranus and Neptune, and in the terrestrial lower mantle. *In situ* X-ray diffraction revealed the presence of a hexagonal lattice with four xenon atoms per unit cell and several possible distributions of oxygen atoms. We combined the diffraction data with *ab initio* calculations in order to solve the crystallographic structure of the compound. **Figure 34** shows the $Xe_2O_6H_6$ unit on which the compound is based.

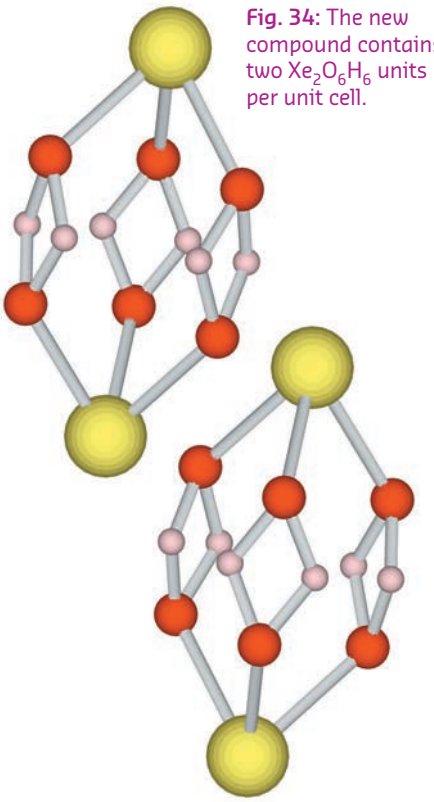

Fig. 34: The new compound contains two $Xe_2O_6H_6$ units per unit cell.

This discovery follows an earlier report of the stability of Xe-doped quartz (SiO_2) at the conditions prevalent deep under the continents on Earth [3], which was confirmed by the later synthesis of pure XeO_2 [4]. This questions in turn the use of xenon isotopes to determine events in the formation of the Earth. Noble gas abundances are widely used by geochemists to assess the order and timing of major terrestrial processes, including atmospheric formation. However, their basic assumption is that noble gases remain inert under all conditions. The present findings show that the chemistry of Xe is much more complex than previously thought.

References
[1] L. Khriachtchev *et al.*, *J. Am. Chem. Soc.* **130**, 6114 (2008).
[2] E. Anders and T. Owen, *Science* **198**, 453 (1977).
[3] C. Sanloup *et al.*, *Science* **310**, 1174 (2005).
[4] D.S. Brock and G.J. Schrobilgen, *J. Am. Chem. Soc.* **133**, 6265 (2011).

ADVANCED AND FUNCTIONAL MATERIALS

RATTLING MODES IN THERMOELECTRIC SODIUM COBALTATE

The design of better thermoelectric materials would enable the reduction of energy consumption in cars by converting waste heat in exhausts into useful electrical power, as well as cooling hot spots on computer chips using solid state refrigerators. However, the need for both high electrical conductivity and low thermal conductivity creates a design conflict. Here we show how rattling modes suppress the thermal conductivity in the electrically conducting thermoelectric oxide, sodium cobaltate.

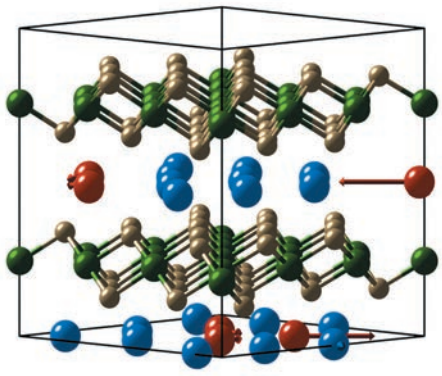

Fig. 35: The supercell of $Na_{0.8}CoO_2$ showing the Einstein-like rattling mode at E ~ 13 meV comprising mainly displacements of the (red) Na *2b* ions inside tri-vacancy clusters. Na *2d* ions are blue, Co is green and O is gold.

The so-called square superstructure of $Na_{0.8}CoO_2$ shown in **Figure 35** comprises arrays of tri-vacancy clusters **[1]**. We have performed first-principles density-functional calculations for the lattice dynamics of this large-period superstructure on the UK's national supercomputer facility HECToR using the CASTEP code, and the results are presented as a colour contour diagram in **Figure 36**. The calculated spectrum differs markedly from that of the stoichiometric compound at energies below E ~ 20 meV. In particular, there is an additional narrow mode at E ~ 13 meV in the superstructure that is completely absent for $NaCoO_2$.

Inelastic X-ray scattering (IXS) measurements were performed on a single crystal of $Na_{0.8}CoO_2$ of a few hundred micrometres in size with the square superstructure using the **ID28** spectrometer. Scans of variable energy transfer were performed at a number of settings of momentum transfer $\boldsymbol{Q}$ along high-symmetry directions, and the fitted peak positions are shown in **Figure 36** as red hexagons. The agreement between the *ab initio* calculations and the IXS experimental data is remarkable.

We observe the approximately flat mode at E ~ 13 meV. It is possible to trace this mode back to the zone centre, and the relative amplitudes of the ionic displacements are shown in **Figure 35**. The blue spheres are Na *2d* sites, and these are fully occupied in the stoichiometric compound. The red spheres are on the inequivalent Na *2b* sites and, because they are associated with clusters of three vacancies, they are expected to be more loosely bound. The atomic displacement pattern is characterised by a predominant in-plane amplitude of vibration of the Na *2b* sites with negligible contribution from other sites. Thus we find that the Na *2b* sites inside tri-vacancy

Principal publication and authors
D.J. Voneshen (a), K. Refson (b), E. Borissenko (c), M. Krisch (c), A. Bosak (c), A. Piovano (d), E. Cemal (a,d), M. Enderle (d), M.J. Gutmann (e), M. Hoesch (f), M. Roger (g), L. Gannon (h), A.T. Boothroyd (h), S. Uthayakumar (a), D.G. Porter (a) and J.P. Goff (a), *Nature Materials* **12**, 1028 – 1032 (2013).
(a) Royal Holloway, University of London (UK)
(b) Science and Technology Facilities Council (UK)
(c) ESRF
(d) Institut Laue-Langevin (France)
(e) ISIS Facility (UK)
(f) Diamond Light Source (UK)
(g) CEA Saclay (France)
(h) Oxford University (UK)

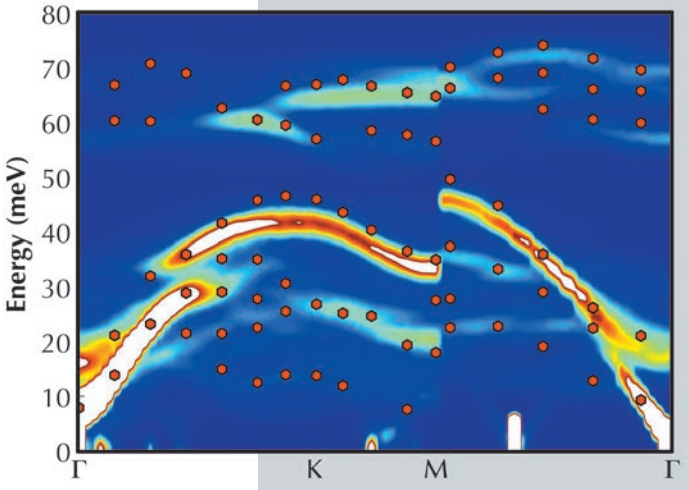

Fig. 36: The phonon dispersion of $Na_{0.8}CoO_2$ in the square superstructure. First-principles density-functional calculations for the square array of tri-vacancy clusters are shown as a colour contour diagram on a hot scale (blue, low intensity; white, high intensity). The IXS data are shown as red hexagons. The superstructure is essential to capture the scattering at lower energies below E ~ 20 meV.

References
[1] M. Roger, D.J.P. Morris, D.A.Tennant, M.J. Gutmann, J.P. Goff, J.-U. Hoffmann, R. Feyerherm, E. Dudzik, D. Prabhakaran, A.T. Boothroyd, N. Shannon, B. Lake and P.P. Deen, *Nature* **445**, 631-634 (2007).

clusters sandwiched between CoO_2 layers are rattler sites, and the mode at E ~ 13 meV is a rattling mode.

The measured energy line widths are sharp, indicating relatively long phonon lifetimes. There is, therefore, no evidence for the level of phonon scattering required by the phonon-glass electron-crystal model. The lattice contribution to the thermal conductivity calculated using the measured phonon dispersion and lifetimes was found to be in quantitative agreement with experiment. The rattling modes at low energy contribute towards the specific heat, but have small propagation velocities, and they suppress the thermal conductivity by a factor of six compared with vacancy-free $NaCoO_2$.

In conclusion, we are able to unambiguously identify an Einstein-like rattling mode at low energy and, as a result, to quantitatively account for the suppression of thermal conductivity for this class of materials. Our approach using IXS can readily be extended to other candidate materials, since we only require tiny crystals, and the results will guide the design of the next generation of thermoelectric materials.

COMPETING INSTABILITIES AND ELECTRON-PHONON INTERACTION IN SUPERCONDUCTING CUPRATES

Principal publication and authors
M. Le Tacon (a), A. Bosak (b), S.M. Souliou (a), G. Dellea (c), T. Loew (a), R.Heid (d), K.-P. Bohnen (d), G. Ghiringhelli (c), M. Krisch (b), and B. Keimer (a), *Nature Phys.* **10**, 52-58 (2014).
(a) Max-Planck-Institut für Festkörperforschung, Stuttgart (Germany)
(b) ESRF
(c) Politecnico di Milano (Italy)
(d) Karlsruher Institut für Technologie (KIT) (Germany)

Superconductivity, a quantum state of matter, characterised by complete disappearance of electrical resistivity, still offers room for new insights, even more than 100 years after its discovery. In particular, a family of cuprates is the focus of our interest due to their high superconducting temperature T_c.

When there is nominally one electron per Cu atom in the CuO_2 planes of a cuprate, their large Coulomb repulsion localises them in a so-called Mott-insulating state in which their spins order antiferromagnetically. When changing the charge carrier concentration of the planes, long range magnetic order is rapidly suppressed and is eventually replaced by superconductivity, through a mechanism that is not fully understood despite 27 years of intense research.

It has been realised that a variety of other ground states could exist in these doped Mott insulators, in particular at low doping levels where unusual spin and/or charge textures could form. Until recently, such phases (*e.g.* stripe phase, in which antiferromagnetically ordered regions are separated by charged domain walls) had been observed experimentally in only a few compounds and their universality questioned.

A recent experimental breakthrough came from the observation of two-dimensional, incommensurate fluctuations of the charge density in one of the most widely studied cuprates, $YBa_2Cu_3O_{6+x}$, using NMR and state-of-the-art synchrotron based techniques [1-3].

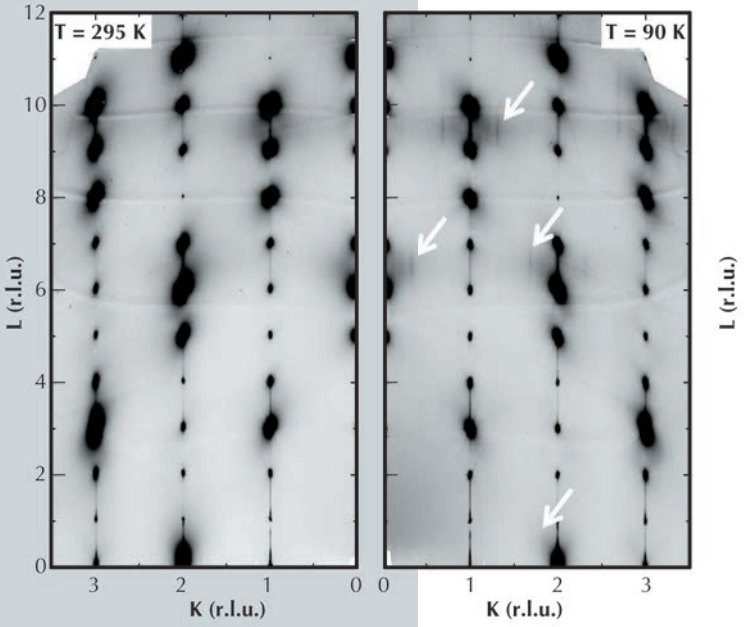

Fig. 37: Diffuse scattering mapping of the **Q** = (0, *K*, *L*) plane at room temperature and at *T* = 90 K. White arrows indicate the CDW superstructure peaks.

Unambiguous signatures of competition of this incipient charge-density-wave (CDW) with superconductivity were further evidenced, offering a new playground for physicists to study the interplay between competing orders in these correlated-electron materials.

Among the issues of particular relevance, the role of the interaction between mobile charge carriers and lattice vibrations (phonons) has been a subject of long-standing debate and remains controversial. Whereas density-functional theory (DFT) predicts only weak electron-phonon interaction (EPI) in these materials, various anomalies in the dispersion relations of both electrons and phonons have been interpreted as evidence of an EPI strength far exceeding these predictions. However, it has proven difficult to disentangle the influence of the EPI on these anomalies from other factors including spin fluctuations and lattice anharmonicity.

The question whether strong electronic correlations substantially modify the EPI in the cuprates with respect to DFT therefore remains open, as do more general questions about the role of the EPI in driving high-temperature superconductivity and/or competing instabilities.

To gain new insight into these issues, we have studied the effect of CDW fluctuations and superconductivity on the lattice dynamics of underdoped $YBa_2Cu_3O_{6.6}$.

To carry out this study, we first assembled a comprehensive map of the diffuse scattering intensity at beamline **ID29**, to identify the places of reciprocal space with the most intense X-ray signatures of CDW formation. In **Figure 37** we show two examples of such maps taken in the (0,K,L) plane of reciprocal space at 295 K and 90 K. In the latter, we can clearly distinguish superstructures between the main Bragg peaks. The large variations of the satellite intensities across the reciprocal space reveal a complex structure factor of the CDW that had not been anticipated.

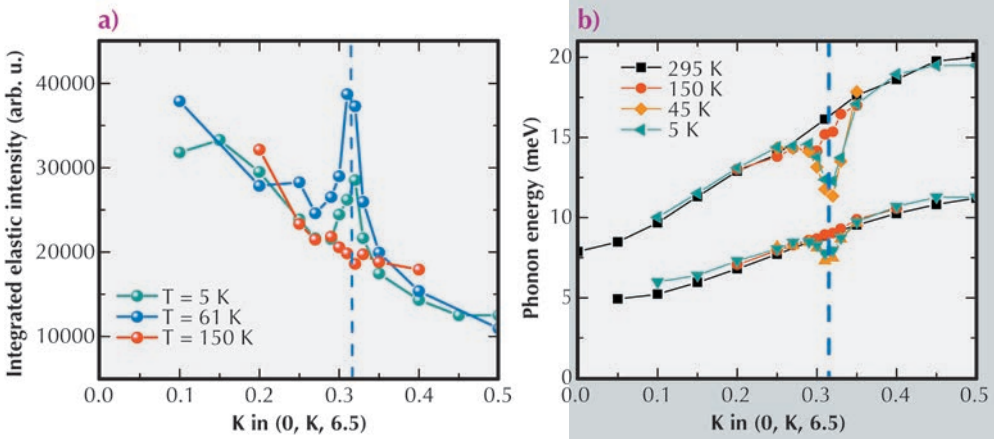

Fig. 38: a) Momentum dependence of the intensity of the central peak at T = 150, 90, 61 and 5 K. b) Dispersion of the two low-energy phonons along the Z-T direction at T = 295, 150, 45, and 5 K.

Then, we used inelastic X-ray scattering (IXS) with high energy resolution (at beamline **ID28**) around the CDW ordering wave-vector Q_{CDW}. The IXS intensity is proportional to the imaginary part of the charge susceptibility $\chi''(\mathbf{Q}, \omega)$. The momentum dependence of the quasi-static (elastic line at $\omega = 0$) and dynamic (at finite ω, corresponding to phonons) components of the charge susceptibility can therefore be resolved (**Figure 38**).

At low temperature, we observed an enhancement of the elastic line, whose intensity at Q_{CDW} is maximised at the superconducting transition temperature, T_c, and persists over a wide temperature range above T_c. In analogy to classical work on structural phase transitions, we interpret the observation of this 'central peak' as evidence of a spatially inhomogeneous state in which lattice defects nucleate CDW nanodomains.

At finite energy, we observed pronounced anomalies in the dispersion of low-energy phonons, in particular a large superconductivity induced renormalisation that likely accounts for a large part of the total EPI.

The effect is, however, highly anisotropic and confined to a narrow window of momentum space. Its momentum-averaged strength appears therefore insufficient to be a significant driving force for superconductivity. The emerging picture is that the EPI favours a CDW instability that strongly competes with superconductivity and reduces the superconducting T_c at moderate doping levels.

References
[1] T. Wu *et al.*, *Nature* **477**, 191-194 (2011).
[2] **G.** Ghiringhelli *et al.*, *Science* **337**, 821-825 (2012).
[3] J. Chang *et al.*, *Nat Phys* **8**, 871-876 (2012).

Principal publication and authors
T. Ritschel (a,b), J. Trinckauf (a), G. Garbarino (c), M. Hanfland (c), M.V. Zimmermann (d), H. Berger (e), B. Büchner (a,b), and J. Geck (a), *Physical Review B* **87**, 125135 (2013).
(a) Leibniz Institute for Solid State and Materials Research IFW Dresden (Germany)
(b) Institute for Solid State Physics, Dresden Technical University (Germany)
(c) ESRF
(d) Hamburger Synchrotronstrahlungslabor (HASYLAB) at Deutsches Elektronensynchrotron (DESY), Hamburg (Germany)
(e) Ecole Polytechnique Federale de Lausanne (Switzerland)

A SUPERCONDUCTING ELECTRONIC CRYSTAL IN 1T-TaS_2 STABILISED BY EXTERNAL PRESSURE

It is an intriguing fact that in many complex materials superconductivity – a state of matter where charge can move through a lattice without any resistance – often exists in close proximity to what appears to be exactly the opposite: the static spatial ordering of charge. But despite intense research efforts, the question if or under which circumstances electronic order competes, coexists with or supports superconductivity remains mostly controversial.

A particularly interesting example is the charge density wave (CDW) system 1T-TaS_2. For this material, measurements of the electrical resistivity revealed that external pressure stabilises a superconducting phase, which again exists in very close proximity to electronically ordered phases. Whether and how this superconductivity is related with the CDW on a microscopic level remained, however, unknown from the experimental point of view.

To clarify this issue, we performed pressure dependent X-ray diffraction (XRD) experiments at beamline **ID09A**. These state-of-the-art synchrotron experiments provide direct access to the microscopic properties of electronically ordered phases. More specifically, the periodic lattice modulations associated with the CDW lead to so-called superlattice reflections, which enable a determination of the amplitude and the modulation wave vector (q-vector) of the CDW. Representative XRD data obtained during this experiment are shown in **Figure 39**.

At low pressure and low temperature 1T-TaS_2 exhibits a commensurate CDW (C-CDW), which is often described as a Mott-insulating phase and which displays a commensurate modulation wave vector q_C as shown in **Figure 39a**. Upon applying external pressure, this phase is rapidly suppressed and a so-called nearly commensurate CDW (NC-CDW) appears. The NC-CDW is characterised by a domain-like structure, consisting of commensurate C-CDW domains separated by metallic domain walls, called discommensurations. The latter can be understood as defects in the electronic C-CDW lattice. But unlike ordinary defects, these discommensurations themselves form a self-organised, long-range ordered structure **[2]** that causes the sharp spots in **Figure 39b**. The corresponding modulation wave vector is labelled as $\mathbf{q}_{NC}$ and its incommensurability $\Delta=|\mathbf{q}_{NC}-\mathbf{q}_C|$ is

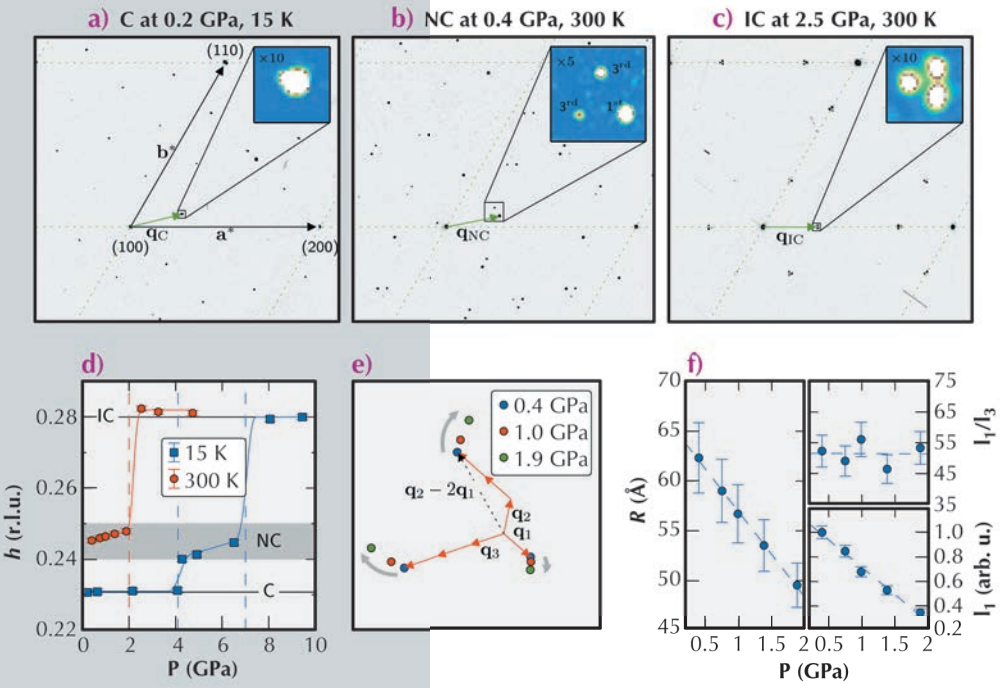

Fig. 39: (a), (b) and (c): Diffraction patterns in the commensurate (C), nearly commensurate (NC) and incommensurate (IC) phase, respectively. (d) In-plane component q as a function of pressure at two temperatures. $\mathbf{q}_{NC}$ exhibits a clear pressure dependence. (e) Pressure evolution of the nearly commensurate super lattice reflections (the same region as in the inset of (b) is shown). $\mathbf{q}_1=\mathbf{q}_{NC}-\mathbf{q}_C$, $\mathbf{q}_2$ and $\mathbf{q}_3$ are obtained by 120° rotations. (f) Pressure dependence of R and the intensities of the first (I1) and third (I3) order superlattice peak.

determined by the distance R between neighbouring commensurate domains (*cf.* **Figure 40** and **Figure 39e**): R ~ 1/ Δ **[3]**. The other reflections shown in the inset of **Figure 39b** and **Figure 39e** are of higher order and their intensities are related to the spatial structure of the discommensurations.

Up to now it was proposed that the insulating C-CDW domains melt with increasing pressure and, hence, the metallic inter-domain regions broaden and become interconnected as sketched in **Figure 40a**. Such a scenario would have distinct consequences for the observed superlattice reflections: (i) R remains essentially constant with increasing pressure and therefore Δ will not change significantly; (ii) The broadening of the domain walls would result in a substantial change of the intensity ratio between the first and higher order satellite reflections.

However, these two characteristic changes of the XRD patterns are not observed experimentally, as demonstrated in **Figure 39f**. Instead we found that the difference vector $\mathbf{q}_1$ substantially changes upon increasing pressure (**Figure 39e**) implying that R decreases pronouncedly. At the same time the intensity ratio between first and higher order reflections remains constant, which indicates that the domain boundaries do not broaden significantly with increasing pressure. We found that this situation does not change upon cooling below the superconducting transition temperature.

These observations therefore provide strong experimental evidence for the scenario indicated in **Figure 40b**, where the lattice of discommensurations shrinks without forming large interconnected metallic regions. Such a behaviour leads to the astonishing conclusion that the ordered structure in total becomes superconducting. In other words, not only the metallic regions support superconductivity, but the whole electronic crystal illustrated in **Figure 40b** forms a coherent macroscopic superconducting state.

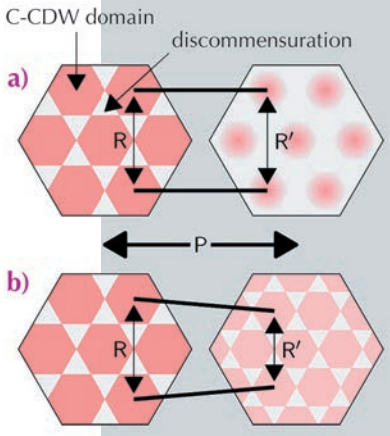

Fig. 40: Real space pressure evolution of the NC phase (a) according to Sipos *et al.* **[1]** and (b) concluded from X-ray diffraction.

References
[1] Sipos *et al., Nature Materials* **7**, 960 (2008).
[2] Spijkerman *et al., Physical Review B* **56**, 13757 (1997).
[3] Nakanishi *et al., Journal of the Physical Society of Japan* **43**, 1509 (1977).

EFFECT OF NANOSTRUCTURING ON THE ELECTRONIC PROPERTIES OF CATHODE MATERIALS

Rechargeable batteries have applications in many fields including portable electronic consumer devices, electric vehicles, and large-scale electricity storage in smart or intelligent grids. $LiCoO_2$ has been extensively used as cathode material in Li-ion batteries because of its best performance in terms of high specific energy density and excellent life cycle **[1,2]**. Nevertheless, a relatively slow diffusion of Li-ions in the bulk system limits its efficiency. Nanostructured electrodes of $LiCoO_2$ have been proposed as a solution to improve the cathode performance since the nanoparticles have unique physical and chemical properties with respect to the bulk materials **[3,4]**. Moreover, there appears to be a critical particle size below which the use of smaller nanoparticles is no longer beneficial **[4]**. In particular, reduction of the crystallite size to less than 15 nm drastically decreases the capacity of $LiCoO_2$.

We have investigated the effect of nanostructuring on the electronic properties of $LiCoO_2$ by high-resolution X-ray absorption and X-ray emission spectroscopy. The measurements reported in **Figure 41** were performed at the former beamline **ID16** on a series of $LiCoO_2$ nanoparticles of different sizes. Panel (a) shows the Co K-edge absorption spectra. Thanks to the wavelength dispersive crystal spectrometer, we were able to achieve

Principal publication and authors
L. Simonelli (a,b), N.L. Saini (c), M. Moretti-Sala (a), M. Okube (d), I. Honma (e), T. Mizokawa (f), and G. Monaco (a,g), *Applied Physics Letters* **103**, 083111 (2013).
(a) ESRF
(b) ALBA Synchrotron Light Facility, Barcelona (Spain)
(c) Dipartimento di Fisica, Università di Roma "La Sapienza" (Italy)
(d) National Institute of Advanced Industrial Science and Technology (AIST), Tsukuba, (Japan)
(e) Multidisciplinary Research for Advanced Materials, Tohoku University, Sendai (Japan)
(f) Department of Physics and Department of Complexity Science and Engineering, University of Tokyo (Japan)
(g) Dipartimento di Fisica, Università di Trento (Italy)

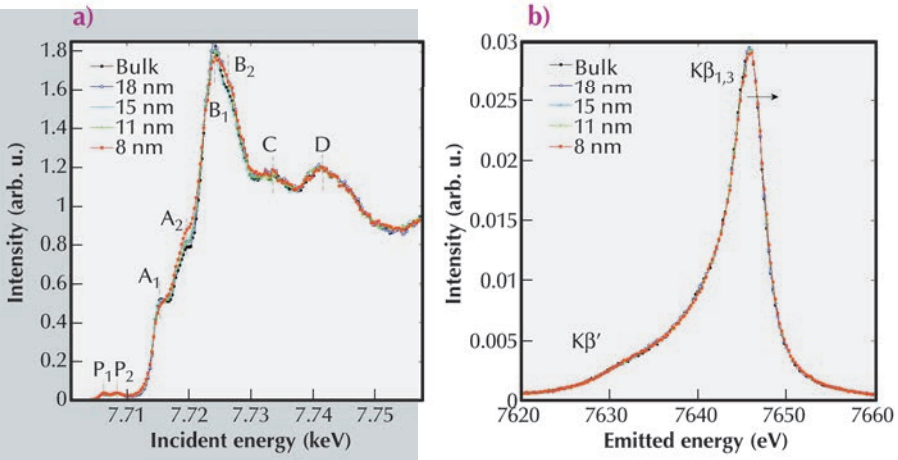

Fig. 41: (a) Normalised partial Kβ fluorescence yield absorption spectra of $LiCoO_2$ across the Co K-edge. Spectra relative to different nanoparticle sizes from the bulk to 8 nm are reported. (b) Co Kβ X-ray emission spectra of $LiCoO_2$ for different nanoparticle sizes.

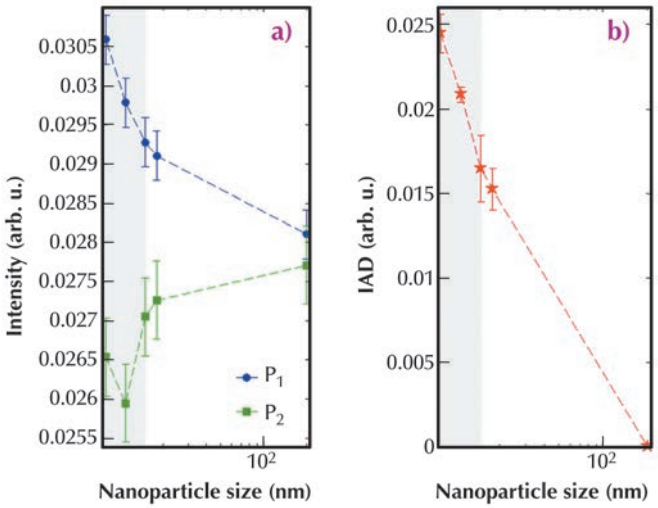

Fig. 42: (a) Evolution of pre-peak features P_1 and P_2 in the Co K-edge XAS spectra as a function of nanoparticle size. While P_1 increases, P_2 tends to decrease with decreasing nanoparticle size, showing an abrupt drop below 15 nm. (b) The integrated absolute value of the difference spectra (IAD) of the Kβ emission spectra with respect to a non magnetic reference are proportional to the local 3d spin magnetic moment, μ. IAD with respect to the bulk is shown as a function of nanoparticle size.

the high resolution necessary to resolve the low energy absorption components P_1 and P_2 (panel (a)). While the pre-peak P_1 is due to 1s → e_g local quadrupole transitions with a dipolar contribution due to Co 4p-3d mixture arising from the distorted octahedral environment of Co, feature P_2 corresponds to 1s → 4p-3d non-local dipole transitions related to oxygen mediated metal-metal interactions. Panel (b) reports the Co Kβ emission spectra (3p → 1s). The absence of a pronounced feature on the lower energy side (Kβ′) is an indication of a low-spin state for the full set of samples. Subtle variations of the emission spectra correspond to the variation of the Co local magnetic moment and of the Co oxidation state as a function of the nanoparticle size.

By analysing the high resolution Co K-edge absorption spectra and the Co Kβ emission spectra we extract quantitative information on the intersite/intrasite hybridisation and on the Co oxidation state and local magnetic moment. We found that reduction of the particle size leads to a change in the electronic structure similar to the delithiation effect [5]. Below a nanoparticle size of 15 nm, the intersite (intrasite) 4p-3d hybridisation shows an abrupt decrease (increase) that is correlated to the variation of the local Co magnetic moment (Figure 42).

Our results provide important information on the understanding of the reduced electrochemical efficiency for $LiCoO_2$ nanoparticle with a critical value of 15 nm.

References
[1] J.-M. Tarascon and M. Armand, *Nature* **414**, 359 (2001).
[2] P. He, H. Yu, D. Li and H. Zhou, *J. Mater. Chem.* **22**, 3680 (2012).
[3] A.S. Arico, P. Bruce, J.-M. Tarascon and W.V. Schalkwijk, *Nature Mater.* **4**, 366 (2005).
[4] M. Okubo, E. Hosono, J. Kim, M. Enomoto, N. Kojima, T. Kudo, H. Zhou, and I. Honma, *J. Am. Chem. Soc.* **129**, 7444 (2007); M. Okubo, J. Kim, T. Kudo, H. Zhou and I. Honma, *J. Phys. Chem. C* **113**, 15337 (2009).
[5] L. Maugeri, A. Iadecola, B. Joseph, L. Simonelli, L. Olivi, M. Okubo, I. Honma, H. Wadati, T. Mizokawa and N.L. Saini, *J. Phys.: Condens. Matter* **24**, 335305 (2012).

FUNDAMENTAL PHYSICS

DOES NUCLEAR RESONANT SCATTERING VIOLATE RECIPROCITY?

Principal publication and authors
L. Deák (a), L. Bottyán (a), T. Fülöp (a), G. Kertész (a), D.L. Nagy (a), R. Rüffer (b), H. Spiering (c), F. Tanczikó (a) and G. Vankó (a), *Phys. Rev. Lett.* **109**, 237402 (2012).
(a) Wigner Research Centre for Physics, Budapest (Hungary)
(b) ESRF
(c) Johannes Gutenberg Universität, Mainz (Germany)

Newton's third law has stated the equality of action and reaction between mechanical bodies. In the nineteenth century, von Helmholtz, Rayleigh and others formulated an analogy for classical waves, the *reciprocity principle*. According to this principle, the source and the detector can be interchanged without any consequence on the waves regardless of where the surrounding objects are located.

A number of physical phenomena can be described by scattering of waves. The signal observed in a scattering experiment is similarly expected to remain unchanged upon reversing the source and the detector. This often fulfilled expectation of the reciprocity principle has been generalised for more complex scattering systems, and, indeed, strict reciprocity theorems were formulated for specific cases. Reciprocity-related publications span the twentieth century, as summarised in the review of Potton [1]. Surprisingly, it turns out that the reciprocity principle does not actually follow from first principles of physics. Although obedience of the reciprocity principle was used in the antenna theory of radio communications in the early twentieth century, its violation in other areas of wave propagation is commonplace. Nowadays non-reciprocal devices such as circulators and isolators are routinely used in microwave and laser optics.

What then is reciprocity? In many studies, it is simply identified as time reversal symmetry. However, in polarisation-independent optics, absorption is known to violate time reversal symmetry, while reciprocity is obeyed. Similarly, the requirement of invariance upon interchanging the source and the detector, reciprocity is conjectured to be identical with a 180° rotation. However, this latter also fails, since there exist examples with no 180° rotational symmetry still obeying the reciprocity principle. Reciprocity, therefore, is neither a mere time-reversal, nor a mere 180° rotational invariance, but it is a special symmetry of the scattering amplitude, as explained in a recent theory of ours [2].

We studied the conditions of a system to obey or violate the reciprocity principle. Our aim was to select an experiment in which reciprocity violation is markedly strong, in order to unquestionably demonstrate whether reciprocity is obeyed or violated in a particular scattering experiment. To this end, nuclear resonant scattering (NRS) of synchrotron radiation was applied at the nuclear resonance side station **ID22N** in two experimental arrangements for ferromagnetic scatterers. Both scattering arrangements, cases shown in **Figures 43a and 43b**, consisted of two 6 μm thick ^{57}Fe foils uniformly magnetised in the plane of the foils in a magnetic field of 0.19 T. The *z*-axis was in the direction of the beam and the *y*-axis aligned with its linear polarisation. The spectra of the scatterers were compared to their reciprocal counterparts. The interchange of the source and the detector was realised by a 180° rotation of the entire sample holder around the *x*-axis [2].

In a typical NRS experiment, the time response of the scatterer to the excitation by a synchrotron pulse is recorded and analysed. The synchrotron radiation pulse excites the hyperfine-split nuclear energy levels simultaneously, leading to characteristic beats in the time spectra. The four time spectra and the corresponding computer simulations are shown in **Figure 44**. The scattering arrangements in **Figure 43** exhibit neither time reversal nor 180° rotational invariance around the *x*-axis. Our NRS experiments prove that the arrangement in **Figure 43a** results in obeying reciprocity in the measured intensities in **Figure 44a**, while the arrangement in **Figure 43b**

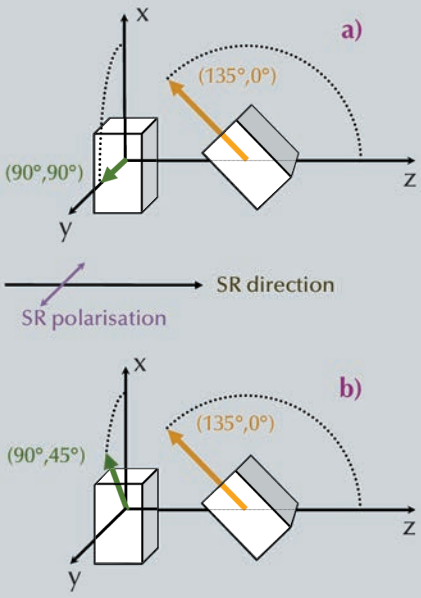

Fig. 43: Geometrical arrangement for a) the reciprocity-obeying and b) the reciprocity-violating case, respectively. The coloured arrows indicate the direction of the magnetic fields.

References

[1] R.J. Potton, *Rep. Prog. Phys.* **67**, 717-753 (2004).

[2] L. Deák and T. Fülöp, *Ann. Phys.* (Amsterdam) **327**, 1050-1077 (2012).

exhibits apparent non-reciprocity in **Figure 44b**. When compared to earlier trials of experimental proof of non-reciprocity, this finding is exceptional due to the huge non-reciprocity. In certain time intervals, intensities in the direct and reciprocal scattering cases of **Figure 44b** differ as much as a factor of one thousand, while on switching back to arrangement **Figure 43a**, the intensities display full reciprocity in **Figure 44a**. (The difference of the spectra in **Figure 44a** is merely due to the difference in the total acquisition time.)

In full agreement with theoretical expectations **[2]**, it has therefore been undoubtedly demonstrated that the magneto-optic Faraday effect does not automatically give rise to non-reciprocity. Applications of switchable non-reciprocity are expected in the field of gamma-optics.

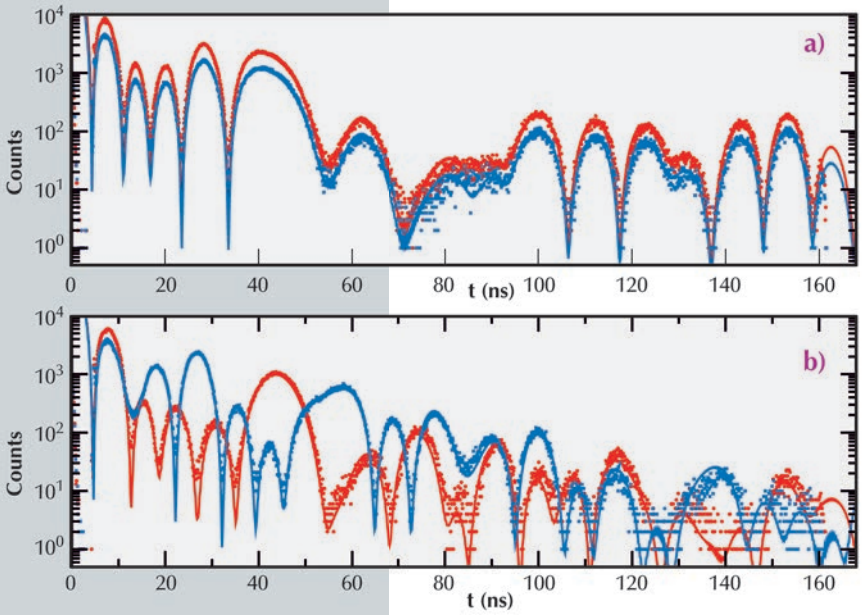

Fig. 44: a) Measured and simulated NRS time spectra for the case displayed in **Figure 43a** in direct (red colour) and reciprocal (blue colour) geometry. b) Experimental data and simulations for the case shown in **Figure 43b** in direct and reciprocal geometry.

STRUCTURAL BIOLOGY

For the ESRF Structural Biology Group, 2013 has been a year in which we have witnessed the end of an era. The last external user experiment at ID14-4, carried out on 6th December, marked the final closure of the ID14 'Quadriga' suite of beamlines, Europe's first dedicated undulator-based beamlines for Macromolecular Crystallography (MX), after 15 years of service to the European Structural Biology Community. During its operational lifetime, crystal structures elucidated from single crystal diffraction data collected at ID14 contributed to almost a quarter of the total European-based deposits in the Protein Data Bank. Science performed at the beamline has provided landmark insights in many areas of Biology including the innate immune complement system, large membrane protein complexes such as Photosystems I and II, and the structures and mechanisms of action of viruses. Experiments at ID14, mostly carried out by beamline staff, shed crucial light on the effect of X-ray induced radiation damage on biological macromolecules, paved the way for the use of UV-visible spectroscopy as a tool to ensure the correct interpretation of crystal structures obtained and helped usher in the technique of high throughput crystallography at the ESRF. Without a doubt though, the achievement for which ID14 will probably be best remembered is its role in the solution of the crystal structure of the ribosome which led to a share of the 2009 Nobel Prize in Chemistry for Venki Ramakrishnan of the MRC Laboratory of Molecular Biology (UK) and Ada Yonath of the Weizmann Institute of Science (Israel) - two long-term users of the ESRF. To mark the contribution of ID14 to European Structural Biology, a one-day symposium will be held in conjunction with the 2013 ESRF Users' Meeting.

The final closure of the ID14 complex aside, 2013 has been a successful and busy year for the beamlines of the Structural Biology Group. The construction and commissioning of the MASSIF facility, ESRF Upgrade Programme project UPBL10, has continued apace: the commissioning of the X-ray optics of both ID30A-1 (MASSIF-1) and ID30A-3 (MASSIF-3) has been completed, the sample environment of MASSIF-1 has begun to take its final shape and we expect these two facilities to take first users in mid- and late-2014, respectively. MASSIF-1 will be a fixed energy (12.7 keV), high intensity end-station offering rapidly variable focal spot sizes (120 μm^2 – 50 μm^2 for sample evaluation and data collection. MASSIF-3 will be a fixed energy microfocus end-station providing X-ray beam less than 10 μm^2 at the sample position. As well as state-of-the art sample changing robotics, both end-stations will be equipped with latest generation pixel detectors (Pilatus3 6M for MASSIF-1, Eiger 4M for MASSIF-3) to ensure the collection of the highest possible quality diffraction data. Progress on ID30B – the 'replacement' of ID14-4 – has also been good and here we expect first users towards the end of 2014. The end is thus in sight for the Phase I upgrade of MX facilities at the ESRF. However, our beamlines will continue to evolve. Current plans include the refurbishment of the ID23-2 microfocus facility to produce, in 2016, a (sub)-micrometre sized beam at the sample position. Additionally, we are actively considering proposals to improve the functionality and X-ray beam characteristics at the two MAD beamlines ID23-1 and ID29.

Despite the resources dedicated to the construction and commissioning of UPBL10 and the availability of only four operational MX beamlines (ID14-4, ID23-1, ID23-2 and ID29), output from the Structural Biology Group beamlines has remained high with, at the time of writing, ESRF-based depositions in the Protein Data Bank for 2013 being close to record levels. An annual refrain is that the articles presented in the Structural Biology Highlights chapter represent only a very small part of the Science reported by the ESRF's external Structural Biology User Community. This remains true for 2013 but we hope that the work presented here provides a true representation of the broad range of research facilitated by our beamlines. Particularly noteworthy are two reports on membrane proteins. The first, by Neutze and colleagues, describes the crystal structure of an aquaporin - involved in cellular water transport – at subangstrom resolution (d_{min} = 0.88 Å). This represents the first truly atomic resolution study of a membrane protein. Here, electron density and difference density maps of unparalleled quality have allowed the unambiguous assignment of both orientation and tautomeric form of amino acid residues crucial to the specificity of aquaporins, and this study has provided true atomic level insight into the control of water homeostasis in living cells. The second, by Sazanov and colleagues, reports the crystal structure of the entire respiratory complex I from *T. thermophilus* at 3.3 Å resolution. With a total molecular mass of 536 kDa and comprising 16 subunits, 9 Fe-S clusters and 64 transmembrane helices, this crystal structure represents the largest asymmetric membrane protein structure thus far solved and suggests a likely mechanism, involving long range conformational changes, for the coupling of electron transfer in the hydrophilic domain to proton translocation in the membrane domain of complex I.

G. LEONARD

Principal publication and authors
U. Kosinska Eriksson (a), G. Fischer (a), R. Friemann (a), G. Enkavi (b), E. Tajkhorshid (b) and R. Neutze (a), *Science* **340,** 1346-1349 (2013).
(a) Department of Chemistry and Molecular Biology, University of Gothenburg (Sweden)
(b) Department of Biochemistry, College of Medicine, Center for Biophysics and Computational Biology, and Beckman Institute for Advanced Science and Technology, University of Illinois, Urbana (USA)

CELLULAR WATER TRANSPORT: SUB-ANGSTROM RESOLUTION INSIGHTS FROM THE CRYSTAL STRUCTURE OF A MEMBRANE PROTEIN

The control of water homeostasis in living cells is facilitated by aquaporins which, like all membrane proteins involved in homeostasis, have to be extremely selective for the molecule that they transport. Aquaporins must exclude both hydroxide (OH^-) and hydronium (H_3O^+) ions as well as preventing the transport of protons (H^+), which can usually be rapidly exchanged between water molecules linked by hydrogen bonds. The crystal structures of aquaporins from several species show that their tertiary structures comprise six transmembrane helices plus a pseudo helix, made up of two aligned half-helices inserted from opposite sides of the membrane, arranged to form a pore through which water can flow (**Figure 45a**). The positioning of the pseudo helix places the dual asparagine-proline-alanine (NPA) motif characteristic of aquaporins close to the centre of the pore (**Figure 45c**), with water specificity supplied by a so-called 'selectivity filter' found close to the extracellular pore entrance (**Figure 45b**). The two half-helices making up the pseudo transmembrane helix focus a positively charged electrostatic dipole at the centre of the channel and this has been proposed to create a barrier preventing the passage of protons, and also to orient the dipoles of water molecules passing though the pore in a way that prevents proton exchange between water molecules *via* a Grotthuss mechanism **[1, 2]**. This hypothesis, however, does not explain the observation that mutations that reduce the strength of this electrostatic barrier increase the transport of Na^+ by aquaporins but not that of H^+ **[3]**.

The ultra-high resolution (d_{min} = 0.88 Å) crystal structure of Aqy1 from *Pichia pastoris*, obtained using data collected at beamline **ID29**, has shed new light on the selectivity mechanisms of water transport by aquaporins. The electron density maps allow the assignment of H-bond interactions of both NPA asparagine residues to passing water

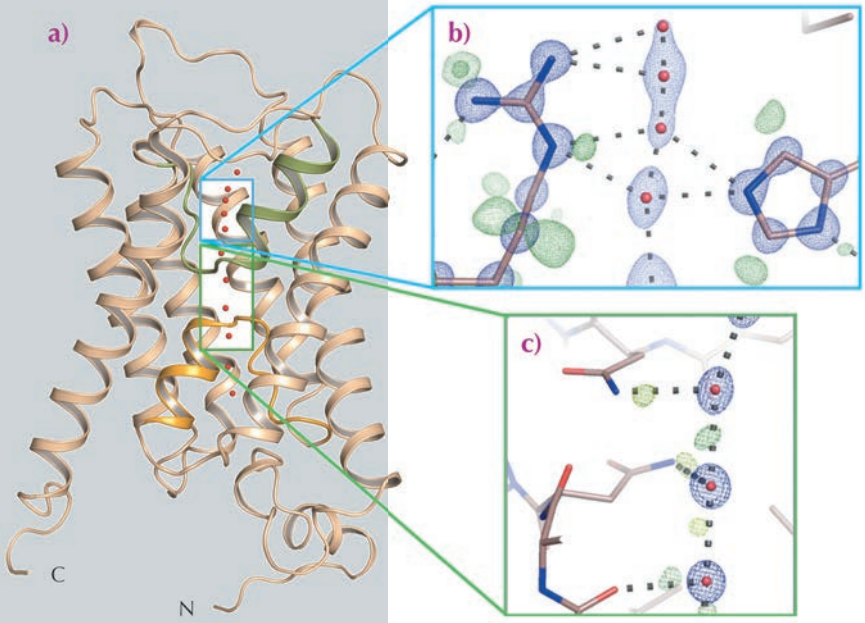

Fig. 45: Sub-angstrom resolution crystal structure of an aquaporin isolated from yeast. a) The fold of an aquaporin monomer comprises six transmembrane helices and one pseudo-transmembrane helix (formed by two aligned half helices, shown in orange and green) arranged to form a pore through which water can flow. b) Electron density for the selectivity filter region of the aquaporin structure solved to 0.88 Å resolution. Blue mesh shows the $2mF_{obs}$-DF_{calc} electron density around the selectivity filter residues Arg227 and His212, as well as around four water molecules identified within the selectivity filter (red spheres). Green mesh represents residual mF_{obs}-DF_{calc} electron density, indicating the presence of electrons associated with hydrogen bonds or involved in covalent bonds between hydrogen and carbon atoms. c) Electron density near the dual asparagine-proline-alanine (NPA) aquaporin signature motif. Blue mesh represents $2mF_{obs}$-DF_{calc} electron density for water molecules (red spheres) near the centre of the aquaporin pore; green mesh reveals electron density for electrons participating in hydrogen bonds with water molecules. H-bond donor interactions from the nitrogen atoms of the two NPA motif alanine residues (Ala112 and Asn224) to passing water molecules are clearly observed.

molecules (**Figure 45c**) and confirm a proposed bipolar distribution of hydrogen bonds between adjacent water molecules within the aquaporin channel. Similarly, both the orientation and tautomeric forms of two conserved selectivity filter residues, His212 and Arg227, can be assigned (**Figure 45b**). Intriguingly, the electron density also revealed stable sites for four water molecules within the selectivity filter (**Figure 45b**). However, the distances between these water positions excludes that all four sites are occupied simultaneously and, in fact, these four positions are made up of two pairs of sites that are partially occupied in a mutually exclusive fashion (*i.e.* sites Wat2 and Wat4 cannot be occupied at the same time as sites Wat1 and Wat3). This suggests a pair-wise movement of water molecules through the aquaporin selectivity filter, analogous to the crystallographically observed pair-wise transport of K^+ through potassium channels **[4]**. As was proposed for potassium transport, the similar occupancy of the four water sites (66% for Wat2 and Wat4; 34% for Wat1 and Wat3) suggests that the binding energies of these pairs are much the same, a situation which is ideal for maximising water conduction rates in aquaporins.

References
[1] E. Tajkhorshid *et al., Science* **296,** 525-530 (2002).
[2]. B.L. de Groot, T. Frigato, V. Helms and H. Grubmüller, *J. Mol. Biol.* **333**, 279-293 (2003).
[3] D. Wree, B. Wu, T. Zeuthen and E. Beitz, *FEBS J.* **278**, 740-748 (2011).
[4] J.H. Morais-Cabral, Y. Zhou and R. MacKinnon, *Nature* **414**, 37-42 (2001).

CRYSTAL STRUCTURE OF THE ENTIRE RESPIRATORY COMPLEX I

Principal publication and authors
R. Baradaran (a), J.M. Berrisford (a,b), G.S. Minhas (a) and L.A. Sazanov (a), *Nature* **494**, 443-8 (2013).
(a) Medical Research Council Mitochondrial Biology Unit, Cambridge (UK)
(b) Present address: European Bioinformatics Institute, Cambridge (UK)

Mitochondria are "cellular power plants", containing a chain of respiratory complexes that utilise NADH (mainly) and oxygen to pump protons across the membrane. This proton-motive force is used to produce the universal energy currency ATP, by ATP synthase, a turbine-like molecular machine. Another example of a molecular machine is complex I, the first and largest enzyme in the respiratory chain. It transfers two electrons from NADH to quinone, coupled to the translocation of four protons across the membrane. Mitochondrial complex I consists of 44 subunits, whilst the prokaryotic enzyme is simpler, usually consisting of 14 "core" subunits with a total mass of about 550 kDa. It represents an important 'minimal' model of human complex I.

Defects, mainly related to complex I, in mitochondrial DNA are one of the most common types of human genetic disorder. So far there is no treatment for these debilitating diseases, which include neurological impairment, deafness, blindness, muscle weakness and cardiovascular disease. To understand the molecular basis of these conditions and as a starting point for drug development, we need to know the structure of the proteins involved. Structures are also necessary, of course, in order to understand the fundamental mechanistic principles of molecular machines.

Complex I, due to its sheer size, resisted structure determination efforts for a long time. Our earlier crystal structures of the hydrophilic domain of complex I from *Thermus thermophilus* established the electron transfer pathway from NADH through the flavin mononucleotide (FMN) and seven iron-sulfur (Fe-S) clusters to the putative quinone binding site **[1]**. Recently we have determined the atomic structure of the membrane domain of *E. coli* complex I (220 kDa, 6 subunits, 55 TM helices) at 3.0 Å resolution **[2]**. The structure revealed many unexpected features of the protein fold, such as the face-to-back arrangement of symmetry-related

Fig. 46: Structure of the entire complex I from *T. thermophilus*. FMN and Fe-S clusters are shown as magenta and red-orange spheres.

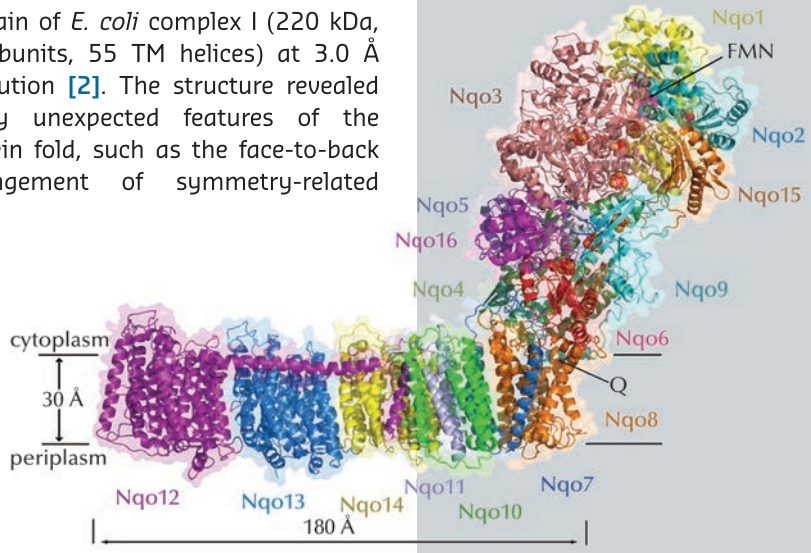

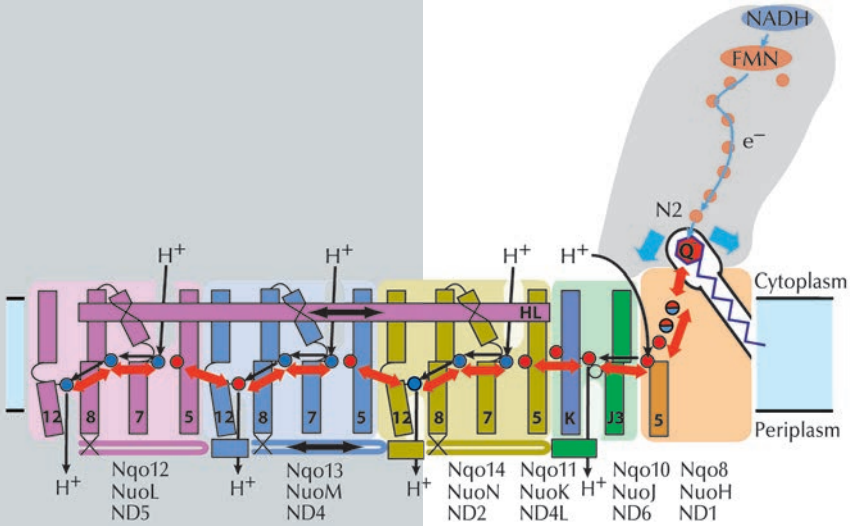

Fig. 47: Proposed coupling mechanism of complex I. Upon reduction, negatively charged quinone initiates conformational changes in the E-channel (Nqo8/10/11). These propagate to the antiporter-like subunits via the central axis (red arrows) of charged and polar residues located around flexible breaks in key transmembrane helices (numbered). Helix HL and the βH element (labelled) help coordinate conformational changes. Key charged residues are indicated by red circles for Glu and blue circles for Lys/His. Conformational changes drive appropriate changes in the pKa's and solvent exposure of key residues so that net result is the translocation of four protons per cycle.

References
[1] L.A. Sazanov and P. Hinchliffe, *Science* **311,** 1430-6 (2006).
[2] R.G. Efremov and L.A. Sazanov, *Nature* **476,** 414-20 (2011).

domains in the three similar antiporter-like subunits, the formation of a single proton-translocation channel from two half-closed channels found in each of these domains, and the central role of lysine residues (rather than usual carboxylates) in the proton channels.

We have now determined the structure of the entire complex I from *T. thermophilus* (536 kDa, 16 subunits, 9 Fe-S clusters, 64 TM helices) to 3.3 Å (**Figure 46**). This is the largest asymmetric membrane protein structure so far determined, and solving it was a major technical challenge. Crystals of the entire complex are twinned, and so, to overcome a problem of model bias, we also crystallised and solved the structure of the isolated membrane domain of *T. thermophilus* complex I. The core fold of subunit Nqo8 (previously missing from structures) is, unexpectedly, similar to a half-channel of the antiporter-like subunits. Small subunits nearby form a linked second half-channel, thus completing the fourth proton translocation pathway (dubbed E-channel due an abundance of glutamates), in addition to the channels in three antiporter-like subunits. The quinone-binding site is unusually long, narrow and enclosed. The quinone head group binds at the enclosed end of this chamber, near cluster N2. This means that quinone, uniquely, moves about 15 Å out of the membrane in order to accept electrons. Such an unusual binding site allows the protein to control quinone protonation and to use the redox energy of charged species to drive conformational changes. The quinone chamber is linked to the fourth proton translocation channel by a "funnel" of charged residues. This link continues over the entire membrane domain as a remarkable flexible central axis of charged and polar residues.

The structure suggests the likely mechanism of coupling between the electron transfer in the hydrophilic domain and proton translocation in the membrane domain through long-range conformational changes (**Figure 47**). It somewhat resembles a steam engine with its coupling rods linking parts of the machine and is Nature's compliment to the turbine-like ATPase.

Principal publication and authors
Y. Nicolet, R. Rohac, L. Martin and J.C. Fontecilla-Camps, *PNAS* **110**, 7188–7192 (2013).
Metalloproteins Unit, Institut de Biologie Structurale J.-P. Ebel CEA-CNRS-UJF, Grenoble (France)

X-RAY SNAPSHOTS OF LIKELY INTERMEDIATES IN THE SYNTHESIS AND DEGRADATION OF BIOLOGICAL Fe_4S_4 CLUSTERS

Fe-S clusters are ancient protein-bound prosthetic groups generally involved in substrate binding and activation, electron transfer and stress sensing in the regulation of gene expression. Alternatively, they can also play a structural role. Their compositions vary from the commonly found Fe_2S_2, Fe_3S_4 and Fe_4S_4 centres to the more complex Fe_7S_9Mo cluster found in the active site of nitrogenase. Facultative microbes can take advantage of the intrinsic sensitivity of Fe-S clusters to O_2-induced damage to switch between anaerobic and aerobic metabolisms, a property used by the fumarate nitrate

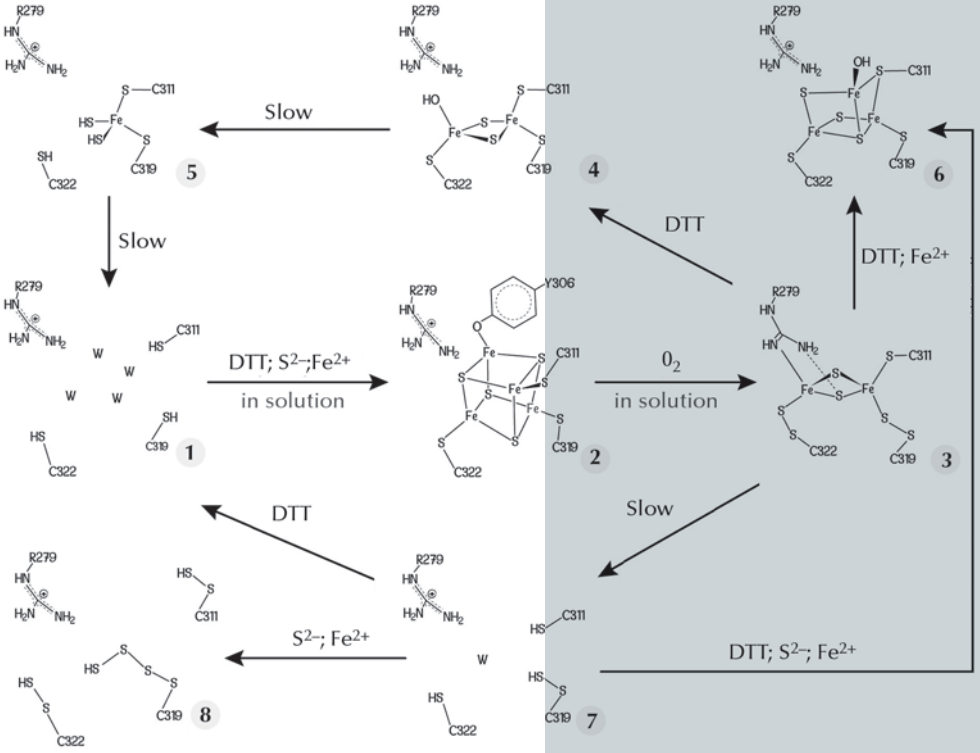

Fig. 48: Postulated Fe-S cluster degradation pathway based on our different TmHydE crystal structures. Unless specified, all reactions were performed within crystals. W in species **1** and **7** represents water molecules.

reduction regulator (FNR). Under 0.5% oxygen, FNR is a protein dimer that coordinates one Fe_4S_4 cluster per monomer and binds specific DNA sequences to either activate or repress gene expression. Conversely, under higher oxygen levels, there is a rapid Fe_4S_4-to-Fe_2S_2 cluster transformation upon which FNR dissociates into monomers that no longer bind DNA. The three dimensional structure of FNR remains unsolved, which imposes a severe limitation in the understanding of this process.

It was thought that Fe_4S_4-to-Fe_2S_2 cluster degradation in FNR involved the release of one Fe^{2+}, one Fe^{3+} and two S^{2-} ions [1]. However, a very recent study, which combined resonance Raman (RR), UV-visible absorption/CD spectroscopy and mass spectrometry [2], indicates that FNR cluster conversion results in an Fe_2S_2 cluster that retains two sulfides as cysteine persulfide ligands. The relevant reactions are:

$$Fe_4S_4^{2+} + O_2 \rightarrow Fe_3S_4^{+} + Fe^{2+} + O_2^{\bullet-} \quad (1)$$

$$2\ \text{Cys-S}^- + Fe_3S_4^{+} + O_2 + 4\ H^+ \rightarrow 2\ \text{Cys-S-S}^- + Fe_2S_2^{2+} + Fe^{3+} + 2\ H_2O \quad (2)$$

The FeFe-hydrogenase maturase HydE from *Thermotoga maritima,* which belongs to the radical *S*-adenosyl-L-methionine (SAM) protein superfamily, binds the Fe_4S_4 cluster typical of these enzymes, along with a more exposed centre that displays variable compositions in our crystals. We have used this exposed site as a template to obtain unprecedented Fe-S clusters that most likely constitute a sequence describing cluster degradation and assembly (**Figure 48**). The cluster with the highest number of Fe ions in our original crystals resembles a standard Fe_3S_4 centre, except that one cysteine ligand bridges two iron ions (**6** in **Figure 48**). We subsequently obtained a new crystal form of *Tm*HydE using a higher salt concentration [3]. This form contains a regular Fe_4S_4 cluster,

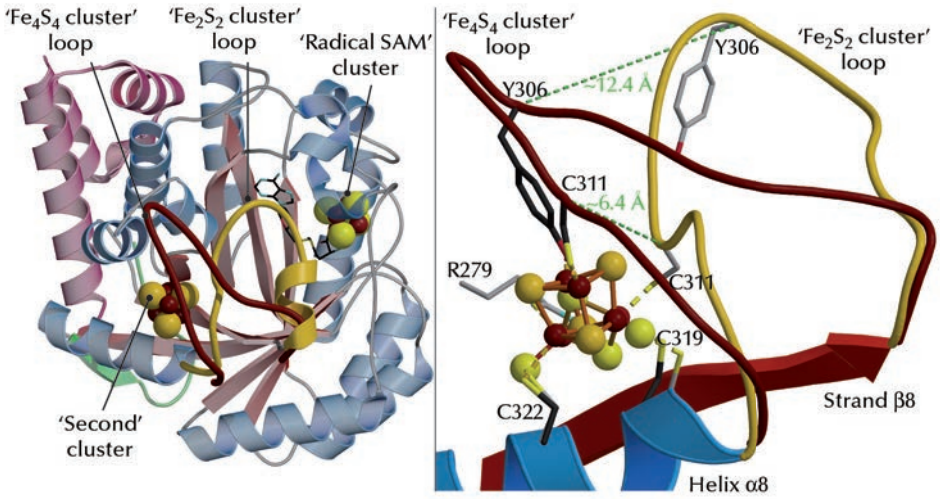

Fig. 49: Structural differences between the Fe_4S_4 and Fe_2S_2 cluster-containing TmHydE proteins. (Left) View of the overall structure depicting the movement of a loop induced by cluster conversion (shown in brown for Fe_4S_4 and gold for Fe_2S_2). (Right) Close-up view of the Fe-S cluster-binding site (colour codes as in left figure). Dashed lines indicate the shifts of positions of the Cα atoms of C311 and Y306 when the two structures are compared.

References
[1] J.C. Crack, A.A. Gaskell, J. Green, M.R. Cheesmant, N.E. Le Brun and A.J. Thomson, *J. Am. Chem. Soc.* **130**, 1749-58 (2008).
[2] B. Zhang, J.C. Crack, S. Subramanian, J. Green, A.J. Thomson, N.E. Le Brun, *et al.*, *Proc Natl Acad Sci* USA **109**, 15734-9 (2012).
[3] Y. Nicolet, R. Rohac, L. Martin and J.C. Fontecilla-Camps, *Proc Nat Acad Sci* USA **110**, 7188-92 (2013).
[4] J.K. Rubach, X. Brazzolotto, J. Gaillard and M. Fontecave, *FEBS Lett.* **579**, 5055-60 (2005).
[5] B.A. Lazazzera, H. Beinert, N. Khoroshilova, M.C. Kennedy and P.J. Kiley, *J. Biol. Chem.* **271**, 2762-8 (1996).

as previously reported for this protein in solution [4], that has a tyrosine side chain as its fourth protein ligand (**2** in Figure 48 and Figure 49). Most relevant to the FNR spectroscopic results [2] is our finding of a structure where the Fe_2S_2 cluster is coordinated by two cysteine persulfide ligands (**3** in Figure 48). Persulfide formation must have resulted from sample exposure to traces of O_2 either in the glove box or during its transfer to it.

A comparison between our structures shows that the reversible transition from the Fe_4S_4 cube to the Fe_2S_2 rhomb requires a major rearrangement of the coordination site in *Tm*HydE (Figure 49). Comparable changes may be responsible for the O_2-induced dimer dissociation in FNR [5]. Taken together, our results and the RR spectroscopic studies mentioned above [2] provide a coherent functional and structural description of the Fe_4S_4-to-Fe_2S_2 cluster conversion that generally takes place upon O_2 exposure in Fe-S cluster-containing proteins. The main proposition derived from our work [3] and reference [2] is the existence of a Fe-S cluster direct repair mechanism involving the reduction of persulfide ligands in a Fe_2S_2 cluster similar to the transition that took place in our crystals:

$$2\ \text{Cys-S-S}^- + \text{Fe}_2\text{S}_2^{2+} + 2\ \text{Fe}^{2+} + 4\ e^- \rightarrow 2\ \text{Cys-S}^- + \text{Fe}_4\text{S}_4^{2+} \quad (3)$$

Such a mechanism represents a considerable economy to the cell because only Fe ions need to be available for the reconstitution of Fe_4S_4 clusters in FNR under anaerobic conditions.

STRUCTURAL ANALYSIS REVEALS THE LxxLL MOTIF HIJACKING STRATEGY DEVELOPED BY PAPILLOMAVIRUS E6 ONCOPROTEINS

Principal publication and authors
K. Zanier (a), S. Charbonnier (a), A.O.M.O. Sidi (a), A.G. McEwen (b), M.G. Ferrario (b), P. Poussin (b), V. Cura (b), N. Brimer (c), K.O. Babah (a), T. Ansari (c), I. Muller (a), R.H. Stote (b), J. Cavarelli (b), S. Vande Pol (c) and G. Travé (a). *Science* **339**, 694-8 (2013).
(a) UMR 7242, Biotechnologie et Signalisation Cellulaire, École Supérieure de Biotechnologie de Strasbourg, Illkirch (France)
(b) Institut de Génétique et de Biologie Moléculaire et Cellulaire (IGBMC) / INSERM U964 / CNRS UMR 7104/ Université de Strasbourg, Illkirch (France)
(c) Department of Pathology, University of Virginia, Charlottesville (USA)

References
[1] H. zur Hausen. *Semin Cancer Biol* **9**, 405 (1999).
[2] S.B. Vande Pol and A.J. Klingelhutz. *Virology* **445**, 115-137 (2013).
[3] K. Zanier *et al.*. *Structure* **20**, 604 (2012).
[4] N.E. Davey, G. Trave and T.J. Gibson, *Trends Biochem Sci* **36**, 159 (2011).

High-risk mucosal human papillomaviruses (hrm-HPVs) provoke cervical cancers [1] by means of two small multifunctional oncoproteins named E6 and E7. hrm-HPV E6 recruits the ubiquitin ligase E6AP and tumor suppressor p53, leading to ubiquitin–mediated degradation of p53 [2]. E6 captures E6AP and many other cellular proteins through acidic leucine-rich motifs containing the LxxLL consensus sequence [2]. Despite its small size, 150 residues, E6 is prone to aggregation, which has long precluded its structural analysis.

We designed strategies to solubilise two E6 proteins from HPV16 (the most tumorigenic HPV type) and BPV1 (an oncogenic bovine papillomavirus). We used the target LxxLL peptide as a solubilising ligand, fused our constructs to the highly soluble and crystallisation prone Maltose-Binding Protein (MBP), and also mutated, on the surface of HPV16 E6, four cysteine and one phenylalanine residues, which we had previously found to promote E6 self-association [3]. This allowed us to crystallise BPV1 E6 and HPV16 E6, respectively bound to LxxLL peptides from the focal adhesion protein paxillin and the ubiquitin ligase E6AP. The structures (Figures 50 and 51) were solved at resolutions of 2.3 Å and 2.6 Å, respectively, by molecular replacement using the known structure of MBP as a template.

The two structures are very similar (Figure 50, Figure 51a). E6 comprises two zinc-binding domains joined by a linker helix (Figure 50, Figure 51a). The LxxLL motif adopts a α-helical

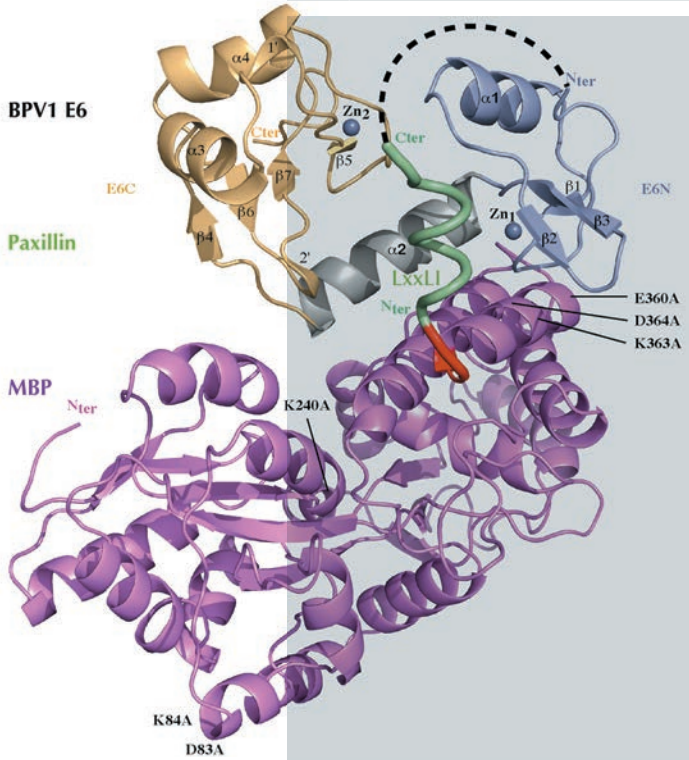

Fig. 50: Crystal structure of a triple fusion protein comprising a crystallisation-prone mutant of MBP, a LxxLL motif from paxillin, and wild-type bovine (BPV1) E6 oncoprotein. Crystallisation-promoting MBP mutations are indicated. Red: triple alanine linker. Green: helical LxxLL motif, corresponding to the 10 N-terminal residues of focal adhesion protein paxillin. Light blue: N-terminal zinc binding domain. Grey: linker helix. Gold: C-terminal zinc binding domain.

conformation and docks within a hydrophobic cavity (**Figure 51b**) formed by the two zinc-binding domains and the linker helix. Surrounding the cavity, several polar or charged residues are involved in maintaining the architecture of the complex (**Figure 51c**). Mutagenesis of a number of polar or charged residues lining the pocket, including several key arginines, disrupted binding of both E6 proteins to the LxxLL motif as well as their oncogenic activities (cellular transformation for BPV1 E6 and p53 degradation for HPV16 E6). Mutagenic data combined with computational analysis of both complexes allowed us to distinguish two distinct roles for the peptide-contacting residues of E6. i) Conserved pocket residues accomodate the invariable leucine side chains and establish sequence-independent contact to the peptide's main chain. ii) Variable "reader" residues discriminate variations of the LxxLL motif through sequence-dependent contacts to variable side-chains of the bound peptide. Such combinations of discriminative and tolerant reading mechanisms clearly must allow different E6 proteins to capture different panels of host proteins bearing variations of the LxxLL motif.

The hijacking of cellular motifs is a well-known viral strategy [4]. Most frequently, viral proteins evolve small sequence fragments, which *mimic* cellular linear motifs, thereby interfering with their functions. In contrast, PV E6 has evolved an entire pocket, composed of two folded domains, which *captures* cellular LxxLL motifs to perform oncogenic functions. The LxxLL-binding pocket of E6, revealed in atomic detail by this work, therefore represents a promising target for therapeutic drugs against HPV-induced cancers.

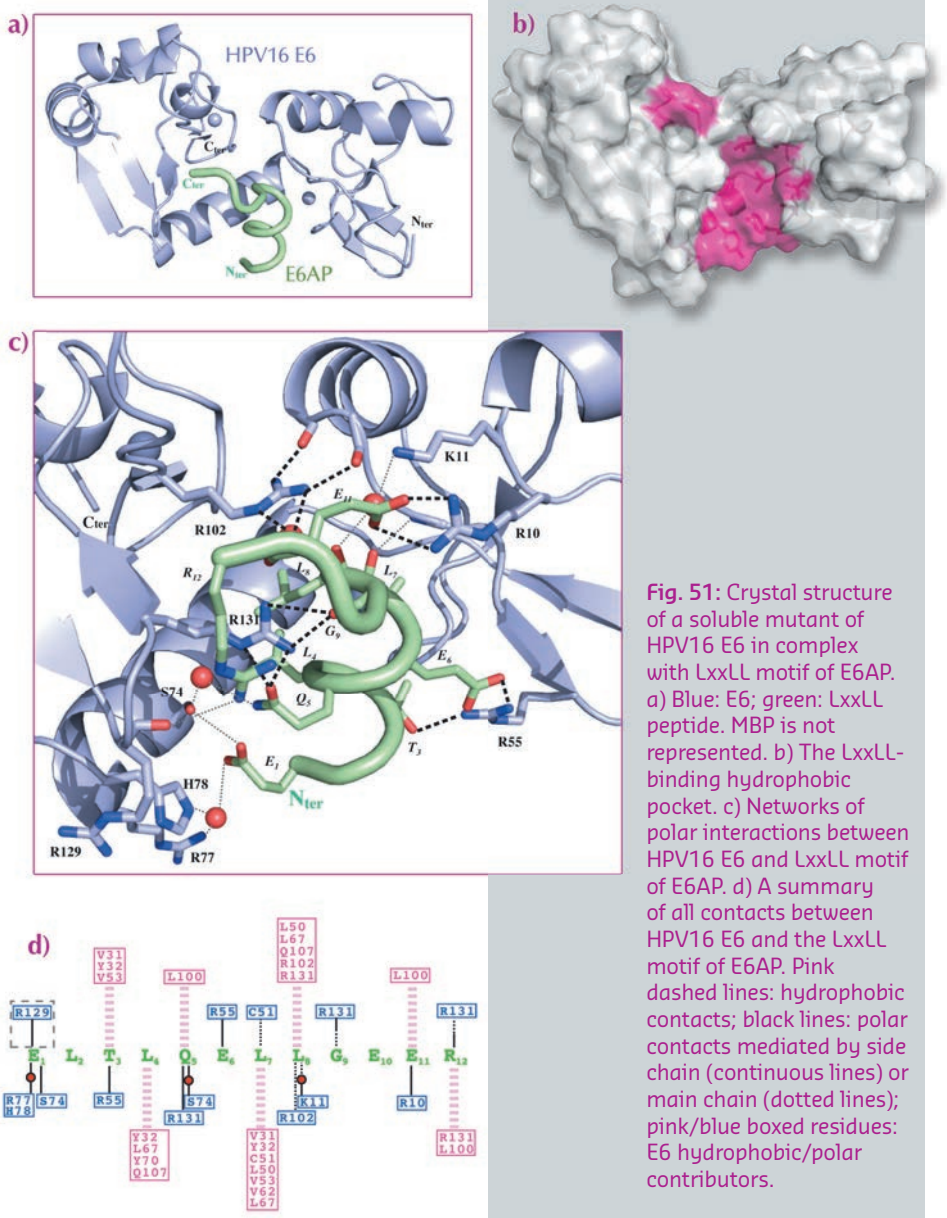

Fig. 51: Crystal structure of a soluble mutant of HPV16 E6 in complex with LxxLL motif of E6AP. a) Blue: E6; green: LxxLL peptide. MBP is not represented. b) The LxxLL-binding hydrophobic pocket. c) Networks of polar interactions between HPV16 E6 and LxxLL motif of E6AP. d) A summary of all contacts between HPV16 E6 and the LxxLL motif of E6AP. Pink dashed lines: hydrophobic contacts; black lines: polar contacts mediated by side chain (continuous lines) or main chain (dotted lines); pink/blue boxed residues: E6 hydrophobic/polar contributors.

STRUCTURAL BASIS FOR ION PERMEATION IN A PENTAMERIC LIGAND-GATED ION CHANNEL REVEALED BY X-RAY CRYSTALLOGRAPHY

Principal publications and authors
L. Sauguet (a,b), F. Poitevin (a), S. Murail (c), C. Van Renterghem (b), G. Moraga-Cid (b), L. Malherbe (a,b), A.W. Thompson (d), P. Koehl (e), P.J. Corringer (b), M. Baaden (c) and M. Delarue (a), *EMBO journal* **32**, 728-41 (2013).
(a) Unité de Dynamique Structurale des Macromolécules, Institut Pasteur, CNRS UMR3528, Paris (France)
(b) G5 Récepteurs-Canaux, Institut Pasteur, CNRS URA2182, Paris (France)
(c) Laboratoire de Biochimie Théorique, IBPC, CNRS UPR9080, Université Paris Diderot Sorbonne Paris Cité, Paris (France)
(d) Synchrotron Soleil, Saint Aubin (France)
(e) Genome Center, Department of Computing science, UC Davis, CA (USA)

Pentameric ligand-gated ion channels (pLGICs) are a major family of membrane receptors that mediate fast chemical transmission of nerve signals in the central and peripheral nervous system [1]. In vertebrates, the family encompasses the cationic selective acetylcholine and serotonine receptors, and the anionic selective glycine and γ-amino-butyric acid receptors. pLGICs are dynamic proteins that couple neurotransmitter binding in their extracellular-domain (ECD) to the opening of ion channels embedded in their transmembrane domain (TMD). The receptors share a common architecture with a large ECD and a TMD that is composed of four α-helices, named M1 to M4, that form a transmembrane pore bordered by the M2 helices (**Figure 52a**). The flow of ions across the membrane is inhibited by a structurally-diverse class of molecules including tricyclic antidepressants, local anaesthetics and certain transition metals that bind to the transmembrane pore. The molecular understanding of ion permeation is thus a central issue in the study of these ion channels.

The crystal structure of GLIC, a prokaryotic homolog of the family was solved in an open form of the channel and provided a significant advance in the possibility to study ion permeation [2-3]. The pore of GLIC is funnel-shaped, with a constriction of 5 Å diameter at the Thr226 and Glu222 level that hosts the charge selectivity filter (**Figure 52a**). However, the molecular mechanisms of ion permeation in pLGICs are complex mechanisms involving protein residues, ions and water molecules that interact together dynamically and transiently as the ions flow down the channel. A proper description of these is difficult to derive from existing structures given the limited resolution achieved.

To understand the molecular mechanisms of ion permeation, we solved the crystal structure of GLIC at 2.4 Å, revealing for the first time the hydration geometry in the pore of a pLGIC (**Figure 52b**). The crystal structure reveals ordered water molecules at the level of two rings of hydroxylated residues (named Ser230 and Thr226). Here, two water molecule pentagons are observed sandwiching a sodium ion between them. Simulations that pull a cation through the pore reveal that the water pentagons observed in the crystal structure actively contribute to cation translocation. More precisely, these ordered water molecules contribute to lower the energy barriers encountered by the permeant ion when it crosses the hydrophobic constriction barriers that are located along the selectivity filter.

To better understand the function of the organised water molecules observed in the pore, it was necessary to identify the monovalent ion binding sites in the transmembrane pore. With this aim, the protein was co-crystallised with Br^-, Cs^+, or Rb^+ and X-ray data were collected at optimised wavelengths for each of these derivatives so as to maximise the anomalous signal (**Figure 52c**). Some

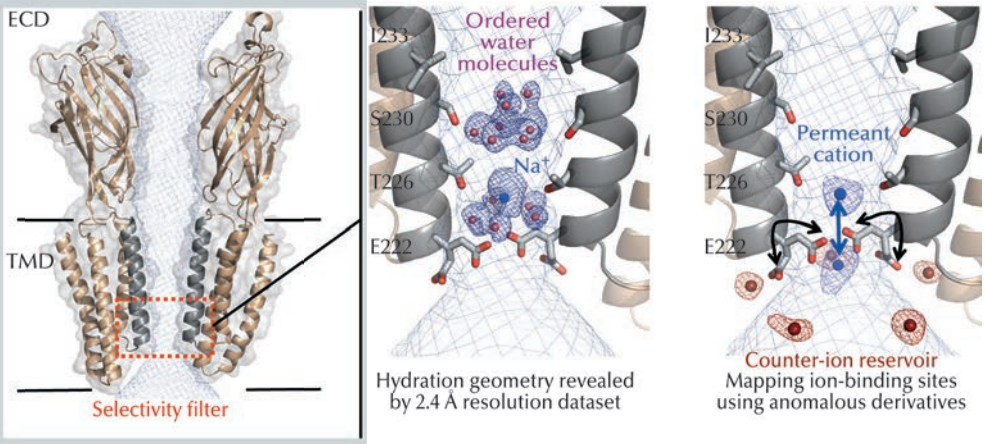

Fig. 52: Left: Cartoon representation of the GLIC ion channel viewed from the side (for clarity only two subunits are shown). The solvent-accessible surface of the channel is shown as a mesh (light blue). The TMD forms a narrow channel lined by the M2 helices from each subunit (grey). The selectivity filter is highlighted in red. Middle: Structurally ordered cation and pentamers of electron density and water molecules in the pore of GLIC. The blue mesh shown is the 2mFo-DFc electrodensity map. Right: Cation and anion binding sites revealed by the use of anomalous scattering from derivatives. The anomalous difference maps calculated for Br^-, Cs^+ or Rb^+ are superimposed and shown as meshes.

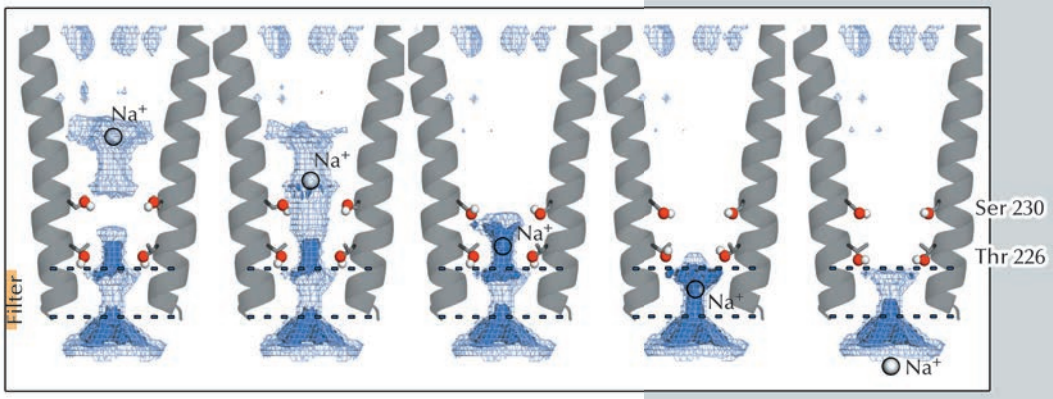

Fig. 53: Optimised set of configurations of the Ser230 and Thr226 side chains can maximise the permeant ion density at five levels in the pore, from its extracellular to its intracellular end.

of these experiments were performed at beamline ID23-1, taking advantage of the tuneable wavelength of the beamline. The permeating ions occupy two preferential positions in the most constricted region of the pore that hosts the selectivity filter. In the GLIC structure, the Glu222 carboxylate groups are flexible and continuously exchange between alternative conformations, thus facilitating ion transport. Finally, the presence of a reservoir of counter-ions located at the intracellular mouth of the pore might help in either retaining the permeant ion or creating a favourable corridor through it.

Electrostatic calculations illustrated the roles of residues Ser230 and Thr226 during permeation. Both residues were shown to facilitate ion transport by reducing electrostatic free energy barriers encountered by the ion during its translocation (**Figure 53**). Due to the strong sequence conservation of M2 pore-lining residues within the pLGIC family, the conclusions presented in this study might be transferable to all the pLGIC channels.

References
[1] P.J. Corringer *et al, Structure* **20**, 941-56 (2012).
[2] N. Bocquet *et al, Nature* **457**, 111-114 (2009).
[3] R. Hilf and R. Dutzler, *Nature* **457**, 115-118 (2009).

STRUCTURAL BASIS FOR STABILISATION OF Hsp70-SUBSTRATE COMPLEXES BY Hip

Principal publication and authors
Z. Li, F.-U. Hartl and A. Bracher, *Nature Structural & Molecular Biology* **20**, 929-935 (2013).
Department of Cellular Biochemistry, Max-Planck-Institute of Biochemistry, Martinsried (Germany)

Under laboratory conditions, many proteins fold spontaneously into their biologically active conformation. In the crowded cytosol of the cell, however, larger proteins in particular have a tendency to mis-fold and aggregate, a process that can disrupt vital cellular processes. Cells therefore strive to maintain 'proteostasis', *i.e.* a healthy proteome, by carefully controlling synthesis and folding of new proteins as well as the degradation of those that are damaged. Failure to do this may lead to the accumulation of potentially toxic, mis-folded protein species and may cause severe conditions such as Alzheimer's or Parkinson's disease. A principal component of the cellular proteostasis machinery, a network of multiple factors, is a set of proteins known as molecular chaperones, which function to prevent protein aggregation and ensure that folding occurs on a physiologically relevant time scale **[1]**.

The highly-conserved molecular chaperone Hsp70 is a central component of the protein folding machinery in bacterial and eukaryotic cells, both interacting with nascent polypeptides on translating ribosomes and cooperating with chaperone factors and protein degradation machineries that act down-stream. Hsp70

References
[1] Y.E. Kim *et al.*, *Annu Rev Biochem* **82**, 323-355 (2013).
[2] M.P. Mayer, *Mol Cell* **39**, 321-31 (2010).
[3] C. Roodveldt *et al.*, *EMBO J* **28**, 3758-3770 (2009).
[4] A.M. Wang *et al.*, *Nat Chem Biol* **9**, 112-118 (2013).

functions as a molecular machine, using ATP hydrolysis to cycle between conformational states with distinct binding properties for non-native polypeptides [2]. Tight interaction with hydrophobic peptide motifs occurs in the ADP-bound state while the binding of ATP triggers substrate release. Because Hsp70 has a low intrinsic ATP hydrolysis activity with slow ADP dissociation, it is critically dependent on so-called cochaperones, which stimulate ATP hydrolysis and accelerate ADP-ATP replacement, J-domain proteins and nucleotide exchange factors, respectively. A plethora of these cofactors, occurring specifically in eukaryotic cells, serve to recruit Hsp70 for specific functions, such as the disassembly of clathrin coats around vesicles after endocytosis. In addition to J-domain proteins and exchange factors, metazoans, plants and numerous protists contain yet another cytosolic Hsp70-co-chaperone named Hip (Hsc70-interacting protein), which stabilises Hsp70-substrate complexes. Together with Hsp70, Hip was implicated in the prevention of aggregation of α-synuclein and the poly-Q androgen receptor as well as in the timely degradation of hyper-phosphorylated Tau. All of these proteins form deposits in neurodegenerative diseases [3,4].

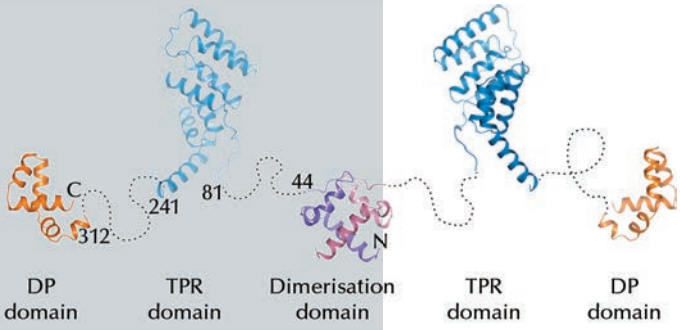

Fig. 54: A tentative model for the structure of a complete Hip dimer. The flexible linkers (dashed lines) are not drawn to scale.

Using SAXS and diffraction data collected at the ESRF, we showed that Hip has a modular domain architecture consisting of an N-terminal dimerisation domain, a central TPR module and a C-terminal DP domain that are connected by flexible linkers (Figure 54). A crystal structure of 1.1 Å resolution revealed that the N-terminal dimerisation domain, comprising only 44 residues from each chain, forms a unique compact helix bundle fold. The TPR domain of Hip is sufficient to mediate the interaction with Hsp70 and, in contrast to other TPR domain cofactors of Hsp70, recognises the nucleotide binding domain (NBD) of Hsp70 and not the C-terminal region of the chaperone.

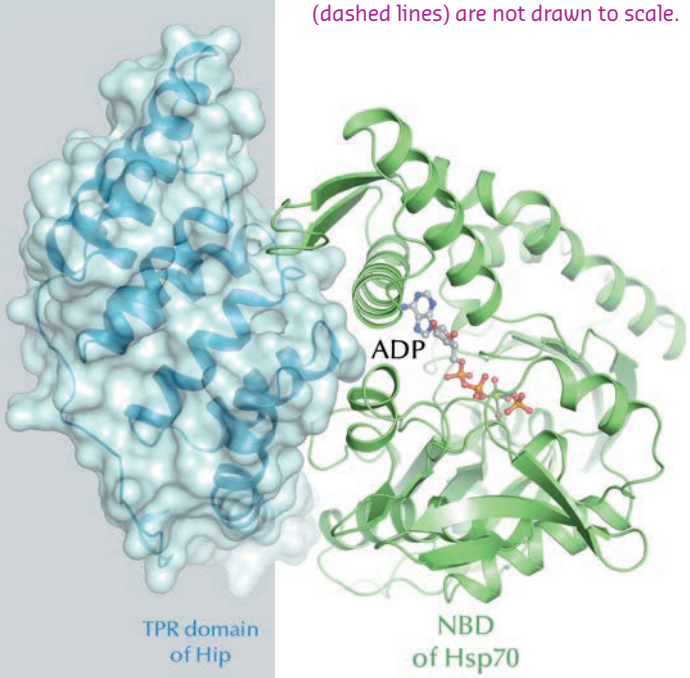

Fig. 55: The crystal structure of the Hip-Hsp70 core complex. ADP and phosphate (shown in stick representation) are locked in the Hsp70 nucleotide binding cleft (NBD).

Biochemical assays showed that ADP dissociation from Hsp70 is slowed by complex formation with Hip. The crystal structure of the core complex of Hip and Hsp70, consisting of the TPR domain of Hip and the NBD of Hsp70, determined with data from beamline **ID23-2**, revealed the structural basis for this interaction (Figure 55). In the complex, Hip acts as a molecular clamp, locking ADP in the nucleotide binding cleft of Hsp70, and occludes the common interaction site for the eukaryotic Hsp70 nucleotide exchange factors, thus blocking active cycling of the molecular chaperone. However, a biologically relevant affinity is reached only when Hip specifically recognises a substrate with its C-terminal domain, or when both arms of the Hip dimer are engaged in interaction with Hsp70, allowing normal processing of bona-fide Hsp70 substrates. This mechanism explains how Hip enhances aggregation prevention by Hsp70 and facilitates the transfer of substrate proteins to down-stream chaperones or the proteasome.

SOLUTION STRUCTURE OF THE HEPATITIS C VIRUS IRES: AN ARTICULATED RNA MOLECULE INVOLVED IN CAP-INDEPENDENT TRANSLATION INITIATION

Principal publication and authors
J. Pérard (a), C. Leyrat (a), F. Baudin (a), E. Drouet (a) and M. Jamin (a), *Nat. Commun.* **4**, 1612 (2013).
(a) Unit of Virus Host-Cell Interactions, Université Grenoble Alpes-EMBL-CNRS, Grenoble (France)

Hepatitis C virus (HCV) infects over 170 million people worldwide, causing chronic liver diseases that can progress to cirrhosis and cancer, and kills more than 350,000 people every year. While recent advances in treatment have been made, there is no vaccine, and HCV remains a significant human health problem. The HCV genome is a positive-sense 9.6 kilobase RNA containing highly structured 5′ and 3′ untranslated regions (UTR). The 5′ UTR comprises an internal ribosome entry site (IRES) encompassing nucleotides 40 to 341, which directs the cap-independent recruitment of both ribosomal subunits, the assembly of a functional translation initiation complex and the translation of a single precursor polyprotein, which is subsequently processed by viral and cellular proteases.

The HCV IRES is a large RNA region comprising a pseudoknot and three structural domains: two long stem loops (domains II and III) and a spur (domain IV) (**Figure 56a**). Two regions, the IIIabc four-way junction and the IIIef/IV pseudoknot, involve tertiary contacts, and the entire IRES adopts a defined ion-dependent fold under physiological conditions, although it does not form a compact, globular structure. Because the HCV IRES is essential for viral replication, and its sequence is well conserved among all HCV genotypes, its structure may represent a novel target for drug design. In recent years, atomic structures of different fragments of this RNA region have been determined, but the presence of several hairpin loops and regions predicted to be single-stranded confers dynamic flexibility to the entire IRES molecule that has so far hampered its complete structural characterisation by X-ray crystallography or electron microscopy. The structural information available about the entire molecule has remained limited to cryo-electron microscopy reconstructions of the IRES bound to different partners.

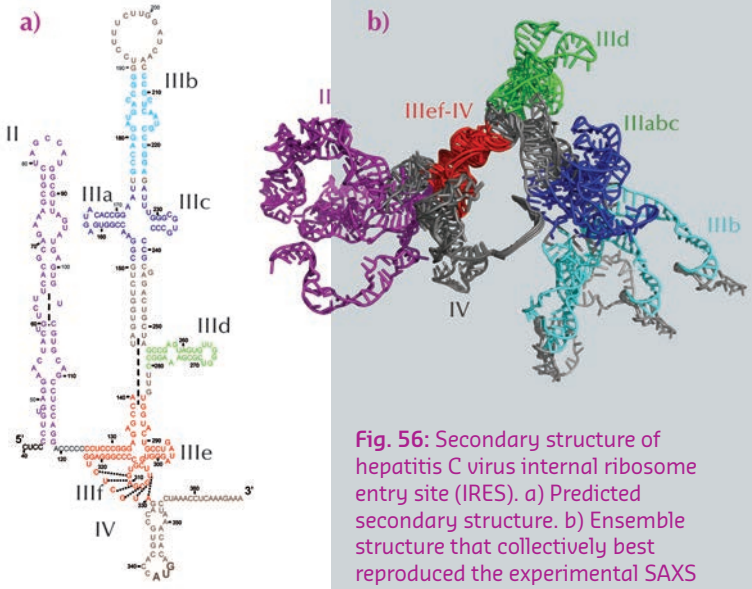

Fig. 56: Secondary structure of hepatitis C virus internal ribosome entry site (IRES). a) Predicted secondary structure. b) Ensemble structure that collectively best reproduced the experimental SAXS curve. The regions for which an experimentally determined atomic structure is available are shown in the same colour in both figures.

An atomic model of full-length hepatitis C virus IRES in solution was constructed on the basis of small-angle X-ray scattering (SAXS) data collected at beamlines **ID02** and **ID14–3** and molecular dynamics simulations. An initial model was constructed by connecting together the known atomic structures of different fragments and constructing the missing parts in accordance with secondary structure predictions (**Figure 56a**). Molecular dynamics simulations in explicit solvent (ESMD) and normal mode analysis were used to generate an ensemble of 8,000 different physically realistic conformations accessible to the RNA molecule in solution. This ensemble was searched and the model that best reproduced the experimental SAXS scattering curve was selected. In the selected conformer, domain II and domain III extend in opposite directions along the main axis of the molecule forming a right angle, whereas subdomain IIId and domain IV protrude

References
[1] J.S Kieft, K. Zhou, R. Jubin, M.G. Murray, J.Y. Lau and J.A. Doudna, *J. Mol. Biol.* **292**, 513-529 (1999).

from each side of the molecule. This model is compatible with footprinting experiments performed with chemical and enzymatic probes [1]. ESMD simulations confirmed the flexibility of this molecule and localised the regions of highest flexibility. Principal component analysis (PCA) performed on the ensemble of physically accessible conformers then revealed collective motions in the molecule. In particular, the dominant motion in solution corresponded to the closure of the molecule, with domains II and III remaining in the same plane, acting like jaws that move towards and away from each other. Further refinement revealed that an ensemble of five or more exchanging conformers reproduces SAXS data better than a single structure suggesting, in combination with results from ESMD and PCA, that the hepatitis C virus IRES is an articulated molecule made of rigid structural elements that move relative to each other around flexible joints (**Figure 56b**). Finally, comparison with the IRES bound to the eIF3 complex and to the ribosomal 40S subunit indicated that motions along the second principal component involving reorientation of domain II relative to domain III must occur upon binding to its partners.

In conclusion, we determined an ensemble structure of the HCV IRES in solution, which highlighted the articulated nature of this RNA molecule. This work offers insights into the conformational changes occurring in IRES upon formation of the translation initiation complex.

HOW ARRESTIN IS ACTIVATED FOR GPCR BINDING

Principle publication and authors
Y.J. Kim (a), K.P. Hofmann (a), O.P. Ernst (b), P. Scheerer (c), H.W. Choe (a,d) and M.E. Sommer (a), *Nature* **497**, 142-146 (2013).
(a) Institut für Medizinische Physik und Biophysik (IMPB), Charité-Universitätsmedizin Berlin (Germany)
(b) Departments of Biochemistry and Molecular Genetics, University of Toronto (Canada)
(c) IMPB, AG Protein X-ray Crystallography, Charité-Universitätsmedizin Berlin (Germany)
(d) Department of Chemistry, College of Natural Science, Chonbuk National University (South Korea)

The large family of G-protein-coupled receptors (GPCRs) controls diverse sensory and physiological responses and is thus a major focus of research and a central drug target. These receptors bind a variety of ligands (*e.g.* light, odorants, hormones, neurotransmitters) and communicate this signal into the cell by coupling to intracellular proteins [1]. One of these binding partners is arrestin, of which the canonical role is either to stop signalling by blocking receptor coupling to G-proteins, or to initiate arrestin-dependent signalling by bringing together other signalling proteins. We have used protein X-ray crystallography to gain insight into how arrestins are activated for receptor binding.

Structurally, arrestins are composed of two near-symmetric lobes (N- and C-domain) that are stabilised by a long C-terminal tail (C-tail) (**Figure 57a**). In their basal state, arrestins are unable to recognise and bind an activated receptor, which must first

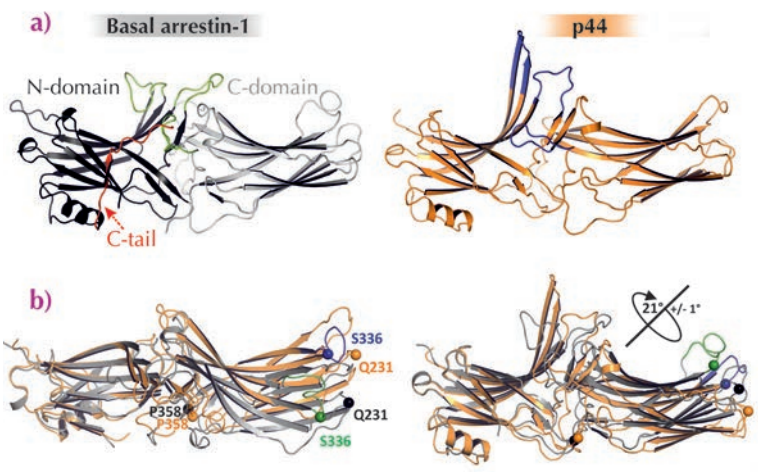

Fig. 57: Structural differences between basal arrestin-1 and p44. a) Ribbon diagrams of basal arrestin-1 (PDB entry 1CF1) and p44. The N- and C-domains of basal arrestin-1 are coloured dark-grey and light-grey, respectively, the C-tail is shown in red and important loops in the central crest region are coloured green. p44 is shown in orange, and key loops coloured blue. b) Side-views of the interdomain rotation in p44 (orange) as compared to basal arrestin-1 (grey). The N-domains are superimposed to show the rotation, evidenced by the change in position of the specific residues S336, Q231 as compared to the reference residue P358.

be phosphorylated by a kinase. and then the receptor-attached phosphates displace the C-tail of arrestin thereby activating arrestin to bind the receptor. Although the crystal structure of basal arrestin was first solved some fifteen years ago, this structure did not indicate how C-tail displacement activates arrestin.

We tackled this problem using X-ray crystallography and site-directed fluorescence spectroscopy on a pre-activated form of arrestin-1, the arrestin subgroup present in the rod cells of the retina.

We pre-activated arrestin by removing its C-tail by mutation and crystallising it in the presence of the GPCR opsin, which was most likely activated by the crystallisation conditions [2,3]. The crystal structure of C-terminally truncated arrestin (called p44) was solved at 3.0 Å resolution using diffraction data collected at beamline **ID14-4**. It differs substantially with that of basal arrestin (**Figure 57a**). Several of the hydrogen-bond networks that stabilise the orientation of the two lobes in basal arrestin are broken in p44, which results in the two lobes of p44 being rotated 21° with respect to basal arrestin-1 (**Figure 57b**). Additionally, several of the flexible loops in the receptor-binding surface of arrestin are significantly rearranged in p44 (**Figure 58**). Overall, the structure of p44 indicates a general mechanism of arrestin activation, whereby C-tail displacement increases flexibility in critical regions of the arrestin molecule that allow a proper fitting to the active receptor.

This activation mechanism is most likely conserved within the small arrestin family (four subgroubs) and this explains how hundreds of different GPCRs are bound by only a few arrestin variants. The overarching theme of activation is an increase in conformational flexibility, which presumably facilitates arrestin binding to different GPCRs at variable receptor stoichiometry [4] as well as to a multitude of other binding partners.

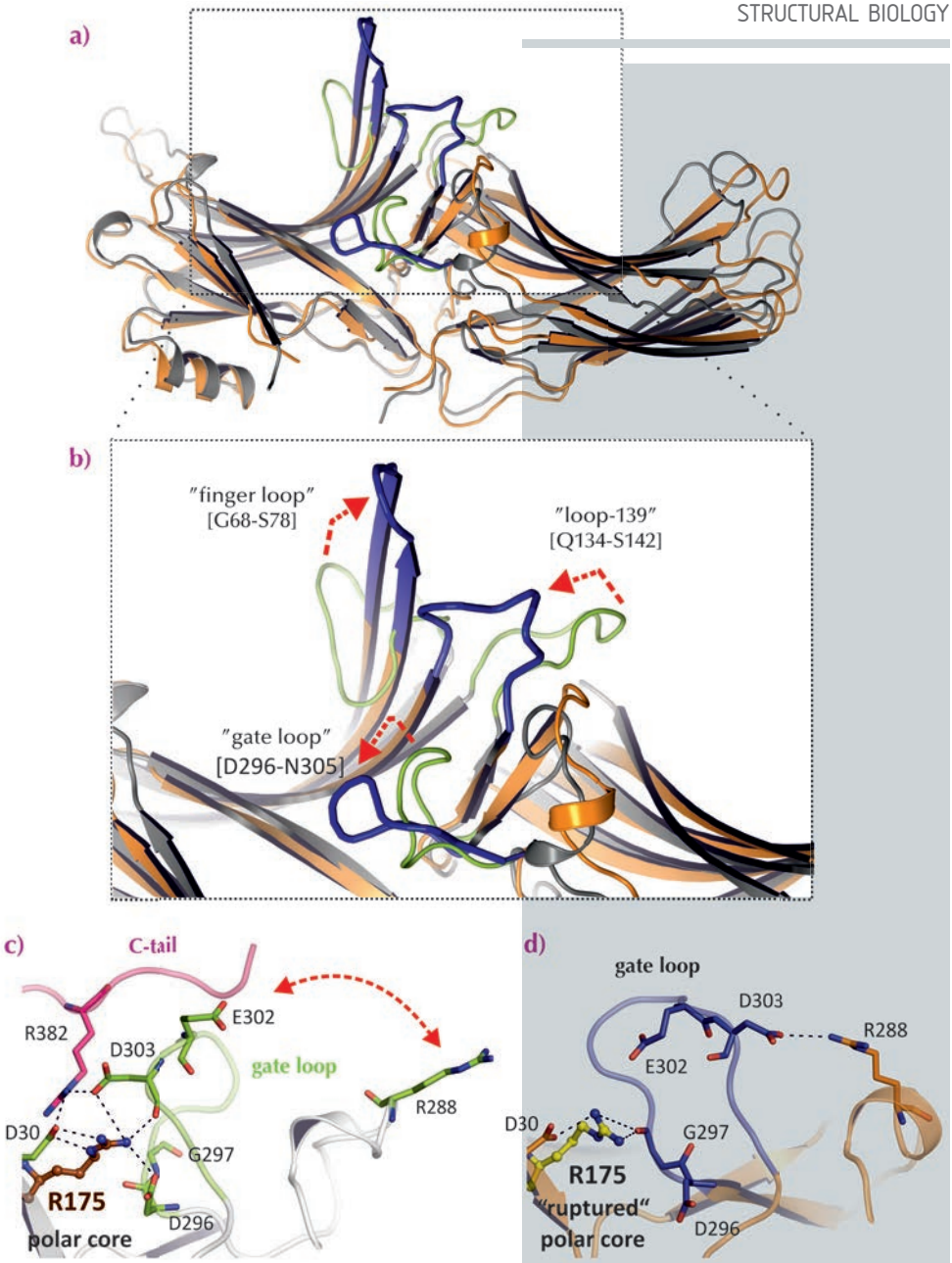

Fig. 58: Comparison of loops that differ between basal arrestin-1 and p44. a) and b) Overall structure and close-up view of superimposed structures of basal arrestin-1 and p44 (coloured as in **Figure 57a**). Critical loops involved in receptor binding are labelled with red arrows indicating activating changes in the structure of these loops. c) and d) The hydrogen-bond network linking the gate loop (green), the C-tail (red) and R175 in the central polar core region of basal arrestin-1 (grey) is broken in p44 (blue/orange).

Our structure of p44 was published in the same journal issue as another report of pre-activated arrestin crystal structure by B.Kobilka and R.Lefkowitz, who shared the Nobel Prize for Chemistry in 2012. That study describes an arrestin that is fixed by a synthetic antibody fragment and bound to a phosphorylated peptide-mimic of the phosphorylated C-terminus of an active GPCR [5]. Remarkably, the two structures are so similar they validate one another and the conclusions concerning arrestin activation described above.

References
[1] K.P.Hofmann et al., *Trends Biochem Sci.* **34**, 540-552 (2009).
[2] P.Scheerer et al., *Nature* **455**, 497-502 (2008).
[3] H.-W.Choe et al., *Nature* **471**, 651-655 (2011).
[4] M.E.Sommer et al., *Nat Comm* **3**, 995 (2012).
[5] A.K.Shukla et al., *Nature* **497**, 137-141 (2013).

Principal publication and authors
R.M. Voorhees (a), D. Mandal (b), C. Neubauer (a), C. Köhrer (b), U.L. RajBhandary (b) and V. Ramakrishnan (a), *Nat Struct Mol Biol* **20**, 641-643 (2013).
(a) Molecular Research Council Laboratory of Molecular Biology, Cambridge (UK)
(b) Department of Biology, Massachusetts Institute of Technology, Cambridge, Massachusetts (USA)

HOW THE RIBOSOME DECODES A MODIFIED 'WOBBLE' POSITION ANTICODON FOR ACCURATE PROTEIN TRANSLATION

Ribosomes are the macromolecular machines required for translating genetic information into proteins using a messenger RNA (mRNA) template and aminoacylated transfer RNA (aa-tRNA) substrates. One of the most remarkable characteristics of the ribosome is its ability to synthesise proteins at rates of between 10 and 20 amino acid residues per second with error frequencies as low as 1 in 10,000. This feat is mainly achieved by correctly pairing the three bases encompassing a 'codon' sequence on the mRNA with the anticodon of cognate aa-tRNA. In theory at least 61 different tRNAs would be required for the canonical Watson-Crick base pairing of all codons possible in mRNA. However, some mismatch base-pairing (*i.e.* non-Watson-Crick) must be allowed as there are less than 50 different tRNA anticodons observed in nature. Such mispairing occurring only at the third codon position (tRNA residue 34) led to the 'wobble hypothesis' proposed by Crick in 1966 [1], and is fundamentally important to understand because nearly 40% of all codons are decoded using this mechanism.

However, a growing number of post-translational modifications of tRNA anticodons have been reported, some of which have been implicated in human disease. The most common modifications are the methylation of uridine, deamination of adenine to inosine and the attachment of lysine to cytosine to form lysidine (k^2C), which was first reported in *Escherichia coli* $tRNA_2^{Ile}$ [2]. The unmodified $tRNA_2^{Ile}$ has a CAU anticodon that is perfectly complementary to the AUG methionine codon. By modifying C34 to k^2C34, a minor AUA isoleucine codon is recognised. A similar modification, the addition of decarboxy arginine to cytosine to form agmatidine (agm^2C), is found in archaea. This suggests that the ability to discriminate between purines in the wobble position (AUA versus AUG) of codons is conserved in nature. To determine structurally how this is achieved, the crystal structure of the 70s ribosome in complex with the AUA codon and $tRNA_2^{Ile}$ was determined using diffraction data collected at beamline **ID14-4**.

Archaeal $tRNA_2^{Ile}$ was observed in both the amino-acyl (A) and peptidyl (P) sites of the 70s ribosome (**Figure 59**), providing an insight into how agmatidine confers specificity for AUA over AUG codons. As expected the ribosome was observed in a 'closed' conformation, with the first and second codon-anticodon positions mediating canonical Watson-Crick interactions. Surprisingly, the A3-agm^2C34 is

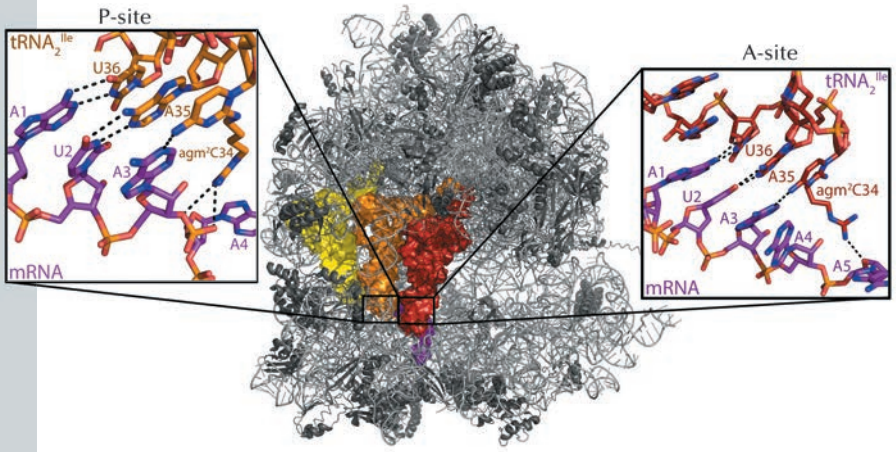

Fig. 59: The crystal structure of the 70s ribosome with mRNA coding for two $tRNA_2^{Ile}$. The mRNA is coloured magenta with the $tRNA_2^{Ile}$ coloured red for the A-site, orange for the P site and yellow for the E-site. The inserts show detailed views of the A and P-site codon-anticodon binding sites and highlight the interactions of the extended agmatidine modification with the sugar-phosphate backbone of downstream mRNA residues. Image credit: A.A. McCarthy, EMBL.

observed in a non-standard geometry in the A-site, forming a single hydrogen bond between the exocyclic amine of agm^{2}C34 and the N1 of A3 (Figure 59). This is mainly due to the extended modification of C34 that hinders the adoption of a more stable tautomer that could potentially form two hydrogen bonds. A similar geometry was observed in the P-site resulting in a shift of both the mRNA and tRNA, which contrasts with previous studies showing the mRNA remaining stationary.

Only a single hydrogen bond is observed in the wobble position, which suggests a thermodynamically unfavourable binding of $tRNA_2^{Ile}$. However, in the crystal structure, a hydrogen bond is formed between the terminal amine of agmatine and the O4′ atom of the ribose of a downstream mRNA nucleotide (Figure 59). A similar interaction is also observed in the P-site, this time between agmatine and the backbone phosphate of a downstream mRNA residue (Figure 59). These hydrogen bonds would also be possible with a lysidine modification of C34, indicating this might be a broadly conserved mechanism of binding $tRNA_2^{Ile}$, compensating for the weaker interaction in the wobble position. A steric clash between the exocyclic amine of agmatidine and a G modelled at the third mRNA codon would prevent a canonical Watson-Crick base pairing, providing insights into how the presence of agmatidine and lysidine would prevent binding of $tRNA_2^{Ile}$ to the near cognate AUG codon. So, even 40 years after the genetic code was first elucidated, we are still unravelling the mysteries of how the ribosome accurately codes protein synthesis.

References
[1] F.H. Crick, *J. Mol. Biol.* **19**, 548-555 (1966).
[2] T. Muramatsu *et al.*, *J. Biol. Chem.* **263**, 9261-9267 (1988).

THE STRUCTURE AND FUNCTION OF A MEMBRANE PROTEIN INVOLVED IN THE ADAPTATION TO HYPEROSMOTIC SHOCK

Principal publication and authors
R.S. Vieira-Pires, A. Szollosi and J.H. Morais-Cabral, *Nature* **496**, 323–328 (2013).
IBMC, Instituto de Biologia Molecular e Celular, Universidade do Porto (Portugal)

All living organisms control their intracellular concentrations of ions, in particular those of sodium and potassium [1, 2]. This is complicated in bacteria, plants, fungi and archaea by the fact that the cells of these organisms do not control their extracellular environment. As a consequence these cells have evolved mechanisms of adaptation to environmental changes such as high salinity and drought that are not present in animal cells. One of these mechanisms of adaptation involves the Trk/Ktr/HKT membrane proteins, a superfamily of Na^+ and/or K^+ transporters.

We have determined the X-ray crystal structure of the KtrAB K^+ transporter (Figure 60) from the bacterium *Bacillus subtilis* at 3.5 Å [3]. It is composed of two different polypeptides, the KtrB membrane protein which is responsible for the permeation (transport) of potassium and sodium ions, and the KtrA regulatory protein, a soluble protein responsible for regulation of transporter activity. KtrB assembles as a dimer and interacts with one of the faces of the octameric ring formed by KtrA (Figure 60).

Strikingly, each KtrB subunit is composed of 4 repeats which display the TM-Ploop-TM architecture first described for the KcsA potassium channel [4]. These 4 repeats assemble around a central axis that defines the ion pore. The KtrA octameric ring is formed as a tetramer of dimers where each dimer adopts the RCK domain fold, also first described in a potassium channel [5]. Each subunit binds an ATP molecule.

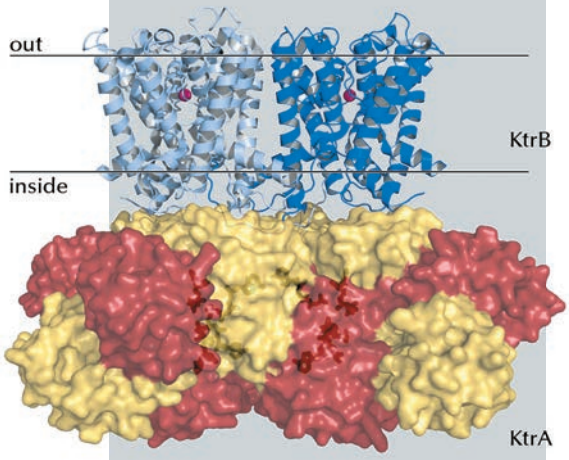

Fig. 60: Crystal structure of the KtrAB K^+ transporter of *Bacillus subtilis*. KtrB subunits are represented as ribbons and are coloured in light and dark blue. K^+ ions are shown as magenta spheres. The horizontal line represents the limits of the membrane bilayer. KtrA is shown in surface representation with its subunits in yellow and red; ATP molecules can be seen through the partially transparent surface in their binding sites facing the inside of the octameric ring.

We have shown that KtrAB activity is increased upon ATP binding and decreased when bound to ADP. Importantly, ATP is not hydrolysed. The two ligands act as signalling molecules so that the activity of the ion transporter is probably controlled by a change in the intracellular concentration ratio of ADP/ATP.

We have also determined the X-ray crystal structure of the isolated KtrA octameric ring bound to ATP and ADP at resolutions of 3.0 and 2.8 Å respectively. While the ATP bound structure is identical to the structure of KtrA as seen in the KtrAB complex, the ADP bound structure shows a different conformation (**Figure 61**). Two of the four subunits forming a ring face have moved apart resulting in an expansion of the ring and a change in its symmetry, the ring is now formed by a dimer of tetramers. Despite the strong structural and functional relationship between KtrAB and K^+ channels, this ADP bound structure implies a mechanism of activation which is very different. In K^+ channels, activation by RCK domain rings is dependent on expansion of the ring [5]. In KtrAB, activation by KtrA appears to be associated with a contraction of the ring.

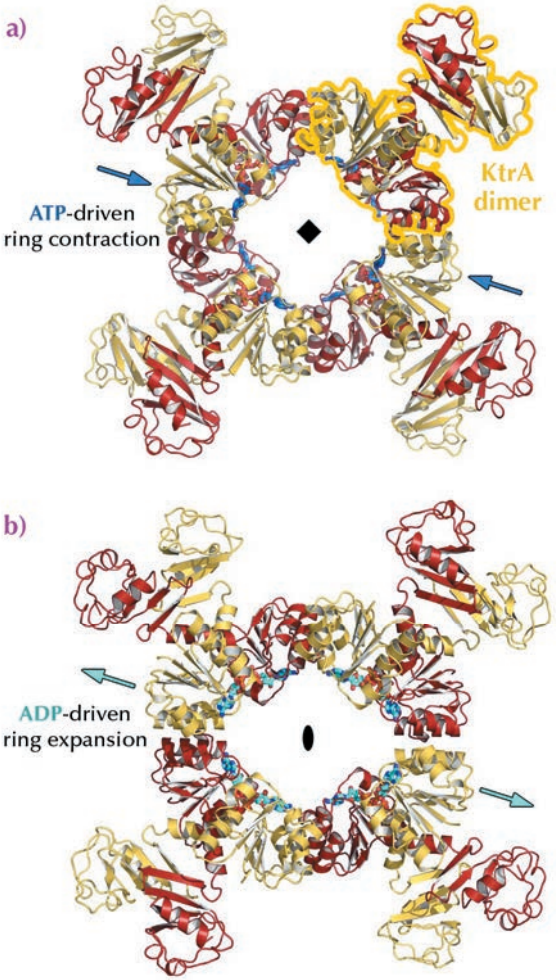

Fig. 61: Conformation of the KtrA octameric rings. a) KtrA-ATP ring with its alternating subunits coloured in yellow and red and ATP molecules in blue facing the inside of the ring; blue arrows indicate the direction of the conformational changes relative to the ADP-bound state. The KtrA dimeric unit is delineated by a yellow border. The black square indicates the 4-fold symmetry axis. b) KtrA-ADP ring with ADP molecules coloured in cyan; arrows indicate the direction of the conformational changes relative to the ATP-bound state. The black ellipse indicates the 2-fold symmetry axis.

References

[1] G. Holtmann, E.P. Bakker, N. Uozumi and E. Bremer, *J Bacteriol.* **185**, 1289-98 (2003).
[2] I. Hänelt, N. Tholema, N. Kröning, M. Vor der Brüggen, D. Wunnicke and E.P. Bakker, *Eur J Cell Biol.* **90**, 696-704 (2011).
[3] R.S. Vieira-Pires, A. Szollosi and J.H. Morais-Cabral, *Nature* **496**, 323-8 (2013).
[4] D.A. Doyle, J. Morais-Cabral, R.A. Pfuetzner, A. Kuo, J.M. Gulbis, S.L. Cohen, B.T. Chait and R. MacKinnon, *Science* **280**, 69-77 (1998).
[5] Y. Jiang, A. Lee, J. Chen, M. Cadene, B.T. Chait and R. MacKinnon, *Nature* **417**, 515-22 (2002).

LONG WAVELENGTH S-SAD PHASING OF THE CRYSTAL STRUCTURE OF FAM3 PANDER REVEALS A NEW CLASS OF SIGNALLING MOLECULES

Principal publication and authors

P. Johansson (a), J. Bernström (b), T. Gorman (c), L. Öster (a), S. Bäckström (b), F. Schweikart (b), B. Xu (b), Y. Xue (a) and L. Holmberg Schiavone (b), *Structure* **21**, 306–313 (2013).
(a) Structure and Biophysics, Discovery Sciences, AstraZeneca, Mölndal (Sweden)
(b) Reagents and Assay Development, Discovery Sciences, AstraZeneca, Mölndal (Sweden)
(c) High-Content Biology, Discovery Sciences, AstraZeneca, Alderley Park, Macclesfield (UK)

Cytokines are a diverse group of soluble proteins or peptides that act as signalling molecules in the body [1]. FAM3B pancreatic derived factor (PANDER) was initially suggested to be a cytokine [2] is involved in insulin signalling and thereby a potential drug target for diabetes. The FAM3 superfamily was predicted to contain classical four-helix bundle cytokines, featuring a typical up-up-down-down fold.

Despite the success of sulfur SAD phasing for high-resolution systems, novel structures solved from low

symmetry or moderate resolution data are still rare. Here we present the S-SAD phasing of FAM3 PANDER. To optimise the PANDER sulfur SAD signal-to-noise ratio, highly redundant data were collected at beamline **ID29** in two kappa wedges using a photon energy of 6 keV ($\lambda \approx 2.06$ Å). Due to the moderate resolution, the anomalous signal did not extend beyond 4.5 Å and an extensive substructure search did not result in any obvious hits. However, by careful analysis and crosschecking of the solutions, a number of recurring super-sulfur atoms could be assigned and split into separate atoms (**Figure 62**). Density modification and NCS averaging identified the remaining sulfur sites, extending the phases to about 3.7 Å resolution. To maximise the phasing power, the substructure parameters were iteratively re-refined using density modified Hendrickson Lattman coefficients as phase restraints, gradually increasing the solvent content. The new phase-estimates were finally subjected to statistical density modification and the phases extended to 2.4 Å resolution.

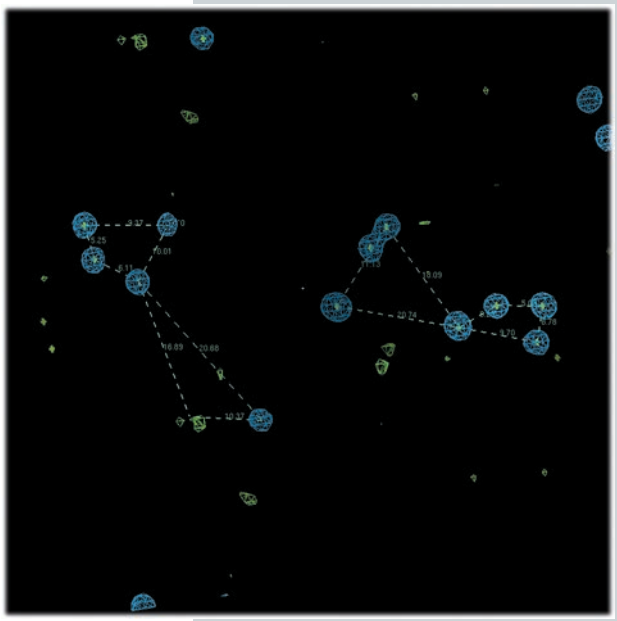

Fig. 62: NCS-relation between the two PANDER molecules in the asymmetric unit of the crystals studied. Partial S-substructure in blue, anomalous LLG map in green.

Even from initial low resolution maps it was clear that PANDER is not an all-α helical protein and, contrary to the previous suggestions, PANDER exhibits a novel globular β-β-α fold (**Figure 63**). The structure is composed of two antiparallel β sheets lined by three short helices. This fold shares no relation to the predicted cytokines but is clearly conserved throughout the FAM3 superfamily.

A search using the PANDER structure as a template in the DALI fold database resulted in a small number of hits with remotely related secondary structure. The most similar structure, with a Z-score of 5.1, was the artificially designed TOP7 protein (PDB code 1QYS), sharing a related C-terminal β-α architecture. The lack of naturally occurring structures with related topology and the partial similarity to TOP7, designed to explore new regions of the protein universe **[3]** indicates that PANDER represents a novel protein fold.

Since the discovery of FAM3B, the view of its function has broadened and become more complex: from an islet specific cytokine with apoptotic activity to that of a hormone involved in negative regulation of beta cell function and liver glucose homeostasis. However, down-stream signalling mechanism(s) for PANDER remains to be elucidated including the identification of a PANDER-specific receptor.

The unexpected PANDER fold together with the potent biological actions of proteins in the superfamily indicate that FAM3 might represent a new class of signalling molecules, strikingly different from the known four-helix bundle cytokines.

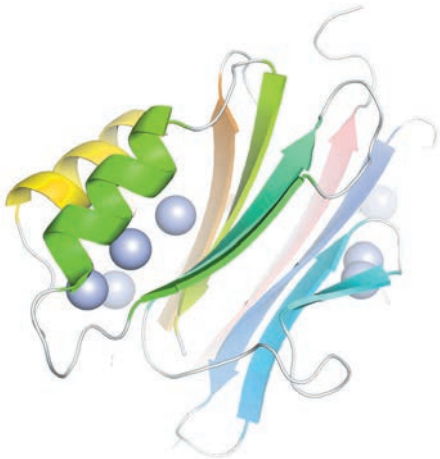

Fig. 63: The FAM3 PANDER β-β-α-fold coloured from blue to red N to C terminus. Sulfur atoms indicated by spheres.

References
[1] X. Wang, P. Lupardus, S.L. Laporte and K.C. Garcia, *Annu Rev Immunol.* **27**, 29-60 (2009).
[2] Y. Zhu, G. Xu, A. Patel, M.M. McLaughlin, C. Silverman, K. Knecht, S. Sweitzer, X. Li, P. McDonnell and R. Mirabile *et al. Genomics* **80**, 144-150 (2002).
[3] B. Kuhlman, G. Dantas, G.C. Ireton, G. Varani, B.L. Stoddard and D. Baker, *Science* **302**, 1364–1368 (2003).

STRUCTURE OF GENE REGULATOR THAT PLAYS KEY ROLE IN CANCER

Principal publication and authors
M. Delvecchio (a,b,c), J. Gaucher (a,b), C. Aguilar-Gurrieri (a,b), E. Ortega (a,b) and D. Panne (a,b), *Nat. Struct. Mol. Biol.* **20**, 1040–1046 (2013).
(a) European Molecular Biology Laboratory, Grenoble (France)
(b) Unit for Virus Host-Cell Interactions, Univ. Grenoble Alpes-EMBL-CNRS, Grenoble (France)
(c) Present address: Diasorin Società per azioni, Saluggia (Italy)

Gene regulation is orchestrated by a large set of transcription factors that bind in a combinatorial fashion to DNA to regulate specific sets of genes. The ability to switch many different genes on or off using combinations of transcription factors is not only useful in the day-to-day regulation of cell function, it is also necessary for processes such as cell differentiation. Dysregulation of these processes frequently underlies diseases such as inflammation and cancer.

Although transcription factors are central to determining which genes become active, they alone are not sufficient to do the job. Cellular DNA in our cells is stored inside densely packed structures called 'nucleosomes' which restrict the DNA's activity. For transcription factors to activate a gene, they work in concert with enzymes called histone acetyltransferases (HATS) that transfer acetate groups to histone proteins in nucleosomes and thereby destabilise their inhibitory structure.

One histone acetyltransferase that is essential to this process is p300. As a central 'hub' protein, p300 allows combinatorial regulation by binding to hundreds of transcription factors allowing integration of a very large number of cellular signalling pathways, including G-protein signalling and most immune and cancer signalling pathways. Upon binding to sets of transcription factors p300 becomes active and acetylates histones to render the chromatin fibre permissive for gene transcription.

The integrity of p300 is key for cellular physiology and aberrant p300 activity contributes to pancreatic, colon, lung as well as gastric and thyroid cancer. For example, ~40% of B-cell lymphomas carry mutations in p300, many of which inactivate the enzyme resulting in cellular transformation. Many of these disease-causing mutations are clustered in the region of the protein that is responsible for histone acetylation and in domains that are responsible for nucleosome binding indicating that dysregulation of chromatin recognition and modification are central aspects of these diseases. In addition to acting as an oncoprotein by promoting tumours, p300 can also act as a tumour suppressor.

To understand how p300 recognises and modifies chromatin and how disease mutations contribute to pathogenesis, we have determined the X-ray crystal structure of the region involved in these activities (**Figure 64**). Crystallising p300 was complicated by the protein's tendency to autoacetylate itself rendering preparations of p300 structurally heterogeneous. We used enzymatic deacetylation to remove the autoacetylation and thus allow isolation of a homogeneous form. We crystallised p300 in complex with a

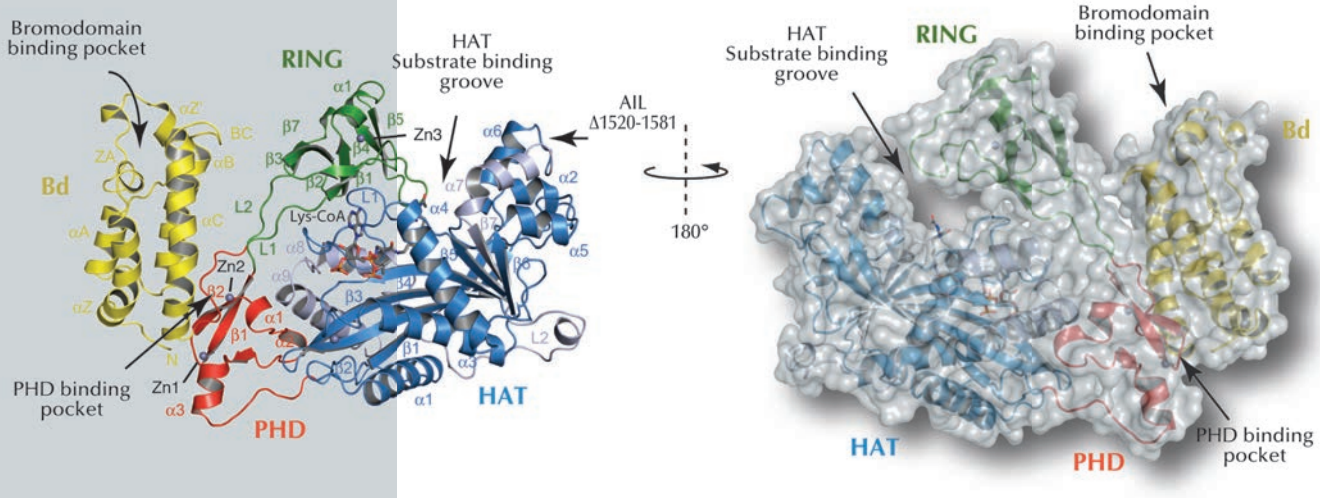

Fig. 64: Ribbon and surface representations of the crystal structure of p300 core with labelling of secondary structure elements. The Bromodomain (Bd), RING- and PHD- domains are shown in yellow, green and red, respectively. The N- and C- subdomains of the HAT domain are shown in blue and grey, respectively. Lys-CoA is shown in stick representation.

bisubstrate inhibitor called Lys-CoA that was developed by Dr. P. Cole at Johns Hopkins University, USA.

The crystal structure of P300 revealed that the chromatin recognition domains comprising the Bromodomain (Bd), the PHD domain and the chromatin modification HAT domain adopt a compact configuration (**Figure 64**). We also discovered a previously unsuspected RING domain that is positioned like a 'lid' over the active site of the acetyltransferase. RING domains are usually E3 ligases, enzymes that catalyse transfer of ubiquitin, a small 8.5 kDa protein, to other protein substrates. Although such an activity had already been described earlier for p300, the location of the active E3 ligase domain was unknown. We found that mutations which inactivate p300 and that have been associated with its role as tumour suppressor are located in the HAT domain that acetylates chromatin. Several of the cancer causing mutations interfere with Acetyl-CoA binding or hydrolysis and inactivate the enzyme.

As the RING domain partially occludes the active site of the HAT domain, we believe that the RING domain has an autoinhibitory function for the enzyme (**Figure 65**). In agreement with this model, mutations that destabilise attachment of the RING domain result in increased p300 activity. Interestingly, a number of such destabilising RING mutations are found in different cancers indicating that p300 hyperactivity is an important aspect of these diseases. Overall, our results suggest that p300 can act not only as a tumour suppressor, but also as an oncogene, an activity that already had been suspected for this protein.

Because of the unique chemical structure and mechanism of regulation of p300, which differs significantly from other cellular HATs, it might be possible to develop inhibitors that work specifically against this family of enzyme and that will allow development of new anti-cancer therapies.

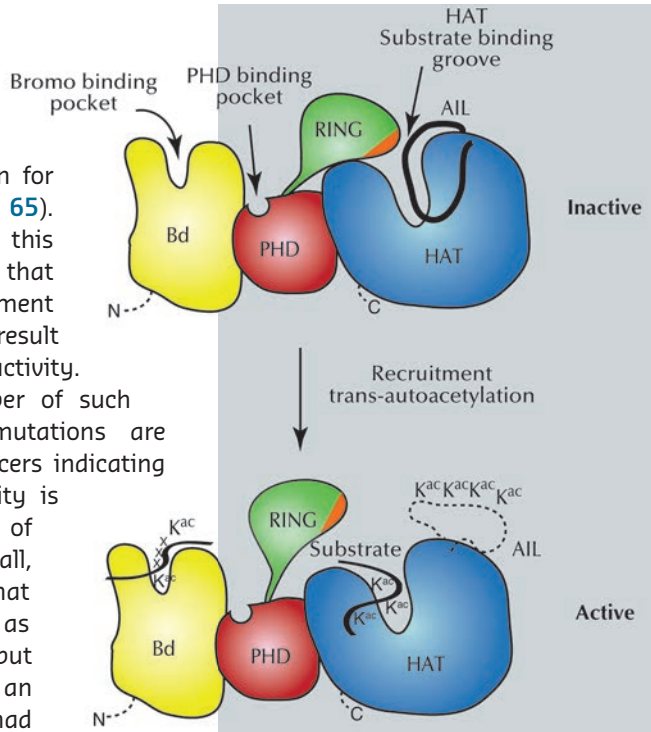

Fig. 65: Model for p300 autoregulation and substrate acetylation. In the inactive state (top), the RING domain blocks the HAT active site. Although not observed in the present structure, we indicate, based on previous work, the docking of the autoinhibitory loop (AIL) loop to the substrate binding site of the HAT domain.

HOW THE CHAPERONE FACT RECOGNISES HISTONES H2A-H2B AND MEDIATES NUCLEOSOME REORGANISATION

The astonishing ability of chromatin to condense metres of DNA into a highly organised, regulated, but tiny structure that fits in the cell's nucleus would not be possible without nucleosomes, the smallest repeating units of chromatin structure. Two coils of DNA wrap around a histone octamer core, which neutralises the DNA's charges and 'packs' the lengthy molecule. However, nucleosomes also create a barrier to processes that require access to our genome such as DNA transcription, replication and repair. A variety of nucleosome remodelling machines and histone chaperones facilitate nucleosome dynamics by depositing or evicting histones and unwrapping the DNA. The eukaryotic FACT complex (composed of the subunits Spt16 and Pob3 in yeast) is an essential and highly conserved chaperone **[1]** that assists the progression of DNA and RNA polymerases and promotes the genome-wide integrity of chromatin structure, including the suppression of cryptic transcription. Genetic and biochemical assays have shown that FACT's chaperone activity is crucially

Principal publication and authors
M. Hondele (a,b), T. Stuwe (b), M. Hassler (a,b), F. Halbach (c), A. Bowman (a), E.T. Zhang (b), B. Nijmeijer (b), C. Kotthoff (a), V. Rybin (b), S. Amlacher (d), E. Hurt (d) and A.G. Ladurner (a,b), *Nature* **499**, 111–114 (2013).
(a) Adolf Butenandt Institute for Physiological Chemistry, Ludwig Maximilians University of Munich (Germany)
(b) Genome Biology Unit and Structural & Computational Biology Unit, EMBL, Heidelberg (Germany)
(c) Department of Structural Cell Biology, Max Planck Institute of Biochemistry, Martinsried (Germany)
(d) Biochemistry Center, University of Heidelberg (Germany)

References

[1] G. Orphanides, W.H. Wu, W.S. Lane, M. Hampsey and D. Reinberg, *Nature* **400,** 284–288 (1999).

[2] R. Belotserkovskaya, *Science* **301,** 1090–1093 (2003).

[3] H. Xin *et al., Mol. Cell* **35,** 365–376 (2009).

[4] D. Su *et al., Nature* **483,** 104–107 (2012).

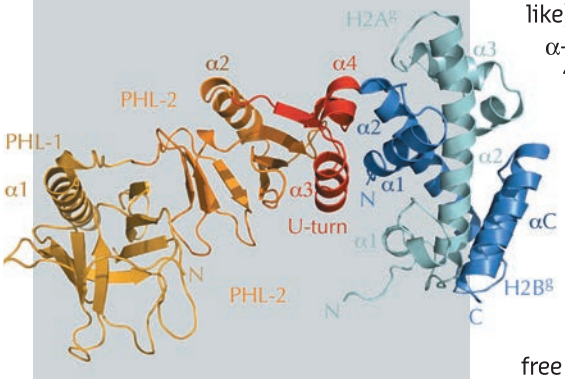

Fig. 66: 2.35 Å structure of the Sp16M chaperone domain (orange/red) in complex with histones H2A-H2B (light green–blue). The interface is formed by the U-turn of Spt16M (red) and the α1 helix of H2B.

Fig. 67: Model for FACT-mediated nucleosome reorganisation. a) Overview of interactions between Spt16M and histones H2B and H3, in the nucleosomal context. b) Superposition of the Spt16M–H2A-H2B complex onto the nucleosome structure. Spt16M and DNA compete for the binding site on H2B α1, therefore Spt16M binding must induce displacement of the DNA resulting in nucleosome breathing.

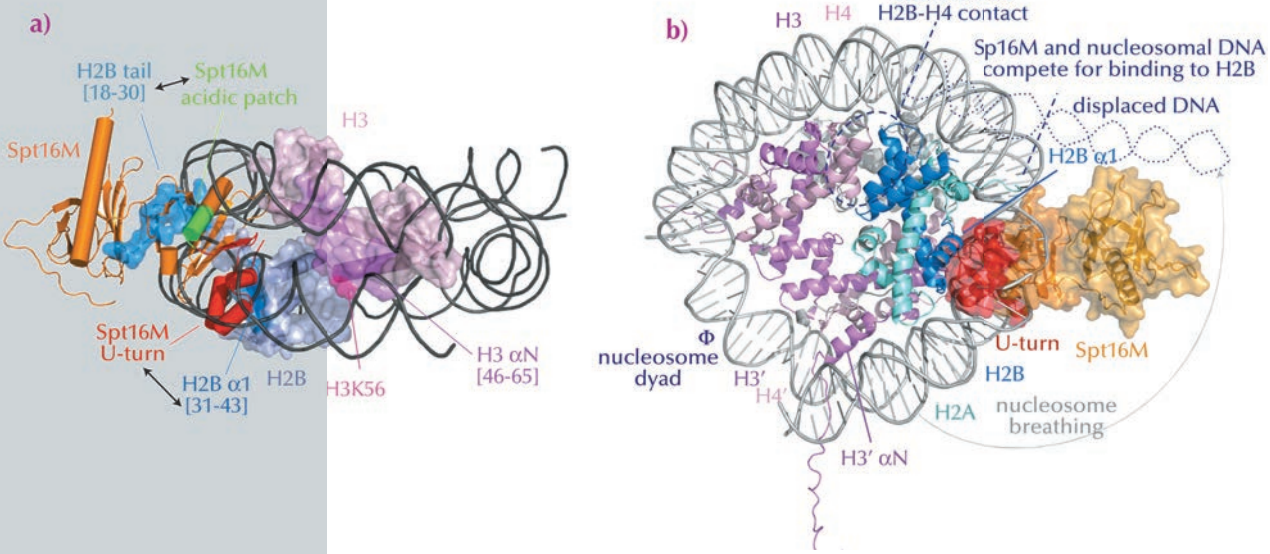

mediated by a direct interaction with the histone H2A-H2B heterodimer [2,3].

However, the structural basis for histone H2A-H2B recognition by FACT, and how this leads to nucleosome reorganisation, was unknown. Therefore, we identified biochemically the evolutionary conserved 'chaperone' domain of FACT, which lies within the Spt16M module. Next, we were able to solve the crystal structure of Spt16M in complex with H2A-H2B at 2.35 Å resolution (Figure 66), the first report of a globular protein in complex with these histones. Spt16M forms a tandem PHL (PH-like) module with a novel C-terminal α-helical motif, which we term the 'U-turn'. The three-helical 'U-turn' clamps the α1-helix of H2B are one of the strongest histone-DNA contacts in the nucleosome. The interface between Spt16M and H2B is hydrophobic and complementary, with little difference in backbone architecture compared to the free proteins. The interaction was verified *in vitro* and *in vivo*: engineered point mutants in the interface on both the histone and the chaperone side abrogate complex formation in isothermal titration calorimetry and size-exclusion chromatography. Furthermore, consistent with the high sequence conservation of the U-turn, mutation of most U-turn residues is lethal in the budding yeast *S. cerevisiae*, indicating that the U-turn motif and its H2A-H2B binding function are essential.

We found that electrostatic interactions contribute to the stability of the histone-chaperone complex. First, the basic N-terminal tail of H2B interacts with a conserved acidic patch on the Spt16M tandem PHL domain, and second, an unstructured stretch of ~80 mostly acidic residues adjacent to Spt16M at the C-terminus of Spt16 contributes a strong interaction with the H2A-H2B dimer. Furthermore, we found that Spt16M also recognises histones H3-H4. Similar to the structurally related chaperone Rtt106, Spt16M binds the αN helix of H3 [4].

In summary, we found that Spt16M makes multiple interactions with histones (Figure 67a), which has led us to suggest a model for FACT-mediated nucleosome reorganisation (Figure 67b). We propose that the chaperone gradually invades the nucleosome. First, it attaches to its binding sites on H3 αN and the H2B N-terminal tail, which are solvent-accessible. There, it would be in a good position to wait until DNA spontaneously dissociates from H2B α1, which happens about 10% of the time. By binding to H2B α1 (as we see in our crystal structure of the complex), Spt16M most likely blocks the strongest interaction surface of H2B with nucleosomal DNA and therefore out-competes and displaces ~30-50 base pairs of DNA, a process called 'nucleosome breathing'. Such loosening of the nucleosome is presumably sufficient for DNA and RNA polymerase passage. The suggested mechanism anticipates that H2A-H2B may not need to be dissociated from the histone octamer, as suggested previously. Such interactions would thus help to preserve chromatin integrity and epigenetic memory.

NUCLEOTIDE SPECIFIC BACTERIAL mRNA 'DECAPPING'

Principal publication and authors
J. Piton (a), V. Larue (b), Y. Thillier (c), A. Dorléans (a), O. Pellegrini (a), I. Li de la Sierra-Gallay (a, d), J.J. Vasseur (c), F. Debart (c), C. Tisné (b) and C. Condon (a), *Proc. Natl. Acad. Sci. USA* **110**, 8858-8863 (2013).
(a) CNRS UPR9073, Institut de Biologie Physico-Chimique, Paris (France)
(b) UMR 8015 CNRS/Université Paris Descartes, Paris (France)
(c) IBMM, UMR 5247 CNRS-Université Montpellier 1-Université Montpellier 2 (France)
(d) IBBMC, CNRS UMR8619, Université Paris-Sud, Orsay (France)

The degradation of messenger RNA (mRNA) is an important means of controlling gene expression in all domains of life. The shorter the half-life of its mRNA, the more rapidly a cell can alter its gene expression programme in response to changes in the environment. While eukaryotic mRNAs are protected from ribonucleases by their 5'-methyl-guanosine cap structure, bacterial mRNAs are protected from degradation by the 5'-triphosphate group that remains on primary transcripts following transcription by RNA polymerase. Intriguingly, the enzymes that remove the cap structure from eukaryotic mRNAs (Dcp2) and the 5'-triphosphate from bacterial mRNAs (RppH) are members of the same ancient family of Nudix phosphohydrolases. In both cases, the resulting RNAs bear 5' monophosphate groups that are targeted for degradation by 5'-3' exoribonucleases or endoribonucleases with stimulatory 5' monophosphate recognition domains.

A typical bacterial cell contains multiple Nudix hydrolases; *Bacillus subtilis* has 6, *Escherichia coli* has 13. It is not easy to tell from a simple homology search which of these proteins has RppH activity. A Blast search for homologs of *B. subtilis* RppH (BsRppH) in *E. coli* only identifies EcRppH in fifth position, for example. Biochemical verification is therefore currently required for enzyme identification. Structural studies of several of these enzymes might ultimately reveal sequence motifs important for distinguishing RppH proteins from other Nudix enzymes.

Using data collected at beamline **ID14-1**, we recently solved the crystal structure of RppH from the Gram-positive model organism *B. subtilis* bound to a two-nucleotide (nt) triphosphorylated RNA molecule (pppGpG). The structure suggested that, in addition to recognising the 5' triphosphate group of the first residue of its substrates, BsRppH contains a pocket specific for guanosine (G) in the second position of bound RNAs (**Figure 68**). Indeed mutation of the guanosine in a known substrate of BsRppH to any other residue (A, C or U) reduced the activity of the enzyme by an order of magnitude. In addition to revealing the substrate specificity of BsRppH, the structure explained, through the relative positions of the magnesium ions in the catalytic site, why the *B. subtilis* enzyme removes the phosphate groups one at a time, while the *E. coli* and *Bdellovibrio bacteriovorus* enzymes release pyrophosphate (PPi) from their mRNA substrates.

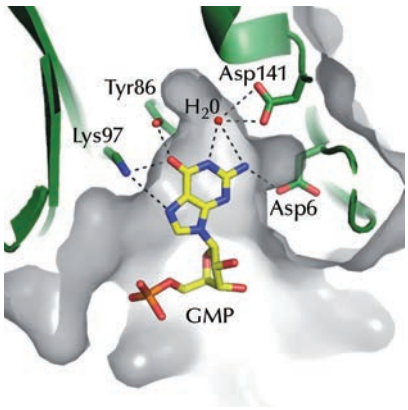

Fig. 68: The guanosine binding pocket of BsRppH. Hydrogen bonds between the protein and GMP are shown as dashed lines.

The crystallography studies were complemented by NMR chemical shift mapping of BsRppH bound to one, two or three triphosphorylated nucleotides. The data showed that at least three nucleotides were required for optimal positioning of the RNA in the catalytic site. The structural studies were also supported by *in vivo* studies on a known substrate of BsRppH, the *B. subtilis yhxA-glpP* mRNA [1]. The second nucleotide of this mRNA is naturally a G-residue, consistent with the enzyme's nucleotide preference in this position. In cells deleted for the *rppH* gene, the *yhxA-glpP* mRNA was stabilised about three-fold compared to wild-type cells. However, when the G in the second position was changed to U, this mRNA was stabilised regardless of the presence or absence of BsRppH in the cell, providing a nice confirmation of the importance of G2 in BsRppH substrates *in vivo*.

When one looks at primary transcripts in *B. subtilis*, it is clear that there is a counter-selection for mRNAs with G in the second position (Figure 69). Only 15% of *B. subtilis* mRNAs contain a G2 residue, compared to 33% having G in position 1 (most RNA polymerases prefer to start with purine, A or G) and 21% in positions 3 to 10. This means that BsRppH can only act on a subset of *B. subtilis* mRNAs. A number of experiments have suggested that *B. subtilis* may have other as yet unidentified RNA pyrophosphohydrolases. It is anticipated that these enzymes will have a different substrate specificity to BsRppH.

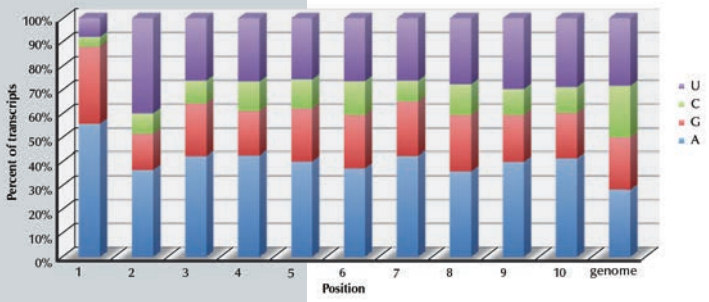

Fig. 69: Identity of the first 10 nucleotides in *B. subtilis* mRNA transcripts. Histogram showing the percent occurrence at each position of the nucleotides U (purple), C (green), G (red), A, (blue). The genome average is also shown.

References

[1] P.-K. Hsieh, J. Richards, Q. Liu and J.G. Belasco, *Proc. Natl. Acad. Sci. USA* **110**, 8864-8869 (2013).

VOLUME-CONSERVING TRANS-CIS ISOMERISATION PATHWAYS IN PHOTOACTIVE YELLOW PROTEIN VISUALISED BY PICOSECOND X-RAY CRYSTALLOGRAPHY

Principal publication and authors

Y.O. Jung (a,b), J.H. Lee (b), J. Kim (b), M. Schmidt (c), K. Moffat (d,e), V. Šrajer (e) and H. Ihee (a,b), *Nature Chem.* **5**, 212–220 (2013).

(a) Center for Nanomaterials and Chemical Reactions, Institute for Basic Science (Republic of Korea)

(b) Center for Time-Resolved Diffraction, Department of Chemistry, KAIST (Republic of Korea)

(c) Physics Department, University of Wisconsin–Milwaukee (USA)

(d) Department of Biochemistry and Molecular Biology, and Institute for Biophysical Dynamics, The University of Chicago (USA)

(e) Center for Advanced Radiation Sources, The University of Chicago (USA)

Many photoreceptor proteins convert external light stimuli into molecular action by virtue of isomerisation of its π-conjugated chromophore. Typically, a π-conjugated organic molecule is thought to isomerise via a one-bond-flip mechanism within the gas or solution phases [1]. However, in an inner cavity of a photoreceptor, the chromophore can no longer proceed via one-bond-flip isomerisation, because it interacts with the surrounding side chains of the protein via hydrogen-bonding interactions and steric constraints. In this restrictive condition, isomerisation occurs in a "volume-conserving" fashion. For instance, photoactive yellow protein (PYP) of *Halorhodospira halophila* has an interior chromophore (*p*-coumaric acid, pCA, Figure 70a) that is known to be isomerised via the volume-conserved bicycle-pedal

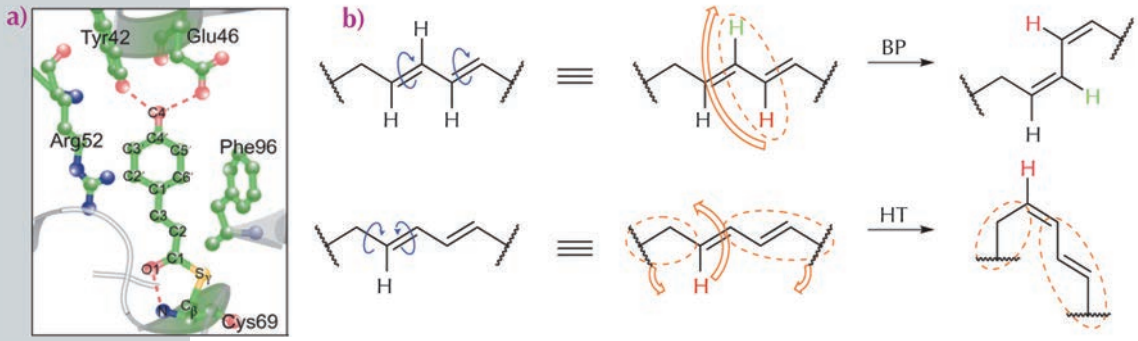

Fig. 70: Isomerisation mechanisms and overview of PYP. a) Close-up of the pCA chromophore and neighbouring residues. b) Schematic description of two volume-conserved isomerisation mechanisms; Bicycle-Pedal (BP), and Hula-Twist (HT).

(BP) mechanism during its photocycle (**Figure 70b**) **[2]**. An alternative, the volume-conserved Hula-Twist (HT) mechanism (**Figure 70b**), has been observed in various systems, but not in PYP **[2]**. Both these volume-conserving mechanisms have been observed individually, but these highly-choreographed atomic motions have not been reported in a single system simultaneously.

We employed time-resolved Laue crystallography at ESRF beamline **ID09TR** and APS beamline ID14 to investigate the mechanism of isomerisation of the chromophore of PYP and the structures of intermediate in the pathway from 100 ps to 1 µs. Time-dependent electron density maps depict a highly-twisted structure early on (less than ns) with movement of nearby amino acid residues sustaining hydrogen-bonding networks. Subsequent kinetic analysis unveiled three time-independent electron density maps and two time constants, suggesting that the first map represents homogeneous structure (I_T), but the second and third maps have heterogeneous structures (I_{CT}+pR_1 and pR_1+pR_2, respectively) (**Figure 71a**). Further structure refinement and kinetic analysis revealed four intermediate structures and bifurcated pathways early in the photocycle. In detail, the first intermediate, I_T, bifurcates into pR_1 (HT pathway) and I_{CT} (BP pathway) with time constants of 3 ns and 1.7 ns, respectively (I_{CT} : pR_1 ~ 6:4). I_{CT} further decays into pR_2 with a time constant of 20 ns (**Figure 71b**). Additional experiments with an E46Q mutant indicates that the hydrogen bond network between pCA and nearby residues plays a crucial role in the bifurcation pathways (**Figure 71c**). Deficiency of one hydrogen bond in the E46Q mutant makes the BP pathway unstable, isomerisation in the E46Q mutant occurs only via the HT pathway. Intensive density functional theory calculations also confirmed that a highly distorted intermediate, I_T, is stabilised as an intermediate rather than a transition state as a result of hydrogen bond formation with nearby residues.

Our results provide several insights, both structurally and kinetically, into the volume-conserving isomerisation in the PYP photocycle. First, we unveiled a long-hypothesised, highly-distorted intermediate along the trans- to cis-isomerisation pathway. This structure provides consistent and appropriate corroboration of previous experimental and theoretical results **[3,4]**. Second, the detailed intermediate structures and dynamics revealed that the hydrogen bonds inside proteins play key roles in photo-isomerisation reactions allowing stabilisation of intermediates and a bifurcated pathway. This bifurcated volume-conserving pathway in a single system was found for the first time. Finally, we controlled the reaction pathway just by modifying one hydrogen bond. This study has potential applications not only to other photoactive protein systems but also to time-resolved experiments performed in next generation synchrotrons with femtosecond time-resolution.

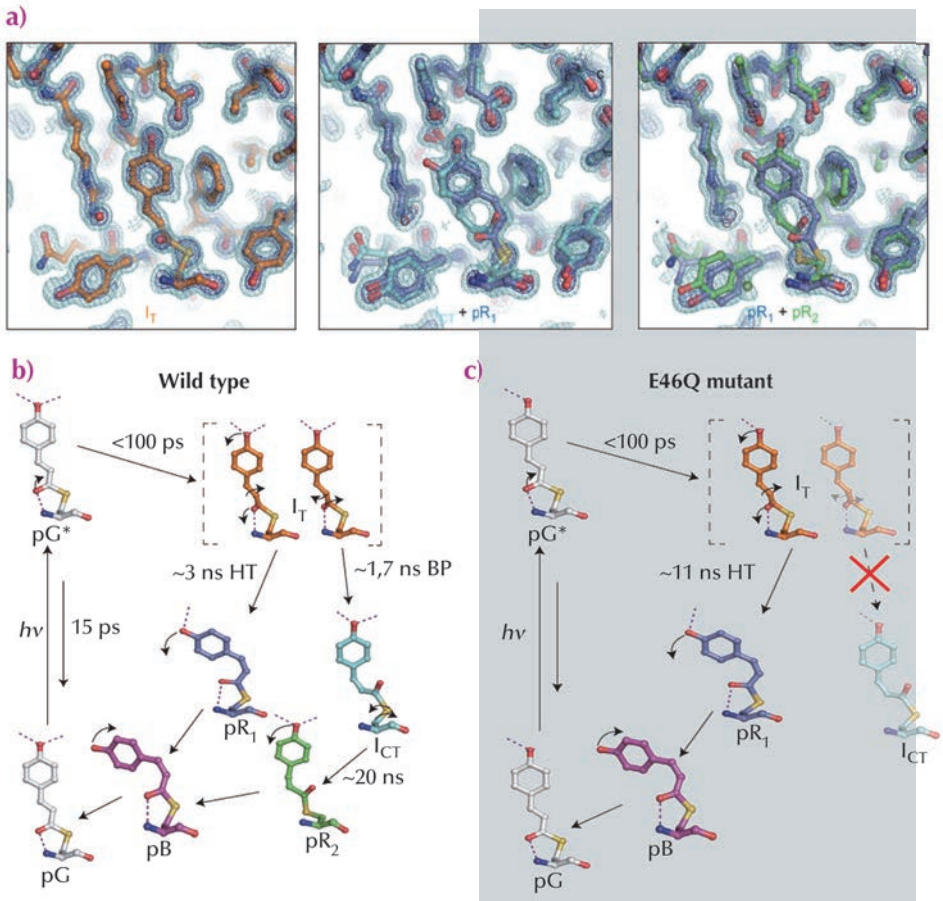

Fig. 71: a) Time-independent intermediates for WT-PYP recovered from kinetic analysis of time-dependent difference electron density maps. b, c) A photocycle consistent with time-resolved electron density maps of WT-PYP (b) and the E46Q mutant (c). The pathway from I_T to I_{CT} via bicycle-pedal mechanism is blocked due to the weaker hydrogen bond between pCA and Q46.

References

[1] R.S. Liu and A.E. Asato, *Proc. Natl. Acad. Sci. U.S.A.* **82**, 259–263 (1985).

[2] Y. Imamoto, M. Kataoka and R.S.H. Liu, *Photochem. Photobiol.* **76**, 584–589 (2007).

[3] L.J.G.W. van Wilderen, M.A. van der Horst, I.H.M. van Stokkum, K.J. Hellingwerf, R. van Grondelle and M.L. Groot, *Proc. Natl. Acad. Sci. U.S.A.* **103**, 15050–15055 (2006).

[4] G. Groenhof, M. Bouxin-Cademartory, B. Hess, S.P. De Visser, H.J.C. Berendsen and M. Olivucci, *et al.*, *J. Am. Chem. Soc.* **126**, 4228–4233 (2004).

SOFT CONDENSED MATTER

This section presents selected exemplary research related to Soft Matter Science and published during the last year. Some of these examples illustrate the maturity of scattering techniques as well as the unprecedented detail that can be revealed by means of quantitative data analysis. A clear deviation from the trend in previous years is that this issue contains many articles related to polymer science. This is certainly encouraging and affirms the importance of synchrotron techniques for the field of polymer science. Indeed, not all the exciting science published during the period could make it into this volume. Some notable omissions include the direct observation of the kinetic pathway of surfactant micellisation [G.V. Jensen *et al.,* JACS, **135**, 7214 (2013)], Dichotomic ageing behaviour of laponite colloidal glasses [R. Angelini *et al.,* Soft Matter, **9**, 10955 (2013)], etc.

It was another very busy year for the beamline group because of upgrade projects, and reviews of beamlines ID13, in spring, and ID10, in the autumn. Both beamlines received very positive reports. The next review is for ID09B, which is scheduled in spring 2014. After 19 years of user operation, beamline ID02 was closed for upgrade in July. The reconstruction work (Upgrade beamline project UPBL9a) is now in full swing and the new beamline is expected to restart user operation in July 2014. The design of the new optical layout for UPBL9b at ID09 has been completed and the beamline will have the new focusing optics and detector in a year's time. At the end of phase I of the ESRF upgrade, ID09 is expected to be fully dedicated to time-resolved pump-probe diffraction/scattering experiments. As part of the upgrade, the Soft Interfaces station of beamline ID10 will receive a new diffractometer (Huber) and ID13 will be equipped with a state-of-the-art Eiger detector from Dectris.

The Science Building in September 2013, constructed as part of the CPER project.

Construction of the Science Building is nearly completed and the full scale operation of the Partnership for Soft Condensed Matter (PSCM) is to begin soon. The PSCM is seeking collaborative partners from academia and industry. Another important change during the year 2014 will be the relocation of scientific staff of the Structure of Soft Matter group to the Science Building, sharing the floor with the corresponding staff of the Large Scale Structures group at the ILL. Together with the PSCM, this will make the Science Building the centre of gravity of Soft Matter activities on the campus and hopefully foster an unprecedented level of synergy. As an effort to promote the use of synchrotron radiation in industrial R&D related to soft materials, full services are offered to industrial customers for techniques such as SAXS, WAXS and microdiffraction.

Finally, Grenoble has made a successful bid to host the next International Soft Matter Conference in 2016 (ISMC2016) under the auspices of the SOFTCOMP network of excellence. This meeting will be jointly organised by the ESRF and ILL, together with Grenoble University, and is expected to attract around 800 participants from all over the world.

T. NARAYANAN

IDEAL POLYETHYLENE NANOCRYSTALS

Principal publication and authors
A. Osichow (a), C. Rabe (b), K. Vogtt (b), T. Narayanan (c), L. Harnau (d), M. Drechsler (e), M. Ballauff (b) and S. Mecking (a), *JACS* **135**, 11645–11650 (2013).
(a) Chemical Materials Science, Department of Chemistry, University of Konstanz (Germany)
(b) Helmholtz-Zentrum Berlin for Materials and Energy and Department of Physics, Humboldt University, Berlin (Germany)
(c) ESRF
(d) Max Planck Institute for Intelligent Systems and Institute for Theoretical Physics IV, University of Stuttgart (Germany)
(e) Bayreuth Institute of Macromolecular Research, University of Bayreuth (Germany)

Polymers such as polyethylene rarely form single crystals and, upon cooling, an entangled polymer melt usually solidifies into crystalline lamellae consisting of regularly folded chains sandwiched between extended amorphous regions. This peculiar nanostructure primarily controls the mechanical properties and aesthetic features of polymers. Thanks to recent advances in catalytic polymerisation, polyethylene-nanocrystals consisting of single lamellae can be formed in aqueous dispersion [1]. Annealing of such crystals leads to a thickening of the crystalline lamella that can be studied with high precision [2]. However, the role of short chain branches and entanglements remained unclear in all studies done so far. A possible approach that overcomes these problems is a compartmentalisation of the polymerisation and then a perfect ordered deposition of the nascent chain on a nanocrystal growth front. We have realised this scheme by means of a new catalyst that produces virtually perfect polyethylene chains that are free of branches.

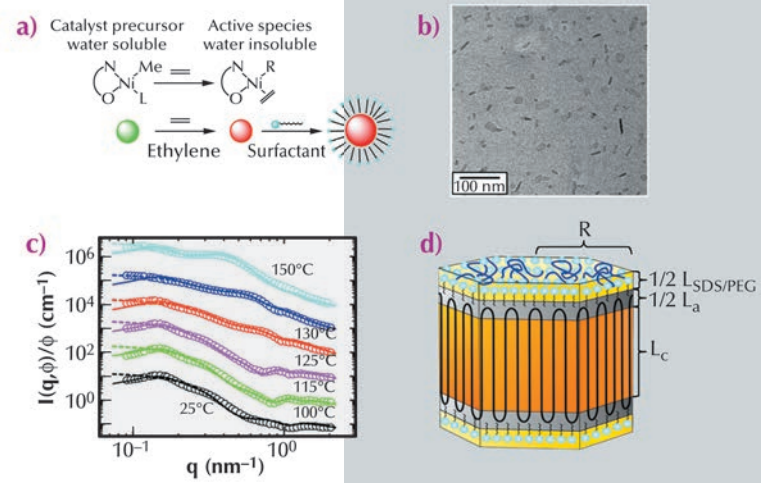

Fig. 72: Catalytic polymerisation of ethylene in aqueous suspension and the formation of poly(ethylene) nanocrystals. (a) Polymerisation of ethylene in water. (b) Cryo-TEM micrograph of the polyethylene-nanocrystals in aqueous dispersion. (c) Normalised SAXS intensities from aqueous suspensions of polyethylene nanocrystals annealed at indicated temperatures. For clarity, successive curves are multiplied by a factor 10. The dashed lines represent the results of the modelling of the SAXS data by a dispersion of non-interacting particles and the solid lines by interacting particles, respectively. (d) Scheme of the platelet-like structure of the nanoparticles used for the SAXS analysis, indicating the thick crystalline part, thin layer of the amorphous turns and outer stabilising surfactant layer.

Figure 72a summarises the main steps of the catalytic polymerisation and the chemical structure of the catalyst. Upon activation, the catalyst becomes lipophilic and polyethylene chains, which are formed immediately, pack into surfactant-stabilised particles. These polyethylene chains were found to be linear (M_n = 4.2 × 10^5 g mol^{-1} and M_w / M_n = 1.4) and virtually devoid of any branches. **Figure 72b** displays a micrograph of the dispersion taken by cryogenic transmission electron microscopy (cryo-TEM), indicating well-defined nanocrystals with relatively narrow size distribution and a faceted shape. To further elucidate the semicrystalline nanostructure, we have performed a comprehensive structural analysis of the polyethylene-nanoparticles by small-angle X-ray scattering (SAXS) at beamline **ID02**. Typical SAXS profiles together with model fits are shown in **Figure 72c**. **Figure 72d** illustrates the platelet model used for the data analysis consisting of a crystalline lamella that is enclosed by two amorphous layers.

SAXS investigation of the annealed samples revealed that the thickness of the crystalline layer increases when annealed at 100°C and 115°C while the thickness of the amorphous layer remains constant. Thus, the crystallinity increases markedly and finally reaches about 88%. This finding supports the idea of an ideal polyethylene-nanocrystal: the absence of branches allows the polyethylene-chains to diffuse through the crystal without melting or major distortion. The amorphous layers hence act like the wheels of a pulley as depicted schematically in **Figure 73**. This in turn shows clearly that the amorphous regions are virtually devoid of entanglements. The growing chains emanating from the catalytic centre are laid down on the facet of the polyethylene-nanocrystals in an orderly fashion, that is, without the formation of entanglements. The high degree of crystallinity was further confirmed by the wide angle X-ray scattering analysis.

In summary, this study could open up a new type of crystal engineering that leads to ideal polymer nanocrystals with improved processing capabilities as a result of their non-entangled nature, especially for ultra-high molecular weights, and robust mechanical performance.

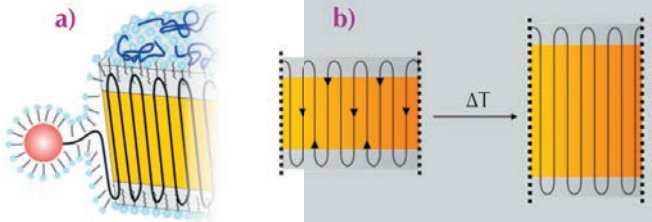

Fig. 73: Proposed mechanism for the formation of ideal polyethylene-nanocrystals. (a) The polyethylene-chain emanating from the catalytic centre is stabilised in the aqueous phase by the adsorbed surfactant SDS. The growing chain is then laid down on a given facet of the polyethylene-nanocrystal in an orderly fashion without entanglements or other defects. (b) Mechanism of thermal annealing in an ideal polyethylene-nanocrystal: the amorphous layers covering both ends of platelets act like the wheels of a pulley, just changing the direction of the chains.

References

[1] C.H.M. Weber, A. Chiche, G. Krausch, S. Rosenfeldt, M. Ballauff, L. Harnau, I. Göttker-Schnetmann, Q. Tong and S. Mecking, S. *Nano Lett.* **7**, 2024-2029 (2007).

[2] C.N. Rochette, S. Rosenfeldt, K. Henzler, F. Polzer, M. Ballauff, Q. Tong, S. Mecking, M. Drechsler, T. Narayanan and L. Harnau, *Macromolecules* **44**, 4845-4851 (2011).

NANO-STRUCTURED FUNCTIONAL MATERIALS THROUGH SELF-ASSEMBLY OF WEDGE-SHAPED MONOMERS

Principal publication and authors
J.J. Hernandez (a), M. Rosenthal (a,b), D.A. Ivanov (a,b), H. Zhang (c), L. Li (c), M. Möller (c) and X. Zhu (c), *Adv. Mat.* **25,** 3543-3548 (2013).
(a) Institut de Sciences des Matériaux de Mulhouse (IS2M-CNRS) (France)
(b) Moscow State University Faculty of Fundamental Physical and Chemical Engineering GSP-1, Moscow (Russian Federation)
(c) Interactive Materials Research - DWI an der RWTH Aachen e.V. and Institute for Technical and Macromolecular Chemistry of RWTH Aachen University (Germany)
(d) Macromolecular Chemistry II, University of Bayreuth (Germany)

The self-assembly of biological molecules is the key for the generation of their well-defined functionality. In this process, water molecules play a significant role in defining the final structure and, consequently, the functionality. It is our ultimate goal to design functional materials with various morphologies that are typical of biological systems. For example, wedge-shaped amphiphilic sulfonate molecules can be viewed as analogue of proteins, which are able to form smectic (cf. β-sheet) or columnar (cf. α-helix) structures, depending on their molecular architecture [1-3]. In this work and previous [4,5], we explored the sequence of humidity-induced phase transitions in a novel wedge-shaped sulfonate molecule, sodium 2,3,4-tris (11'-acryloylundecyl-1'-oxy) benzene sulfonate (A-Na) (Figure 74), which serves as a model of a nano-channel-forming ion-selective membrane, using beamline **BM26B**.

For the resulting supramolecular system containing ionic nano-channels, we demonstrate that a small amount of water can efficiently create highly conductive pathways for ions. Moreover, swelling of the initial hexagonal structure (Col_{hd}) by water gives rise to a phase transition to bicontinuous phases (Cub_{bi}), which is accompanied by formation of a percolating network of ion-conductive paths (Figure 74). The appearance of Cub_{bi} phases on swelling further improves the conductivity, and can be of much interest for membrane technologies. Unlike columnar phases, the Cub_{bi} phases would not require macroscopic channel alignment to maximise ion transport across the membrane due to their interwoven 3D channel networks. Our results provide a detailed view of the processes occurring in an ion-channel-forming system upon swelling. Importantly, it was shown that the supramolecular structures such as Col_{hd} and Cub_{bi} phases can be preserved upon polymerisation of their acrylic end-groups resulting in free-standing membranes with efficient ion-conduction. This work paves the way for the fabrication of mechanically stable nanoporous membranes with a tailored ion channel structure for applications in separation and catalysis.

Another application of molecular wedges could be in the design of functionalised micro-containers. Thus, we have shown that a liquid-crystalline complex of a polybase such as poly(2-vinylpyridine) (P2VP) and amphiphilic wedges bearing sulfonic acid groups at the tip (Figure 75a) forms onion-like multilamellar nano-sized vesicles in aqueous suspension. The structure of the complex in the vesicles is found to be similar to that in the bulk, where polymer backbones are sandwiched between the bilayers formed by the ligand molecules.

In contrast to conventional polymersomes, the polymer chains in this system are mainly parallel to the vesicle surface, contributing to their mechanical stability (Figure 75b). A large amount of remaining free binding sites (*i.e.* pyridine groups) makes it possible to incorporate functional molecules into the vesicles. Furthermore, a collapse of the vesicles can be induced by UV irradiation because of the trans–cis transition of the azo groups, which leads to isotropisation of the layered structure (Figure 75c). This feature can make this system promising for controlled delivery applications.

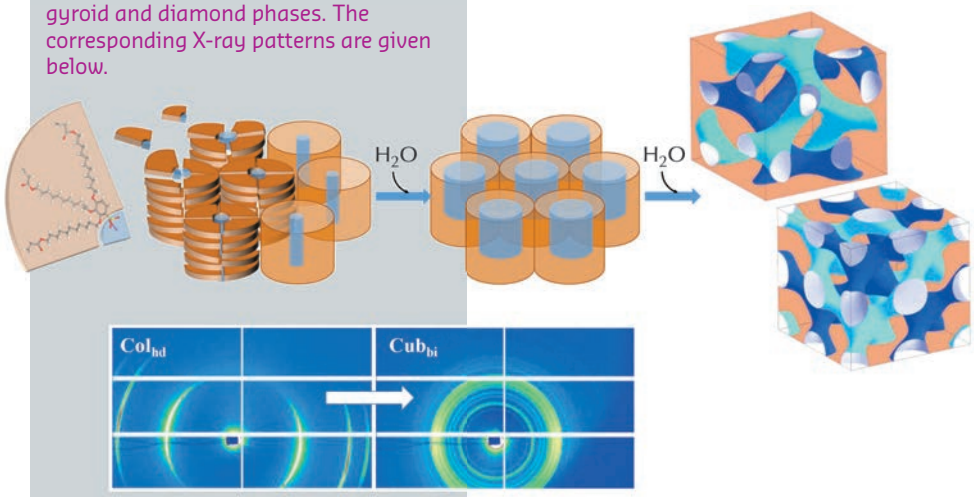

Fig. 74: Schematics of the self-assembly process of a wedge-shaped sulfonate forming supra-molecular columnar structures. The ionic nano-channels resulting from such a process swell upon water uptake (from left to right). At high relative humidity, the columnar structure transforms into bicontinuous gyroid and diamond phases. The corresponding X-ray patterns are given below.

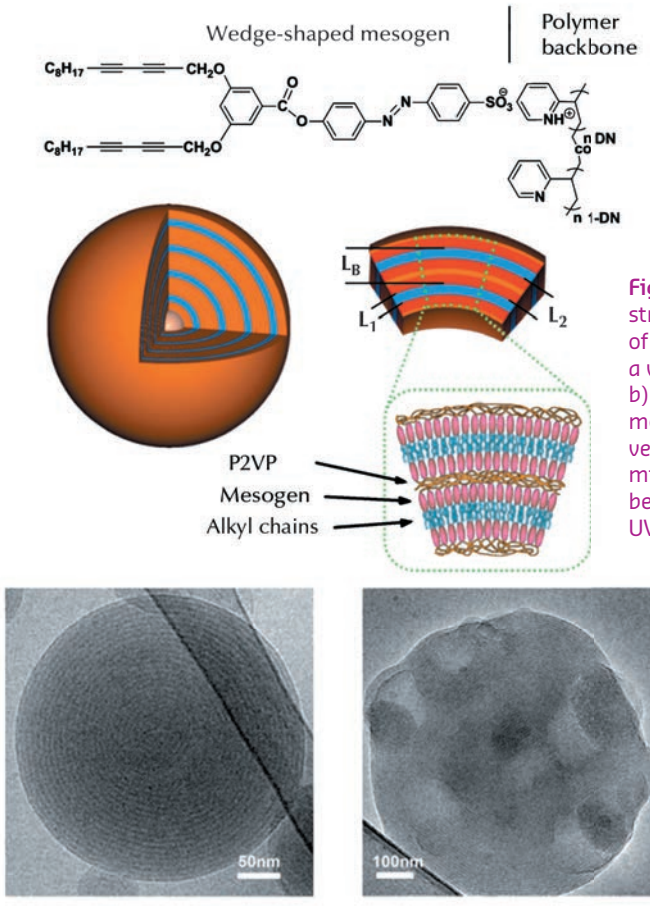

Fig. 75: a) Chemical structure of the complexes of poly(2-vinylpyridine) and a wedge-shaped mesogen. b) Proposed molecular model of the onion-like vesicles. c) Cryo-TEM micrographs of the vesicles before (left) and after (right) UV irradiation.

References
[1] U. Beginn, *Prog. Polym.* Sci., **28**, 1049 (2003).
[2] G. Ungar, Y. Liu, X. Zeng, V. Percec and W-D. Cho, *Science* **299**, 1208 (2003).
[3] V. Percec, A.E. Dulcey, V.S.K. Balagurusamy, Y. Miura, J. Smidrkal, M. Peterca, S. Nummelin, U. Edlund, S.D. Hudson, P.A. Heiney, H. Duan, S.N. Magonov and S.A. Vinlogradov, *Nature* **430**, 764 (2004).
[4] M. Rosenthal, L. Li, J.J. Hernandez, X. Zhu, D.A. Ivanov and M. Möller, *Chem. Eur. J.* **19**, 4300-4307 (2013).
[5] L. Li, M. Rosenthal, H. Zhang, J.J. Hernandez, M. Drechsler, K.H. Phan, S. Rütten, X. Zhu, D.A. Ivanov and M. Möller, *Angew. Chem.: Int. Ed.* **124**, 11784 –11787 (2012).

ELECTRIC FIELD INDUCED SELECTIVE DISORDERING OF LAMELLAR BLOCK COPOLYMERS

Principle publication and authors
M. Ruppel (a), C.W. Pester (b), K.M. Langner (c), G.J.A. Sevink (c), H.G. Schoberth (b), K. Schmidt (d), V.S. Urban (a), J.W. Mays (a) and A. Böker (b), *ACS Nano* **7**, 3854 (2013).
(a) Oak Ridge National Laboratory (ORNL) (USA)
(b) RWTH Aachen University (Germany)
(c) Leiden University (The Netherlands)
(d) SLAC National Accelerator Laboratory (USA)

Block copolymers consist of two or more chemically distinct polymer segments. They readily self-assemble into a wide range of periodic structures, which exhibit characteristic feature sizes on nanoscopic length scales (10 – 100 nm).

Generally, the spontaneous ordering of soft matter is driven by weak noncovalent interactions between its molecular constituents. While these weak interactions drive self-organisation over mesoscopic length scales, they also permit high densities of structural imperfections. Such defects, however, severely limit the spatial coherence of self-organised soft matter. Consequently, a wide range of techniques are being explored to direct the formation of highly ordered structures that exhibit both translational and orientational order on macroscopic length scales.

At beamline **ID02** we studied the effect of an external electric field on the orientational and translational order of block copolymer lamellae close to the order-disorder transition (ODT). Typically, lamellar alignment proceeds via two distinct alignment mechanisms: rotation of grains (RG) and nucleation and growth (NG) [1]. The main selection criterion is the segregation strength between chemically unlike components. Strongly segregated block copolymers align through the migration and annihilation of grain boundary defects, which enables the rotation of entire lamellar grains (RG). Contrary to this, less strongly segregated lamellae may

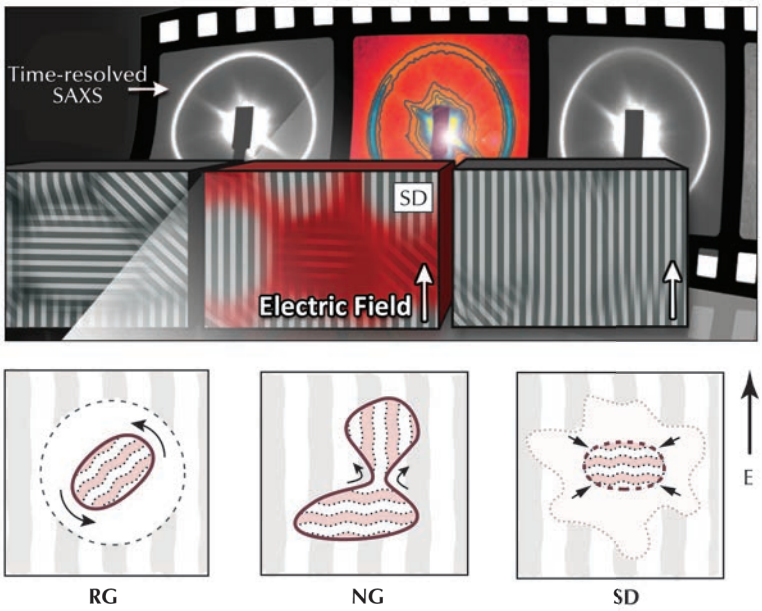

Fig. 76: Time-resolved SAXS data obtained from a lamellar block copolymer solution close to ODT upon the inception of an electric field indicating the selective disordering (SD) of ill-aligned lamellae. The images in the front illustrate the situation in real-space (top). Electric field-induced lamellar alignment typically proceeds via either rotation of grains (RG) or nucleation and growth (NG) for strongly and moderately segregated lamellae, respectively. SD occurs in proximity to the ordering transition (bottom).

align through NG. Here, perpendicularly aligned lamellae are destabilised and field-induced undulations nucleate the formation of parallel-aligned lamellae (Figure 76).

Yet another mechanism can be envisaged close to ODT, that is, for weak segregation. Here, ill-aligned lamellae selectively disintegrate in the presence of an electric field, forming patches of a disordered melt, which may spawn parallel-aligned lamellae when the applied field ceases (Figure 76). Selective disordering (SD) relies on a small difference between the order-disorder transition temperatures (T_{ODT}) between ill-aligned lamellae [2], which has long been seen to be too marginal to be of any practical importance. However, recent computer simulations suggest that SD might yet be within experimental reach [3].

The electric field-induced alignment of a lamellar phase generally gives two populations of lamellar orientations: a major population that is aligned parallel to the electric field, and a minor population that remains perpendicularly aligned where the lamellar interface is oriented parallel to the capacitor's electrodes. An X-ray area detector conveniently allowed us to monitor the evolution of translational order for all lamellar orientations, simultaneously. To quantify its degree, we used the transverse correlation length ξ between distinct lamellae, that is, the length scale over which lamellar layers are spatially correlated.

Figure 77a depicts the time evolution of ξ upon inception of an electric field of 1 kV/mm in proximity to ODT. Data are shown for lamellae, which are aligned parallel and perpendicular to the applied field. Notably, ξ drops substantially for perpendicularly aligned lamellae, while ξ remains mostly unaffected for lamellae that are already oriented parallel to the field direction. Indeed, ξ for perpendicularly aligned lamellae approaches values that are usually found above ODT in the disordered phase. That is, any long-range transitional order is lost.

Fig. 77: Time-evolution of the translational correlation length ξ upon inception of an electric field of 1 kV/mm at ΔT = -1K below T_{ODT} (a). The degree of the asymmetric response of ξ for parallel and perpendicularly aligned lamellae delineates a small region below ODT, where SD becomes prevalent (b).

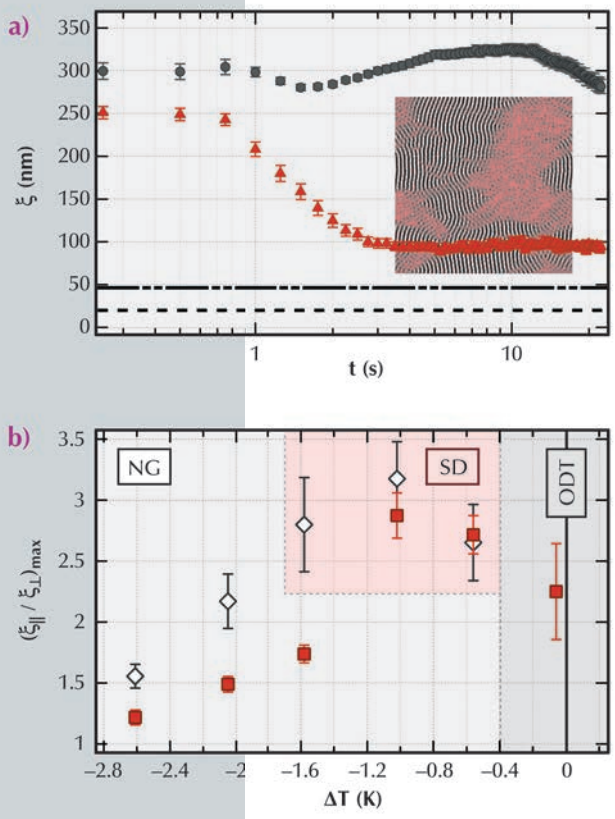

Examining the degree to which lamellae lose translational order depending on orientation and distance from ODT unveiled a narrow region in proximity to ODT where SD becomes significant (**Figure 77b**). In this region, ill-aligned lamellae dissolve, while parallel-aligned lamellae remain mostly unaffected. This mechanism was further sustained through dynamic density-functional theory (DDFT) simulations, which illustrate the situation in real space (**Figure 77a inset**). Our findings suggest that moderate electric fields may well be sufficient to alleviate grain boundary defects even close to the ordering transition.

Indeed, by examining the evolution of the translational order for all known orientation mechanisms, we found that long-range translational order may well be improved through the application of an electric field for either strongly and weakly segregated block copolymer lamellae. However, we find no improvements on the long-range translational order when alignment proceeds through NG.

References
[1] A. Böker, H. Elbs, H. Hänsel, A. Knoll, S. Ludwigs, H. Zettl, V. Urban, V. Abetz, A.H.E. Müller and G. Krausch, *Phys. Rev. Lett.* **89**, 135502 (2002).
[2] K. Amundson, E. Helfand, X.N. Quan, S.D. Hudson and S.D. Smith, *Macromolecules* **27**, 6559 (1994).
[3] G.J.A. Sevink, M. Pinna, K.M. Langner and A.V. Zvelindovsky, *Soft Matter* **7**, 5161 (2011).

UNDERSTANDING CRYSTALLISATION FEATURES OF POLYMERS UNDER CONFINEMENT TO OPTIMISE FERROELECTRICITY IN NANOSTRUCTURES

Principal publication and authors
M.C. García-Gutiérrez (a), A. Linares (a), I. Martín-Fabiani (a), J.J. Hernández (b), M. Soccio (a), D.R. Rueda (a), T.A. Ezquerra (a) and M. Reynolds (c), *Nanoscale* **5**, 6006–6012 (2013).
(a) Instituto de Estructura de la Materia (IEM-CSIC), Madrid (Spain)
(b) Institut des Sciences de Matériaux de Mulhouse (France)
(c) ESRF

Ferroelectric polymers have emerged as cost-effective functional materials for organic electronic devices due to their high electric breakdown field, low dielectric loss, light weight and high flexibility. Poly(vinylidene fluoride) (PVDF) and its copolymers with trifluoroethylene, P(VDF-TrFE), are ferroelectric polymers with a relatively high remnant polarisation, large piezoelectric coefficient, high dielectric constant, and low dielectric loss. P(VDF-TrFE) thin films and low aspect ratio nanostructures have been extensively studied and used in various dielectric and ferroelectric device applications such as non-volatile organic memories **[1]** among others. High aspect ratio (length/diameter) one-dimensional (1D) nanostructures are appropriate for studying size-dependent processes with length scales comparable to the nanostructure's size and may also have greater potential for high density energy storage applications due to the dramatically increased surface area over thin films and low aspect ratio nanostructures.

The phase diagrams and the kinetics of phase transformation processes of matter in confined space can deviate considerably from the respective dependencies observed in bulk. Polymer crystallisation is an example of these phenomena as it is known that a size limitation at the nanometre scale can affect crystal nucleation, growth and orientation. Furthermore, in a previous study concerning PVDF, we reported the crystal phase transition from the α-nonpolar crystal form with chains of an alternating trans–gauche conformation (TGTG) to the γ-ferroelectric crystalline structure with a TTTG sequence, due to PVDF confinement within nanopores **[2]**. However, the most highly ferroelectric and desired crystalline form is the β-phase, where chains of all-trans (TTTT) conformation exhibit iso-oriented dipoles in a pseudohexagonal crystal packing. P(VDF-TrFE) copolymers crystallise more readily in the β-phase than the homopolymer PVDF because the presence of the third fluorine in the TrFE monomer unit sterically hinders the formation of the TGT conformation.

Fig. 78: a) SEM image of the cross-section of a sample infiltrated by solution wetting and fractured in liquid nitrogen. The inset is a magnified image of the interface between the residual polymer film (right) and the nanorod array and alumina membrane (left). b) Schematic diagram of the scanning μ-XRD set-up.

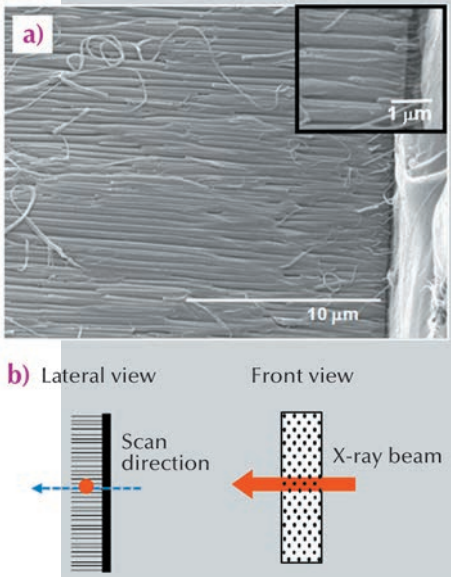

References
[1] D.E. Martínez-Tong, M. Soccio, M.C. García-Gutiérrez, A. Nogales, D.R. Rueda, N. Alayo, F. Pérez-Murano and T.A. Ezquerra, *Appl. Phys. Lett.* **102**, 191601 (2013).
[2] M.C. García-Gutiérrez, A. Linares, J.J. Hernández, D.R. Rueda, T.A. Ezquerra, P. Poza and R.J. Davies, *Nano Lett.* **10**, 1472–1476 (2010).

High aspect ratio 1D nanoarrays of P(VDF-TrFE) copolymers supported by a residual polymer film have been prepared by melt and solution wetting, using porous anodic aluminum oxide (AAO) as a template. X-ray microdiffraction (μ-XRD) experiments were carried out at **ID13** to explore the heterogeneities along the 1D nanostructures in order to select the optimum parameters for improving the ferroelectric character of polymer nanoarrays. Scanning μ-XRD with a 1 μm diameter beam was accomplished along the cross-section of the samples (Figure 78).

From diffraction patterns collected at regular intervals between the residual polymer film (bulk) and the nanorod array, several structural features such as crystallinity and crystal phase type could be investigated (Figure 79). The evolution of different polymorphs from the mixture of paraelectric and ferroelectric crystal forms (bulk) to the pure ferroelectric form (nanorod array), due to the copolymer confinement within the nanopores of the AAO membrane, was observed for the samples prepared by solution wetting. Samples prepared by melt wetting however exhibited only the ferroelectric phase for both the residual film and nanoarray. The crystal nuclei formed in the residual polymer film connected to the nanoarray play a key role in determining the formation of a gradient crystallinity distribution, where the crystallinity decreases along the first 5-10 micrometres in the nanorods, reaching a steady value afterwards. The above crystallisation features of P(VDF-TrFE) copolymers under confinement indicate potential for optimising the ferroelectric character of polymer nanostructures.

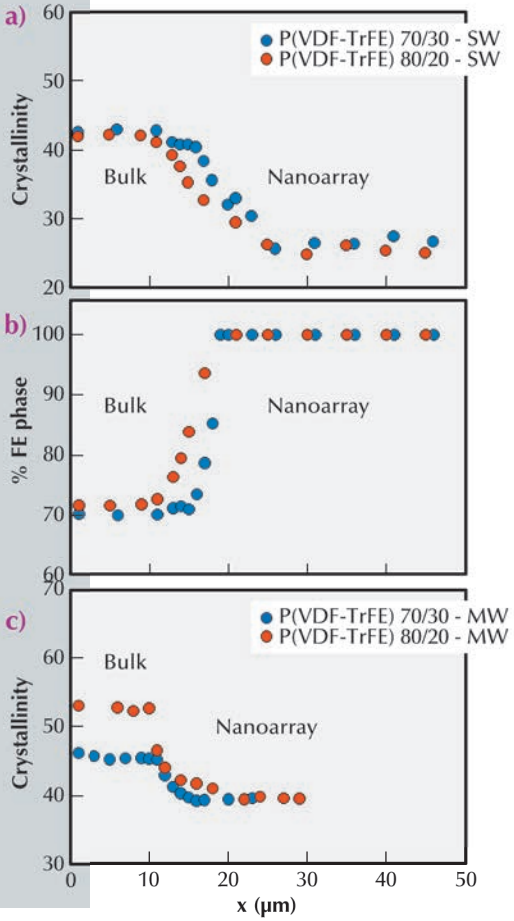

Fig. 79: Spatial evolution, going from the residual polymer film (bulk) towards the nanorod array: a) degree of crystallinity and b) fraction of the ferroelectric form for samples prepared by solution wetting (SW) and c) degree of crystallinity for samples prepared by melt wetting (MW).

Acknowledgements
The authors are grateful for the financial support from the MINECO (grants MAT2011-23455 and FPI BES-2010-030074) and from the CSIC and Fondo Social Europeo (FSE) (JAE-Doc contract), Spain. We thank P. Poza for SEM micrographs and M. Burghammer for his support during measurements at ESRF.

THIN FILM SELF-ASSEMBLY BEHAVIOUR OF ORGANIC ELECTRONIC MOLECULES

Principle publication and authors
T.G. Dane (a), P.T. Cresswell (a), G.A. Pilkington (a), S. Lilliu (b), J.E. Macdonald (c), S.W. Prescott (a), O. Bikondoa (d, e), C.F.J. Faul (a) and W.H. Briscoe (a), *Soft Matter* **9**, 10501-10511 (2013).
(a) School of Chemistry, University of Bristol (UK)
(b) Nano-Optics and Optoelectronics Research Laboratory, Masdar Institute of Science and Technology, Abu Dhabi (UAE)
(c) School of Physics and Astronomy, Cardiff University (UK)
(d) XMaS, The UK-CRG Beamline at the ESRF (France)
(e) Department of Physics, University of Warwick (UK)

Conducting organic materials have promising potential applications in low-cost, solution-processable, flexible electronic devices such as photovoltaics and field-effect transistors. The efficiency of such devices is intimately related to the arrangement of the constituent molecules. The active layer of conducting polymer is typically required to be a few hundred nanometres thick. Within this "thin film" regime, the self-assembly behaviour can differ significantly from the bulk material due to additional interactions at the substrate-film and air-film interfaces. It is therefore of great importance to characterise and control the self-assembly of such molecules when confined to thin films.

Our strategy for preparing well-ordered thin films is two fold. First, we use short

oligomers of the conducting polymer poly(aniline) (PANI). Oligomers have the advantage of being more soluble (and thus processable) than PANI. Additionally, the oligomers can be prepared in high purity, overcoming the structural defects inherent in PANI [1]. Secondly, when combined with acid surfactants, oligo(aniline)s self-assemble into well-defined structures stabilised by secondary intermolecular interactions [2]. In this work, we have studied how oligo(aniline)-surfactant complexes self-assemble when confined to films of approximately 350 nm thick. The structure of these films has been examined at beamline **BM28**, using grazing-incidence X-ray scattering (GIXS) (**Figure 80b**). This technique allows us to elucidate the packing and orientation of molecules in extremely thin films.

Two oligomers were studied, TANI (four monomers) and OANI (eight monomers) (**Figure 80a**). Films of these oligomers and their complexes with the surfactant BEHP (bis(ethyl hexyl)phosphate) were prepared using a simple drop-casting method onto silicon substrates. In addition to studying the as-cast films, the structural response of the oligomer-surfactant films to thermal annealing was monitored *in situ*.

Films of the pure oligomers were completely disordered. When treated with BEHP, however, clear diffraction features were observed in the GIXS patterns, indicating the presence of well-ordered self-assembled structures in the thin film (**Figure 81a** and **d**). The GIXS pattern for TANI(BEHP)$_{0.5}$ (TANI:BEHP molar ratio 1:2) presented spot-like diffraction features, indicating the formation of a highly ordered structure, with a high degree of orientation relative to the underlying substrate. The large number of reflections observed allowed us to determine that the molecules adopted a large unit cell, which was hexagonal in two dimensions (lattice parameters $a = b = 2.53$ nm, $c = 2.91$ nm, $\gamma = 120°$). It was assumed that the molecules adopted a bilayer arrangement in which bilayers of TANI molecules were separated by interdigitated alkyl tails from the BEHP molecules as depicted in **Figure 81b**. The high degree of preferential molecular orientation

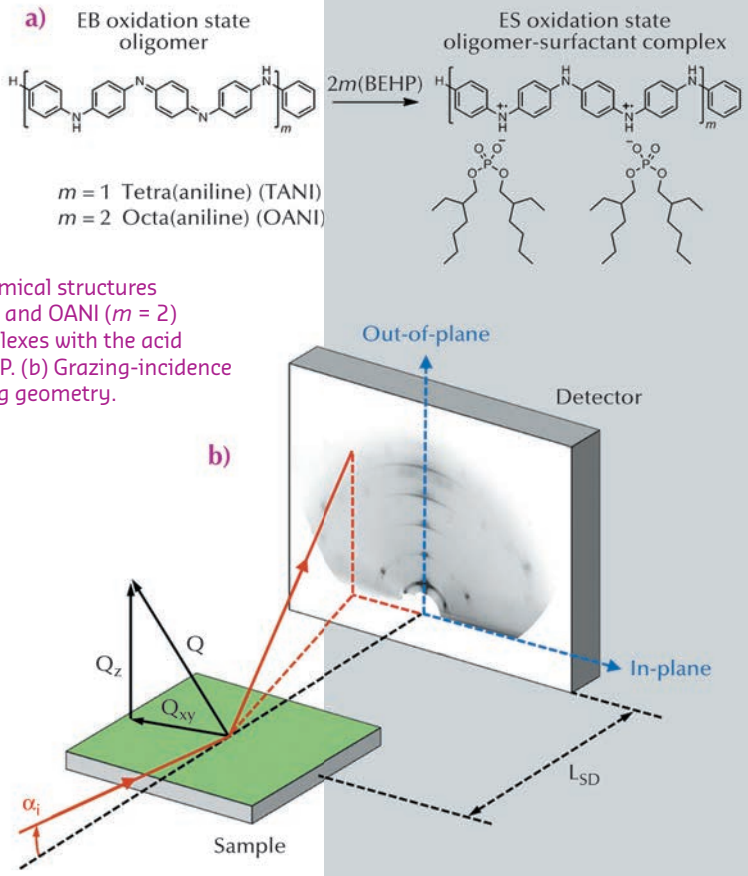

Fig. 80: (a) chemical structures of TANI (m = 1) and OANI (m = 2) and their complexes with the acid surfactant BEHP. (b) Grazing-incidence X-ray scattering geometry.

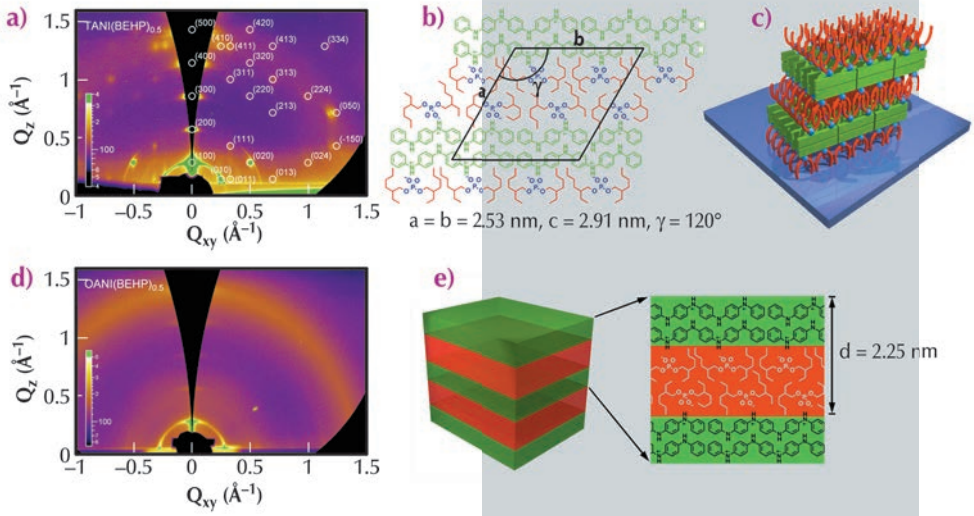

Fig. 81: GIXS pattern (a), 2D lattice structure (b) and 3D surface orientation (c) for TANI(BEHP)$_{0.5}$ thin film; GIXS pattern (d) and lamellar structure (e) for OANI(BEHP)$_{0.5}$ thin film.

(**Figure 81c**) indicates that this system is likely to offer efficient charge-transport properties.

In the case of OANI(BEHP)$_{0.5}$, the diffraction features in the GIXS patterns were broad rings rather than the spots seen for TANI(BEHP)$_{0.5}$ (**Figure 81d**). This observation indicates that the ordered domains were randomly oriented on the surface. Furthermore, OANI(BEHP)$_{0.5}$ adopted a simple lamellar structure, showing only one-dimensional order in contrast to the 3D order present for the TANI(BEHP)$_{0.5}$ system as shown

pictorially in Figure 81e. The difference in behaviour between these two systems arises from their differing molecular architectures. By doubling the chain length, the OANI oligomer has more degrees of freedom for rotation about phenyl-amine-phenyl bonds than TANI, which provides a greater entropic barrier to the formation of ordered thin films.

Thermal annealing of the two films revealed further differences in their behaviour. At approximately 90°C the TANI(BEHP)$_{0.5}$ film underwent an order–disorder transition. Upon cooling, the hexagonal structure reformed, however, the crystalline domains had an even greater preferential alignment relative to the silicon substrate. In the case of OANI(BEHP)$_{0.5}$, the thermal energy was not great enough to induce any significant structural changes.

The detailed structural information of both films reveals, for the first time, how such oligomer-surfactant complexes self-assemble when confined to thin films at surfaces. The BEHP surfactant was pivotal in inducing structure formation and the resulting structures differed from those previously seen for the bulk phase materials. The exact morphology of the oligo(aniline) films could be altered through variation of the oligomer molecular architecture and thermal annealing. These results will guide the selection and processing of materials for future device fabrication.

References
[1] Z.X. Wei and C.F.J. Faul, *Macromol. Rapid Commun.* **29**, 280-292 (2008).
[2] T.G. Dane, P.T. Cresswell, O. Bikondoa, G.E. Newby, T. Arnold, C.F.J. Faul and W.H. Briscoe, *Soft Matter* **8**, 2824-2832 (2012).

THE DYNAMICS OF NANOROD SELF-ASSEMBLY AT THE LIQUID/AIR INTERFACE STUDIED WITH GISAXS

Principal publication and authors
F. Pietra (a), F.T. Rabouw (a), W.H. Evers (a,b), D.V. Byelov (c), A.V. Petukhov (c), C. de Mello Donegá (a) and D. Vanmaekelbergh (a), *Nano Letters* **12**, 5515–5523 (2012).
(a) Condensed Matter and Interfaces group, Utrecht University (The Netherlands)
(b) Present address: Department of Chemical Engineering, Delft University of Technology (The Netherlands)
(c) Physical and Colloid Chemistry group, Utrecht University (The Netherlands)

The ability to manipulate the chemical and physical properties of colloidal nanocrystals at the atomic level, together with the ability to assemble them into ordered 2D membranes and 3D solids is currently one of the most fascinating and challenging directions of nanoscience [1]. In particular, direct formation of nanocrystal membranes at the liquid-air interface is emerging as a promising method to fabricate functional ultra-thin films [2]. Previous research has mainly focused on characterisation of the final structures formed after self-assembly of the nanocrystal building blocks. However, in order to achieve a high degree of control over the ordering of the final superstructure, it is pivotal to understand the dynamics and mechanism of the self-assembly process.

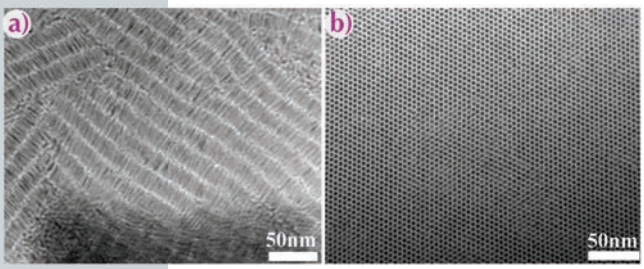

Fig. 82: Bright-field TEM images of the final self-assembled structures for the case of: (a) short NRs and (b) long NRs.

Using grazing-incidence small-angle X-ray scattering (GISAXS) we have studied dynamics of self-assembly of CdS/CdSe core/shell nanorods (NRs). These NRs have promising optical and electronic properties, as well as high (photo)chemical stability. Self-assembly by controlled solvent evaporation is known to result in membranes in which the NRs have both positional and orientation order over micrometres. Such membranes have potential applications as active layers in lasers, LEDs and solar cells.

We used NRs with diameters of 4 nm and lengths from 15 to 50 nm. In a first set of experiments, we used ex situ transmission electron microscopy (TEM) on the finished self-assembled structures to show that the final orientation of the NRs can be tuned by changing the NR length and/or the initial NR concentration in the dispersion. More specifically, short NRs (< 20 nm) or a low concentration of the initial NR dispersion results in self-assembled structures with the NRs lying flat at the liquid/air interface (Figure 82a). In contrast,

longer NRs (> 20 nm) or high initial NR concentrations yield structures with the NRs standing up (**Figure 82b**).

To investigate the dynamics of NR self-assembly and understand the tunability of the final NR orientation, we have performed *in situ* GISAXS experiments at beamline **ID10**. During evaporation of the NR dispersion, an X-ray beam at grazing incidence probes the toluene/air interface at which the NRs self-assemble. We developed an experimental cell with the NR dispersion in toluene on top of an immiscible liquid layer of diethylene glycol (DEG). This allowed us to keep the toluene/air at constant height with respect to the X-ray beam while the NR dispersion evaporated, by continuously injecting additional DEG into the cell. In this way, we achieved a time resolution of a minute, sufficient to follow the complete process of self-assembly, which takes roughly 30 minutes.

Our study shows first of all that NR self-assembly occurs at the liquid/air interface. Long NRs form ordered structures within minutes that later orient at the liquid/air interface, giving rise to in-plane scattering at *q*-values relating as 1:√3:2, which is characteristic of 2D hexagonal ordering of NRs standing upright. Short NRs do not show order until after 20 minutes. The final structure shows out-of-plane scattering characteristic of a hexagonal ordering of NRs lying down. Our most striking finding is for NRs of medium length, where we monitored the transition from an intermediate state (**Figure 83a**), in which the NRs are hexagonally ordered lying down at the liquid/air interface (**Figure 83c**), to the final superstructure (**Figure 83b**) which consists of hexagonally ordered upstanding NRs (**Figure 83d**).

Based on the real-time GISAXS data, we developed a model of hierarchical self-organisation that accounts for the dependence of the geometry of the final superstructure on the NR length and the initial NR concentration. According to our model, NRs form ordered bundles already in the bulk dispersion due to mutual van der Waals (vdW) interactions. These bundles are adsorbed at the interface, where they pack together to form a uniform membrane. The orientation of NRs in the final structure depends on the way in which the bundles are adsorbed at the interface, which in turn depends on their size in the bulk dispersion. More precisely, the size of NR bundles increases if the bulk NR concentration increases, or if the NRs are longer, which results in stronger mutual vdW interactions. Our results provide insights into the mechanism of the NR self-assembly at the liquid/air interface, thus paving the way for the exploration of promising applications and sophisticated strategies for the development of functional materials.

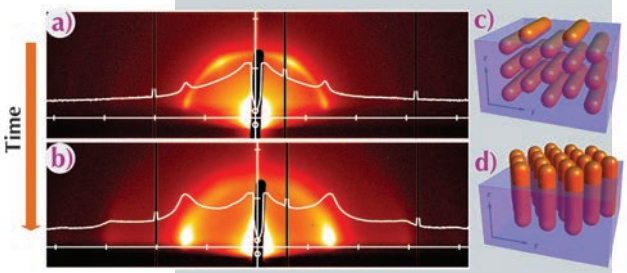

Fig. 83: GISAXS patterns of superstructures of medium-length NRs at different times of solvent evaporation: (a) 12 min and (b) 16 min. (c, d) Schematics of the NRs structures (c) at the intermediate stage, and (d) at the end of the self-assembly process.

References
[1] D. Vanmaekelbergh, *Nano Today*, **6**, 419-437 (2011).
[2] A. Dong, J. Chen, P.M. Vora, J.M. Kikkawa and C.B. Murray, *Nature*, **466**, 474-477 (2010).

DIRECTION-DEPENDENT DIFFUSION OF SPINDLE-SHAPED HEMATITE PARTICLES BY MEANS OF X-RAY PHOTON CORRELATION SPECTROSCOPY

Colloidal particles consisting of hematite α-Fe_2O_3 align with their long axis perpendicular to an external magnetic field even at moderate flux densities of several millitesla. This is due to a negative anisotropy of their magnetic susceptibility. Monodisperse, spindle-shaped hematite particles can be prepared with a tunable aspect ratio $\nu = L/D$ defined by the length L and

Principal publication and authors
J. Wagner (a), C. Märkert (a), B. Fischer (b) and L. Müller (b), *PRL* **110**, 048301 (2013).
(a) Institut für Chemie, Universität Rostock (Germany)
(b) DESY, Hamburg (Germany)

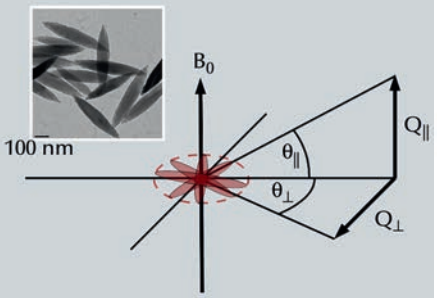

Fig. 84: Transmission electron micrograph of spindle-shaped particles and schematic view of the scattering geometry of an ensemble of spindles aligned perpendicular to an external magnetic field $\mathbf{B}_0$. For scattering vectors parallel to $\mathbf{B}_0$, only diffusive motions perpendicular to the particle axis are probed. For scattering vectors perpendicular to $\mathbf{B}_0$, all angles $0 < \phi < 2\pi$ between the long particle axis and **Q** are realised. In this direction the average diffusion coefficient $\langle D \rangle_\phi = (D_{//} + D_\perp)/2$ is probed.

equatorial diameter D of the particles (**Figure 84**). Dark-field electron micrographs show that they are single-domain particles.

Dynamic scattering experiments probe the projection of motions in the direction of the scattering vector **Q**. Choosing the direction of the scattering vector **Q** parallel and perpendicular to an external magnetic field **B**, the diffusive motion of an ensemble of aligned particles can be studied in dependence on the direction of **Q** with respect to the external field. Due to the negative magnetic anisotropy of hematite, the spindles align with their long axis perpendicular to the external field, not like a compass needle. At a flux density of B = 120 mT, the particles are completely aligned perpendicular to the field direction [1]. The spindles, however, can still rotate freely around their short axis forming an ensemble of particles with an orientational distribution function (ODF) $f(\theta) = \delta(\theta - \pi/2) / (2\pi)$. Choosing Q parallel to the field, only diffusive motions perpendicular to the particle axis are probed in the direction of the scattering vector. In this direction, the diffusion coefficient $D_\perp$ is directly accessible. Since the ODF does not depend on the polar coordinate ϕ for $\mathbf{Q} \perp \mathbf{B}$, both diffusive motions in the direction of and perpendicular to the direction of the particle axis are observed. In this configuration, according to Fokker-Planck equation, the average diffusion coefficient $\langle D \rangle_\phi = (D_{//} + D_\perp)/2$ is probed.

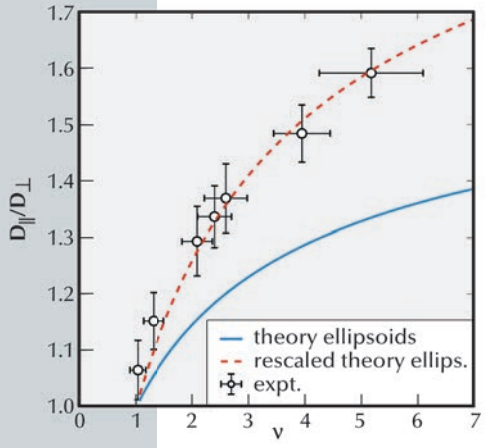

Fig. 85: Ratio of diffusion coefficients $D_{//} / D_\perp$ for spindle-shaped particles in dependence on the aspect ratio ν. The solid line represents the prediction for prolate ellipsoids [2]. The experimental data can heuristically be described via a rescaled Perrin approach.

For the experiments, highly diluted suspensions of hematite particles in water were used. The water contained 10^{-3} molL^{-1} potassium chloride to screen electrostatic interactions originating from surface charges. The samples were sealed in quartz capillaries. All experiments were carried out at beamine **ID10** at room temperature with an incident energy of 8 keV and a beam size of 10 × 10 μm^2. The scattered intensity was detected using an avalanche diode with an aperture of 50 × 50 μm^2 at a distance of 2.20 m from the sample. The intensity autocorrelation function of both the scattered intensity and the monitor signal, was obtained by employing a digital FLEX correlator. At a volume fraction Φ =10^3 with $S(Q) \equiv 1$ no translational correlations between the particles were observed. Under these conditions the particles diffusive freely.

For particles with aspect ratios $1 < \nu < 5$, the diffusion coefficients $D_\perp$ and $\langle D \rangle_\phi = (D_{//} + D_\perp)/2$ were determined from the first cumulants of correlation functions $g_2(\mathbf{Q}_{||\mathbf{B}}, t)$ and $g_2(\mathbf{Q}_{\perp\mathbf{Q}}, t)$. With these two quantities, the diffusion tensor of the axial-symmetric hematite particles was determined.

The ratio $D_{//} / D_\perp$ which depends on the aspect ratio is compared to the theoretical prediction for prolate ellipsoids of revolution derived by Perrin [2]. Spindles differ from ellipsoids by apices forming singularities in the surface curvature of the mesoscale particles. For hematite spindles the ratio $D_{//} / D_\perp$ increases significantly faster with the aspect ratio than predicted for ellipsoids and can heuristically be described via the rescaled Perrin ratio for ellipsoids (**Figure 85**).

These experiments demonstrate the capability of XPCS to probe slow dynamic processes in soft matter that depend on the direction. Since aligned soft matter structures play a key role in many technical applications, *e.g.* liquid crystals in displays or magnetic nanoparticles in ferrofluids, XPCS can help to monitor dynamic processes in such systems on mesoscopic scales of space and time. Hereby, XPCS can provide new insights that will help to optimise technical applications of soft matter.

References

[1] C. Märkert, B. Fischer and J. Wagner, *J. Appl. Cryst.* **44**, 441-447 (2011).

[2] F. Perrin, *J. Phys. Radium* **5**, 497-511 (1934).

THE INFLUENCE OF OSTEOCYTES ON BONE MATERIAL

Principal publication and authors
M. Kerschnitzki (a), P. Kollmannsberger (a, b), M. Burghammer (c), G.N. Duda (d), R. Weinkamer (a), W. Wagermaier (a) and P. Fratzl (a), *J Bone Miner Res* **8**, 1837 - 1845 (2013).
(a) Max Planck Institute of Colloids and Interfaces, Potsdam (Germany)
(b) ETH Zurich (Switzerland)
(c) ESRF
(d) Charité, Berlin (Germany)

Bone is a unique biological material made of inorganic hydroxyapatite particles that are embedded in an organic matrix of collagen [1, 2]. Bone is constantly being remodelled by bone cells, namely osteoblasts and osteoclasts. Osteocytes, another type of bone cells, are thought to be involved in mechanosensing, that is, they respond to external mechanical stimuli and thereby control bone remodelling. It is also suspected that they have a direct impact on the mineral homeostasis, by depositing and resorbing some of the bone mineral. Osteocytes form a spatial network of lacunae (voids in which the cells reside) and canaliculi (interconnecting the lacunae) throughout the bone. The total surface of this network in adult humans is enormous and, thus, it is conceivable that osteocytes interact with their surrounding material. In this case, bone material adjacent to osteocytes and their cell processes should show traces of osteocytic action and thus express different mineral properties.

In this study, we first visualised the osteocyte network topologically in different bone sections by confocal laser scanning microscopy. These three-dimensional datasets were quantified by computational methods to characterise density and organisation of lacunae and canaliculi. In the same sample regions, scanning small-angle X-ray scattering (SAXS) was performed at beamline **ID13** with an effective beam size of 1 µm. This high resolution was needed to resolve potential inhomogeneities of bone material in relation to the osteocyte network architecture. We analysed mineral particle size and arrangement in the immediate vicinity of the osteocyte cell network and compared it with the corresponding properties further away from the cell network. The measurements were performed on fibrolamellar ovine bone sections. Due to the high scanning resolution, measured areas with sizes in the order of 200 × 150 µm consisted of several thousand data points.

The high resolution maps of mineral particle orientation and thickness reveal a strong correlation with structural features of the osteocyte network (**Figure 86**). Our results show a distinct structural organisation of bone material in the direct vicinity of the osteocytes compared with areas further away from the cells. The osteocyte cell network in the studied bone sections features areas of dense (mineral near cells) and loose (mineral far from cells) network organisation (**Figure 86a**). The values for bone mineral particle thickness in these areas are in the range of about 2.3 nm to 3 nm. We find gradients around osteocyte lacunae with thinner particles in the immediate vicinity of osteocytes (**Figure 86b** and **86c**). However, the average mineral particle thickness in areas with loose cell network organisation is in the range of 2.3 nm, which is thinner when compared with mineral particles present in areas with densely organised

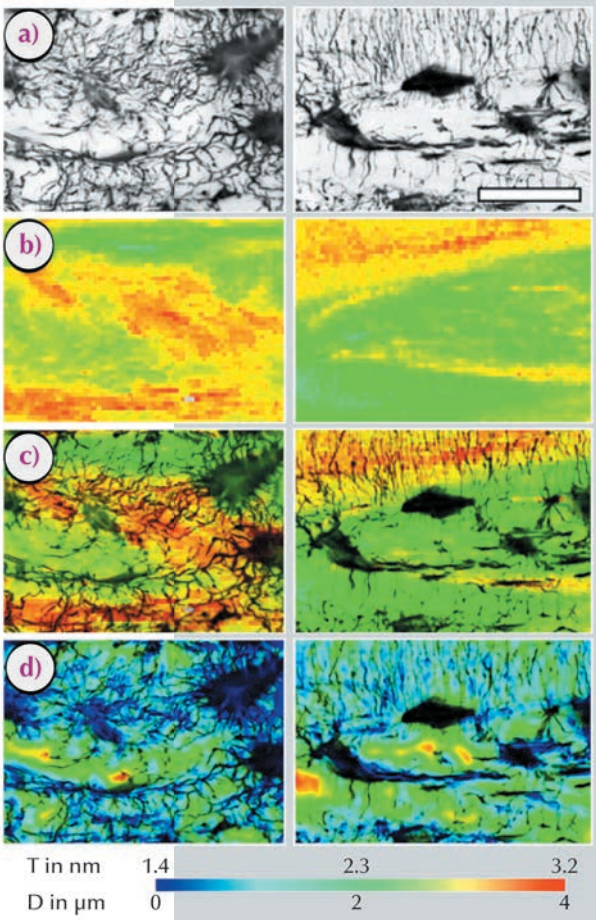

Fig. 86: Osteocyte network organisation and mineral particle thickness (parameter T) in fibrolamellar ovine bone: (a) CLSM image showing areas of dense and loose osteocyte network organisation, (b) parameter T, (c) T merged with CLSM, (d) calculated mineral – cell distance (D) merged with CLSM. Mineral particle thickness is elevated in areas of shorter mineral – cell distances (densely organised osteocyte cell network). Scale bar 20 µm.

osteocytes (around 3 nm). This relation becomes even more apparent after plotting the distance between mineral and the nearest cell which can be calculated from the microscopy (CLSM) images (**Figure 86d**). Here a strong correlation between large T-parameters and short mineral – cell distances is found.

Such unorganised bone material featuring rather loose osteocyte cell network organisation is usually found in so-called woven bone which is known to be primarily deposited during osteogenesis [3]. Even though this bone type is highly mineralised [1, 3], we find that the average mineral particle thickness is substantially lower than highly organised bone deposited during later stages of bone development. This may denote that, during rapid processes of initial mineralisation in woven bone, more mineral crystals are nucleating simultaneously to reach higher degrees of mineralisation in shorter periods of time. Consequently, due to spatial constraints, higher packing of particles leads to smaller final mineral particle dimension.

In conclusion, our scanning SAXS measurements on bone show interesting local inhomogeneities of submicrometre material properties that correlate with the architecture of the osteocyte network. It is notable that the majority of the mineral is located within less than one micrometre from the cellular network and that mineral particle properties depend on the local density of the cellular network and on the distance from cells and blood vessels. The results of this work improve the understanding of the active role of osteocytes during dynamic processes of bone formation and remodelling and support the hypothesis that osteocytes directly contribute to bone mineral homeostasis.

References

[1] S. Weiner and H.D. Wagner, *Ann Rev Mater Sci* **28**, 271-298 (1998).
[2] P. Fratzl, H.S. Gupta, E.P. Paschalis and P. Roschger, *J Mater Chem* **14**, 2115 - 2123 (2004).
[3] M. Kerschnitzki, W. Wagermaier, P. Roschger, J. Seto, R. Shahar, G.N. Duda, S. Mundlos and P. Fratzl, *J Struct Biol* **173**, 303 - 311 (2011).

A VIRAL PROTEIN NANOCAGE ASSEMBLY PROBED *in vitro*

Principal publication and authors

G. Tresset (a), C. Le Cœur (b), J.-F. Bryche (a), M. Tatou (a), M. Zeghal (a), A. Charpilienne (c), D. Poncet (c), D. Constantin (a) and S. Bressanelli (c), *J. Am. Chem. Soc.* **135**, 15373-15381 (2013).

(a) Laboratoire de Physique des Solides, Université Paris-Sud, CNRS (France)
(b) Institut de Chimie et des Matériaux Paris-Est, Université Paris-Est, CNRS (France)
(c) Laboratoire de Virologie Moléculaire et Structurale, CNRS, INRA (France)

Noroviruses are the first cause of non-bacterial gastroenteritis in humans, as well as in animals, causing about 250 million cases of gastrointestinal distress and over 200,000 deaths each year. They are made up of a protein nanocage called the capsid (~20-40 nm in diameter), enclosing the genetic material, or genome, in the form of RNA. For noroviruses and many other viruses, the capsid consists of 180 copies of a single structural protein arrayed in an icosahedron, *i.e.* a solid with 20 triangular faces and 12 vertices. Remarkably, the norovirus capsid proteins can self-assemble reversibly *in vitro*, without the assistance of the genome or any cellular components, solely by the interplay of solution pH and ionic strength [1]. The molecular mechanisms of such efficient and precise capsid protein self-assembly still remain unknown to date and the nature of the intermediate species is much debated.

The self-assembly kinetics of capsid proteins is a multiscale process that requires heterogeneous molecular species with nanometre sizes to be probed over a time scale ranging from milliseconds to hours. The classical techniques used to probe self-assembly kinetics such as time-course light scattering provide temporal traces from which characteristic time scales can be inferred, but no structural information can be extracted. In contrast, time-resolved small-angle X-ray scattering (TR-SAXS) permits a determination of the shape and the organisation of particles with a spatial scale in the range of a few angstroms to thousands of angstroms, and with time resolution below 100 ms [2].

We have thereby investigated the self-assembly of capsid proteins derived from a norovirus, by exploiting the exceptional quality and time resolution of beamline **ID02**. Via a stopped-flow

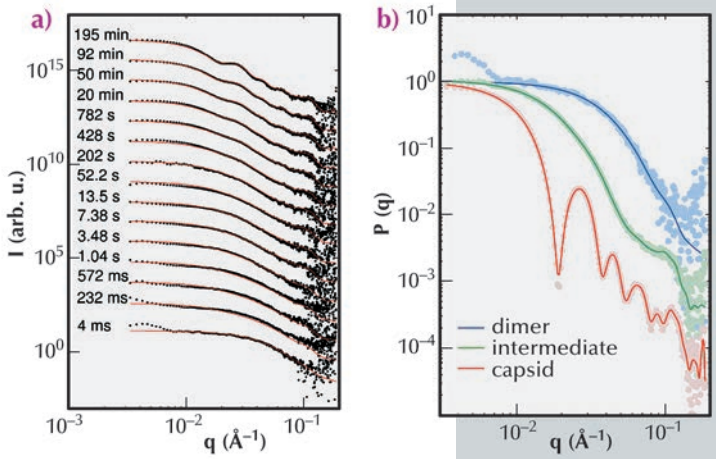

Fig. 87: (a) TR-SAXS patterns of self-assembling norovirus capsid proteins collected from 4 ms to 11,721 s. Black dots are the experimental data and solid lines are reconstructed patterns from a kinetic model. (b) Form factors *P(q)* of the three main species in solution. (c) Mass fractions of the three main species as a function of time estimated by a kinetic model. The vertical dashed line marks the end of the experimental data.

device, protein dimers were rapidly mixed with a buffer solution triggering the self-assembly and injected into a scattering cell. **Figure 87a** shows TR-SAXS patterns collected during the capsid formation. We devised a kinetic model with three main species – dimers, intermediates and capsids – exchanging matter at reaction rates that were determined by fitting the experimental data.

An original global fitting procedure applied to the experimental data allowed us to extract the form factor of the intermediate species (**Figure 87b**) as well as to estimate the mass fraction of each species over time (**Figure 87c**). The three-dimensional structure, at nanometre resolution, of the intermediate species was then obtained by *ab initio* shape determination from its extracted form factor.

The analyses thus revealed that in the first step, some ten dimers combine to form a stave-shaped intermediate, possibly made of two pentamers of dimers connected by an interstitial dimer (**Figure 88**). In the subsequent, slower step, which takes hours, these intermediates interlock into a capsid. In contrast, capsids form by sequential addition of dimers in many other viruses such as the hepatitis B virus.

By clarifying the kinetics involved in norovirus assembly, this study provides a better understanding of the physical processes at work in the self-assembly of a viral capsid. It could also advance efforts to treat or prevent these infections, and it could be applied to engineer viral nanoparticles to make diagnostic agents and tailored therapeutics.

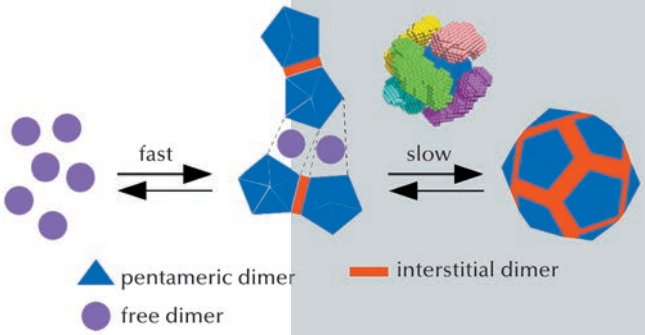

Fig. 88: Kinetic scheme of norovirus capsid assembly. Free dimers are represented in magenta, dimers related by five fold symmetry in the final capsid in blue, and interstitial dimers in red. Above the last assembly step, a representation of interlocking intermediates is given as a possible mechanism. Six intermediates, each in a different colour, have been positioned above the six contiguous fragments made of two pentamers of dimers connected by an interstitial dimer.

References
[1] G. Tresset, V. Decouche, J.-F. Bryche, A. Charpilienne, C. Le Cœur, C. Barbier, G. Squires, M. Zeghal, D. Poncet and S. Bressanelli, *Arch. Biochem. Biophys.* **537**, 144-152 (2013).
[2] I. Grillo, *Curr. Opin. Colloid Interface Sci.* **14**, 402-408 (2009).

FILMING THE BIRTH OF MOLECULES AND SOLVENT REARRANGEMENT

Principal publication and authors
J.H. Lee (a), M. Wulff (b), S. Bratos (c), J. Petersen (d), L. Guerin (b), J.-C. Leicknam (c), M. Cammarata (b), Q. Kong (b), J. Kim (a), K.B. Møller (d) and H. Ihee, (a), *J. Am. Chem. Soc.* **135**, 3255-3261 (2013).
(a) Institute for Basic Science, Center for Time-Resolved Diffraction, Department of Chemistry, KAIST (Republic of Korea)
(b) ESRF
(c) Laboratoire de Physique Théorique de la Matière Condensée, Université Pierre et Marie Curie (France)
(d) Centre for Molecular Movies, Department of Chemistry, Technical University of Denmark (Denmark)

Solvent plays an important role in solution-phase chemical reactions by serving as an energy source to activate the reaction as well as a heat bath to stabilise the products. As a result, the properties of the solvent significantly affect the energy landscape, rates, and pathways of a reaction in solution. The interplay of solute and solvent molecules and its effect on the outcome of chemical reactions has been a topic of intense research in the field of reaction dynamics over several decades, and the kinetic and spectral signatures of the solvation process have been elucidated on femto- to picosecond time scales [1, 2]. It is still challenging experimentally to probe the bonds that are formed during a chemical reaction, especially the changes between solute and solvent accompanying the structural change of reacting solute molecules.

Geminate recombination of iodine atoms (Figure 89a) to form molecular I_2 in solution after photodissociation is a good example of a prototype solution-phase reaction and has been investigated by spectroscopic studies and quantum chemistry [3]. However, the change in the molecular structure (*i.e.* bond length change) and the response of the surrounding solvent cage have never been directly observed. Time-resolved X-ray liquidography (solution scattering) is well suited for monitoring this solution-phase reaction because it directly probes the atom-atom distance distribution as a function of time. By using the time-slicing scheme where data are collected at earlier time delays and with finer time increments (down to 10 ps) than the X-ray pulse width (~100 ps) (Figure 89b) and the deconvolution data processing, we can extract the dynamics that occur faster than the X-ray pulse width and monitor the evolution of both the atom-atom distance distribution of iodine atoms in solvent and the solute-solvent distance distribution at the early stages of I-I bond formation within the solvation shell.

In this study, we measured the dynamics of geminate recombination and vibrational relaxation of I_2 in two different solvents, CCl_4 and cyclohexane, in real time using picosecond X-ray liquidography at beamline **ID09TR**. The birth and vibrational relaxation of I_2 molecules and the associated rearrangement of solvent molecules are mapped out in the form of temporally varying interatomic distance distribution. The atom-atom distance distribution clearly shows the time-dependent progression of the I-I distance (Figure 90a,b). The relaxation of elongated iodine distribution is followed by bi-exponentials, which is well in agreement with previous spectroscopic observations [4] and our molecular

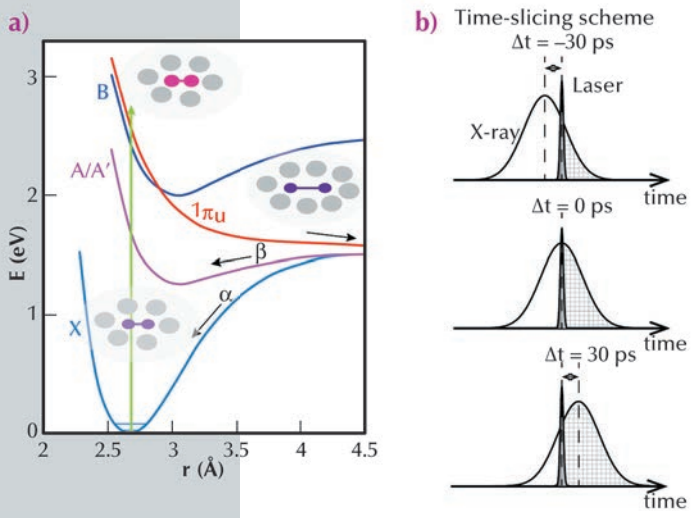

Fig. 89: a) Potential energy surface of I_2 in CCl_4. The processes α and β represent the geminate recombination of two I atoms in the X and A/A' states, respectively. The process γ represents nongeminate recombination through the solvent. b) Schematic of the time-slicing experiment. At a negative time delay (for example –30 ps), the X-ray pulse arrives (effectively) earlier than the laser pulse, but the X-ray pulse, which is much longer in time than the laser pulse, is still present after the interaction with the laser pulse and thus scattered off the laser-illuminated sample. At time zero, half of the X-ray pulse probes the laser-illuminated sample.

dynamics (MD) simulation. Also iodine atoms can be separated by larger distances in cyclohexane than in CCl_4 and the vibrational relaxation of a newly born "hot" I_2 molecule occurs faster in CCl_4 than in cyclohexane. In addition to the structural progression of the solute molecule, the concomitant swelling and shrinking of the solute-solvent cage were also clearly observed. The atom-atom distribution change that appeared above 5 Å is well reproduced by the MD simulation, which indicates the solvation dynamics of newly formed iodine molecules in the course of a vibrational cooling process (**Figure 90c,d**).

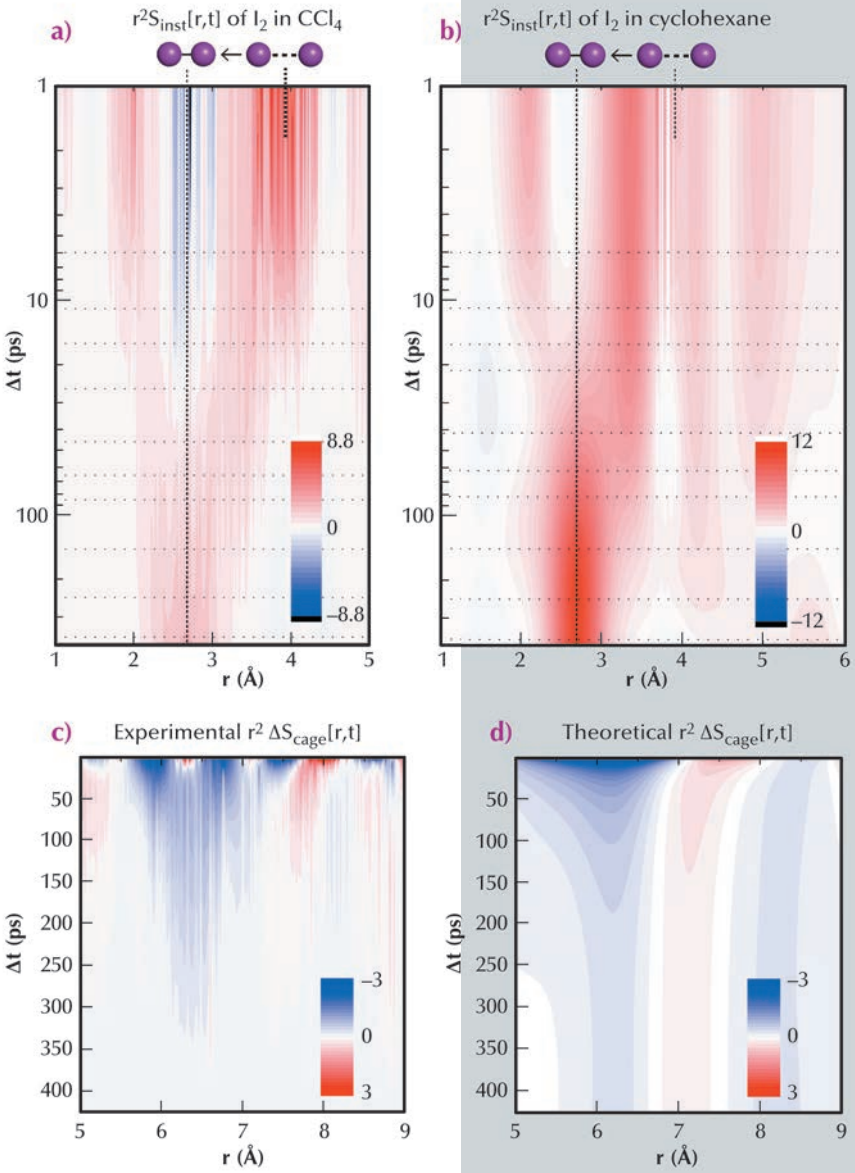

Fig. 90: a) Time-dependent I-I distance distribution functions ($r^2S_{inst}[r,t]$) corresponding to I_2 in CCl_4. b) The $r^2S_{inst}[r,t]$ of I_2 in cyclohexane. c) The experimental $r^2\Delta S_{inst}[r,t]$ curves at large r values: time-dependent solute-solvent distance distribution functions. d) Theoretical $r^2\Delta S_{inst}[r,t]$ based on the experimental data from (a) and MD simulation.

References

[1] R. Jimenez, G.R. Fleming, P.V. Kumar and M. Maroncelli, *Nature*, **369**, 471–473 (1994).

[2] W.P. de Boeij, M.S. Pshenichnikov and D.A. Wiersma, *Annu. Rev. Phys. Chem.* **49**, 99–123 (1998).

[3] A.L. Harris, J.K. Brown and C.B. Harris, *Annu. Rev. Phys. Chem.* **39**, 341–366 (1988).

[4] D.M. Jonas, S.E. Bradforth, S.A. Passino and G.R.J. Fleming, *Phys. Chem.* **99**, 2594–2608 (1995).

ELECTRONIC STRUCTURE AND MAGNETISM

The year 2013 has brought many changes to the Electronic Structure and Magnetism Group. After nearly 12 years as Group Head, Nick Brookes has stepped down as from the 1st October. As former Deputy and on behalf of the whole group, I would like to thank Nick for his outstanding guidance and commitment. It will be a big challenge for me to take over from him.

The structure of the Group has also been slightly modified. The high brilliance X-ray spectroscopy beamline ID26 has joined our group this year. ID26 offers a combination of XAS, XES and RIXS spectroscopy methods, covering many different areas such as mineralogy/geology, catalysis, materials science, magnetism, biology and cultural heritage. ID26 complements other beamlines in the group, extending the ID08 RIXS activity towards the hard X-rays, and the BM23 XAS activity towards higher dilution and higher energy resolution. Moreover, XES and RIXS at ID26 combined with time resolved XAS on ID24 and BM23 provide an ideal platform for *in situ* and operando studies of catalysts. These three beamlines not only share labs and equipment, but also a number of common user groups.

This year also marks an important benchmark for beamline ID12, which was successfully reviewed in November. High pressure XAS and XMCD studies at very low energies appear as one of the most exciting new emerging areas of application for ID12, complementing the extreme conditions activities on ID24 and BM23. And not surprisingly, the year 2013 has seen the start of collaboration between beamline staff in the area of high pressure research.

Clearly, all these happenings during the year 2013 have increased the synergy between the different beamlines in the Group.

Another major event this year was the closure of ID08, scheduled within the ESRF Upgrade Programme, to be replaced by the Upgrade beamline project UPBL7, which is being built at ID32. After nearly 19 years of operation (summing the lifetime at ports ID12B and ID08) this beamline was closed in October and immediately dismantled. The major components of UPBL7 have all been delivered. As the year comes to an end, in the new experimental hall facing the Belledonne chain, the 10 m RIXS spectrometer has just been moved successfully for the first time on air pads. Most of the components of the optics hutch have been mounted and aligned and are ready for vacuum conditioning in January, when the last mirrors will take their place. If all goes as planned, ID32 will take first beam in February, and full user operation is foreseen for the end of 2014. At that point, with both UPBL11 and UPBL7 in operation, Upgrade Phase I will be over for the ESM Group. But, we are already actively involved in the definition of the science case for Phase II and in particular for two out of the five selected themes: "nano and man-made materials" and "extreme conditions".

During this year of transition from Phase I to Phase II, producing scientific results has remained our core activity and has continued at full speed. In the pages that follow, we have included our choice of some of the most exciting topics of research from the beamlines in 2013. A large variety of different scientific fields are covered: from bacteria and catalysts (articles 1-3), to bulk metallic glasses, luminescent materials, superconductors and ferrimagnets (articles 4-7). Studies of two dimensional systems for novel materials with high potential for future devices and characterised by complex interplay between charge, orbital and spin degrees of freedom continue to represent a large portion of the activity of the Group (articles 8-11). The last article of our chapter, from the XMaS CRG beamline, also falls into this category. Here X-ray magnetic scattering was employed in the discovery of a simple mechanism for controlling magnetic order in magnetoelectrics.

S. PASCARELLI

Principal publication and authors
J. Baumgartner (a), G. Morin (b), N. Menguy (b), T. Perez Gonzalez (a), M. Widdrat (a), J. Cosmidis (b) and D. Faivre (a), *PNAS* **110**, 14883-14888 (2013).
(a) Department of Biomaterials, Max Planck Institute of Colloids and Interfaces, Potsdam (Germany)
(b) IMPMC, UPMC, Paris (France)

THE FORMATION OF A BIOLOGICAL COMPASS NEEDLE

A unique feature of living organisms is their evolutionary acquired adaptation to ecological niches. Consequently, all organisms specialise in a very specific set of nutrient sources prevalent in their natural environment and they try to avoid unfavourable conditions such as predators or toxic conditions. When they find themselves in the wrong surrounding they respond, if they can, by migrating.

Migratory behaviour is known for many higher animals such as birds, mammals and fish. Animals use all kinds of sensory information to reach decisions about when and where to migrate. Maybe the most impressive examples are given by migratory birds that can navigate accurately over thousands of kilometres in the search for reliable food sources.

At a very basic level, this ability to 'migrate' upon a sensory input is already ingrained in single cellular organisms and some of the cells in our bodies. These cells are able to sense chemicals through receptors and, upon recognition of a nutrient, can move towards its source, or in the case of a poisonous compound, move away from it. This behaviour is termed chemotaxis.

Aquatic bacteria found in the environment also populate very specific niches and use chemotaxis to find a suitable habitat in their surroundings. One of the most important discriminators in bodies of water is the oxygen concentration. Some species require high oxygen concentrations and are therefore primarily found close to the water's surface, while for others oxygen is toxic and they are found preferentially near the bottom. Some bacteria, called microaerophiles, require intermediate environments with rather low but still sufficient oxygen concentration. These conditions can be met in very narrow layers in the water column that are found at specific distances from the surface where oxygen diffuses into the water.

However, for a bacterium, the task to find its habitat in a three dimensional environment can be fairly challenging. Brownian motion and other disturbances force these organisms on a random walk against which the bacteria have to struggle with great effort. But evolution has helped some of the microaerophiles a little: they found a 'trick' to perform the search more efficiently. These are the magnetotactic bacteria, which have the ability to use the geomagnetic field to assist their navigation towards their favoured habitat zones. Because the field lines in the northern and southern hemispheres are inclined with respect to the Earth's surface, they provide a vector that helps the bacteria to find the direction to the right conditions. This ability is owed to the formation of intracellular organelles called magnetosomes, which are linearly aligned vesicles filled with the magnetically susceptible iron oxide magnetite (**Figure 91**). In an external magnetic field, this intracellular "compass needle" orients the whole cell in the direction of the field vector. The bacteria now only need to swim up or down the field instead of randomly choosing a path.

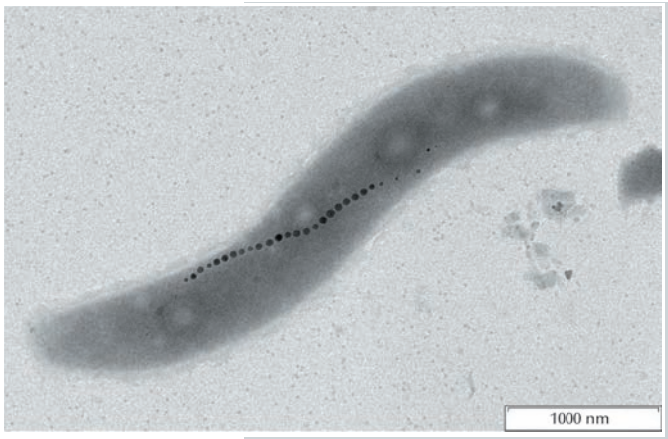

Fig. 91: A magnetotactic bacterium with its intracellular magnetosome organelles, a biological compass needle.

To study the mineral formation that enables this behaviour, we conceived an experiment in which the bacteria were starved of iron to suppress the formation of the particles. The bacteria were then supplied with an iron source to follow the time course of particle formation and to investigate potential intermediates in the process.

The high brilliance of beamline **ID26** allowed us to study the minutest amounts of iron in the bacteria during the earliest mineralisation stages by X-ray absorption spectroscopy (**Figure 92**). We found that the organisms rapidly accumulate iron from their environment and store it intermediately in an amorphous ferric phosphate compound, most likely a bacterial ferritin, a protein for iron storage. We were able to elucidate its chemical structure and to observe the subsequent transformation over time into the iron oxide magnetite. As magnetite is a mixed-valence compound containing both Fe(II) and Fe(III), we could follow the reductive chemical reaction from the ferric precursor by XAS. Further studies by complementary microscopy

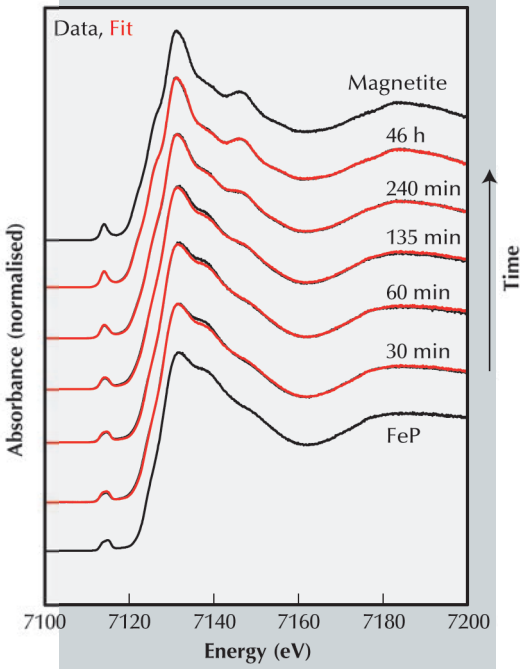

Fig. 92: X-ray absorption spectra from various stages in the mineralisation process.

techniques revealed the distribution of the iron species involved within the organism. This knowledge can now be used to help interpret the roles of various genes suspected to play a part in the formation of the biological compass needle.

Birds and other animals are also able to navigate using the geomagnetic field. Although our knowledge about their sensory systems is still very limited, understanding of the bacterial systems might provide a basis for studies of such organisms as well.

Principal publication and authors
E. Gallo (a), F. Bonino (b), J.C. Swarbrick (a), T. Petrenko (c), A. Piovano (d) S. Bordiga (b), D. Gianolio (e), E. Groppo (b), F. Neese (c), C. Lamberti (b) and P. Glatzel (a), *ChemPhysChem* **14**, 79–83 (2013).
(a) ESRF, Grenoble CEDEX (France)
(b) Department Chemistry, University of Turin (Italy)
(c) Max-Planck Institute for Bioinorganic Chemistry, Mülheim (Germany)
(d) ILL, Grenoble (France)
(e) Diamond Light Source Ltd., Didcot (UK)

PREFERENCE TOWARDS FIVE-COORDINATION IN Ti silicalite-1 UPON MOLECULAR ADSORPTION

Meso- and micro-porous Ti-zeotype materials are often good catalysts for selective oxidation reactions and thus are of interest for the petrochemical industry. One of the most extensively used is titanium silicalite-1 (TS-1) [1,2]. Analysing the Ti K-edge extended X-ray absorption fine structure (EXAFS), it has been established that Ti is preferentially located inside a tetrapodal structure within the silicalite framework. EXAFS has also been used to investigate the catalyst under *in situ* conditions and to understand the mechanism of the catalytic transformations using water and ammonia as probe molecules due to their importance in various catalytic transformations [1,2]. However, the EXAFS data were not conclusive and other techniques such as microcalorimetric measurements have been employed. It was proposed that the Ti coordination number is close to six upon adsorption of water and ammonia [1], *i.e.* two adsorbed molecules on Ti. But these molecules can also adsorb on the zeolite-framework, therefore the number of adsorbed molecules per Ti centre was obtained by subtracting the same signal obtained on a Ti-free silicalite-1. Unfortunately, the reliability of this method is under debate.

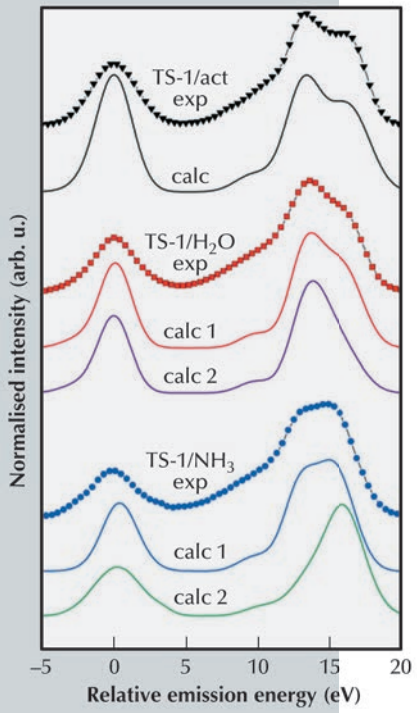

Fig. 93: Experimental (exp) and calculated (calc) vtc-XES spectra of TS-1/act, TS-1/H_2O and TS-1/NH_3. In both cases we calculated two spectra with one (calc 1) and two (calc 2) adsorbed molecules. The vtc-XES spectra are offset along the intensity axis for clarity.

To address this problem we have performed a valence-to-core X-ray emission spectroscopic (vtc-XES) investigation on TS-1 exposed to ammonia (50 torr) and water (vapour pressure) at beamline **ID26**. vtc-XES allows the valence electronic levels just below the Fermi energy to be probed and thus is a valuable tool for studying the chemical bond between metal ion and ligands [3]. We have modelled the experimental spectra using density functional theory (DFT) calculations based on Ti-centred clusters that mimic the environment of Ti in the activated catalyst (TS-1/act), in interaction with water (TS-1/H_2O) and ammonia (TS-1/NH_3) [3]. One or two molecules of water/ammonia can adsorb on the Ti ion and thus we have built clusters with one (calc1) and two (calc2) molecules directly bonded to the metal centre.

Figure 93 shows the vtc-XES of TS-1/act, TS-1/H_2O and TS-1/NH_3 in comparison with the theoretical spectra computed using the ORCA package.

We observe that the theoretical vtc-XES of TS-1/act, TS-1/H_2O (calc1) and TS-1/NH_3 (calc1) present similar relative changes in intensity as the experimental vtc-XES spectra. When one molecule is adsorbed on the Ti centres, the degeneracy of the molecular orbitals (MOs) linked to the main features of the vtc-XES (see **Figures 93** and **94**) is removed and new transitions involving MOs with $O^{water}(2p)$ and $N^{ammonia}(2p)$ atomic character arise in the $K\beta_{2,5}$ region [3]. The calculation reproduces the shift of the feature A (Kβ'' emission lines), which we attribute to the presence of transitions involving MOs with $O^{water}(2s)$ and $N^{ammonia}(2s)$ atomic character.

In summary, we find strong experimental evidence that only one molecule is adsorbed on the Ti centres in TS-1. Knowledge of the number of molecules coordinated to the Ti centres in TS-1 under *in situ* conditions is of paramount importance for understanding the catalytic path of the catalyst and provides crucial input for theoretical estimates of efficiency and kinetics of a reaction. Our conclusion mainly relies on the comparison between experiment and quantum chemical calculations. The recent progress in modelling of XES data using density functional theory makes this a viable approach that allows a detailed understanding of the underlying modifications of the electronic structure.

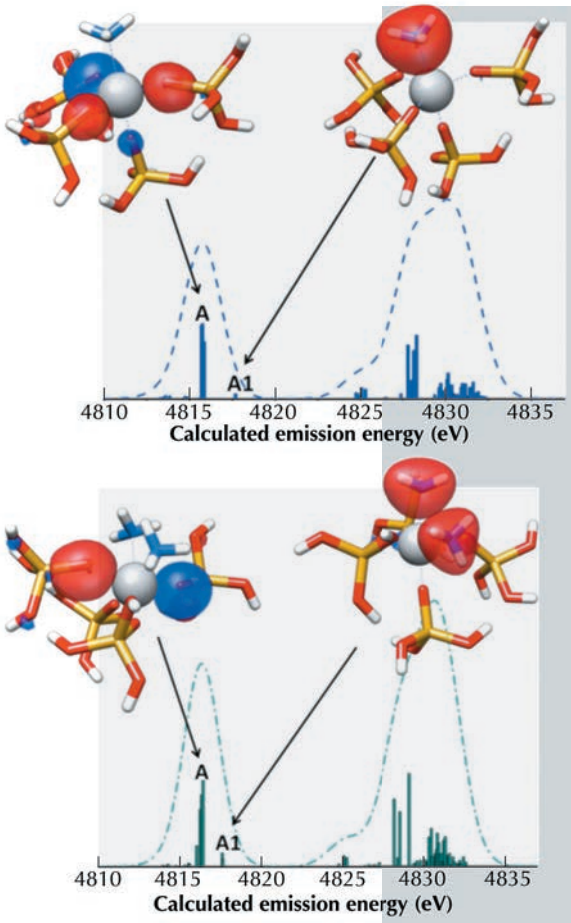

Fig. 94: vtc-XES of two clusters of TS-1 with one (**calc1**, top) and two (**calc2**, bottom) molecules of ammonia adsorbed. The molecular orbitals that affect the emission line A (*i.e.*, Kβ'') are also reported. The colour code is grey for Ti, red for O, blue for N and yellow for Si.

References
[1] S. Bordiga, F. Bonino, A. Damin and C. Lamberti, *Phys. Chem. Chem. Phys.* **9**, 4854-4878 (2007).
[2] S. Bordiga, E. Groppo, G. Agostini, J. A. van Bokhoven and C. Lamberti, *Chem. Rev.* **113**, 1736-1850 (2013).
[3] E. Gallo, C. Lamberti and P. Glatzel, *Phys. Chem. Chem. Phys.* **13**, 19409-19419 (2011).

PRODUCTION OF Ru NANOPARTICLES OVER ACTIVATED CARBONS: CHEMICAL INTERACTIONS OF THE METAL PRECURSOR WITH SURFACE FUNCTIONAL GROUPS

Principal publication and authors
F.R. García-García (a), M. Fernández-García (b), M.A. Newton (c), I. Rodríguez-Ramos (b) and A. Guerrero-Ruiz (a), *ChemCatChem* **5**, 2446–2452 (2013).
(a) Facultad de Ciencias, UNED, Madrid (Spain)
(b) Instituto de Catálisis y Petroleoquímica, CSIC, Madrid (Spain)
(c) ESRF

Carbon–based materials such as activated carbon, nanotubes, graphene and fibres are gaining interest as supports for catalytic materials or as catalysts themselves. These types of carbon-based materials are also promising targets for the production of a new generation of heterogeneous catalysts, which are required for bio-refining raw organic substrates obtained

from the biomass [1]. Therefore, the preparation of metallic nanoparticles anchored to carbon surfaces is at present an important technological topic. But many basic aspects of the preparation-activation procedures for synthesising these catalysts are still not well established. For instance activated carbon (AC) surfaces are usually considered as inert material; however the presence of oxygen surface groups (chemical species such as carboxyl acids, hydroxyls, carbonyls and lactones) can be decisive for the anchoring of metallic precursors as well as for the generation of nanoparticles during the reduction-activation treatments. These surface groups can also play a decisive role in the final catalytic site structures, and consequently in their catalytic properties. They can affect the electronic properties of the metallic nanoparticles [2] and they can be destabilising for metallic aggregates and sintering phenomena. In this latter case, the desorption of oxygen surface groups during the decomposition/reduction of the metal precursor can also lead to surface reconstructions of the metal nanoparticles during the starting-up of a catalytic material for a given process.

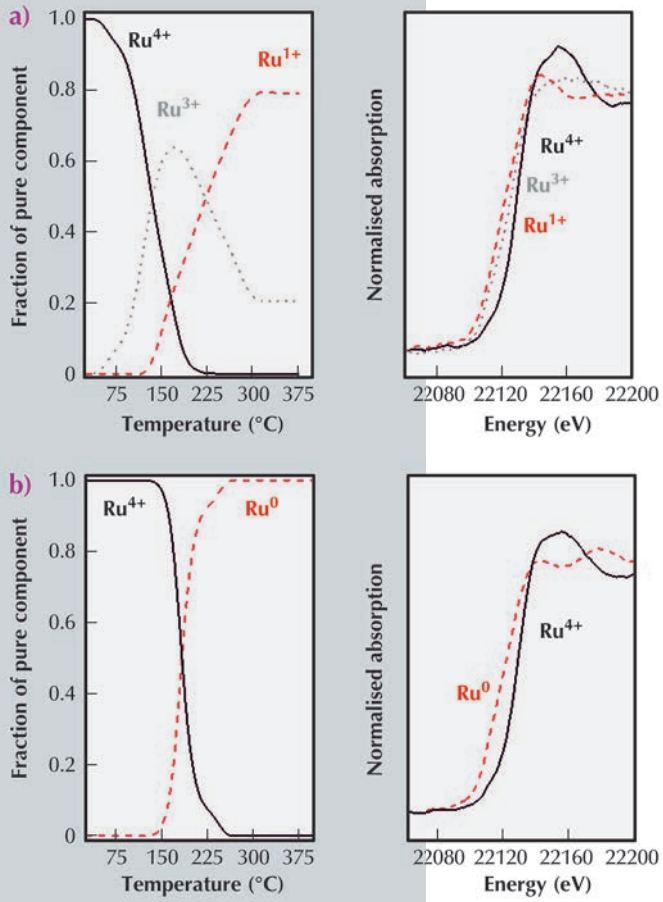

Fig. 95: Concentration profiles obtained from Ru K-edge XANES spectra of the different Ru species (Ru^{+4}, Ru^{+3}, Ru^{+1} and Ru^{0}) observed during TPR of $Ru(NO)(NO_3)_3$ precursor supported on AC-ox (a) and AC-f (b).

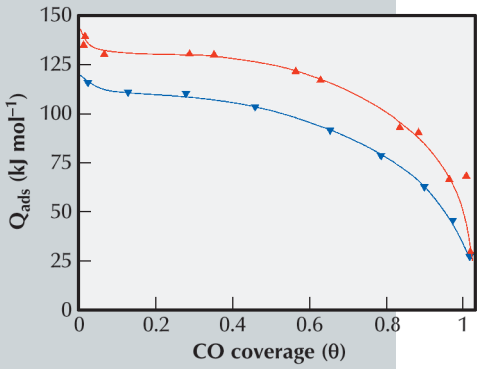

Fig. 96: Differential heats of CO adsorption as a function of the surface coverage (▲) 2%Ru/AC-ox and (▼) 2%Ru/AC-f catalysts.

To shed light on these surface chemical phenomena taking place over the carbon surfaces by solid-solid reactions with the metal precursor, we have previously performed studies including temperature programmed reduction (TPR), characterisation of the final surface properties of the generated metal nanoparticles, including detection of electronic properties by CO chemisorptions coupled with calorimetry, and determination of catalytic properties in several test reactions. An important conclusion from these studies is that we need to pursue the evolution of the chemical species in the solids *in situ*, instead of determining the final states of the metal nanoparticles *a posteriori*, in order to understand the genesis of the metallic nanoparticles. Thus, we want to evaluate the chemical processes from the point of view of the solids (carbon support and metal precursor) which evolve during catalyst activation. We have already been able to follow the progress of the oxidation states of Ru atoms when a $Ru(NO)(NO_3)_3$ complex is reductively decomposed over AC surfaces. In fact, we have comparatively studied the interaction of this inorganic catalytic precursor over two activated carbons, one thermally treated to remove all oxygen groups (AC-f) and the second that is the as-received material (AC-ox), where the surface contains significant amounts of oxygen functional groups. Note that these oxygen surface groups can also be produced at the initial steps of the metallic precursor decomposition [3]. Performing an *in situ* XANES analysis of the Ru K-edge at beamline **ID24**, we tracked the behaviour of Ru precursors under a hydrogen atmosphere and analysed the reduction mechanism as a function of the surface state of the

AC support (Figure 95). In particular, we found that oxygen groups exposed on the AC-ox surfaces generate a multi-step mechanism for the reduction of the Ru species. In the case of clean graphitic surfaces (AC-f), a single step was observed.

This study may thus reveal details of the specifity of the carbon-nanometal interaction that could be important when these materials are used as catalysts. Figure 96 displays the significant differences in electronic properties that were detected by microcalorimetry of CO chemisorptions, when the exposed surface metallic sites (Ru) are supported on ACs, with or without initial oxygen functionalities. Note that these materials present a similar Ru primary particle size. These interactions have a significant consequence on the catalytic properties. Ru nanoparticles generated on the AC-f exhibit five times higher catalytic activity than when supported on AC-ox for the ammonia decomposition reaction.

References
[1] P. Gallezot, *Chem. Soc. Rev.* **41**, 1538–1558 (2012).
[2] F.R. García-García, J. Álvarez-Rodríguez, I. Rodríguez-Ramos and A. Guerrero-Ruiz, *Carbon* **48**, 267-276 (2010).
[3] E. Gallegos-Suarez, M. Perez-Cadenas, A. Guerrero-Ruiz, I. Rodríguez-Ramos and A. Arcoya, *Appl. Surf. Sci.* **287**, 108-116 (2013).

LOCAL ATOMIC STRUCTURE OF CERIUM-BASED BULK METALLIC GLASSES UNDER EXTREME CONDITIONS OF PRESSURE AND TEMPERATURE

Principal publications and authors
L. Belhadi (a), F. Decremps (a), S. Pascarelli (b), L. Cormier (a), Y. Le Godec (a), S. Gorsse (c), F. Baudelet (d), C. Marini (b) and G. Garbarino (b), *Appl. Phys. Lett.* **103**, 111905 (2013).
(a) IMPMC, Universite Pierre et Marie Curie, Paris (France)
(b) ESRF
(c) CNRS, ICMCB, Universite de Bordeaux, Pessac (France)
(d) Synchrotron SOLEIL, Gif Sur Yvette (France)

Bulk metallic glasses (BMGs) are of growing interest worldwide due to their remarkable physicochemical properties with regard to their crystalline counterparts. These amorphous materials combine the electric conductivity of metals with glassy structural disorder, thus hold promise for industrial products with outstanding performance.

Recently, rare earth based metallic glasses have been found to display thermo-plastic behaviour with very low glass transition temperature (T_g < 373 K) and low Young's modulus in comparison to classical amorphous matter [1]. At room temperature, these alloys are strong (elastic strain of 2 % [2]) and brittle. However, in their supercooled-liquid state, these materials can be repeatedly shaped into very fine structures down to the nanometre-scale, which is of great interest for micro electromechanical systems or nanotechnology applications such as high density data storage [3].

The cerium based metallic glasses (Ce-BMGs) exhibit polyamorphism under pressure (phase transition between amorphous phases with change of density and local structure at transition). This transition, unexpected in such spatially compact systems, leads to structural changes under pressure which were not clearly identified. Furthermore, the role of the cerium constituent during this transition seems decisive but only a few studies report the link between the properties of the pure cerium and the polyamorphism in the Ce-BMGs [4,5].

Using X-ray techniques at high-pressure (0-15 GPa) at beamline **BM23**, we investigated polyamorphism in $Ce_{69}Al_{10}Cu_{20}Co_1$. EXAFS measurements at the Ce K-edge (40.4 keV) were carried out for the first time at high pressure on Ce-BMG, revealing important modifications of the cerium local environment (Figure 97 and Figure 98).

Results from this first set of EXAFS experiments provide direct experimental evidence that local structural changes occur in compressed Ce-rich BMGs that cannot be

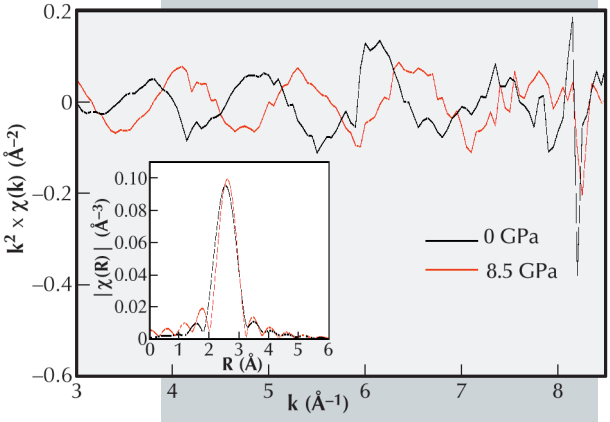

Fig. 97: $Ce_{60}Al_{20}Cu_{20}$ EXAFS functions at ambient pressure (low density amorphous) and 8.5 GPa (high density amorphous). Our analysis demonstrates that the difference of signal is not compatible with a uniform compression of the ambient pressure structure. Inset: the corresponding amplitude of the Fourier transform.

References
[1] E. Lutanie, *Mater. today* **12**, 12 (2009).
[2] B. Zhang, D.Q. Zhao, M.X. Pan, W.H. Wang and A.L. Greer, *Phys. Rev. Lett.* **94**, 205502 (2005).
[3] G. Marsh, *Materials Today* **6**, 38 (2003).
[4] H.W. Sheng, H.Z. Liu, Y.Q. Cheng, J. Wen, P.L. Lee, W.K. Luo, S.D. Shastri and E. Ma, *Nature Mater.* **6**, 192 (2007).
[5] M. Duarte, P. Bruna, E. Pineda, D. Crespo, G. Garbarino, R. Verbeni, K. Zhao, W. Wang, A. Romero and J. Serrano, *Phys. Rev. B* **84**, 224116 (2011).
[6] F. Decremps, L. Belhadi, D. Farber, K. Moore, F. Occelli, M. Gauthier, A. Polian, D. Antonangeli, C. Aracne-Ruddle and B. Amadon, *Phys. Rev. Lett.* **106**, 065701 (2011).

described by simple compression. We observe a structural rearrangement compatible with a splitting of the Ce-Ce shell, in agreement with numerical simulations [4]. These local structural changes are accompanied by modifications in the electronic structure, whereby the Ce 4f states acquire a more delocalised character. This polyamorphism involves an important Ce-Ce bond shortening at the transition (almost 10% from this data analysis) and is obviously electronically-driven by the 4f electron of cerium.

This last point is particularly interesting if observed from a crystal *vs* amorphous perspective. A previous study by our group [6], focused on the structural evolution of pure crystalline cerium along the $\gamma \leftrightarrow \alpha$ transition induced by a 4f electronic delocalisation under pressure, demonstrated the existence of a critical point in the p, T diagram at the end of the $\gamma \leftrightarrow \alpha$ transition line. Based on this unexpected behaviour, we carried out X-ray elastic diffusion measurements at high pressure and high temperature in order to compare the disordered phase diagram of the Ce-BMGs with that of pure crystalline cerium. Our study did not reveal a clear occurrence of such a critical point in the range of pressure/temperature probed (0-15 GPa, 300-340 K).

This work will encourage further investigations on Ce-based metallic glass phase diagrams in order to support, or even refute, the actual theoretical understanding of polyamorphism.

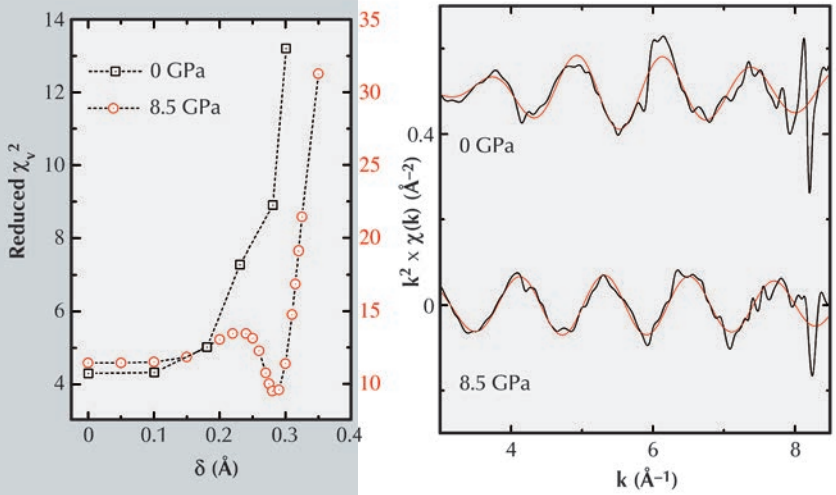

Fig. 98: Left: Evolution of the quality of the fits (reduced χ^2) as a function of the splitting of the Ce-Ce distance in $Ce_{60}Al_{20}Cu_{20}$ metallic glass (δ) for both the ambient (black) and the high pressure (red) data. Right: best fit (red) to EXAFS data (black) at ambient pressure (above) and 8.5 GPa (below).

Principal publication and authors
K. Korthout, A.B. Parmentier, P.F. Smet and D. Poelman, *Phys. Chem. Chem. Phys.*, **15**, 8678-8683 (2013).
LumiLab, Department of Solid State Sciences, Ghent University (Belgium)

DEFECT CLUSTERS OF LANTHANIDE IONS IN LUMINESCENT MATERIALS

Phosphor converted light emitting diodes (pc-LEDs) have a much lower energy consumption and a longer lifetime than traditional light sources, such as incandescent lamps, and are quickly taking over the market of general lighting. Usually a pc-LED is a combination of a blue emitting LED and a yellow emitting luminescent material (or phosphor). The overall emission spectrum of this combination often lacks sufficient output in the red part of the spectrum and as such the colour rendering is poor. This has encouraged the research into materials for LED applications showing a saturated red emission.

Europium doped Ca_2SiS_4 is an interesting candidate due to its bright yellow-to-red emission [1]. While samples with low Eu dopant concentrations (< 15%) crystallise in the orthorhombic structure of Ca_2SiS_4, highly doped samples (> 50%) have the monoclinic structure of Eu_2SiS_4. The dopant concentration also strongly affects the emission characteristics (**Figure 99a**). At low dopant concentrations, the emission spectrum consists of two broad bands (564 nm and 660 nm) due to the presence of two inequivalent lattice sites for the Eu ions. At higher concentrations, only a single band is visible which linearly

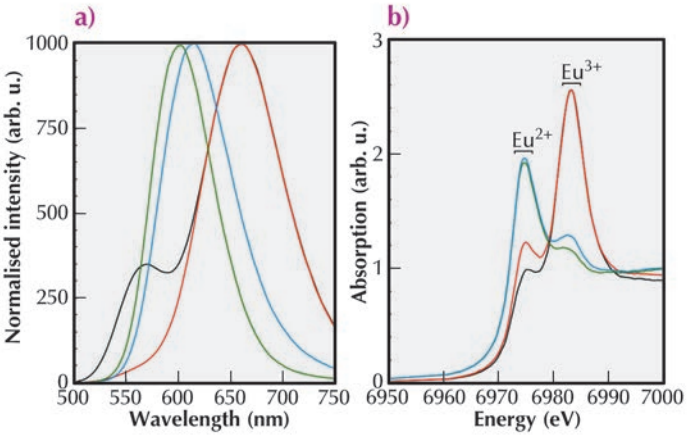

Fig. 99: (a) Photoluminescence emission spectra of Eu doped Ca_2SiS_4 with different dopant concentrations (excitation wavelength = 450 nm). (b) Eu L_3 XANES spectra of Eu doped Ca_2SiS_4 with different dopant concentrations. For both figures: (**black**) 2 molar%, (**red**) 10 molar%, (**blue**) 50 molar% and (**green**) 75 molar %. (c) In the lightly doped samples defect clusters are observed; one of these defects is represented schematically.

shifts from 614 nm to 577 nm upon increasing Eu concentration.

The emission of Eu^{2+} ions is highly dependent on their local environment. To study this local environment, we performed X-ray absorption near edge (XANES) measurements at the Eu L_3 edge at **BM26A** and extended X-ray absorption fine structure (EXAFS) measurements at the Eu K edge at **BM23** [2].

The measured europium L_3 edge XANES spectra are shown in **Figure 99b**, exhibiting two strong white lines. These originate from the coexistence of the two common valence states of the Eu ions (Eu^{2+} and Eu^{3+}). While the Eu ions are mainly present in a trivalent state for the lightly doped samples [3], divalent Eu is dominant in the highly doped samples.

The local structure around the Eu ions was addressed by Eu K edge EXAFS. For all samples, the Eu occupancy of both sites in the structure was investigated. The coexistence of both valence states was implemented in the simulations in the lightly doped samples, while only the presence of Eu^{2+} was modelled in the highly doped samples.

Firstly, lets consider the low dopant concentrations. In earlier work it was reported that the Eu ions occupy both inequivalent Ca sites in the Ca_2SiS_4 host crystal, and this was confirmed by the EXAFS data. Most of the Eu^{3+} ions substitute on the Ca2 site, while the divalent ions mainly occupy the Ca1 site. Upon increasing the dopant concentration the relative occupancy of the Ca1 site increases. This agrees well with the optical data: upon increasing the dopant concentration the relative intensity of the emission band caused by the Ca1 site (at 660 nm[4]) increases.

The presence of trivalent Eu ions on divalent Ca sites can cause disorder and structural defects in the samples. Using EXAFS we were able to prove that in the sample with a dopant concentration of 2% no such defects are present. For the more heavily doped samples, *i.e.* 7.5% and 10%, the following defects were found from EXAFS model fitting: (a) One trivalent Eu ion at a Ca2 site, and a vacancy and the other Eu^{3+} ion at a Ca1 site; (b) Both trivalent ions on a Ca2 site, and a vacancy appearing at a Ca1 site (**Figure 99c**).

In contrast, for the high dopant concentrations, the structure of highly doped samples can be described as Ca ions substituting for Eu ions in a Eu_2SiS_4 crystal. The EXAFS analysis shows that the Ca ions preferentially occupy the Eu2 site in the lattice. This preferential distribution decreases with an increase in Eu concentration until an equal distribution of the Eu ions in Eu_2SiS_4 is obtained.

Based on these results we could explain the concentration dependence of the emission spectra of $(Ca,Eu)_2SiS_4$. At low Eu concentrations (< 10%) the dopant ions substitute for the Ca ions at both inequivalent crystallographic sites, albeit that some preferential substitution is observed. At higher concentrations (> 40%) the Ca ions occupy both europium sites in the monoclinic Eu_2SiS_4 structure. Furthermore an unexpected large fraction of trivalent europium ions is found in the XANES spectra of lightly doped thiosilicates, although no Eu^{3+} emission is found in the photoluminescence spectra.

References
[1] P.F. Smet, N. Avci, B. Loos, J.E. Van Haecke and D. Poelman, *J. Phys.: Condens. Matter* **19**, 246223 (2007).
[2] J.J. Joos, K. Korthout, S. Nikitenko, D. Poelman and P.F. Smet, *Opt. Mater. Express* **3**, 1338-1350 (2013).
[3] K. Korthout, K. Van den Eeckhout, J. Botterman, S. Nikitenko, D. Poelman and P.F. Smet, *Phys. Rev. B* **84**, 085140 (2011).
[4] A.B. Parmentier, P.F. Smet and D. Poelman, *Opt. Mater.* **33**, 141–144 (2010).

PERSISTENT MAGNETIC EXCITATIONS IN SUPERCONDUCTING AND NON-SUPERCONDUCTING $La_{2-x}Sr_xCuO_4$

Principal publication and authors
M.P.M. Dean (a), G. Dellea (b), R.S. Springell (c), F. Yakhou-Harris (d), K. Kummer (d), N.B. Brookes (d), X. Liu (e,a), Y.-J. Sun (e,a) J. Strle (f,a), T. Schmitt (g), L. Braicovich (b), G. Ghiringhelli (b), I. Bozovic (a) and J.P. Hill (a), *Nature Materials* **12**, 1019–1023 (2013).
(a) Department of Condensed Matter Physics and Materials Science, Brookhaven National Laboratory, Upton, New York (USA)
(b) Dipartimento di Fisica, Politecnico di Milano (Italy)
(c) Interface Analysis Centre, University of Bristol (UK)
(d) ESRF
(e) Beijing National Laboratory for Condensed Matter Physics, and Institute of Physics, Chinese Academy of Sciences, Beijing (China)
(f) Department for Complex Matter, Jozef Stefan Institute, Jamova, Ljubljana (Slovenia)
(g) Swiss Light Source, Paul Scherrer Institut, Villigen (Switzerland)

The phenomenon of high-temperature superconductivity (HTS) in the copper-oxygen-based or cuprate materials has been puzzling researchers for over a quarter of a century. A key question relates to the cause of the disappearance of superconductivity in the highly doped or overdoped cuprates. One of the most intensely studied proposals to explain HTS postulates pairing by the exchange of magnetic excitations [1] and it was therefore suggested that HTS disappears in the overdoped cuprates because magnetic excitations are completely suppressed by doping [2]. We used resonant inelastic X-ray scattering (RIXS) measurements to show that some magnetic excitations actually persist in the overdoped cuprates. The destruction of HTS with overdoping is therefore not caused by the simple overall disappearance of magnetic excitations, a fact that must now be explained in any successful theory of HTS.

When one examines the phase diagram of the cuprate $La_{2-x}Sr_xCuO_4$, as shown in **Figure 100a**, an exciting opportunity to gain insights into HTS presents itself. Superconductivity is seen to disappear at high dopings ($x > 0.3$), where the sample shows metallic behaviour. In conventional superconductors, a higher electronic density of states usually increases the superconducting transition temperature, so identifying the crucial change that destroys HTS in the overdoped cuprates has great potential to provide insights into the HTS mechanism. This motivated many neutron scattering experiments, where researchers observed that the intensity of the magnetic excitation they measured was reduced as the doping concentration (x) was increased, and by $x = 0.3$ the magnetic excitations appear to have effectively disappeared [2]. As a consequence of this, it has been argued that the disappearance of HTS in the overdoped cuprates is simply because there are no magnetic excitations available to mediate the pairing [1-2].

Due largely to the extremely high brightness of synchrotron sources, resonant inelastic X-ray scattering (RIXS) is a highly sensitive probe of magnetic excitations. We used RIXS to measure the magnetic excitations for samples with doping levels that span the whole phase diagram of $La_{2-x}Sr_xCuO_4$. The example spectra, shown in **Figure 101**, demonstrate that magnetic excitations persist in the heavily overdoped cuprates – proving that these samples are not simple non-magnetic metals.

The apparent contradiction between the persistent intensity measured in the RIXS experiment and the reduction of intensity measured by neutrons, can be resolved by noting that each technique focuses on different regions of the Brillouin zone, shown in **Figure 100b**. The RIXS measurements were taken along the (0,0) to (0.5, 0) symmetry line. In this region of reciprocal space, the intensity of the magnetic excitations is below the signal-to-noise ratio of current inelastic neutron scattering experiments on doped cuprates. Instead, inelastic neutron scattering experiments focus on the higher intensity excitations around (0.5, 0.5). Together, the RIXS and neutron scattering results show that doping does not uniformly rescale the magnetic excitation spectrum of the cuprates, rather the changes in the spectrum vary significantly depending

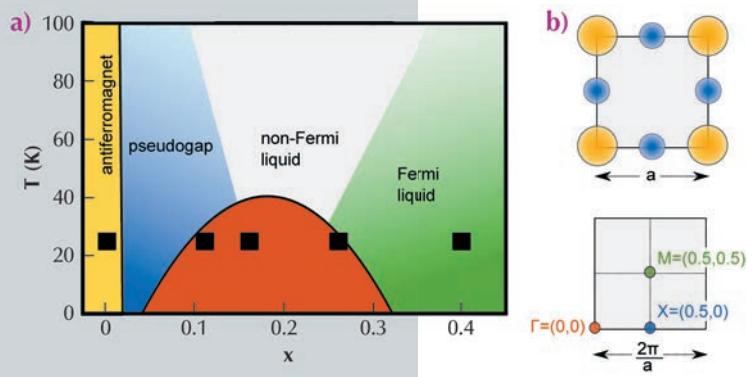

Fig. 100: a) A schematic phase diagram for $La_{2-x}Sr_xCuO_4$ as a function of the doping level, *x*. The doping levels of the samples studied here are marked by black squares. b) Top, the basic structural unit of the cuprates: a CuO_2 plaquette with Cu atoms in orange and O atoms in blue separated by distance a = 3.8 Å. Bottom, the reciprocal lattice with high symmetry points marked and labelled in reciprocal lattice units (r. l. u.).

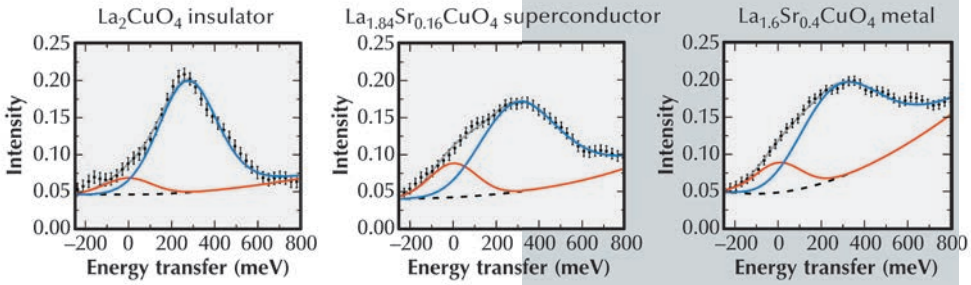

Fig. 101: Example spectra of $La_{2-x}Sr_xCuO_4$ for insulating, superconducting and metallic (non-superconducting) samples. The magnetic response, outlined in blue, appears with similar energy and intensity in all samples. Only the width changes significantly. The additional intensity seen at high energy transfers results from a broadening of the orbital excitations, which lie at 1-3 eV in energy.

on which region of the Brillouin zone is studied. Our results show that the demise of HTS in the overdoped cuprates is not due to dramatic changes in the high-energy magnetic excitations, as these remain roughly constant as the doping (x) increases. The change in the superconducting transition temperature must, therefore, be driven by other factors. It might be that the low-energy magnetic excitations around (0.5,0.5) drive the formation of HTS, as these excitations, unlike the high energy excitations studied here, are known to change dramatically in the overdoped cuprates.

References
[1] D.J. Scalapino, *Rev. Mod. Phys.* **84**, 1383 (2012).
[2] S. Wakimoto *et al.*, *Phys. Rev. Lett.* **98**, 247003 (2007).

INSIDE A FERRIMAGNET: PROBING MAGNETIC SUBLATTICE REORIENTATION AT HIGH MAGNETIC FIELD

Principal publication and authors
C. Strohm (*a*), T. Roth (*a*), C. Detlefs (*a*), P. van der Linden (*a*) and O. Mathon (*a*), *Physical Review B* **86**, 214421 (2012).
(a) ESRF

Ferrimagnets are materials composed of different magnetic constituents. These may be different sites occupied by the same element, different elements or combinations thereof. Examples range from magnetite as one of the earliest known magnetic materials, to rare-earth transition-metal intermetallics which are of interest in the quest for hard magnetic materials, and double perovskites with characteristics making them candidates for spintronics applications. The strength of the magnetic interactions is determined by electronic and structural properties. The equivalent molecular fields can be very high, therefore one often needs equally high magnetic fields to explore their magnetic phase diagrams. Probing the behaviour of the individual constituents has remained challenging today and requires isotope-, site-, element- and orbital specific probes, offered by various X-ray techniques, - in high fields. Here, we used Fe K-edge XMCD in fields up to 30 T to probe the Fe magnetisation in the ferrimagnetic garnet $Er_3Fe_5O_{12}$.

In the rare earth iron garnets, the magnetic ions are located at the centres of oxygen polyhedra with different symmetries. The exchange interactions over the oxygen atoms at the vertices lead to ferrimagnetic behaviour on two very different scales: On one side, the coupling between the two octahedral and three tetrahedral Fe sites is very strong and the antiferromagnetic alignment is only broken at the Curie temperature of 560 K or in excessively high fields. On the other side, the interaction of the Er ions with the unbalanced Fe net moment is much weaker, yet still requires applied fields of the order of tens of Tesla to compete with the molecular fields. Figure 102 shows the phase diagram of a simplified isotropic two sublattice model for the interaction of Er ions with the Fe-net moment. At high temperatures, the Er behaves like a paramagnet, polarised by the net Fe moment. With decreasing temperature, the Fe and the Er sublattices reverse orientation with respect to an applied field at the compensation temperature T_{comp} = 78.8 K, where the Er

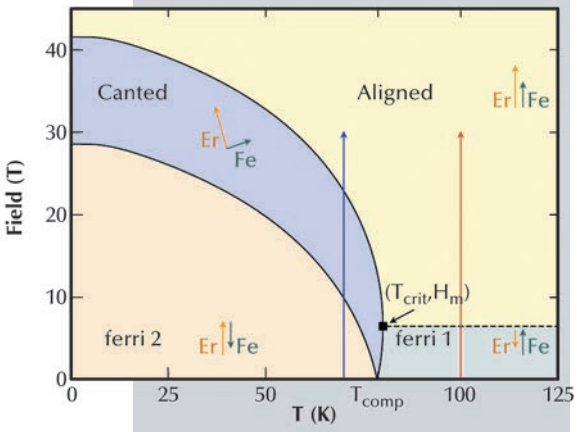

Fig. 102: Isotropic two sublattice model for the phase diagram of $Er_3Fe_5O_{12}$. Above the critical temperature, the Er sublattices behave as a paramagnet whose field dependence is offset through the molecular field created by the net moment of the Fe ions. A canted phase, bounded by second order transitions (solid lines) emerges below the critical temperature for the ordering of the Er ions. The red and blue arrows represent the field dependences shown in **Figure 103**.

magnetisation outweighs that of the Fe sites. However, the most intriguing manifestation of the different interactions becomes apparent in the field dependence of the Fe sublattice magnetisation. In our experiment, we used a miniature pulsed magnet system to reach 30 T and energy dispersive XMCD at **ID24**, that has an intrinsically simultaneous acquisition scheme, particularly suitable for differential experiments in time varying fields.

Above T_{crit}, (**Figure 102**, red arrow) the Er ions first become thermally demagnetised when the applied field compensates the molecular field from the Fe sublattice (dashed line) and eventually becomes aligned with the Fe and the applied field. While the bulk magnetisation rises continuously, XMCD reveals that the Fe-sublattice magnetisation remains independent of the applied field up to 30 T (**Figure 103**, right panels). Below T_{crit}, (**Figure 102**, blue arrow) the applied field gradually increases the Er magnetisation. When it matches the difference between the molecular fields of the Fe- and the Er sublattices, the Fe sublattice starts to rotate continuously, reversing by 180 degrees to align with the applied field after which it remains saturated again (**Figure 103**, left panels). Bounded by second order transitions, this canted phase remains barely visible in the bulk magnetisation, which grows continuously. The Fe-K edge XMCD (**Figure 103**, left panels) clearly shows first the opposite configuration, then the complete reversal within the canted phase, and finally the alignment with the applied field.

In conclusion, we have used energy dispersive XMCD in pulsed high magnetic fields at the Fe-K-edge to probe the Fe-sublattice magnetisation in ferrimagnetic $Er_3Fe_5O_{12}$. The field independent parts of the Fe magnetisation indicate the strong interaction between the tetrahedral and octahedral sites, whereas the continuous reorientation in the canted phase is the signature of the weak coupling of the Er sublattice to the Fe net moment.

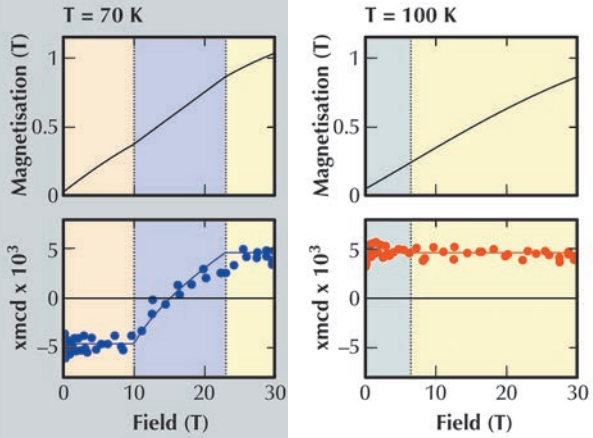

Fig. 103: Calculated bulk magnetisation (top) and Fe K-edge XMCD (bottom) below and above the critical temperature. The bulk magnetisation rises continuously at both temperatures. The XMCD shows that the net magnetisation of the Fe sublattices remains saturated and aligned with the applied field at 100 K. At 70 K, it is opposite to the applied field and reverses continuously in the canted phase.

DIRECT EVIDENCE FOR SIGNIFICANT SPIN-POLARISATION OF EuS IN Co/EuS MULTILAYERS AT ROOM TEMPERATURE

Principal publication and authors
S.D. Pappas (a), P. Poulopoulos (a,b), B. Lewitz (b), A. Straub (b), A. Goschew (b), V. Kapaklis (c), F. Wilhelm (d), A. Rogalev (d) and P. Fumagalli (b), *Scientific Reports* **3**, 1333 (2013).
(a) University of Patras (Greece)
(b) Freie Universität Berlin (Germany)
(c) Uppsala University (Sweden)
(d) ESRF

Materials for spintronic applications need to have both magnetic and semiconducting properties. However, an intrinsic semiconductor which is magnetic at room temperature has yet to be found. The europium chalcogenides (EuO, EuS, EuSe, EuTe) are promising wide band-gap semiconductors, but they have very low Curie temperatures. Here, for the first time, we provide clear evidence that EuS layers can be spin-polarised at room temperature in proximity to a ferromagnet, such as Co, using XMCD at the Eu-$L_{2,3}$ edges. Therefore, manipulation of the electron spin and charge in these materials should be feasible in the near future.

Most work in the literature has focused on diluted magnetic semiconductors. However, earlier measurements carried out at beamline **ID12** proved that there is no sign of intrinsic

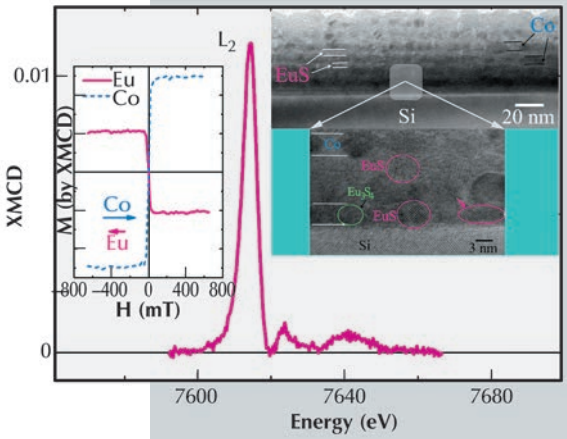

Fig. 104: R.T. spin polarisation of Eu in EuS layers in proximity to Co. Inset: element-specific hysteresis loops are traced for both, Co and EuS, at R.T. The cross-section transmission electron microscopy images support the successful formation of the Co/EuS multilayers. A few Eu_3S_4 crystallites are also visible. (We thank Dr. A. Delimitis for the microscopy images.)

ferromagnetic interaction between Co substitution (dopant) ions in ZnO in diluted semiconductors. The Co ions showed purely paramagnetic or superparamagnetic response [1].

In this work, Co/EuS multilayers were prepared by e-beam evaporation in ultrahigh vacuum. High-resolution cross-section transmission electron microscopy showed good quality of layering (see right inset of **Figure 104** for a Co (4 nm)/EuS (3.5 nm) multilayer). However, defects resulted in a partial loss of stoichiometry and the appearance of both, divalent and trivalent Eu. Only divalent Eu contributes to ferromagnetism while the trivalent Europium possesses J = 0.

Element-specific XMCD measurements were performed at the $L_{2,3}$ edges of Eu at beamline **ID12** at temperatures between R.T. and 2.5 K and under fields as large as 17 T. **Figure 104** shows a clear XMCD signal at the L_2 edge of Eu recorded on a Co (7 nm)/EuS (2 nm) multilayer at R.T. Comparison with the low temperature (T = 2.5 K) XMCD signal leads to the conclusion that divalent Eu shows a relatively large magnetic response at R.T. (magnetic moment per ion surprisingly similar to the one of bulk Ni). Element-specific hysteresis loops at R.T. (inset) showed that there is no need of an external field to spin polarise EuS, so this is an effect of the direct exchange coupling J_{int} at the interface with Co. We also observe that the Co and Eu moments are always antiparallel. No significant change of the magnitude of the magnetisation of each element occurs up to 0.65 T.

Mainly two parameters may have led to the strong magnetic response of EuS at R.T. First, EuS layers are very susceptible to effective fields due to the J = 7/2 character of the system. In **Figure 105**, we show that the same effective field, in a mean-field theory (MFT) approach, polarises a J = 7/2 system almost by a factor of three more than a J = 1/2 system at the same reduced temperature above T_C. Secondly, in

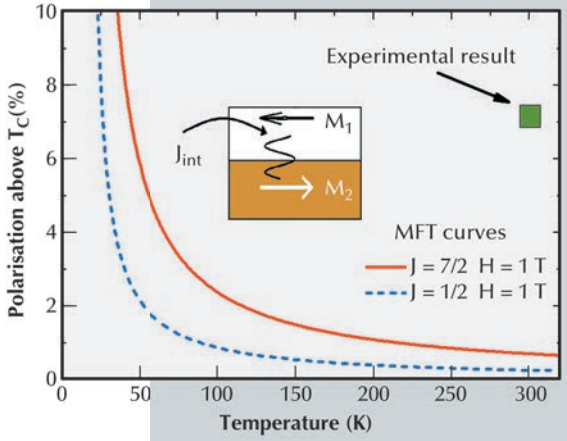

Fig. 105: MFT curves show that a J = 7/2 system is more susceptible than a J = 1/2 system for moderate effective fields at the same reduced temperature t = T/T_C; (here T_C is supposed to be 16.6 K in both calculations, therefore, t scales as T). However, the strong spin polarisation of the 2 nm EuS by Co cannot be understood by MFT. The reduced dimensionality of EuS layers may provide a more plausible explanation.

this work, we used very thin layers approaching the two dimensional-limit (2 nm of EuS correspond to about 6 atomic (100) planes). Two-dimensional ferromagnets are not stable against thermal fluctuations at finite temperatures. However, even moderate fields are able to suppress the spin fluctuations and result in significant T_C enhancement of ultrathin ferromagnetic films. Similarly in exchange coupled layers, like Co and EuS, the exchange coupling at the interface plays the role of an effective field of the order of 1 T. Interestingly, a MFT without taking into account the presence of two-dimensional magnetic fluctuations in ultrathin films would underestimate substantially (even by one order of magnitude) the T_C enhancement in these layers.

In conclusion, here we show promising employment of Co/EuS or similar layered structures in spintronics. The R.T. ferromagnetism in combination with tuneable optical properties of very thin EuS layers, due to quantum confinement effects, may render EuS-based layered structures useful for novel optoelectronics-spintronics applications [2].

References
[1] A. Ney *et al.*, *PRL* **100**, 157201 (2008).
[2] S.D. Pappas *et al.*, *Scientific Reports* **3**, 1333 (2013).

Principle publication and authors
S. Geprägs (a), S. Meyer (a), S. Altmannshofer (a), M. Opel (a), F. Wilhelm (b), A. Rogalev (b), R. Gross (a,c) and S. T. B. Goennenwein (a), *Appl. Phys. Lett.* **101**, 262407 (2012).
(a) Walther-Meißner-Institut, Bayerische Akademie der Wissenschaften, Garching (Germany)
(b) ESRF
(c) Physik-Department, Technische Universität München, Garching (Germany)

INVESTIGATION OF INDUCED Pt MAGNETIC POLARISATION IN $Pt/Y_3Fe_5O_{12}$ BILAYERS

Recently, a novel magnetoresistive effect was discovered in Pt deposited on ferrimagnetic $Y_3Fe_5O_{12}$ (YIG) thin films, which is fundamentally different from the other magnetoresistive phenomena [1,2]. The main characteristic of this novel effect found in normal-metal/ferrimagnetic insulator (NM/FMI) bilayers is the dependence of the NM resistance on the magnetisation direction in the FMI. A possible explanation of the effect is based on static magnetic proximity effects, resulting in a finite magnetic polarisation in the NM layer as known for normal-metal/ferromagnetic metal (NM/FMM) heterostructures. In turn, this leads to ferromagnetic like transport properties in the NM thin film [2]. An alternative explanation is based on the (inverse) spin Hall effect (SHE) in the NM layer. A charge current flowing in the NM thin film is accompanied by a perpendicular spin current due to the SHE. This spin current is absorbed or reflected at the interface to the FMI depending on its magnetisation orientation. While the reflected spin current induces a charge current via the inverse SHE leaving the longitudinal resistance of the NM layer unchanged, the spin current transmitted across the NM/FMI interface represents an additional dissipation channel and thus increases the resistance [1,3].

The fundamental difference of both models is the presence or absence of an induced magnetic polarisation in the NM layer in equilibrium. Therefore, a careful investigation of this induced magnetic polarisation in NM/FMI heterostructures is essential for the correct interpretation of the reported magnetoresistance in Pt/YIG bilayers.

We investigated a series of Pt/YIG samples by XMCD at the Pt L_3-edge. Taking advantage of an ultra-high vacuum cluster system, the ultrathin Pt layers with different thicknesses (3 nm, 7 nm, 10 nm) were deposited *in situ* by electron-beam evaporation immediately after the pulsed-laser deposition of the about 62 nm thick YIG films on (111)-oriented $Y_3Al_5O_{12}$ substrates. For comparison, we fabricated a NM/FMM sample composed of a 10 nm thick Pt layer on a 10 nm thick Fe film.

X-ray absorption near edge spectra (XANES) were recorded at the beamline **ID12** around the Pt L_3-edge with right and left circularly polarised light under grazing incidence as well as positive and negative magnetic fields using the total fluorescence yield (TFY) detection mode. The X-ray magnetic circular dichroism (XMCD) was calculated after averaging up to 34 single XANES per bilayer either with right and left circularly polarised light or while applying positive and negative magnetic fields. **Figure 106a** shows the XANES normalised to an edge jump of unity of a Pt(7 nm)/YIG bilayer and the XMCD spectra of all measured Pt/YIG bilayers around the Pt L_3-edge. The XMCD signals do not show any indication of a finite induced magnetic moment in Pt down to a noise level of < 0.2%. To cross-check our experimental approach, XANES and XMCD spectra were recorded from the Pt(10 nm)/Fe(10 nm) reference

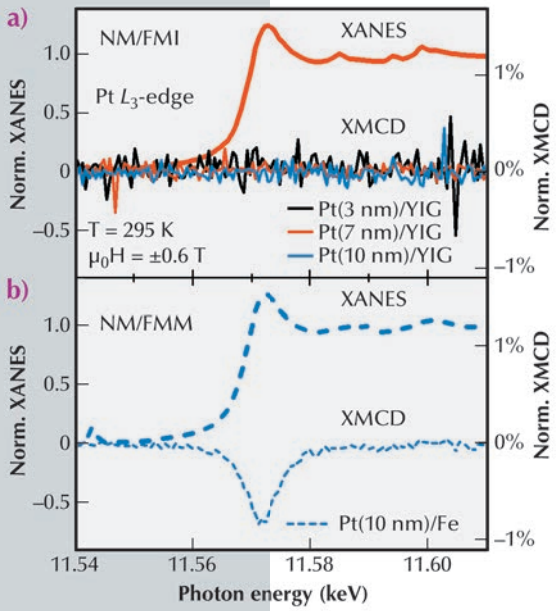

Fig. 106: a) Normalised XANES and XMCD spectra of normal-metal/ferromagnetic insulator (NM/FMI) samples composed of Pt layers with different thicknesses (3 nm, 7 nm, 10 nm) fabricated on YIG thin films. b) Normalised XANES and XMCD spectra of the normal-metal/ferromagnetic metal (NM/FMM) reference sample, consisting of a Pt(10 nm)/Fe(10 nm) bilayer.

sample at the Pt L_3-edge (**Figure 106b**). Here, a clear XMCD signal is visible, demonstrating the presence of induced magnetic moments in NM/FMM heterostructures. By integrating the XMCD spectra, the total moment of Pt is calculated via the standard magneto-optical sum rules to (0.0325 ± 0.0004) μ_B per Pt atom in the Pt/Fe bilayer. Using the same method, an upper limit for the induced total magnetic moment of (0.003 ± 0.001) μ_B per Pt can be estimated in Pt/YIG bilayers. If we consider that only the first layer of the Pt thin film is polarised, then the Pt atoms at the interface would carry an induced moment, which is at least 30 times smaller than that of the Pt atoms at the interface in Pt/Fe bilayers.

In summary, taking advantage of the element-specific XMCD technique, we found that the induced magnetic polarisation of Pt in Pt/YIG bilayers is negligible and at least 30 times smaller than in the corresponding Pt/Fe reference sample. With respect to the reported novel magnetoresistive effect in Pt/YIG bilayers, our data support the model explanation based on spin currents due to the spin Hall effect [1,3] and disagree with explanations based on magnetic proximity [2].

References
[1] H. Nakayama *et al.*, *Phys. Rev. Lett.* **110**, 206601 (2013).
[2] Y. M. Lu *et al.*, *Phys. Rev. Lett.* **110**, 147207 (2013).
[3] M. Althammer *et al.*, *Phys. Rev.* B **87**, 224401 (2013).

CHARGE TRANSFER AT EPITAXIAL INTERFACES

Differences in the work functions between the constituents of semiconductor interfaces are known to cause charge transfer, band bending and the formation of space charge regions. At interfaces of correlated oxides, the situation can be even more complex since the charge, orbital and spin degrees of freedom can be modified. The materials forming the interface may experience significant modification of their electronic response from the variations in carrier density associated with charge transfer. These modifications occur as a consequence of the very different electronic ground states that coexist in narrow regions of the phase diagrams [1]. We have studied the effect of charge transfer and modified bonding at the interface formed between two Mott-insulators: $LaFeO_3$ (LFO) and Sm_2CuO_4 (SCO). While $LaFeO_3$ remains insulating and with an antiferromagnetic ground state when moderately doped, Sm_2CuO_4 becomes metallic and even superconducting upon doping with electrons. In experiments using X-ray absorption spectroscopy with linear polarisation at beamline **ID08**, we have shown that charge transfer occurs at this interface and as a consequence the heterostructure formed by two insulating materials becomes metallic.

We have grown superlattices consisting of six bilayers of 14 unit cells (u.c.) of LFO and N u.c. SCO ($[LFO_{14}/SCO_N]_6$) on TiO_2 terminated $SrTiO_3$ (STO) substrates in a high-pressure pure oxygen sputtering system. Thin films of LFO and SCO were also grown as control samples. The unit cell of SCO and LFO and the schematic of the resulting interface structure are show in **Figure 107**. The heterostructures are fully strained

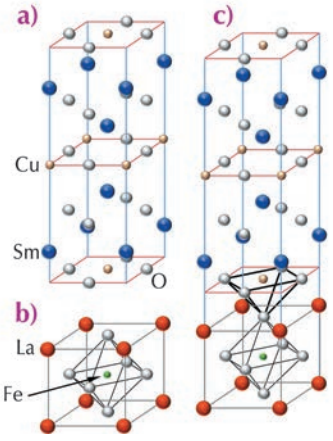

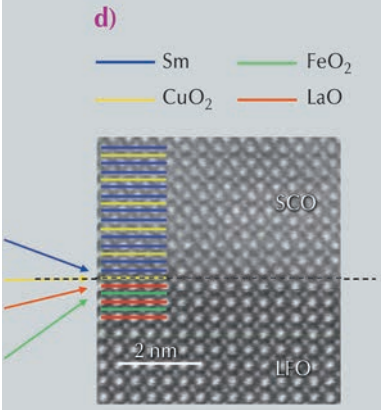

Fig. 107: Crystal structure of (a) Sm_2CuO_4 (T'-phase), (b) pseudocubic representation of $LaFeO_3$, and (c) interface formed by these compounds. In (c) the interfacial Cu-O pyramid is highlighted. (d) High-resolution scanning transmission electron microscopy image of a $[LFO_{14}/SCO_4]_6$ heterostructure.

Principal publication and authors
F.Y. Bruno (a), R. Schmidt (a), M. Varela (a,b), J. Garcia-Barriocanal (a), A. Rivera-Calzada (a), F.A. Cuellar (a), C. Leon (a), P. Thakur (c), J.C. Cezar (c), N.B. Brookes (c), M. Garcia-Hernandez (d), E. Dagotto (b,e), S.J. Pennycook (b) and J. Santamaria (a), *Advanced Materials* **25**, 1468–1473 (2013).
(a) GFMC. Dpto. Física Aplicada III, Universidad Complutense de Madrid (Spain)
(b) Materials Science and Technology Division, Oak Ridge National Laboratory (USA)
(c) ESRF
(d) Instituto de Ciencia de Materiales de Madrid, Consejo Superior de Investigaciones Cientificas, Cantoblanco (Spain)
(e) Department of Physics and Astronomy, University of Tennessee, Knoxville (USA)

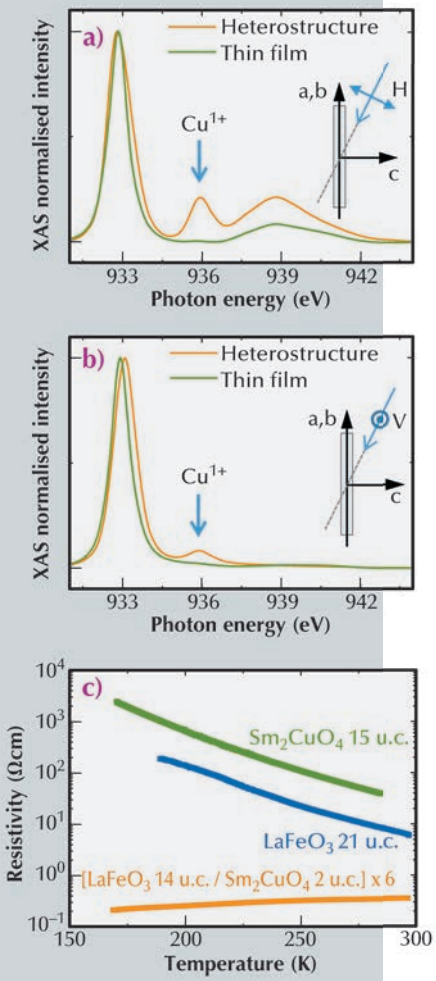

Fig. 108: X-ray absorption spectra obtained with (a) vertical and (b) horizontal polarisation. The spectra corresponds to a $[LFO_{14}/SCO_2]_6$ superlattice (orange) and a SCO 15 u.c. thick film (green). (inset) schematics of the of the experimental setup. (c) Resistivity as a function of temperature of samples: $[LFO_{14}/SCO_2]_6$, LFO_{21} and SCO_{15}.

as confirmed by reciprocal space maps obtained at beamline **BM25**. The high quality of the interface formed between these oxides was extensively studied by scanning transmission electron microscopy. An atomic-resolution high-angle annular dark-field (ADF) image (also known as Z-contrast) of the interface is shown in **Figure 107d**. Through analysis of the elemental maps with atomic resolution, we were able to discern the atomic plane stacking, as indicated in the figure by colour bars.

To study the electronic configuration of Cu, we have performed X-ray absorption spectroscopy (XAS) measurements at beamline **ID08** with linearly-polarised light. **Figure 108** shows the Cu L_3 absorption spectrum normalised to the edge jump obtained with horizontal (H) and vertical (V) polarised light, respectively, for a thin film 15 u.c. thick of SCO (green) and a $[LFO_{14}/SCO_2]_{x6}$ superlattice (orange). Schematics of the experimental setup to measure the XAS spectra with H and V-polarised photons, which probe mainly out of plane and in plane orbital states, are shown in the insets. The main peak $L_3 \approx 932.8$ eV observed in the spectra is associated with transitions from the Cu^{2+} ground state $2p^63d^9$ to the $2p_{3/2}3d^{10}$ excited state, where $2p_{3/2}$ denotes a $2p_{3/2}$ hole.

The remarkable difference between the spectra of both samples is the feature observed at 935.6 eV associated with the presence of Cu^{1+}, clearly visible for the superlattice with H and V polarised light. Nevertheless, in the case of H polarisation the associated peak is more intense indicating the out of plane character of these states. In the case of the superlattice, the Cu atoms in the interfacial CuO_2 planes have apical oxygens (**Figure 107c**), whilst it is known that there are no apical oxygens in bulk SCO. This provides evidence of the existence of a Cu^{1+} $3d_{3z^2-r^2}$ - apical O $2p_z$ bond resulting from an orbital reconstruction at the interfacial plane. The temperature dependent resistivity of $[LFO_{14}/SCO_2]_6$, LFO_{21} and SCO_{15} is displayed in **Figure 108c**. As expected, the two thin films displayed insulating ($dR/dT<0$) character while the SCO/LFO heterostructure show metallic-like behaviour ($dR/dT>0$) in the temperature range 300-170 K. Dielectric spectroscopy methods allow the temperature range to be extended to lower values revealing a metal to insulator transition, suggesting an insufficient doping level for superconductivity nucleation.

In summary, we have realised electron doping of SCO by charge transfer in superlattices of SCO/LFO, *i.e.* between Mott insulators. High resolution electron energy loss spectroscopy measurements and X-ray absorption spectroscopy provided evidence of extra electrons in the Sm_2CuO_4 *d*-band. As a consequence of the charge transfer, the heterostructures become metallic as confirmed by a combination of DC transport and dielectric spectroscopy measurements.

References
[1] H.Y. Hwang *et al.*, *Nature Mat* **11**, 103 (2012).

ORBITAL RECONSTRUCTION AND INTERFACE MAGNETISM IN $SrTiO_3$ BASED HETEROSTRUCTURES

The electronic properties of the 2D electron system created at the $LaAlO_3$/$SrTiO_3$ (LAO/STO) interface [1] hold promise for applications in oxide electronics. This system features especially striking properties, like electric field tuneable Rashba spin orbit coupling, superconductivity [2] and

magnetism [3]. The mechanism leading to such phenomena is a subject of lively debate. While many experimental results are consistent with the so-called "polarisation catastrophe" mechanism, other hypotheses have been considered including a metallic state induced by stoichiometric defects. In particular La/Sr substitution and oxygen vacancies influence the LAO/STO properties by localising electrons in Ti^{3+} states, thus affecting the transport properties of the 2D electron system. It has been suggested that these Ti^{3+} electrons could induce exotic magnetic order, possibly coexisting with superconductivity [4].

To clarify these issues we used X-ray absorption spectroscopy (XAS) at the titanium $L_{2,3}$ edge to study the orbital anisotropy and the magnetism of Ti-3d states of LAO/STO heterostructures deposited by pulsed laser deposition at the University of Geneva and at the University of Augsburg. The experiments were performed at beamline **ID08**. We studied standard LAO/STO samples, grown in oxidising conditions ($P[O_2]$ = 8 x10^{-5} mbar) and annealed in 200 mbar of O_2 after the deposition, and non-standard LAO/STO which were not annealed after the deposition to introduce some amount of oxygen vacancies and associated localised Ti^{3+} states.

A conceptual schematic of the experiment is presented in Figure 109 and a summary of the experimental results is shown in Figure 110. The linear dichroism spectra of Figure 110a are defined as the difference between XAS acquired with linear polarisation perpendicular and parallel to the interface, which select out-of-plane (d_{xz}, d_{yz}, and d_{z^2}) and in-plane (d_{xy}, $d_{x^2-y^2}$) XAS final states respectively. The data demonstrate that an inversion of the orbital hierarchy is obtained at the LAO/STO interface as soon as one complete LAO layer is deposited on top of a TiO_2-terminated STO. In particular, the LAO/STO heterostructures have $3d_{xy}$ orbitals being lower in energy than $3d_{xz,yz}$, opposite to bulk STO. This orbital reconstruction is accompanied by a substantial relaxation of the STO atomic layers even before the appearance of a mobile electron system, as shown by a refinement of surface diffraction data acquired at the **ID03** beamline. Thus the orbital inversion does not only involve the fraction of titanium sites occupied by electrons (and having a Ti^{3+} valence) but rather all of the titanium sites at the interface.

Interfacial magnetism was investigated by X-ray magnetic circular dichroism (XMCD). Since empty Ti^{4+} sites are

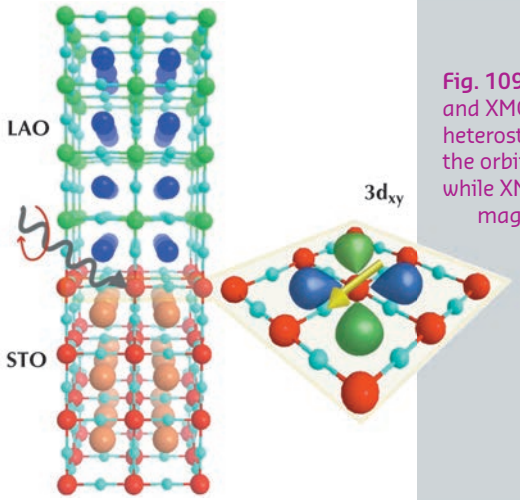

Fig. 109: a) Schematic of the XAS, XLD and XMCD experiments on LAO/STO heterostructure. LD is able to determine the orbital anisotropy of the system while XMCD is able to determine the magnetic moment of titanium-sites. In the figure, we show the case of an electron occupying a Ti^{3+} $3d_{xy}$ state.

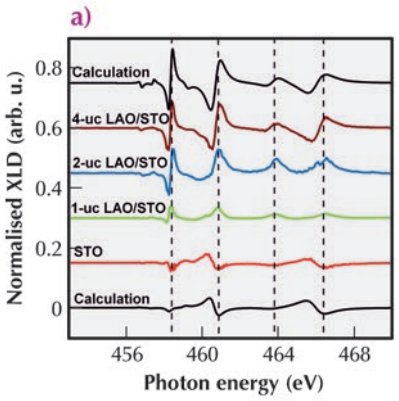

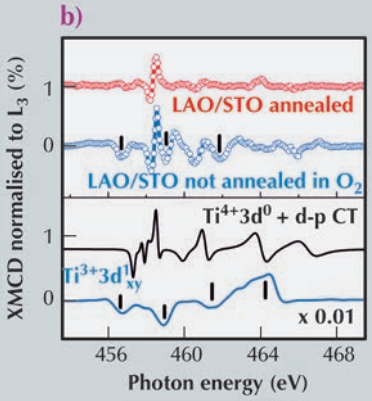

Fig. 110: a) XLD (I_c-I_{ab}) at 8 K as function of the number of LAO layers and comparison with multiplet scattering calculations for anisotropic Ti^{4+} in STO (bottom black-line) and LAO/STO (upper black-line). (b) X-ray magnetic circular dichroism (8 K and B = 5 T parallel to the interface (grazing incidence)) for annealed LAO/STO (red circles) and LAO/STO containing oxygen vacancies (blue circles). Calculated XMCD using multiplet scattering theory for Ti^{4+} + Charge Transfer (CT) (black-line) and localised Ti^{3+} (blue-line). A negative exchange of 10 meV was used for the Ti^{4+} component while a positive exchange (Ti^{3+} spins parallel to the external magnetic field) reproduces the features observed in the data for an LAO/STO interface containing oxygen vacancies. The black sticks label the position of the Ti^{3+} features.

Principal publication and authors
M. Salluzzo (a), S. Gariglio (b), X. Torrelles (c), Z. Ristic (a), R. Di Capua (a), J. Drnec (d), M.M. Sala (d), G. Ghiringhelli (e), R. Felici (d), and N.B. Brookes (d), *Advanced Materials* **25**, 2333 (2013);
M. Salluzzo (a), S. Gariglio (b), D. Stornaiuolo (b), V. Sessi (d), S. Rusponi (f), C. Piamonteze (g), G.M. De Luca (a), M. Minola (e), D. Marrè (h), A. Gadaleta (h), H. Brune (f), F. Nolting (g), N.B. Brookes (d) and G. Ghiringhelli (e), *Physical Review Letters* **111**, 087204 (2013).
(a) CNR-SPIN and Università di Napoli (Italy)
(b) Département de Physique de la Matière Condensée, University of Geneva (Switzerland)
(c) Institut de Ciencia de Materials de Barcelona (CSIC) (Spain)
(d) European Synchrotron Radiation Facility (France)
(e) CNR-SPIN and Dipartimento di Fisica, Politecnico di Milano (Italy)
(f) Ecole Polytechnique Fédérale de Lausanne, (Switzerland)
(g) Swiss Light Source, Paul Scherrer Institut (Switzerland)
(h) CNR-SPIN and Dipartimento di Fisica, Università di Genova (Italy)

non-magnetic, we do not expect any XMCD signal from STO. Any magnetic signal should come either by localised Ti^{3+} spins, either by itinerant electrons or by electrons in charge transfer states. Electrons in the conduction band can couple to these localised spins by screening the impurity sites (as in a Kondo-metal) or by mediating a magnetic interaction between far away magnetic moments following an RKKY scheme. **Figure 110b** presents a comparison between the XMCD data acquired on oxygen annealed and non-annealed LAO/STO samples at 5 T and 8 K. Similar data were obtained at the X-TREME beamline of the Swiss Light Source. The data show that any ordered magnetic moment is very small in the case of optimally oxygenated LAO/STO interfaces. On the other hand, samples containing oxygen vacancies have Ti^{3+} localised spins, as seen by features resonating with energies typical of t_{2g} Ti^{3+} XAS peaks. Together with the Ti^{3+} signal, we observe also features resonating at the main Ti^{4+} peaks. The latter reflect the contribution to the XMCD from electrons in charge transfer Ti3d-O2p states, including itinerant electrons of the 2D electron system. The sign of the XMCD contribution reveals that the exchange coupling with localised Ti^{3+} is negative. Thus the data show that the localised Ti^{3+} impurities induced by oxygen vacancies interact with the 2D electron system with an antiferromagnetic exchange coupling.

Since a magnetic moment is detected only in the case of samples containing oxygen vacancies, magnetism is not an intrinsic property of this system. An alternative explanation should invoke magnetism not coming from Ti-states, or some exotic magnetic order with average null magnetisation, such as the spiral order proposed in [5].

References

[1] A. Ohtomo and H.Y. Hwang, *Nature* **427**, 423 (2004).
[2] N. Reyren *et al.*, *Science* **317**, 1196 (2007).
[3] A. Brinkman *et al.*, *Nature Materials.* **6**, 493 (2007).
[4] 1 J.A. Bert *et al., Nature Physics* **7**, 767 (2011).
[5] 1 S. Banerjee, O. Erten and M. Randeria, *Nature Physics* **9**, 626 (2013).

MAGNETOELECTRONICS: HARNESSING THE COUPLING BETWEEN MAGNETIC AND ELECTRIC PARAMETERS

Principal publication and authors

P.J. Ryan (a), J.-W. Kim (a), T. Birol (b), P. Thompson (c,d), J.-H. Lee (a), X. Ke (e), P.S. Normile (f), E. Karapetrova (a), P. Schiffer (g), S.D. Brown (c,d), C.J. Fennie (b) and D.G. Schlom (h), *Nature Communications* **4**, 1334 (2013).

(a) X-ray Science Division, Argonne National Laboratory, Illinois (USA)
(b) School of Applied Engineering Physics, Cornell University, New York (USA)
(c) Department of Physics, University of Liverpool (UK)
(d) XMaS, the UK-CRG, ESRF
(e) Quantum Condensed Matter Division, Oak Ridge National Laboratory, Tennessee (USA)
(f) Instituto Regional de Investigación Científica Aplicada (IRICA) and Departamento de Física Aplicada, Universidad de Castilla-La Mancha, Ciudad Real (Spain)
(g) Department of Physics and Materials Research Institute, Pennsylvania State University (USA)
(h) Department of Materials Science and Engineering, Cornell University, New York (USA)

Although scientists have been aware that magnetism and electricity are two sides of the same proverbial coin for almost 150 years, researchers are still trying to find new ways to use a material's electric behaviour to influence its own magnetic behaviour, or vice versa.

Our research has led to the discovery of a simple mechanism for controlling magnetic order in a particular class of materials known as "magnetoelectrics". The name derives from the fact that the magnetic and electric properties are coupled to each other. Because this physical link potentially allows for significantly increased efficiencies in both memory and logic devices, scientists have taken a special interest in these materials.

We focused on the compound $EuTiO_3$ (europium-titanium oxide), which is a simple perovskite system with a known magneto-dielectric coupling phenomenon making it especially well suited to this experiment [1]. The titanium atom sits in the middle of a cage constructed of the europium and oxygen atoms. By first compressing the cage through the growth of a thin film of $EuTiO_3$ on a similar crystal with a smaller lattice and then applying a voltage, the titanium shifts slightly, electrically polarising the system, and more importantly, changing the effective magnetic order of the material [2].

Underlying this behaviour is the interesting fact that $EuTiO_3$ intrinsically has both coexisting ferromagnetic and antiferromagnetic interactions [3]. Typically the latter is much stronger and dominates the material, however through the tailored distortion induced in the strained film, the relative magnetic energies are brought closer

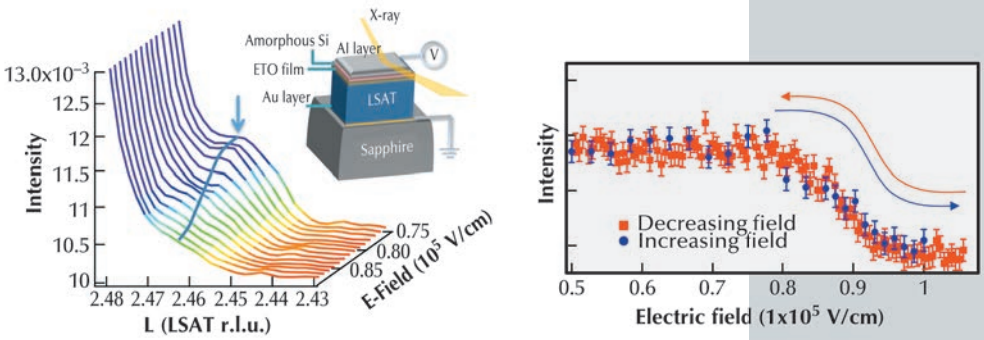

Fig. 111: Left panel: A series of reciprocal scans through the decreasing antiferromagnetic signature reflection with incrementally increasing electric field. Inset: A depiction of the *in situ* sample environment used in the experiment. Right panel: Presents a plot of the magnetic reflected intensity with both increasing and decreasing electric field.

and thus the spin order becomes less stable and more susceptible to external influence. In this case, an electric field induces an electric polarity within the typically paraelectric system.

The titanium atom determines the electric character while the europium atom contributes the magnetic element, however the titanium also plays an important role in the mediation of the europium spin ordering. It allows the europium spins to communicate, the strength of this interaction is dependent upon how well aligned the Eu and Ti atoms are. The interactions are strongest when they form a straight line, however if either atom deviates from this line, then the interaction between the Eu spins falls off. On the other hand, the ferromagnetic interactions do not depend upon the Ti atom and so are not affected. The precariously balanced spin state shifts with Ti displacement under applied field suppressing the AFM order until eventually the FM exchange interactions begin to locally determine the spin order.

Employing a combination of experimental measurements including X-ray magnetic scattering with advanced density functional theory calculations, we could both monitor the extinction of the magnetic order and predict roughly with what electric field strength this phenomenon would occur (**Figure 111** and **Figure 112**). This feat illustrates the strength of using both approaches to understand the intricate mechanisms driving such physical properties.

A particularly interesting aspect of this finding is the concept that multiferoicity or specifically a feroelectric-ferromagnet is not necessary to generate a giant ME effect. Rather, a far more common paraelectric antiferromagnet insulator has presented exactly this effect with a simple but powerful underlying mechanism.

This new approach to cross-coupling magnetoelectricity could prove a key step towards the development of next-generation memory storage, improved magnetic field sensors, and many other long dreamed of applications. Potential magnetic and electric memories each have a distinct appeal to researchers. Electric memories – such as the kind used into today's electronics – allow computers to write data fast and very efficiently. Magnetic memories are less energy efficient, but are extraordinarily robust. Because the electric and magnetic parameters in these particular materials are so strongly linked, engineers might also be able to use them in the future to create non-binary memories.

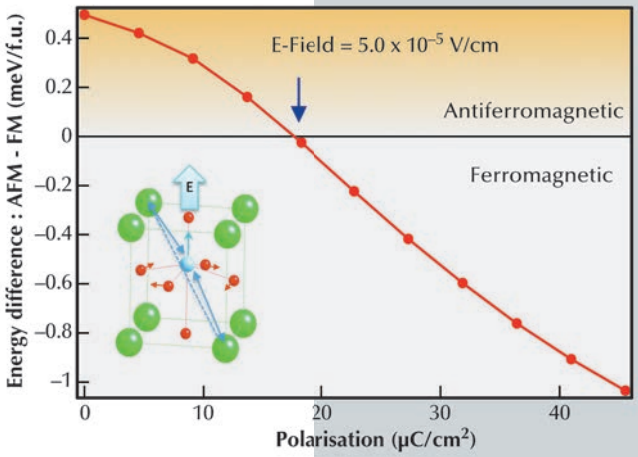

Fig. 112: Presents density functional theory calculated energy differences between the AFM and FM state with increasing titanium displacement from the central position. With an equivalent calculated electric field of 1e10–5 V/cm, both the AFM and FM order become degenerate. Inset: Illustrates the simple Ti displacement, distorting the Eu-Ti-Eu alignment leading to AFM suppression.

References

[1] T. Katsufuji and H. Takagi, *Phys. Rev. B* **64**, 054415-054419, (2001).

[2] J. H. Lee *et al.*, *Nature* **466**, 954 (2010).

[3] H. Akamatsu *et al.*, *Phys. Rev B* **83**, 214421 (2011).

STRUCTURE OF MATERIALS

One of the principal uses of synchrotron radiation is the investigation of the microscopic structure of materials, extending from macromolecules and pharmaceutically active compounds through to surfaces and nano-structures that make up devices used in high-technology applications. Structural information can be obtained over wide range of length scales, from detail of interactions at the atomic level through to the complex structures of devices and composites, and the grain structure of metals and alloys. Such information is essential to understand the properties and performance of a system. Many of the studies performed using ESRF instruments are of direct relevance to modern materials systems and can provide information fundamental for improvements and further developments.

The highlights from ESRF and CRG beamlines selected for 2013 illustrate a number of areas where the use of the synchrotron and advanced X-ray detectors is essential. The production of brilliant beams focused to the nm scale coupled with the exploitation of coherence allow the characterisation of defects, strain and the microstructure that affect the properties and performance of nanoscale semiconductor structures grown in the fabrication of electronic devices. Quantitative information can be derived, such as the number of dislocations and the size of a defected volume, which can then be correlated with the fabrication process and the resulting performance.

The high intensity of synchrotron radiation allows systems that are evolving with time to be investigated, such as the structure and chemical state of an industrial catalyst in a realistic operating environment, or the setting of cement - one of the most ubiquitous materials in the modern world - and the influence of additives that help improve the handling, flow, and final strength of the product. In the latter study, the setting was followed on the sub-second time scale, with the cement suspended in an acoustic levitator to ensure that the walls of a container did not influence the chemical reactions under investigation.

Novel materials continue to be devised in chemistry laboratories and synchrotron radiation plays a vital role in determining their structures. New systems recently studied at ESRF include zinc oxide, a wide band-gap semiconductor, with incorporated amino acids that influence the crystal lattice strain and the band gap. Microporous materials such as zeolites and metal-organic framework materials (MOFs) are of current interest as they can be used in a wide range of applications, including catalysis, and are potentially useful for storing gasses such as hydrogen or for sequestration of carbon dioxide. The crystal structures and properties can be understood using synchrotron studies and this information can be fed back for the design and creation of yet more novel materials with desired properties.

The past year has been especially busy for the Structure of Materials Group with final detailed planning for the construction of two Upgrade Programme beamlines and major modifications to two more of the group's beamlines, in addition to the ongoing development and refinement of experimental capabilities in general. Both ID01 and ID31 closed down in December 2013. ID01 will be reconstructed as upgrade beamline project UPBL1, «Diffraction imaging for nanoanalysis», a long beamline extending into the new experimental hall, with nanofocus capabilities, at energies up to 45 keV, for coherent diffraction nano-imaging and anomalous scattering. Construction of upgrade beamline project UPBL2, «High energy beamline for buried interface structures and materials processing», starts at ID31 in January 2014, again a long beamline, with nanofocus capabilities extending up to photon energies of 150 keV. This beamline represents a major enhancement of current capabilities at ID15.

The high resolution powder diffraction beamline is moving from ID31 to ID22, where it will benefit from reduced horizontal divergence on a high-β sector of the storage ring and an increase in its operational range to 80 keV. In late 2014, a large 2d medical imaging detector will be acquired to complement studies made using the high-resolution scanning detector system. The final beamline to be rebuilt in the current phase 1 of the ESRF Upgrade Programme is ID15, which will be redeveloped, incorporating on the B branch high pressure diffraction (relocation of ID09A), and on the A branch continuation of the high energy facilities for materials characterisation and materials chemistry, including use of the white beam as needed.

A. FITCH

COUNTING DISLOCATIONS IN MICRO-CRYSTALS USING COHERENT X-RAY MICRODIFFRACTION

Principal publication and authors
V.L.R. Jacques (a), D. Carbone (a), R. Ghisleni (b) and L. Thilly (c), *Physical Review Letters* **111**, 065503 (2013).
(a) ESRF
(b) Laboratory for Mechanics of Materials and Nanostructures, EMPA, Swiss Federal Laboratories for Materials Testing and Research, Thun (Switzerland)
(c) Institut PPrime, CNRS-University of Poitiers-ENSMA, SP2MI, Futuroscope (France)

For semiconductor device miniaturisation to reach the nanoscale, one of the most important challenges is to obtain perfectly crystalline micro- or nano-crystals. Any deviation from the perfect atomic arrangement constitutes a 'defect' that can dramatically reduce the performance of a device. This is especially true for the so-called 'phase' defects such as dislocations that induce

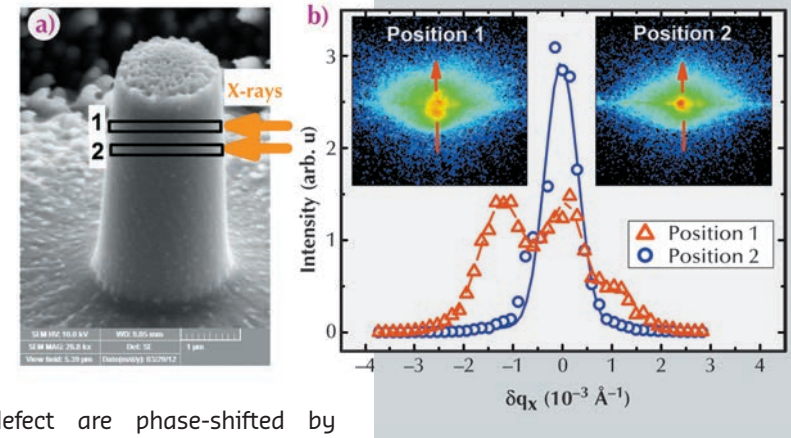

Fig. 113: a) Scanning Electron Microscopy image of the pillar studied here. The volumes probed at positions 1 and 2 are indicated. b) Insets: Coherent diffraction patterns on the 202 Bragg reflection recorded at positions 1 and 2. Graph: Projection of the patterns along vertical direction of the detector.

a shift of one part of the crystal with respect to another. A technique that can directly evaluate the number of defects in a device is thus highly desirable. But estimating the amount of defects in a non-destructive way is challenging, especially in the case of low defect density. In this work, we show that coherent X-ray diffraction can provide an answer to this important material science problem thanks to its high sensitivity to "phase" defects in crystals.

We have studied an InSb micropillar (**Figure 113a**) in which lattice defects were induced in a controlled way via mechanical deformation up to the early plastic regime using a nano-indenter **[1]**. Only a few (partial) dislocations are expected to appear from this deformation, leaving stacking faults that induce a phase shift of adjacent parts of the crystals of $4\pi/3$ in the direction [101]. We used a focused coherent beam at beamline **ID01**, using slits to select the coherent part of the beam and Fresnel Zone Plates to obtain a 200 (v) x 500 (h) nm^2 beamsize. Diffraction images on the 202 Bragg reflection were measured with a Maxipix 2D pixel detector at different positions of the pillar. A sharp Bragg reflection was found at most positions (*e.g.* position 2 in **Figure 113b**), but several maxima were found at a specific position of the pillar (position 1, **Figure 113b**). The sharp peak measured at position 2 accounts for a perfect crystalline arrangement in the sample, while several peaks recorded at position 1 are interferences due to the defects induced in the pillar, namely the phase shifted regions separated by stacking faults **[2]**.

Simulations were performed to estimate the number of stacking faults contained in the volume probed at position 1. They take into account the geometry of the experiment (**Figure 114a**). **Figure 114b** displays a computed real space phase configuration in which N=20 defects have been randomly inserted in a fraction V = 50% of the total illuminated volume. Adjacent volumes separated by a defect are phase-shifted by $4\pi/3$. The corresponding calculated diffraction pattern is displayed in **Figure 114c**. Several peaks due to complex interferences are visible on this pattern, as measured in the experiment. However, varying the number of defects and the size of the defected volume can lead to qualitatively similar diffraction patterns, which makes it impossible to retrieve the exact real space configuration of the stacking faults in the illuminated volume. This problem is well know for the imaging of crystals by phase retrieval algorithms. Interestingly, we found that the maximum intensity on the diffraction pattern is extremely sensitive to the number of defects and to the defected volume size, especially for small numbers of defects, as shown in **Figure 114d**. This behaviour allowed us to evaluate the number of dislocations and the size of the defected volume at position 2 of the investigated sample (N~15 defects in V~50%).

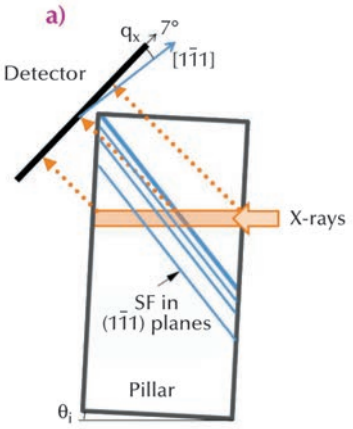

Coherent X-rays can thus be exploited not only to reveal the presence of crystal defects but to quantify them, *i.e.* estimate their number and the size of the defected volume. This approach can be used to relate the devices performance with the presence and extent of defects in a crystalline micro-structure.

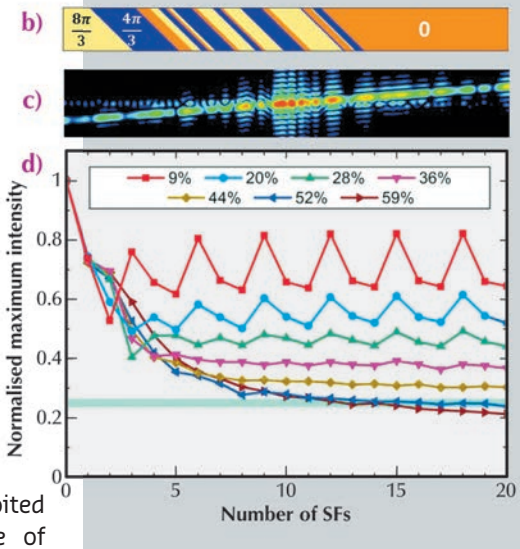

Fig. 114: a) Geometry of pillar, stacking faults (SF), and scattering. b) Simulation of the phase of the illuminated sample volume with 20 defects (SF_s), located in a volumic fraction V = 50%. c) Calculated coherent diffraction pattern corresponding to the volume displayed in a). d) Maximum intensity of the diffraction patterns calculated with increasing number of defects in different fractions of illuminated volume. The blue straight line represents the maximum intensity recorded during the experiment in the defected part relatively to the one measured in the perfect regions.

References

[1] L. Thilly, R. Ghisleni, C. Swistak and J. Michler, *Philosophical Magazine* **92**, 3315 (2012).

[2] V.L.R. Jacques, S. Ravy, D. Le Bolloc'h, E. Pinsolle, M. Sauvage-Simkin and F. Livet, *Physical Review Letters* **106**, 065502 (2011).

PERFECT GERMANIUM CRYSTALS ON SILICON FOR HIGH-RESOLUTION X-RAY DETECTORS

Principal publication and authors
C.V. Falub (a), M. Meduňa (b,c), D. Chrastina (d), F. Isa (d), A. Marzegalli (e), T. Kreiliger (a), A.G. Taboada (a), G. Isella (d), L. Miglio (e), A. Dommann (f) and H. von Känel (a), *Scientific Reports* **3**, 2276 (2013).
(a) Laboratory for Solid State Physics, ETH Zürich (Switzerland)
(b) Department of Condensed Matter Physics, Masaryk University, Brno (Czech Republic)
(c) CEITEC, Masaryk University, Brno (Czech Republic)
(d) L-NESS, Department of Physics, Politecnico di Milano, Como (Italy)
(e) L-NESS, Department of Materials Science, Università di Milano-Bicocca, Milano (Italy)
(f) Centre Suisse d'Electronique et Microtechnique, Neuchatel (Switzerland)

Highly-perfect epitaxial semiconductor layer stacks are quintessential for many low-dimensional quantum structures such as ultrafast transistors, solid state lasers and detectors. While the world's semiconductor industry is overwhelmingly focused on silicon (Si), the first solid-state transistor was made from germanium (Ge) in 1947 [1]. Ever since then, the complexity of semiconductor technology has been increasing, driven by smaller, faster, and more cost-effective devices. For the last few decades, industry has been surprisingly successful in meeting or even surpassing the prediction of Moore's law [2], that axiom of microprocessor development, which states that the density of transistors in integrated circuits should roughly double every two years. However, dimensional scaling following Moore's law is approaching fundamental limits, calling for functional scaling, often described as "More-than-Moore" [3]. This involves the use of other semiconductor materials with optical and electrical properties superior to those of Si. Combining Si with other semiconductor materials raises, however, serious concerns about processing compatibilities, since in general these materials are neither lattice-matched to the Si substrate, nor are they likely to exhibit similar thermal properties. Consequently, defect formation and wafer bowing are serious obstacles.

Faced with the task of producing very thick crystalline active layers made from Ge for high-efficiency and high-resolution X-ray detectors monolithically grown on Si CMOS substrates, we have shown that these problems can be solved by replacing continuous layers with arrays of closely spaced individual crystals, the fusion of which is inhibited by a new mechanism of self-limiting lateral expansion (Figure 115a) [4].

The interpretation of high-resolution X-ray diffraction experiments performed with a laboratory source on such arrays was complicated by the averaging over thousands of crystals. Therefore, in order to map strain status and crystal quality locally, X-ray scanning nanodiffraction experiments were performed on individual crystals at beamline **ID01** using a tightly-focused beam produced by Fresnel zone plates. To avoid signal contributions from adjacent scatterers, chosen crystals were isolated by etching and subsequent removal of their nearest neighbours. By scanning along their height, we showed that the plastic strain generated by the large mismatch of the lattice parameters between Si and Ge causes these crystals to be slightly tilted with respect to each other. Hence, the apparent mosaicity of the order of 0.1°, previously measured with laboratory sources, could be explained in terms of individual tilts of thousands of crystals. Most importantly, after reaching sufficient height, the Ge crystals become indistinguishable from perfect, defect-free single crystals (Figure 115b).

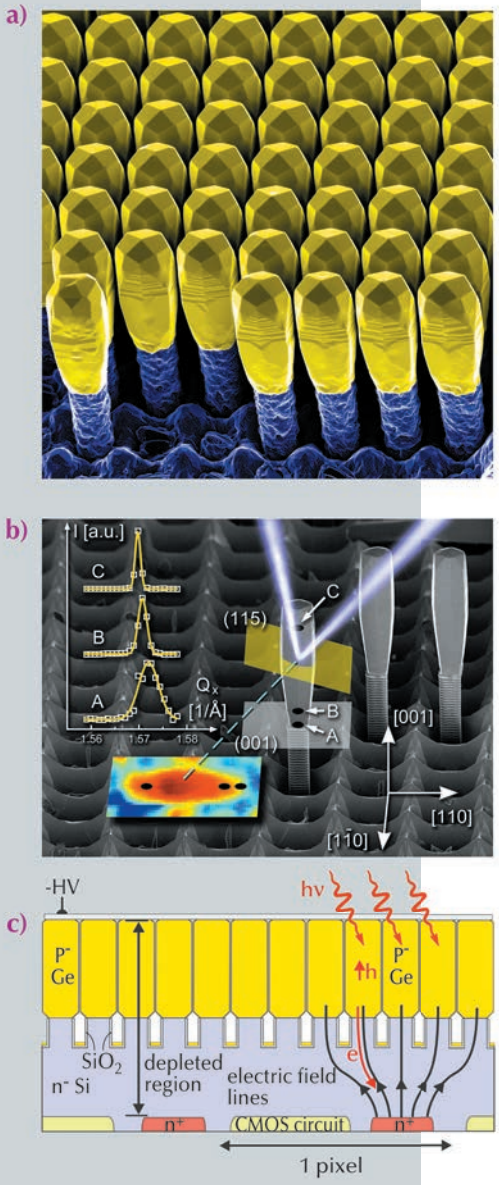

Fig. 115: a) Colourised SEM micrograph of 8 µm tall Ge crystals grown epitaxially on Si substrates deeply patterned at the micrometre scale. b) Scanning X-ray nanodiffraction of an isolated, 11 µm tall Ge crystal. The superimposed colour map represents the scattered intensity collected around the Ge(115) peak when the incident beam was moving along the length of the crystal. The three cross-sections (yellow) of the Ge(115) peak, measured at the positions A, B and C, reveal how the Ge crystal gradually evolves into a perfect monolithic structure away from the dislocated interface. c) Concept of a high-resolution X-ray imaging detector with a monolithically integrated Ge absorber on a CMOS chip.

This first demonstration of perfect strain-free single crystals evolving from a heavily distorted interface with a mismatched substrate could pave the way for device applications hampered so far by dislocations, substrate bending and layer cracking. Especially the fabrication of high-brightness light-emitting diodes, radiation detectors, power transistors and multiple-junction solar cells might profit from the elimination of mismatch related defects.

As far as the ESRF's own interests are concerned, the X-ray detection applications are probably the most interesting, because such dense arrays of perfect Ge crystals a few micrometres in width and epitaxially grown on a CMOS chip could open a route to new imaging detectors with unrivalled spatial resolution. The concept of such a detector is schematically depicted in **Figure 115c**. Here, the absorber layer is made from lightly p-doped Ge crystals grown on the back face of a thinned, highly resistive n-doped Si wafer. The CMOS readout circuits are fabricated on the front face of the wafer in implanted p-wells. The Ge crystals, mutually isolated electrically by an oxide passivation of the Si pillars, and the substrate together form heterojunction p-n diodes, which, under a reverse bias voltage, permit the separation of electron-hole pairs generated by X-ray photons in the Ge absorber.

References
[1] W. Shockley, J. Bardeen and W.H. Brattain, *Science* **108**, 678 (1948).
[2] G.E. Moore, *Electronics* 38 (8), pp. 114–117 (1965) reproduced in *Proc. IEEE*, 86, 82 (1998).
[3] "More-than-Moore" White Paper, W. Arden *et. al.* (2010); http://www.itrs.net/Links/2010ITRS/IRC-ITRS-MtM-v2 3.pdf.
[4] C.V. Falub, H. von Känel, F. Isa, R. Bergamaschini, A. Marzegalli, D. Chrastina, G. Isella, E. Müller, P. Niedermann and L. Miglio, *Science* **335**, 1330 (2012).

In situ COHERENT X-RAY DIFFRACTION REVEALS THE SURPRISINGLY HIGH STABILITY OF A SINGLE NANO-OBJECT

Principal publication and authors
S.T. Haag (a,b), M.-I. Richard (b,c), U. Welzel (a), V. Favre-Nicolin (d,e), O. Balmes (c), G. Richter (a), E.J. Mittemeijer (a,f) and O. Thomas (b), *Nano Lett.* 13, 1883–1889 (2013).
(a) Max Planck Institute for Intelligent Systems, Stuttgart (Germany)
(b) Aix-Marseille Université, CNRS, IM2NP UMR 7334, Marseille (France)
(c) ESRF
(d) CEA-UJF, INAC, SP2M, Grenoble (France)
(e) Université Grenoble-Alpes, Grenoble (France)
(f) Institute for Materials Science, University of Stuttgart (Germany)

The fascination of nanoparticles arises from both their diminutive size and the consequential size effects. They can have properties that are different from their bulk counterparts and even some characteristics that are completely new. When the dimensions are reduced, the influence of surfaces and interfaces rises disproportionately. Thermodynamics has to account for the high fraction of surface or interface atoms and reaction kinetics can be highly accelerated by fast diffusion and high reactivity at interfaces. This typically decreases the thermal stability of nano-objects. Fortunately, some nano-objects can be prepared with exceptionally perfect crystalline quality. The low defect density, steep concentration gradients and local strains can eventually decelerate diffusion and enhance the stability **[1, 2]**. For applications, their stability is of critical importance for functionality and reliability.

The analytical methods for studying the microstructure down to the atomic scale are constantly being improved. It is, however, still challenging to study nano-objects without averaging over non-identical objects and level inhomogeneities, and to avoid destructive sample preparation. In recent years, X-ray lens-less microscopy is gaining interest with the publication of successful studies showing an increase in spatial resolution. When the coherence length of the incident beam is larger than the diffracting object, the three-dimensional diffraction patterns can be regarded as the conversion of the object to reciprocal space. Information on the object in terms of the local density and lattice strains can be extracted. This led to the idea of adapting this method to study the interrelation between stress and diffusion.

For the experiment, an Ag/Au core-shell nanowire was chosen as a model system for several reasons: a single-crystalline structure can be prepared with virtually no growth defects and a smooth interface between Ag and Au, the interdiffusion is not complicated by the formation of intermetallics, and no oxide film forms on the surface.

References

[1] Z. Erdelyi and D.L. Beke, J. *Mater. Sci.* **46**, 6465 (2011).

[2] J. Svoboda and F.D. Fischer, *Acta Mater.* **59**, 1212 (2011).

Ag nanowires were grown and coated with Au inside an ultra-high-vacuum system. Single nanowires with a diameter of about 100 to 300 nm and length of several micrometres were selected and transferred to small sample-holders using ion-beam-cutting within an electron microscope. The diffraction experiment requires a large coherence length of the X-ray beam, focusing of the beam intensity on the small object, and a sensitive two-dimensional high-resolution detector, as available at beamline **ID03**.

From the three-dimensional diffraction patterns, two-dimensional slices could be extracted and analysed in detail (**Figure 116**). Characteristic features in the diffraction patterns such as streaks, fringes and asymmetry could be directly correlated to structural features (facetted shape, size and strains) in direct space. Simulated diffraction patterns (**Figure 117**), considering the strain field expected from the different lattice parameters of Ag and Au, matched the experimental result well.

This nanowire was then subjected to *in situ* annealing. Even after annealing for more than one hour at 400°C, a core-shell morphology was preserved. From bulk, single-crystal diffusion data, much faster intermixing was expected for these temperatures.

This coherent diffraction experiment at beamline **ID03** proved the feasibility of such an *in situ* diffusion study and it also revealed an increased stability of a nano-object due to its low defect-density.

For future experiments, further advancements of the experimental conditions together with improved phase-retrieval algorithms should allow the inversion of three-dimensional diffracted intensity for different beam energies. The strain and concentration fields could then be evaluated "directly", which should unveil more surprises from the nano-world.

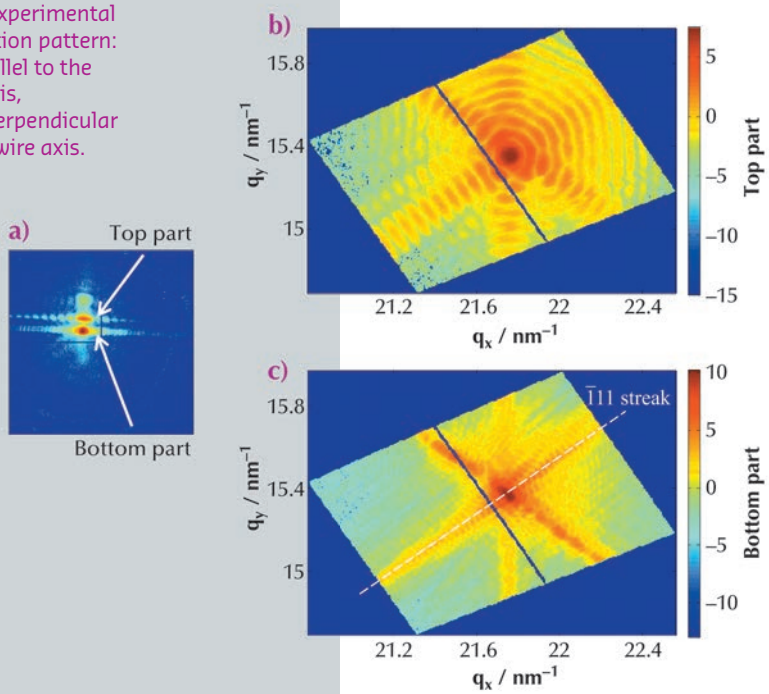

Fig. 116: Two-dimensional slices of an experimental diffraction pattern: a) parallel to the wire axis, b)-c) perpendicular to the wire axis.

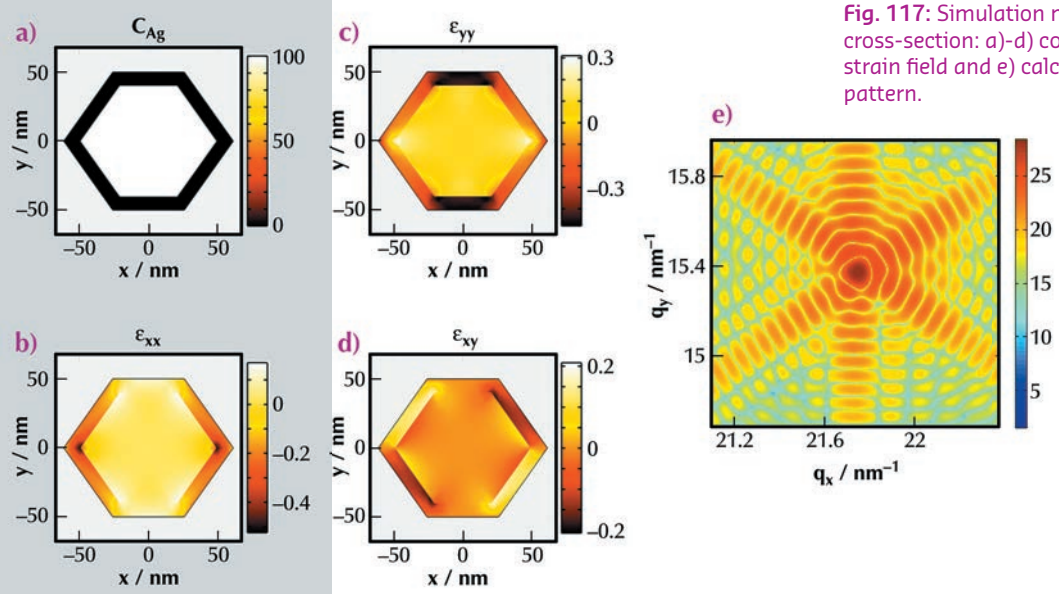

Fig. 117: Simulation model of the wire cross-section: a)-d) concentration and strain field and e) calculated diffraction pattern.

LOCAL STRUCTURE OF ORGANIC PHOTOVOLTAIC DEVICES BY COMBINED X-RAY DIFFRACTION AND FLUORESCENCE INVESTIGATION

Principal publication and authors
B. Paci (a), D. Bailo (a), V. Rossi Albertini (a), J. Wright (b), C. Ferrero (b), G.D. Spyropoulos (c,d), E. Stratakis (d) and E. Kymakis (c), *Advanced Materials* **25**, 4760–476 (2013).
(a) Istituto di Struttura della Materia, C.N.R., Rome (Italy)
(b) ESRF
(c) Technological Educational Institute of Crete, Heraklion (Greece)
(d) Foundation for Research and Technology-Hellas and University of Crete, Heraklion (Greece)

In the continuous quest for inexpensive, low-environmental impact, renewable energy sources, the advent of polymer-based organic photovoltaic (OPV) devices has paved the way for the introduction of cheap and efficient methods to produce energy from light conversion into electricity.

Nowadays, polymer-based materials are ubiquitous in almost every aspect of modern society, as they display important advantages such as simple chemical processing and inexpensive fabrication of thin films via vacuum evaporation or solution casting technologies.

Tremendous progress in OPV devices has been achieved with the introduction of bulk heterojunction (BHJ) solar cells based on donor-acceptor blends, typically a conjugated polymer and a soluble fullerene derivative [1-3]. However, device efficiency has not yet reached the level of maturity needed to cope with the stringent requirements of routine industrial production. Novel solutions must therefore be found to harvest light in a more efficient way. A promising approach is the use of metallic nanoparticles, which strongly absorb light in the UV–visible region. This feature is attributed to both light scattering and localised surface plasmon resonance (LSPR) effects. In this respect, plasmonic nanoparticle-based OPV devices could herald a technological revolution towards high performance and durable solar cells [2,3].

An unprecedented experiment combining X-ray diffraction (XRD) and fluorescence (XRF) with nanometre resolution on post-fabricated OPV devices doped with Au nanoparticles was performed at beamline **ID11**. By scanning the OPV cross-section with a ~ 100 nm focused X-ray beam, the structural properties of the different layers and interfaces comprising the device as well as the nanoparticle distribution were investigated *in situ*.

The layout of the OPV cell used for the experiment is shown in Figure 118. During the measurements, the device was translated vertically from the Al top electrode to the ITO layer, while the XRD patterns were continuously recorded (Figure 118). As the beam size was comparable to the thickness of the different layers, the scanning procedure allowed us to discriminate the diffraction signals from the individual layers.

The measurements provided an accurate space-resolved description of the molecular ordering of the polymer component of the photo-active layer. Such information is crucial, since the photovoltaic energy conversion rate strongly depends on the nanoscale phase separation during the donor/acceptor heterojunction formation as well as the nanomorphology of the interfaces formed between the active and the charge-collecting layer.

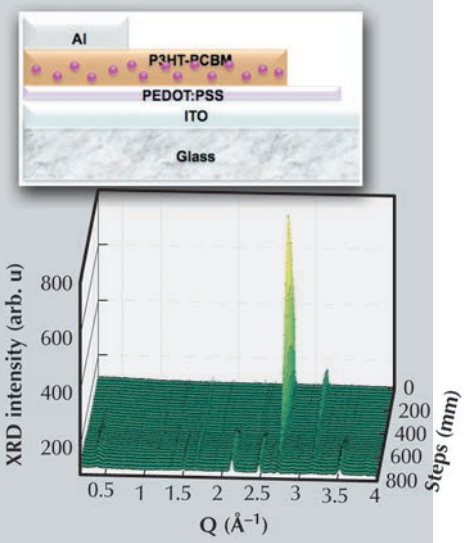

Fig. 118: Schematic representation of the OPV cell studied and waterfall diagrams of XRD patterns collected during a vertical scan of the device.

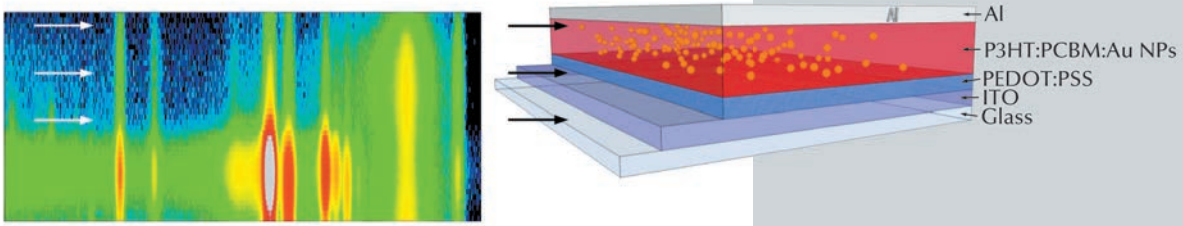

Fig. 119: *In situ* spatially-resolved X-ray study of an integrated organic photovoltaic device: fluorescence line intensities versus vertical scanning.

The accuracy of the experimental technique also made it possible to measure the nanoparticle distribution profile across the device thickness.

Thermal annealing performed *in situ* allowed the chemical-physical phenomena to be uncovered. This modification of the local nanostructure and organisation, interface effects and interdiffusion processes occur as a consequence of the annealing process that is applied to optimise organic solar cell efficiency. The results are in agreement with the significant improvement of the photovoltaic performance for the annealed devices as compared to that of pristine devices: the PV efficiency (calculated from the measured current–voltage characteristics under a solar simulator) was almost quadrupled.

The simultaneous XRF measurements are consistent with XRD findings and corroborate them. The fluorescence line intensities are shown in **Figure 119** versus the vertical scanning step for each metallic element in the OPV.

These results represent a big step towards the elucidation of the structure-property relationships that link different length scales, from local nano/hetero structures and interfaces to large-scale devices. As such, they may be considered as a milestone in a better understanding of how the performance of OPV cells is correlated to the morphology of their respective components on the nanoscale, an essential step towards new strategies for the development of highly efficient devices.

References
[1] A.C. Mayer, S.R. Scully, B.E. Hardin, M.W. Rowell and M.D. Mc Gehee, *Mater. Today* **10**, 11, 28 (2007).
[2] B. Paci, A. Generosi, V.R. Albertini, G.D. Spyropoulos, E. Stratakis and E. Kymakis, *Nanoscale* **4**, 7452 (2012).
[3] B. Paci, G.D. Spyropoulos, A. Generosi, D. Bailo, V.R. Albertini, E. Stratakis and E. Kymakis, *Adv. Funct. Mater.* **21**, 3573 (2011).

HEMD RESOLVES DIFFERENT DEFORMATION MODES IN HIGHLY NANOTWINNED Cu

Principal publication and authors
T.A. Furnish (a), J. Lohmiller (b), P.A. Gruber (b), T.W. Barbee, Jr. (c) and A.M. Hodge (a), *Applied Physics Letters* **103**, 011904 (2013).
(a) Department of Herospace and Mechanic Engineering, University of Southern California (USA)
(b) Institute for Applied Materials, Karlsruhe Institute of Technology (Germany)
(c) Physical and Life Sciences, Lawrence Livermore National Laboratory (USA)

Mechanical engineers dream of optimum materials with the highest strength and formability. Reducing the grain size of a metal down to the nanoscale (< 100 nm) is a common strengthening approach, but typically accompanying the strength is a decrease in the metal's ability to deform plastically (*i.e.* ductility), which is critical for many applications. A recent alternative approach to this problem is to introduce high densities of nanoscale growth twins into the metal. The boundaries separating the twins (*i.e.* twin boundaries) act similarly to normal grain boundaries in strengthening the material, but the symmetry allows dislocations, the main carriers of plastic deformation, to travel across or along the boundaries, thus maintaining some ductility. Unfortunately, the overall deformation behaviour of the unique microstructure of highly nanotwinned metals is not yet fully understood.

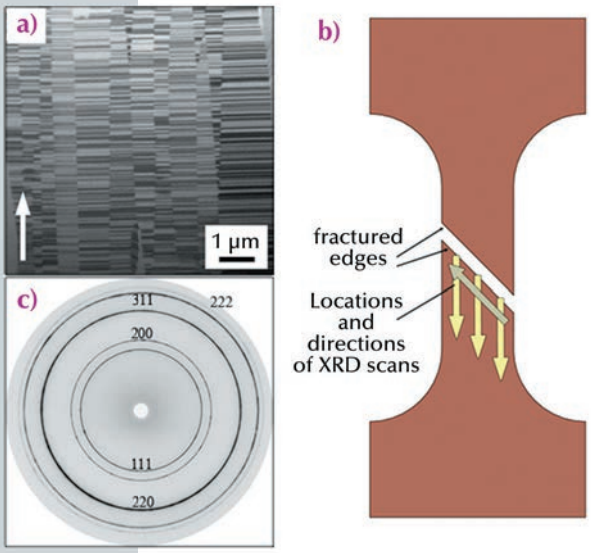

Fig. 120: (a) FIB micrograph of the as-prepared microstructure. (b) Schematic of the scan locations. (c) Diffraction pattern for the as-prepared sample.

We have already shown that columnar grained highly nanotwinned Cu (shown in **Figure 120a**) tensile tested at room temperature (RT) and 77 K is deformed primarily through localised shear bands **[1,2]**, which was perplexing as this is not typical for pure Cu. In addition,

increases in both strength and elongation-to-failure (*i.e.* "ductility") were observed in the sample tested at 77 K. However, the development of the shear bands and their exact role in the deformation behaviour, in particular the enhanced strain, was unclear.

The deformation behaviour and the evolution of the microstructure of nanocrystalline bulk metals during deformation can be followed using high energy microdiffraction (HEMD) at beamline **ID15A** [3]. The microstructure within nanotwinned Cu specimens was investigated after mechanical testing using a microfocussed, monochromatic high energy X-ray beam (beam size: 8 µm × 20 µm, energy: 69.7 keV). The relatively small beam size permitted the microstructure to be probed locally, and good statistics were obtained since the beam transmits the entire sample. Diffraction patterns comprising several complete Debye-Scherrer rings were obtained using an area detector (165 mm MAR CCD) and were taken every 20-30 µm along and across the shear bands and fractured edges (shown schematically in **Figure 120b**). For reference, the diffraction pattern of the as-prepared microstructure can be found in **Figure 120c**. In addition, cross-sectional focused ion beam (FIB) micrographs were prepared at similar locations to directly compare the diffraction patterns with the actual microstructure.

Figure 121 shows an optical micrograph, diffraction patterns, and FIB micrographs of one half of the fractured dogbone sample tested at 77 K (arrow represents the scan direction in this case). The results can be separated into three distinct regions with increasing distance d from the fracture edge: d < 120 µm (Region I), 120 µm < d < 1550 µm (Region II), and d > 1550 µm (Region III), where changes in the diffraction patterns correspond to the visible deformation in the sample (specifically, the areas of fracture, shear bands, and outside major deformation). In region I, the diffraction patterns display only individual spots without any observable texture, indicating a severely coarsened material, which is confirmed in the accompanying FIB micrograph. In Region II, a texture is observed consisting of six-fold symmetries with maxima intensities for (111), (200), (311), and (222) reflections in the tensile direction and minima in intensity for the (220) reflection. This texture typically corresponds to dislocation-mediated plasticity and, in this case, is most likely formed by rotation of the columnar grains into directions of preferred slip. Region III shows diffraction patterns and a microstructure very similar to the undeformed as-prepared case. The sample tested at RT developed the same texture within the shear banded region; however, the texture was much more localised and, intriguingly, no coarsening of the microstructure at the fracture edge was found.

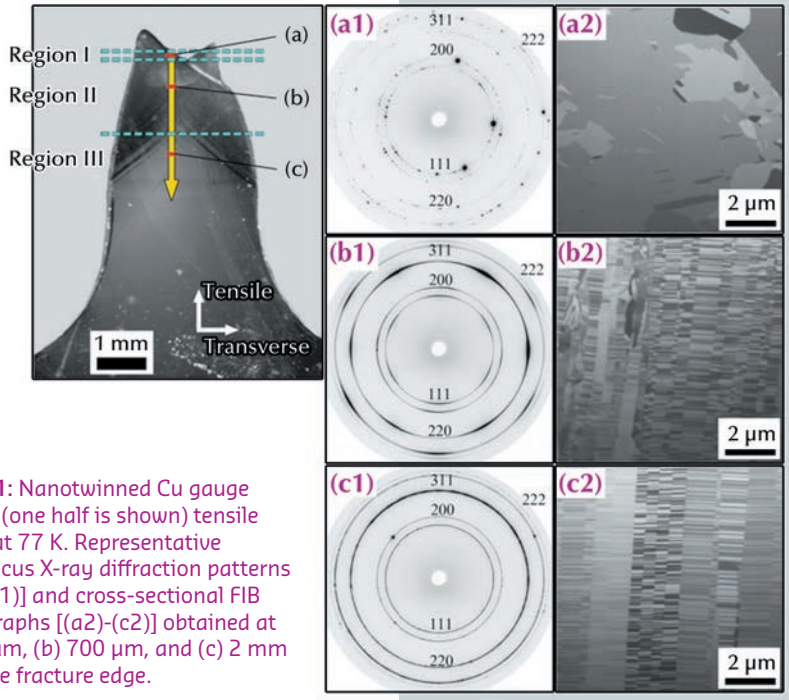

Fig. 121: Nanotwinned Cu gauge section (one half is shown) tensile tested at 77 K. Representative microfocus X-ray diffraction patterns [(a1)-(c1)] and cross-sectional FIB micrographs [(a2)-(c2)] obtained at (a) 50 µm, (b) 700 µm, and (c) 2 mm from the fracture edge.

This space-resolved high-energy microdiffraction study performed on the tensile tested nanotwinned Cu samples allowed the deformation mechanisms and shear band formation to be explored. The texture in the shear-banded areas identified dislocation-mediated plasticity as the governing deformation process; additionally, the data from the 77K samples allowed the formulation of several theories regarding the apparent increased ductility due to the development of multiple shear bands. This information will contribute to the overall knowledge of nanotwinned metals and their potential use in high strength applications.

References
[1] A.M. Hodge, Y.M. Wang and T.W. Barbee Jr., *Scripta Mater.* **59**, 163-166 (2008).
[2] A.M. Hodge, T.A. Furnish, A.A. Navid and T.W. Barbee Jr., *Scripta Mater.* **65**, 1006-1009 (2011).
[3] J. Lohmiller, M. Grewer, C. Braun, A. Kobler, C. Kübel, K. Schüler, V. Honkimäki, H. Hahn, O. Kraft, R. Birringer and P.A. Gruber, *Acta Mater.* **65**, 295-307 (2014).

WATCHING ICE CRYSTALS GROWING IN COLLOIDAL SUSPENSIONS

Principal publication and authors
S. Deville (a), J. Adrien (b), E. Maire (b), M. Scheel (c) and M. Di Michiel (c), *Acta Materialia* **61**, 2077–2086 (2013).
(a) Laboratoire de Synthèse et Fonctionnalisation des Céramiques, UMR3080 CNRS/Saint-Gobain, Cavaillon (France)
(b) Université de Lyon, INSA-Lyon, MATEIS CNRS UMR5510, Villeurbanne (France)
(c) ESRF

Ice crystals growing in a colloidal suspension is a phenomenon encountered in a variety of natural processes such as the freezing of soils in northern regions and the growth of sea ice, or everyday life and engineering situations such as frozen dessert processing, materials science, cryobiology, filtration or water purification, and the removal of pollutants from waste.

The phenomenon by itself is surprisingly simple to describe: a solidification interface, usually the water/ice interface, is propagating through a colloidal suspension of particles, cells or micro-organisms. This simplicity is nevertheless misleading and we are still far from a correct understanding and control of the phenomenon. If the various manifestations of colloid freezing can be observed in numerous natural or technological occurrences, precise and quantitative observations are required in order to understand the process. Current approaches, both direct such as optical microscopy and X-ray radiography and indirect such as X-ray scattering only provide partial, averaged or indirect observations.

The velocity range of interest (1–50 $\mu m.s^{-1}$), corresponding to the usual occurrences of colloids freezing, nevertheless requires high resolution, fast imaging capabilities. Here, we demonstrate that fast X-ray computed tomography allows time-lapse, three-dimensional *in situ* imaging of ice crystal growth in a colloidal silica suspension. We took advantage of recent upgrades and developments at beamline **ID15**, which, due to the high flux of high energy X-rays available, allows us to perform a complete tomographic acquisition at high resolution (voxel size: 1.786 x 1.786 x 1.786 μm^3) within a second, providing thus a time-lapse view at ice crystals growing in a colloidal suspension (**Figure 122**).

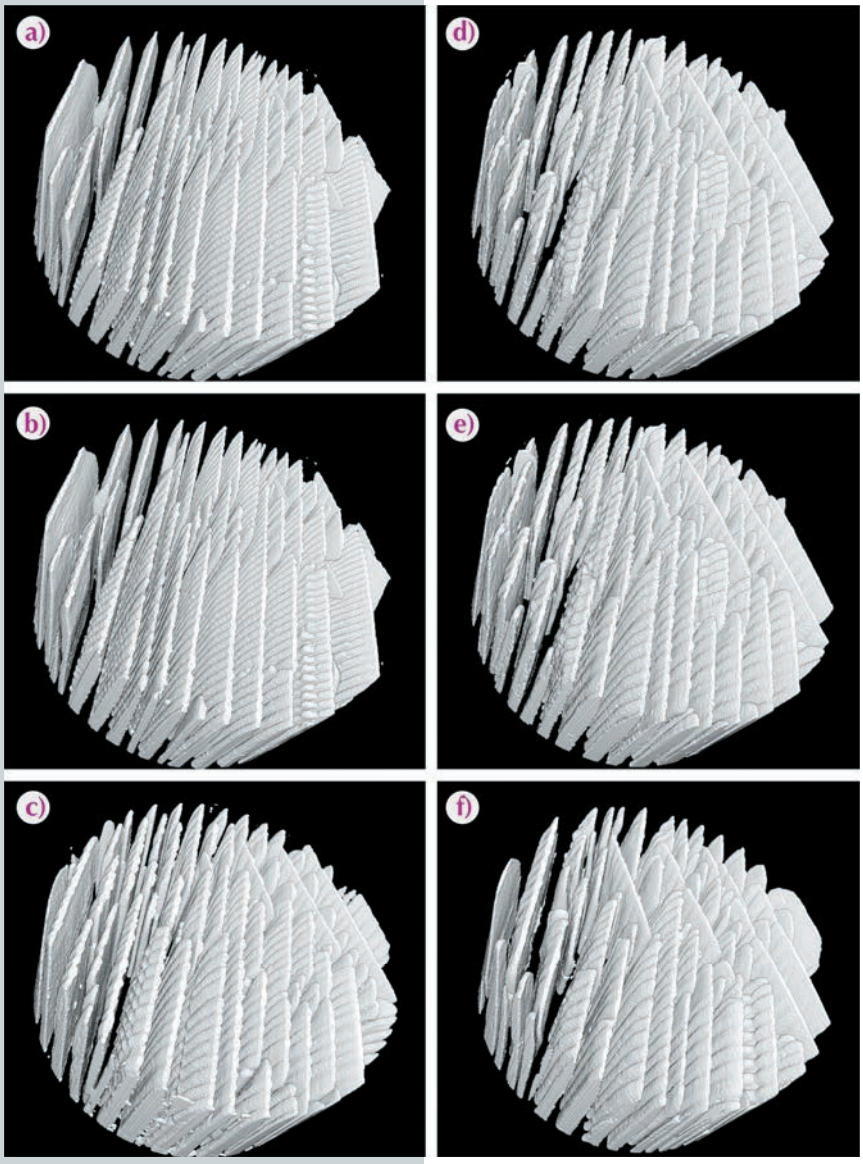

Fig. 122: Time-lapse sequence of ice crystals morphology. 3D reconstruction of the ice crystals, from tomographs taken every minute. The diameter of the reconstruction region is 860 µm. The colloids, concentrated between the growing crystals, are not shown on the reconstruction. Voxel size: 1.786 x 1.786 x 1.786 μm^3.

Three dimensional *in situ* observations of such solidification systems have never been obtained so far. What is new and unique here can be placed in three main categories:

• Qualitative observations: the actual morphology of the ice crystals growing into a colloidal suspension have never been observed before. Our observations reveal, for instance, the specific morphology of the tip of the crystal, which is strongly asymmetric (inset in **Figure 123**). This is very different from the usual dendritic morphologies observed in solidification, where the tip is highly symmetrical.

• Quantitative observations: the growth kinetics can be measured

both along the temperature gradient and perpendicular to the temperature gradient, a measurement that has never been obtained thus far. The measurements (**Figure 123**) show that for the latter, the growth kinetics is constant until the particle concentration in the inter-crystals space becomes really high. The presence of particles in this case has thus very little influence over the growth kinetics, until the particles are closely packed. We can also compare the growth kinetics in both directions (parallel and perpendicular to the temperature gradient) and conclude that they are actually quite similar. This is an important result since the lateral growth kinetics dictates the conditions for particle redistribution between the crystals, which in turn influence the behaviour or properties of the frozen assembly.

• X-ray computed tomography is a very popular and powerful technique for solidification studies. These results also highlight some limitations of the technique for this very particular and sensitive system, in particular regarding the influence and absorption of the beam. We found here that aqueous systems are highly sensitive to small variations of temperature (a few degrees), which can drastically affect the solidification behaviour and resulting morphologies. Further improvement of the imaging conditions should nevertheless allow us to obtain artefact-free observations.

There are currently no alternatives to this fast-tomography imaging approach permitting such qualitative and quantitative information to be obtained. This approach proved critical for our understanding of the complex process of crystallisation from a colloidal suspension.

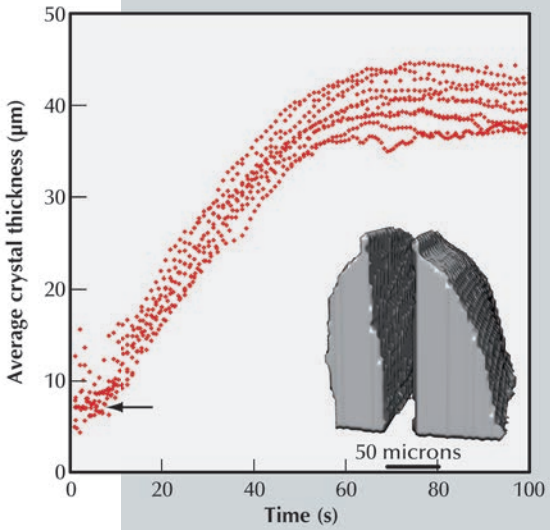

Fig. 123: Evolution of ice crystal thickness. The corresponding crystals tip morphology is shown in the inset.

PAIR DISTRIBUTION FUNCTION COMPUTED TOMOGRAPHY

Recent times have seen the development of a number of X-ray analytical methods that enable the mapping of chemical and structural information from bulk objects in 3, 4 and even 5D **[1]**. Notably, this includes the development of X-ray diffraction computed tomography (XRD-CT) which allows a chemical and physical insight into solid-state chemistry processes as well as the mapping of physical parameters such as crystallite size **[2,3]**. However, obtaining quantitative structural information for nanoscale objects is a challenge since they lack crystalline order. The X-ray pair distribution function (PDF) method offers a way forward to obtain reliable, quantitative information on nanostructures. Here we demonstrate the successful coupling of pair distribution function analysis with computed tomography (CT) to yield the first data obtained by PDF-CT, enabling physicochemical profiling of the nano-properties of materials and their distribution in 3D space with micrometre resolution.

Initial studies focused on the determination of the composition of a mixture of amorphous and semi-crystalline materials. The images of the distributions of each component are shown in **Figure 124**. The distributions found by PDF-CT are shown (a-e) with the Compton scatter image shown in (f). Representative XRD and PDF patterns from a voxel containing each component are also shown in the figure for comparison. The PDF-CT images were obtained by fitting a linear combination of the PDFs of each component in each voxel and then plotting the fraction of each phase. The resulting images give a clean separation of the different

Principal publication and authors
S.D.M. Jacques (a, b), M. di Michiel (c), S.A. J. Kimber (c), X. Yang (d), R.J. Cernik (a), A.M. Beale (b, e, f) and S.J.L. Billinge (d,g), *Nat. Commun.* **4**, 2536 (2013).
(a) School of Materials, University of Manchester (UK)
(b) Research Complex at Harwell, Rutherford Appleton Laboratory, Didcot (UK)
(c) ESRF
(d) Materials Science and Engineering, Columbia University, New York (USA)
(e) Department of Chemistry, University College London (UK)
(f) Inorganic Chemistry and Catalysis, Debye Institute for Nanomaterials Science, Utrecht University (The Netherlands)
(g) Condensed Matter Physics and Materials Science Department, Brookhaven National Laboratory, Upton (USA)

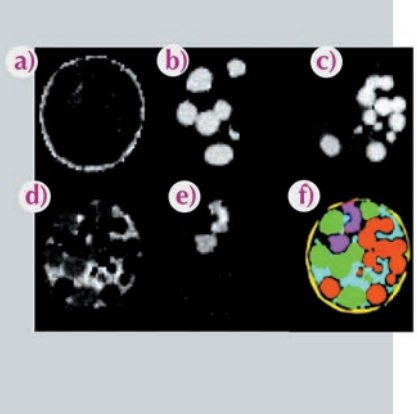

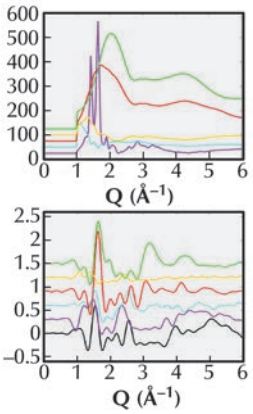

Fig. 124: (left) A-E distribution of Kapton™ (a), basalt (b), red (c), polystyrene (d) and PMMA (e) respectively, as determined by XRD-CT (top) and the PDF-CT (bottom). Shown in image (f) of the XRD-CT data is the corresponding Compton image, whilst image F in the PDF-CT is the colour coded composite image determined from components A-E coloured accordingly: yellow (Kapton™), green (basalt), red (glass), pink (polystyrene) and PMMA (cyan). The line graphs, right, show portions of XRD (top) and PDF's (bottom) for the individual components coloured in accordance with the composite image.

species present with virtually no misassignment. In many cases the nature of the shortest chemical bond is sufficient to distinguish between the components rendering the technique capable of providing chemical bond or species contrast tomography irrespective of kinetic state.

The second study focused on catalyst bodies which comprise mm-sized porous support units (typically cylinders/spheres) loaded with metals/metal oxides and used in large-scale industrial catalysis. In this demonstration study, we chose to study the distribution of Pd species that comprise the active component for both hydrogenation and oxidation reactions. **Figure 125** (left) shows the reconstructed distributions of selected atomic scattering pairs pertaining to the same crystalline phases, *e.g.* the components with peaks at 3.44 and 2.71 Å in the radial distribution functions due to Pd-Pd pairs in PdO and fcc Pd, respectively. In the treated sample, the XRD-CT map in **Figure 125** suggests a preferential distribution of both PdO and Pd phases at the sample periphery. In contrast whilst PDF-CT confirms the preferential concentration of the Pd/PdO seen in XRD-CT, 'diffraction silent' metallic Pd particles are also present inside the catalyst body. The observation of diffraction silent Pt in the core of the catalyst is verified further by quantitative analysis of representative PDFs from voxels from the periphery and the core shown in **Figure 125** (right). The PDF signal from the "diffraction silent" nanoparticles in the centre of the catalyst body dies out very quickly suggesting these nanoparticles must be very small. Using a spherical model as an approximation of the particles present to the calculated PDF, a good fit for a nanoparticle diameter of ~ 1.4 nm was obtained. In contrast, the particles located at the sample periphery exceed ~ 4 nm.

This new technique is likely to have a significant impact in a wide range of research disciplines from materials science, biomaterials, geology, environmental science, palaeontology and cultural heritage to health.

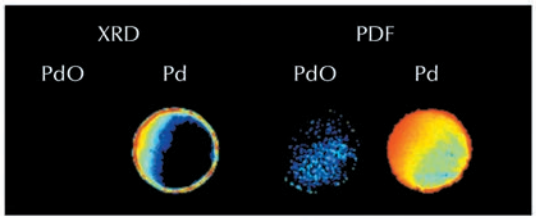

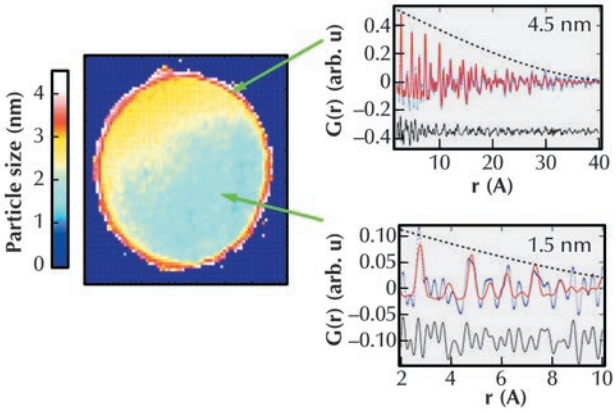

Fig. 125. (Top) Comparison of information from XRD-CT (left) and PDF-CT (right) after sample reduction. (Bottom) Distribution of particle sizes of fcc Pd within the catalyst body under reducing conditions. (Bottom Right) portions of the PDF data for selected pixels at the edge and interior of the catalyst body.

References

[1] A.M. Beale, J. Ruiz-Martinez and B.M. Weckhuysen, *In situ* characterisation of heterogeneous catalysts, Eds. J.A. Rodriguez, J.C. Hanson, P.J. Chupas and J. Wiley & Sons, Chichester (2013).

[2] P. Bleuet, E. Welcomme, E. Dooryhee, J. Susini, J.L. Hodeau and P. Walter, *Nat. Mater.* **7**, 468 (2008).

[3] S.D.M. Jacques, M. di Michiel, A.M. Beale, T. Sochi, M.G. O'Brien, L. Espinosa-Alonso, B.M. Weckhuysen and Paul Barnes, *Angew. Chem. Int. Ed.* **50**, 10148, (2011).

BIO-INSPIRED BAND-GAP ENGINEERING OF ZINC OXIDE: HR-XRD STUDY OF AMINO ACID INTRA-CRYSTALLINE INCORPORATION

Principal publication and authors
A. Brif (a), G. Ankonina (a), C. Drathen (b) and B. Pokroy (a), *Adv. Mater.* (2014); DOI: 10.1002/adma.201303596.
(a) Materials Science & Engineering and the Russell Berrie Nanotechnology Institute, Technion - Israel Institute of Technology, Haifa (Israel)
(b) ESRF

Crystals produced by organisms are attracting extensive scientific interest because they present enhanced structural properties as compared to non-biogenic crystals. Particular attention has been directed to biogenic calcium carbonate owing to its enhanced fracture toughness. This is achieved by the presence of intra-crystalline organic molecules within individual crystals. These intra-crystalline molecules have also been shown to strongly influence crystal shape, morphology and coherence length [1]. Another outcome of their presence is the existence of systematic anisotropic lattice strain [2]. We have shown previously that incorporation of proteins and even of single amino acids into synthetically grown calcium carbonate leads to similar lattice strain [3].

So far, we know of no studies showing that amino acids or biological molecules can become incorporated into the lattice structures of non-carbonate materials. By high-resolution X-ray powder diffraction at beamline **ID31,** we found that in a manner similar to that observed for calcium carbonate, amino acids can be incorporated into the crystal lattice of ZnO. We show, moreover, that such incorporation exists and that the induced lattice strain accompanying the incorporation leads to systematic changes in the band gap of the semiconductor host.

Our first objective was to determine whether amino acids could become incorporated into the lattice of ZnO. To this end we grew ZnO in the presence of various amino acids at different solution concentrations. In the test case of serine, we found that serine indeed became incorporated and induced lattice strain of up to about 0.2% in the ZnO host. As the level of incorporation increased, so did the strain. Moreover, similarly to that observed in biogenic and biomimetic calcium carbonate, the strain relaxed upon mild thermal air annealing (300°C for 90 min) and a unique microstructure developed, characterised by broadening of the diffraction peaks (**Figure 126a**).

We then screened all the common amino acids and found that a reasonable number of them do indeed become incorporated at different levels (along both a-axis and c-axis) into the ZnO lattice, with resulting lattice strain (**Figure 126b**).

These results clearly demonstrated that the incorporation of amino acids into other crystalline materials is feasible and might even be a widespread phenomenon. We believe that these findings can have considerable impact on tuning the properties of new functional materials. In the present case, because ZnO is a semiconductor, we expected that the incorporation of organic molecules within the host lattice and the resulting lattice strain induction would alter the electronic properties as compared to pure ZnO crystals. We therefore measured the optical band gap of our amino acid-incorporating ZnO crystals.

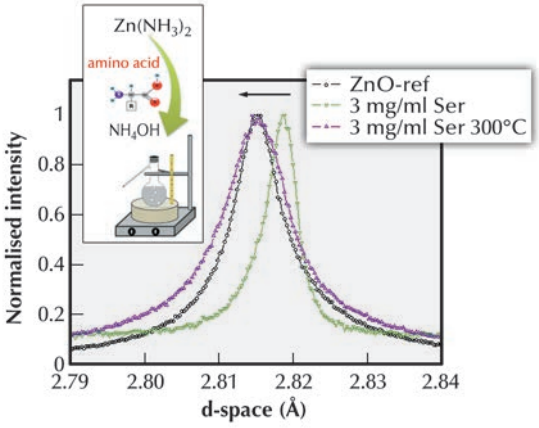

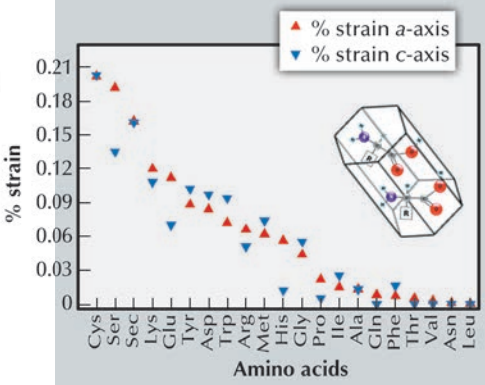

Fig. 126: a) (100) Diffraction peak of ZnO crystals of pure ZnO (dashed black), ZnO grown in the presence of 3 mg/ml serine before (green) and after annealing at 300°C for 90 min (purple). b) Lattice strain of ZnO with incorporated amino acids along the a-axis (red) and along the c-axis (blue).

References
[1] A. Berman, J. Hanson, L. Leiserowitz, T.F. Koetzle, S. Weiner and L. Addadi, *Science* **259**, 776 (1993).
[2] B. Pokroy, J.P. Quintana, E.N. Caspi, A. Berner and E. Zolotoyabko, *Nat. Mater.* **3**, 900 (2004).
[3] S. Borukhin, L. Bloch, T. Radlauer, A. H. Hill, A. N. Fitch and B. Pokroy, *Adv. Funct. Mater.* **22**, 4216 (2012).

By collecting diffuse reflectance spectra with a UV-spectrophotometer and applying the Kubelka-Munk method, we screened the band gap alternation of ZnO/amino acid composites, before and after thermal annealing, compared to a reference sample (**Figure 127**). It was interesting to observe, firstly, that the band gap was indeed altered due to the amino acid incorporation, and secondly that there is a linear relationship between the magnitude of strain induced by the incorporation and the change in band gap of the ZnO crystalline host .

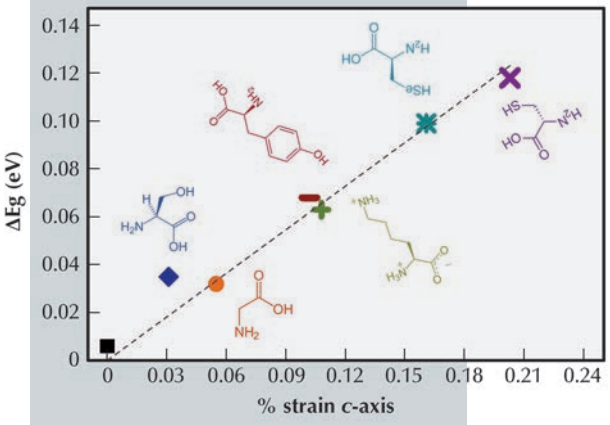

Fig. 127: Band gap energy values variation before and after annealing (ΔEg) as a function of c-axis strain of ZnO samples crystallised in the presence of different amino acids.

The key experimental results obtained were (1) that amino acids can be incorporated into other inorganic crystalline hosts, ZnO in the present case, and (2) that incorporation of amino acids into an inorganic crystalline semiconductor host induces not only lattice strain, as previously observed in biogenic and biomimetic calcium carbonate, but also a considerable band gap shift. We believe, moreover, that this could announce a new bio-inspired route, in addition to and in combination with current methods, for tuning of the band gaps of semiconductors.

In situ REDUCTION STUDY OF COBALT MODEL Fischer-Tropsch SYNTHESIS CATALYST

Principal publication and authors
H.E. du Plessis (a), R.P. Forbes (a), W. Barnard (a), W. Erasmus (a), A. Ferreira (a) and A. Steuwer (b,c), *PCCP* **15**, 11640-11645 (2013).
(a) Sasol technology R&D Pty Ltd, Sasolburg (South Africa)
(b) MAX IV Laboratory, Lund (Sweden)
(c) Nelson Mandela Metropolitan University, Port Elizabeth (South Africa)

Fischer Tropsch (FT) catalysis is an important industrial process for the manufacture of a variety of hydrocarbons and oxygenated hydrocarbons from a mixture of carbon monoxides and hydrogen (in the presence of a catalyst). It generally involves several chemical reactions which can be summarised by:

$$(2n + 1)\,H_2 + n\,CO \rightarrow C_nH_{(2n+2)} + n\,H_2O$$

where n is an integer. For cobalt catalysts these reactions occur in the temperature range of 200 - 250°C, and increase in efficiency with pressures [1]. The FT reaction is widely used in industrial plants worldwide in regions of rich natural gas resources to produce liquid fuel products. Cobalt-based catalysts appear to provide the best compromise between performance, life-time and cost for the synthesis of hydrocarbons from CO/H_2 mixtures [2]. Cobalt catalysts, like other oxide-

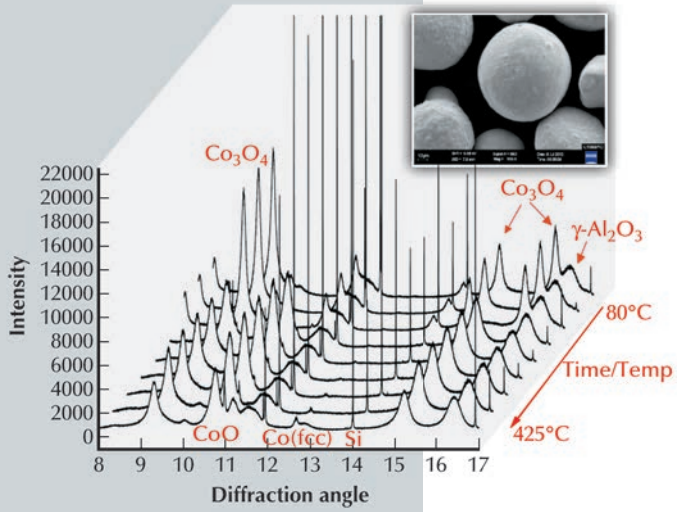

Fig. 128: The experimental diffractograms during reduction from 80°C to 425°C, indicating, in particular, the peaks from the Si reference (very narrow), and the evolution of the cobalt oxide to metallic cobalt.

based catalysts, undergo a reduction or activation treatment before FT can occur. Cobalt is not used as pure solid, but often supported, *i.e.* deposited on inert material such as alumina. The insert in **Figure 128** shows one such alumina particle (of about 80 µm size) on the surface of which the cobalt oxides are deposited (of sub-micrometre size).

A fundamental understanding of the exact reduction pathway of supported cobalt oxides and the intermediates can assist in developing improved industrial supported cobalt catalysts. However *in situ* investigations of the activation process are challenging given the temperature and pressure requirements, and of course the ability to penetrate metallic substances. Thus, the penetration capability and brilliance of hard X-rays from a synchrotron source provide a unique tool for the investigation of chemical processes under *in situ* conditions and in a time-resolved manner.

Here we present a synopsis of the results from measurements made during *in situ* reduction of a model Co/alumina catalyst using *in situ* synchrotron X-ray diffraction at beamline **ID31** using both conventional XRD and total scattering (PDF), the latter adds the ability to probe local structures.

The experiment used a wavelength of 0.3999 Å, which is equivalent to 31.0 keV. The powder diffractograms were collected to a maximum angle of 60°2θ (step size 0.001°2θ) to obtain the resolution required for accurate structure refinement, as well as PDF analysis. Longer counting times were used at higher *q*-space values (the range of *q*-space probed was thus 1.00 to 14 $Å^{-1}$). An inert reference standard, Si, was added to the sample as internal reference to determine the amorphous content in the catalyst during reduction. The reduction was done at ambient pressure in hydrogen with a flow rate of 16 $L.g\text{-}cat^{-1}.hr^{-1}$. The *in situ* reduction measurements were optimised by measuring 20 minute diffractograms at the following selected temperatures: 80, 160, 200, 240, 260, 280, 320, 360 and 425°C. Six diffractograms were measured at 425°C during a holding time of 2 hours. The heating rate was 10°C/min between measurements, resulting in an average heating rate of 1.6°C/min over the complete reduction. The diffractograms were analysed in Rietveld mode using Topas, and the software package PDFGui. **Figure 128** show the diffractograms as collected from 80°C to 425°C. The Si reference peaks are clearly visible, as is the reduction of the cobalt oxide, Co_3O_4. It is clear that Co_3O_4 was completely reduced to CoO at around 240°C. The reduction of CoO to cobalt metal was slower with the maximum phase abundance of CoO at 280°C. The gradual decrease of CoO phase abundance coincided with an increase in amorphous content as well as cobalt metal abundance. The quantification of the amorphous content shows the limits of the Rietveld technique, but the total scattering approach provided the additional information contained in the diffuse scattering, **Figure 129**. Comparison with the ICP-OES results proved that only the total scattering approach can account for all the cobalt in the catalyst.

Hard synchrotron X-rays have been successfully used to study the reduction process of Co-based, aluminium supported catalyst *in situ*. The collected diffractograms allowed the refinement of the different crystalline phases, their structures and volume fractions, as well as probing the local structure (disorder) using PDF refinement. The PDF refinement accounted for all cobalt present in the catalyst sample and showed that after reduction mainly Co metal remained. This is a novel approach to *in situ* PDF analysis of catalysts containing a mixture of phases.

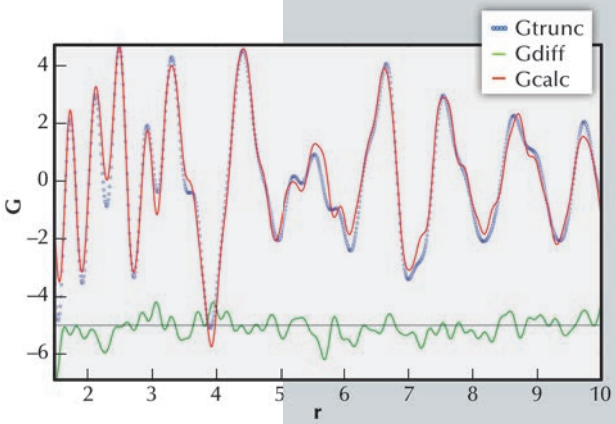

Fig. 129: The PDF fit of the reduced catalyst (Experimental (blue); calculated (red); difference (green)).

References
[1] E. Iglesia, *Appl. Cat. A* **161**, 59–78 (1997).
[2] C.G. Visconti, E. Tronconi, L. Lietti, P. Forzatti, S. Rossini and R. Zennaro, *Top Catal* **54**, 786–800 (2011).

Principal publication and authors
M.-C. Schlegel, A. Sarfraz, U. Mueller, U. Panne and F. Emmerling, *Angew. Chem. Int. Ed.* **51**, 4993–4996 (2012).
BAM Federal Institute of Materials Research and Testing, Berlin (Germany)

FAST TIME-RESOLVED CEMENT HYDRATION STUDIES

Modern architecture cannot get along without concrete, no matter whether it is a giant skyscraper or an underground project. Concrete is made from sand, gravel, additives, water, and cement. Cement is the component in concrete that holds the other components together. To control the properties of concrete, it is necessary to know what occurs as it hardens. We have studied the first seconds in this process, the first few seconds in the "life of a building", by means of X-ray diffraction. Furthermore, these studies made it possible for us to understand the role of superplasticisers added to the initial cement water mixture.

Ordinary Portland cement (OPC) is a mixture of finely ground limestone, clay, sand, calcium silicates, aluminum and iron compounds and sulfates. Directly after mixing with water, chemical reactions between the components of cement and water lead to solidification and hardening. The rapidly initiated reaction of the cement clinker component C3A($Ca_3Al_2O_6$) with sulfate (SO_4^{2-}) to form ettringite ($Ca_6Al_2(SO_4)_3(OH)_{12}\cdot 26H_2O$) is one of the important steps [1]. The enormous stability of concrete stems from crystalline needles of ettringite that are formed during this process. These needles are firmly interlocked with each other.

Different additives are used to optimise the properties of concrete. These additives improve the flow of the concrete, making it easier to process. Furthermore, the water content can be reduced which improves the compressive strength of concrete. A typical class of superplasticisers is based on polycarboxylate-ether (PCE) [2].

The formation of the phases at the beginning of the hydration process was not understood in detail. Detailed insight into the different stages of the

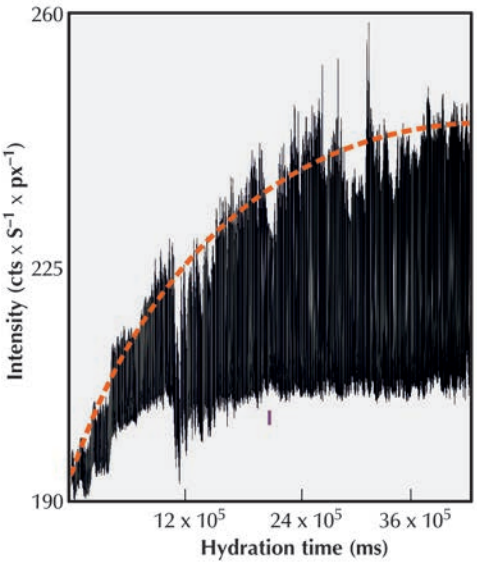

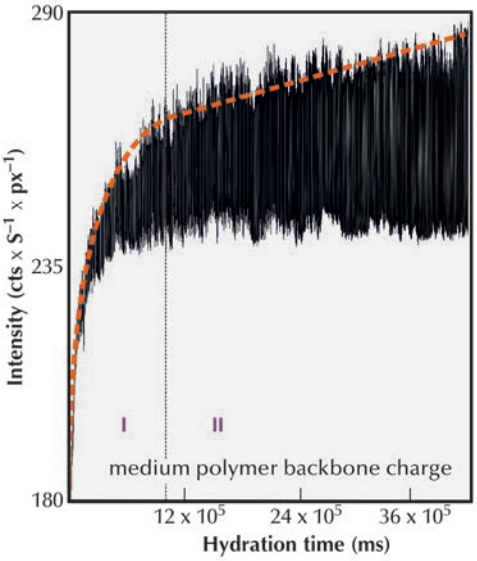

Fig. 131: Side view of the ettringite (100) reflection as a function of time. Top: Ordinary Portland cement; bottom: OPC with PCE admixtures. The growth process can be separated into an initial exponential (I) and into a linear (II) increase of the reflection intensity (dashed line).

Fig. 130: Contact free analysis of the hydration of cement using an acoustic levitator.

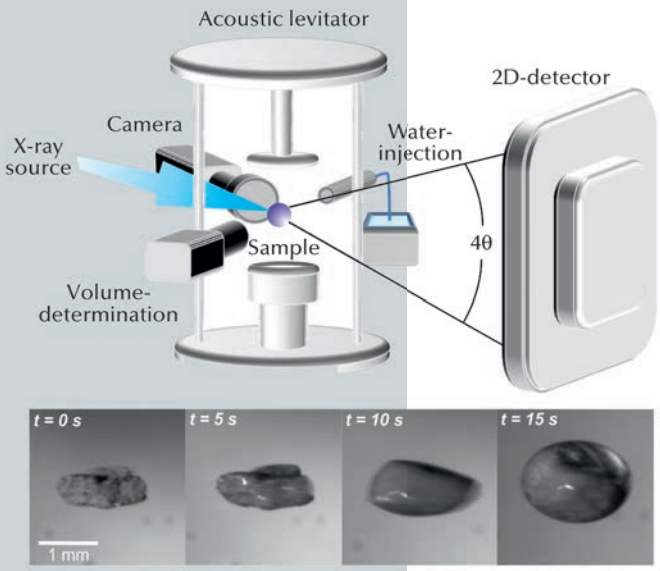

hydration process is essential for a more complete understanding of how these processes can be effectively influenced. Time resolved *in situ* X-ray diffraction experiments with a resolution of 500 ms were carried out at beamline **ID11** to follow this reaction. The reaction was carried out in an acoustic levitator (see **Figure 130**). A piece of Portland cement was held in suspension by acoustic waves in this sample environment. The reaction was initiated by spraying a defined amount of water onto the levitated sample. The experiment was repeated with samples containing different amounts of PCE superplasticisers. To characterise the influence of the superplasticisers, the development of the ettringite reflection (100) was investigated in detail. The hydration behaviour of the cement specimen is driven by the anionic charge densities of the PCE. The C3A in pure OPC reacts to ettringite as a function of the residual sulfate in the pore solution. This hydration behaviour results in a high initial formation of ettringite and its amount increases as a function of time (see **Figure 131**). The ettringite formation in PCE containing OPC is additionally influenced by the backbone charge density of the respective PCE. During the reaction with water, PCE is replaced by sulfate ions from the pore solution. An equilibrium between PCE adsorption and its replacement by SO_4^{2-} anions leads to a linear increase in the amount of ettringite. Consequently, a higher polymer backbone charge leads to a retarded adjustment of the equilibration state. Fewer sulfate ions replace PCE and the formation of ettringite is decelerated. Immediately after the contact between water and cement, the PCE adsorbs onto the surface of the clinker C3A. The particles, sterically stabilised in this way, remain in suspension and the PCE is then gradually replaced by sulfate ions, which retards the incipient ettringite crystallisation. Consequently, more free water is left in the system, dissolving more crystalline components and the resulting concrete can thus flow for a longer period and becomes more dense.

References
[1] A.N. Christensen, T.R. Jensen and J.C. Hanson, *J.Solid State Chem.* **177**, 1944–1951 (2004).
[2] R.J. Flatt, I. Schober, E. Raphael, C. Plassard and E. Lesniewska, *Langmuir* **25**, 845–855 (2009).

FIXED-ENERGY X-RAY ABSORPTION VOLTAMMETRY

To understand the phenomena occurring while a chemical reaction is in progress requires a determination of the oxidation state of a given element, which depends on several factors including its chemical environment and physicochemical conditions. This represents crucial information, whether the element plays the role of reactant/product or of catalyst, since most catalytic cycles involve continuous, periodic transitions between two or more oxidation states of the catalytic centre. This is particularly true in the study of heterogeneous catalysts, where the co-presence of different types of surface sites and the need for a supporting material makes investigation difficult.

X-ray absorption spectroscopy (XAS) represents the tool of choice here since it allows an element selective investigation of the oxidation state and chemical surroundings of a material under *"in situ"* or *"in operando"* conditions. Accepting the need for synchrotron radiation, the main limit of XAS is the time required for the recording of spectra and their interpretation. This aspect is partially compensated by QEXAFS (quick scanning EXAFS), allowing the acquisition of spectra within seconds. However, QEXAFS requires a continuous motion of the monochromator, and it is not available at all beamlines. Dispersive XAS can also allow the acquisition of a spectrum in the millisecond scale, but it requires a sophisticated and dedicated beamline.

Here, we introduce fixed-energy X-ray absorption voltammetry (FEXRAV) as a novel rapid XAS technique that can be applied to electrochemical systems for the *in situ* study of electrode materials.

Principal publication and authors
A. Minguzzi (a), O. Lugaresi (a), C. Locatelli (a), S. Rondinini (a), F. D'Acapito (b), E. Achilli (c) and P. Ghigna (c), *Anal. Chem.* **85**, 7009–7013 (2013).
(a) Dipartimento di Chimica, Università degli Studi di Milano, Milan (Italy)
(b) CNR-IOM-OGG c/o ESRF-GILDA, Grenoble (France)
(c) Dipartimento di Chimica, Università di Pavia, Pavia (Italy)

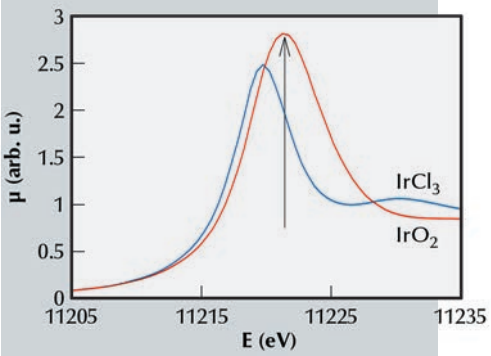

Fig. 132: Normalised XANES spectra of IrO_2 (red) and $IrCl_3$ (blue). The arrow marks the energy chosen for the FEXRAV measurements (11221.0 eV) reported in **Figure 133**.

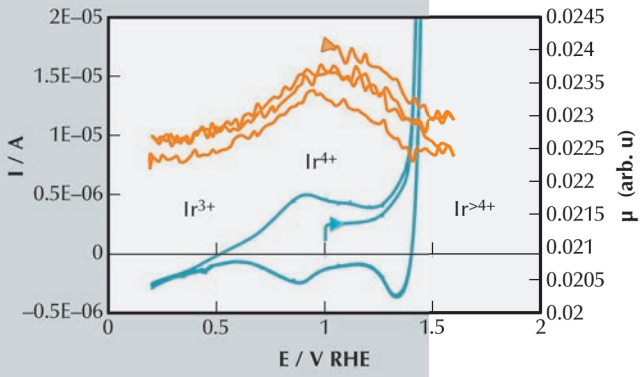

Fig. 133: Conventional cyclic voltammetry (blue line) and the relevant FEXRAV curve (red lines) and of iridium oxide recorded at 1 mV s^{-1}.

References
[1] A. Minguzzi, O. Lugaresi, E. Achilli, C. Locatelli, A. Vertova, P. Ghigna and S. Rondinini, *submitted*.

It consists of recording the X-ray absorption coefficient μ at a fixed energy while varying the electrode potential according to a predefined time function. The most common example is a triangular-shaped profile (cyclic voltammetry, CV), but any other shape is in principle applicable. The energy is chosen on the absorption edge in order to give the maximum contrast between different oxidation states of a given element. It follows that any shift from the original oxidation state determines a variation of the absorption coefficient.

Here we show that FEXRAV allows the variation of the oxidation states of the element under study within a selected potential window to be rapidly determined. With this aim, we used highly-hydrated iridium oxide films.

IrO_x has been studied for about four decades as one of the most active electrocatalysts for water oxidation, which is the limiting reaction in electrochemical or photoelectrochemical processes that lead to the production of hydrogen, *i.e.* for effective extraction of energy from renewable sources.

Figure 132 describes the basic idea of FEXRAV. The XAS spectrum at the Ir-L_{III} edge of IrO_2 (used as a standard for Ir^{4+}) is plotted with that of $IrCl_3$ (used as a standard for Ir^{3+}). It is evident that fixing the energy at the maximum of the absorption coefficient for IrO_2 (at 11221.0 eV, as indicated by the arrow) gives the maximum contrast between Ir^{3+} and Ir^{4+}.

With the X-ray energy fixed at 11211.0 eV, the FEXRAV curve plotted in **Figure 133** shows that the mean oxidation of Ir state crosses at least three different values while the applied potential was varied. The maximum of μ is in fact located at about 1 V (RHE) that corresponds to Ir^{4+}.

At lower potentials, the decrease in μ indicates the change of oxidation state toward a lower value, *i.e.* Ir^{3+}. At larger potentials, *i.e.* for E >1.0 V, μ decreases with increasing Ir average charge state. This last evidence is strictly related to the role of IrO_x as electrocatalyst for water oxidation [1].

In conclusion, FEXRAV allows us to rapidly study any species that can be immobilised onto a conductive substrate, in terms of its oxidation state (or any other property that causes a change in the X-ray absorption coefficient) while being dependent on the applied potential. We can screen samples for the application of more detailed local structural probes (XANES, EXAFS), rapidly define the potential windows at which each oxidation state is prevalent, extract important information on the reaction mechanisms, and extract kinetic constants or follow the reaction progression. Also, the latter case is useful especially considering that the FEXRAV signal is not influenced by "parasitic" electrochemical phenomena.

PUSHING THE LIMITS: GIANT NEGATIVE COMPRESSIBILITY

When squeezed uniformly, the overwhelming majority of materials shrink in all directions. We have discovered that the crystalline compound zinc dicyanoaurate, $Zn[Au(CN)_2]_2$, actually expands under such hydrostatic pressure in a range of directions, and does so at a rate that is many times greater even than the usual compressibility of conventional ceramics. This negative linear compressibility (NLC) response

has potential applications in the development of next-generation actuators, pressure sensors, and even artificial muscles [1].

The intuition that materials should shrink under pressure is grounded (rightly) in the underlying thermodynamics: pressure causes the free energy of a system to increase unfavourably unless there is an accompanying reduction in volume. The particular 'trick' of NLC materials such as $Zn[Au(CN)_2]_2$ is to couple volume reduction to linear expansion in one or more directions. In other words, their structures become longer as they become more dense. The wine-rack and honeycomb topologies are two examples of network geometries that respond to pressure in this way [2]. Indeed, we identified $Zn[Au(CN)_2]_2$ as a NLC candidate because its hexagonal crystal structure is based on the quartz topology, itself a three-dimensional honeycomb network (Figure 134).

Variable-pressure powder X-ray diffraction (PXRD) measurements, carried out using **BM01A,** the Swiss-Norwegian beamline, enabled us to determine how the crystal structure of $Zn[Au(CN)_2]_2$ changes when exposed to pressures of up to 14 GPa. From the variation in lattice parameters, we determined the crystal compressibilities, and by refining structural models against the diffraction intensities we could also monitor the accompanying changes in network geometry.

The compressibilities of conventional ceramics are usually around 5 TPa^{-1}, meaning a decrease in length of 0.5% for each 1 GPa pressure interval. For $Zn[Au(CN)_2]_2$, we measured compressibilities of +52(6) and –42(5) TPa^{-1} along directions perpendicular and parallel to the [001] hexagonal crystal axis. These values become smaller at the very highest pressures (as one expects); nevertheless by the end of our experiment the sample had grown by roughly 10% along the NLC direction (Figure 135). The long-standing 'record' response amongst the dozen or so previously-known NLC materials was just –1.2 TPa^{-1} (for elemental selenium), making the 'giant' NLC effect of $Zn[Au(CN)_2]_2$ all the more remarkable.

Our structural refinements revealed two key features responsible for such large compressibilities in this material. The first is that throughout the entire experiment there is remarkably little change to individual bond lengths and coordination geometries: the open framework structure, assembled from zinc 'nodes' and dicyanoaurate 'linkers' simply flexes in a way that would be expected to carry very little energy cost. The second feature is that the 'shock' of compressing this network so very rapidly in directions perpendicular to the [001] axis is accommodated by atomic-scale 'springs' assembled from highly polarisable gold atoms. So our study shows how a combination of structural engineering and supramolecular chemistry motifs might be coupled in order to design functional materials with counterintuitive mechanical responses.

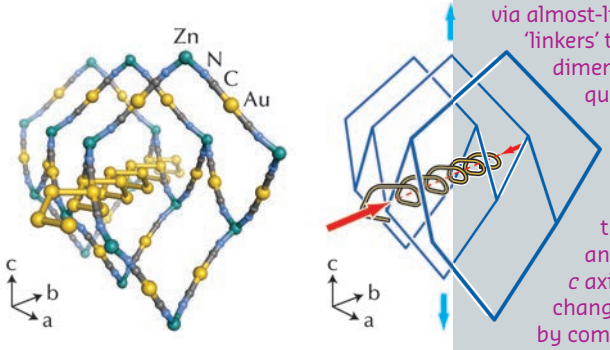

Fig. 134: The crystal structure of $Zn[Au(CN)_2]_2$ is assembled from tetrahedral Zn 'nodes', connected via almost-linear dicyanoaurate 'linkers' to give a three-dimensional network with the quartz topology. Under increasing hydrostatic pressure, this network reduces its volume by compressing along the *a* and *b* directions and expanding along the *c* axis. Rapid geometric changes are accommodated by compression of spring-like chains of gold atoms connected via weak 'aurophilic' interactions.

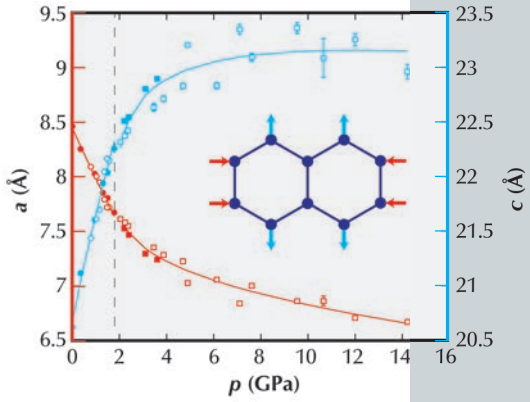

Fig. 135: Pressure-dependent variation in lattice parameters measured using PXRD. The NLC behaviour of $Zn[Au(CN)_2]_2$ is evident in the anomalous increase in the *c* lattice parameter with pressure. The vertical dashed line denotes a displacive phase transition to a related superstructure that also shows NLC.

Principal publication and authors
A.B. Cairns (a), J. Catafesta (b,c), C. Levelut (c) J. Rouquette (b), A. van der Lee (d), L. Peters (e), A.L. Thompson (a), V. Dmitriev (f), J. Haines (b) and A.L. Goodwin (a), *Nature Materials* **12**, 212–216 (2013).
(a) Inorganic Chemistry Laboratory, Department of Chemistry, University of Oxford (UK)
(b) Institut Charles Gerhardt, Université Montpellier 2, Montpellier (France)
(c) Laboratoire Charles Coulomb, Université Montpellier 2, Montpellier (France)
(d) Institut Européen des Membranes, Université Montpellier 2, Montpellier (France)
(e) Institut für Kristallographie, RWTH Aachen, Aachen (Germany)
(f) Swiss-Norwegian beamline, ESRF

References
[1] R. Baughman, S. Stafstrom, C. Cui and S. Dantas, *Science* **279**, 1522-1524 (1998).
[2] J. Grima, D. Attard, R. Caruana-Gauci and R. Gatt, *Scr. Mater.* **65**, 565-568 (2011).

MIXED-LINKER HYBRID SUPERPOLYHEDRA FOR LARGE-PORE IRON(III) CARBOXYLATE METAL–ORGANIC FRAMEWORKS

Principal publications and authors
H. Chevreau (a), T. Devic (a), F. Salles (b), G. Maurin (b), N. Stock (c) and C. Serre (a), *Angew. Chem. Int. Ed.*, **52**, 5056-5060 (2013).
(a) Institut Lavoisier de Versailles, CNRS, Université de Versailles St-Quentin en Yvelines (France)
(b) Institut Gerhardt, CNRS, ENSCM, Université de Montpellier (France).
(c) Institut fur Anorganische Chemie, Christian-Albrechts-Universität, Kiel, (Germany)

Metal organic frameworks (MOFs) are attracting great interest for their potential in various applications ranging from gas capture to storage to catalysis. While most of the solids reported in the literature are based on M^{2+} cations (*e.g.* Zn^{2+}, Cu^{2+}, Ni^{2+}), M^{n+} with $n \geq 3$ (Fe^{3+}, Al^{3+}, Cr^{3+}, Zr^{4+}, Ti^{4+}) species have been shown to induce higher chemical stabilities [1], which is often a prerequisite for further industrial applications. Among these cations, Fe^{3+} deserves special attention due to its low toxicity, which makes the resulting solids highly suitable for bio-applications such as drug release [2]. While the structural diversity is mainly induced by building structures with more and more complex organic ligands, an alternative consists of the use of a mixture of simple ligands with different symmetries. Applying such a strategy with linear dicarboxylic and planar tricarboxylic ligands, we were able to generate two series of original Fe^{3+} MOFs built up from hybrid polyhedra. Contrary to the case of the n = 2 counterparts, MOFs based on $n \geq 3$ are very often produced in a polycrystalline form, and as a consequence, their structures cannot be solved using laboratory single crystal X-ray diffractometers. Taking advantage of the versatility of the image-plate detector available at **BM01A**, the Swiss-Norwegian beamline, we solved the structures by a combination of single crystal and powder diffraction analyses, assisted with molecular simulations. Using a mixture of 1,4-benzenedicarboxylic acid (H_2-bdc) (**Figure 136b**) and 1,3,5-tris(4-carboxyphenyl)benzene (H_3-btb) (**Figure 136c**), we have generated two solids, both based on the same inorganic unit, which consists of three corner sharing FeO_6 octahedra surrounded by six carboxylate groups (**Figure 136a**). Organic and inorganic units assemble to define hybrid super-polyhedra, built up from Fe trimers at their corner and ligands on their edges (when ditopic) or faces (when tritopic). The structure of the first solid (later called MIL-143, MIL stands for Materials Institut Lavoisier), which was isolated at shorter reaction time, was solved from powder diffraction. Its cubic structure consists of an alternation of two types of hybrid super-tetrahedra, one based on bdc and identical to those found in the single ligand solid MIL-101 [3], and the second one based on btb (**Figure 136**). This defines an extended ß-cristobalite topology and mesoporous cages (**Figure 136**) leading to a high surface area (S_{BET} above 2000 $m^2.g^{-1}$). The structure of the second phase (denoted MIL-142), which was isolated at longer reaction

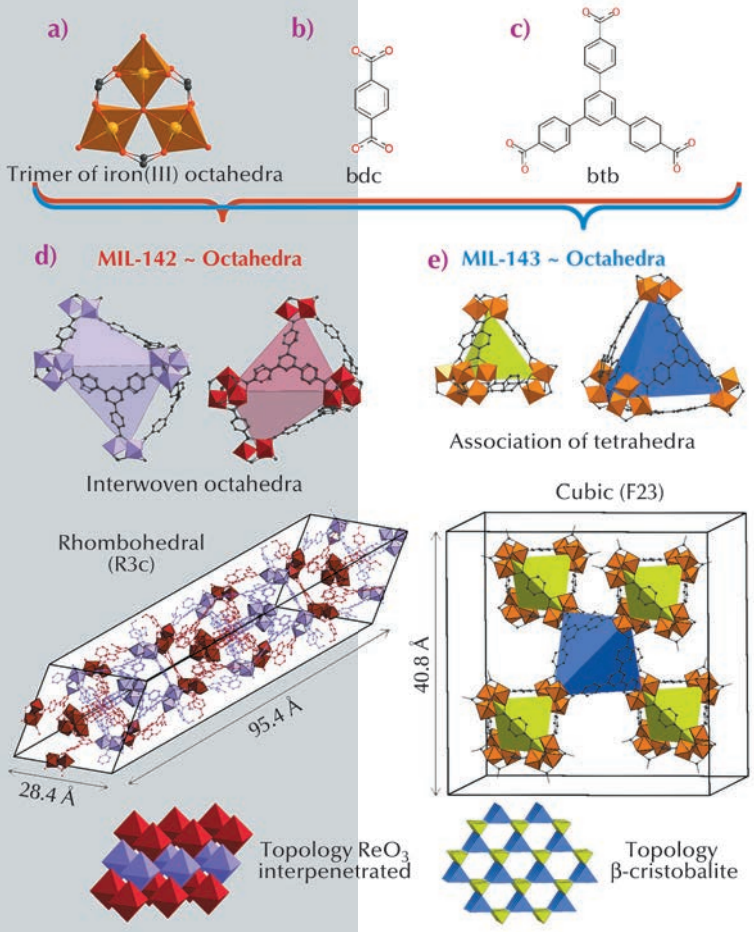

Fig. 136: (a) Trimers of iron(III) octahedra. (b) Terephthalate linker. (c) 1,3,5-tris(4-carboxyphenyl)benzene linker. (d) & (e) Representation and topology of MIL-142 and MIL-143, respectively. Hydrogen has been omitted for clarity.

time, was solved from single crystals. It crystallises in a rhombohedral system with an unusually large *c* parameter (~ 95 Å), and is constructed from a single type of hybrid super-octahedron (SO). The latter is built up from a mixture of ligands, with four faces occupied by btb linkers, and one face defined by three bdc ligands, the remaining faces not being occupied (**Figure 136**). Such SOs assemble to define a ReO_3 network type, the whole structure being ultimately built from two such interwoven networks, leading to micropores (~ 7-10 Å) and a surface area around 1500 $m^2.g^{-1}$.

In a last step, using longer, functionalised dicarboxylate ligands, the MIL-142 and MIL-143 series were extended through an isoreticular approach. The structure of these solids was determined through a computational assisted approach (experimental unit-cells combined with simulated structures derived from the known ones); analyses included the impact of the functionalisation on the pore size and shape.

References
[1] J.J. Low, A.I. Benin, P. Jakubczak, J.F. Abrahamian, S.A. Faheem and R.R. Willis, *Journal of the American Chemical Society* **131**, 15834-15842 (2009).
[2] P. Horcajada, T. Chalati, C. Serre, B. Gillet, C. Sebrie, T. Baati, J.F. Eubank, D. Heurtaux, P. Clayette, C. Kreuz, J.-S. Chang, Y.K. Hwang, V. Marsaud, P.-N. Bories, L. Cynober, S. Gil, G. Férey, P. Couvreur and R. Gref, *Nat. Mater.* **9**, 172-178 (2010).
[3] G. Férey, C. Mellot-Draznieks, C. Serre, F. Millange, J. Dutour, S. Surblé and I. Margiolaki, *Science* **309**, 2040-2042 (2005).

FROM DISCOVERY TO INVENTION – RATIONAL DESIGN OF ZEOLITES

Since their discovery, zeolites have become the heavy duty molecular machinery of the chemical industry. With their unique porous frameworks, these crystalline aluminosilicates are essential as catalysts and adsorbents for a wide range of applications in petrochemistry, environmental chemistry and water treatment. Despite their importance, the fraction of zeolites used in commercial applications represents less than 10% of all zeolite frameworks hitherto described. This contrast originates from the fact that new zeolites, up to now, have either been discovered in geological deposits or in trial and error syntheses. Until now, rational design of new frameworks to fulfil a specific function in chemical processes has been out of reach. However, the need for reconversion of our fossil fuel based economy makes the availability of zeolites with a tailored framework structure and functionality more important than ever.

Currently, zeolite synthesis exploits mono-, oligo- and polymeric sources of framework elements. The resulting zeolite topologies depend on a large number of parameters and the outcome of most syntheses remains unpredictable. Envisioning rational zeolite design, pre-fabricated building units have been proposed as an alternative to monomeric or colloidal species. Re-assembly of building units existing in a known zeolite provides a promising route. Such building units can for example be harvested by controlled disassembly of existing zeolites. Upon isolation, the building units obtained can be rearranged. Essentially, this comes down to the transformation of existing zeolites into new frameworks with tailored properties.

Recently, two new zeolites COK-14 and –COK-14 were created via this approach. COK-14 is the first material with a new all-silica framework topology (OKO framework) with a two-dimensional channel system and interconnecting 8-, 10- and 12-membered rings (**Figure 137**). In its interrupted form, called –COK-14, the zeolite additionally has silanol groups pointing systematically into the 12-membered ring (**Figure 137**). To synthesise these zeolites, building units from the existing IM-12 zeolite were harvested and selectively rearranged. The structure of IM-12 zeolite consists of all-silica sheets interconnected by cubic struts containing one germanate and one silicate four-ring (4R). Acid treatment selectively removes the germanate 4R from the framework leaving the silicate 4R attached to the intact silicate sheets. This structure is consequently recycled as a building

Principal publication and authors
E. Verheyen (a), L. Joos (b), K. Van Havenbergh (c), E. Breynaert (a), N. Kasian (a, d), E. Gobechiya (a), K. Houthoofd (a), C. Martineau (e), M. Hinterstein (f), F. Taulelle (e), V. Van Speybroeck (b), M. Waroquier (b), S. Bals (c), G. Van Tendeloo (c), C. E.A. Kirschhock (a) and J.A. Martens (a), *Nat. Mater.* **11,** 1059-1064 (2012).
(a) Center for Surface Chemistry and Catalysis, KU Leuven, Heverlee (Belgium)
(b) Center for Molecular Modeling, Ghent University, Zwijnaarde (Belgium)
(c) Electron Microscopy for Materials Science, University of Antwerp (Belgium)
(d) L.V. Pisarzhevsky Institute of Physical Chemistry, National Academy of Sciences of Ukraine, Kyiv (Ukraine)
(e) Tectospin, Institut Lavoisier, UMR 8180 Université de Versailles Saint Quentin en Yvelines (France)
(f) Institut für Werkstoffwissenschaft, Technische Universität Dresden (Germany)

unit and reconnected into COK-14 or –COK-14, depending on the hydration state. Overall, the transformation from IM-12 to COK-14 involves the removal of one layer of T-atoms and as such is the first experimentally observed inverse sigma transformation.

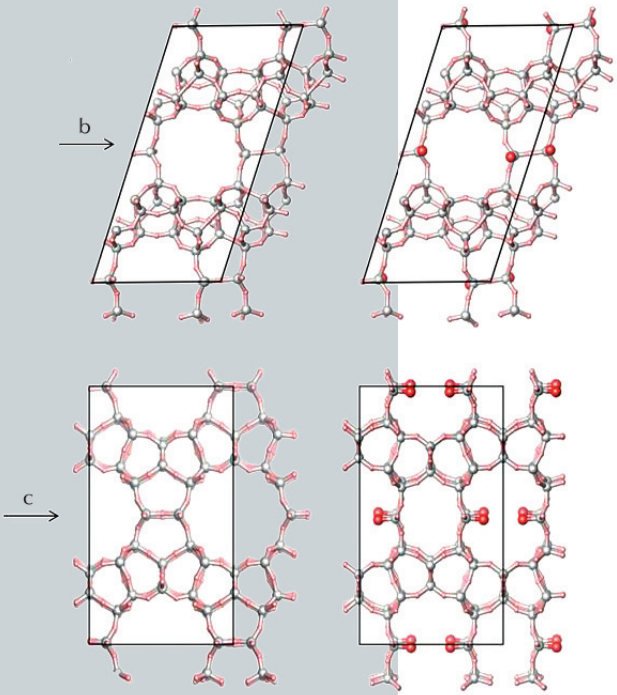

Fig. 137: COK-14 framework (left) and -COK-14 framework (right). OH groups in –COK-14 are highlighted in red.

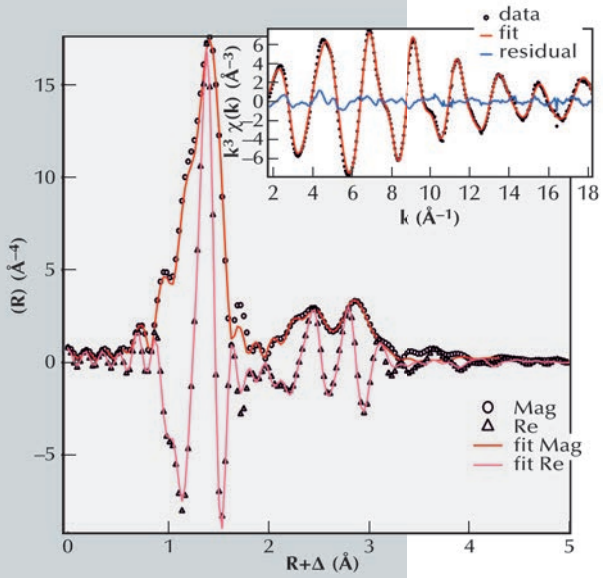

Fig. 138: k_3 weighted Ge K-edge EXAFS data as inset and its Fourier transform (magnitude/ real part) for IM-12.

The choice for IM-12 zeolite as a source of building units resulted from its interesting geometry of silicate layers connected by germanate and silicate four-rings. The arrangement of germanium (Ge) in this zeolite was analysed by Ge K-edge EXAFS at **BM01B**, the Swiss Norwegian Beamline (SNBL), in collaboration with **BM26**, DUBBLE Beamline. EXAFS analysis revealed that each Ge centre was connected to 4 oxygen atoms (3+1) at respectively 1.75 Å and 1.85 Å **(Figure 138)** and two Ge neighbours at 3.16 Å. In combination with high resolution powder X-ray diffraction (HRXRD) data obtained from the same sample, this geometric unit was localised unambiguously as a germanate 4R in the cubic unit connecting all-silicate layers in the structure of IM-12.

Ge K-edge EXAFS and HRXRD measurements were of key importance to reveal the Ge distribution in IM-12. The presence of a Ge four-ring in the structure allowed us to isolate separate silicate building units. These can be alternatively stacked to form new zeolites in a more rational zeolite synthesis approach. Discovering the ordered arrangement of Ge in IM-12 zeolite not only led to the synthesis of new zeolites –COK-14 and COK-14. With this knowledge, we are now studying the synergy between the overall zeolite synthesis conditions and the final Ge arrangement in the framework. This leads to several new synthesis approaches for obtaining similar Ge distributions in a zeolite.

ENABLING TECHNOLOGIES

Enabling technologies and associated research & development programmes are typically science-driven, but experience shows that new technologies can also enable new science. One of the challenges of the Upgrade Programme is to find a fair balance between the developments driven by new beamlines and the mid- and long-term R&D programmes that will set the stage for the next-generation instrumentation and therefore new scientific programmes. Indeed, the high level of sophistication and integration of synchrotron radiation instrumentation demands new strategies, where every element must be conceived within the global picture of the instrument and its expected performance. The collection of highlights selected this year illustrates this paradigm, where engineering, software and computing technologies are intricately intertwined with scientific applications. Several key developments initiated during the Upgrade Programme Phase I are presented: some focus on applications whilst others on instrumentation developments.

The first article presents a new imaging technique using a 2D detector to obtain phase contrast with edge-illumination. The feasibility of this technique, originally developed for incoherent sources, has been proven for the first time on a partially coherent synchrotron source over a wide energy range. Thanks to a long sample-to-detector working distance, high angular resolution was achieved, translating into detection of very weak density gradients.

The second article reminds us that sometimes managing a coherent beam for imaging applications can be tricky. A number of lens-less full-field techniques have been developed with the clear advantage of being fast but requiring a homogeneous incoming wavefront. The so-called near-field ptychography may be seen as a hybrid between ptychography and holography methods but it has the potential to be superior for quantitative imaging at the nanoscale since it takes into account wavefront distortion in the incoming beam.

The third article is a good example of how "old" techniques like topography can contribute to characterisation of new materials such as silicon solar cells. The way the solar cells are manufactured, and in particular the use of aluminium paste for the back contact, induces lattice distortion in the silicon and in this way affects its voltaic efficiency. The relation between distortion and strain in silicon and the voltaic performance of those components has been characterised by coupling Xray topography and nanodiffraction.

Next come two articles that emphasise the importance of instrumentation developments for synchrotron macromolecular crystallography. The first deals with automatic processing of diffraction data, which was initiated in 2010 through work at the ESRF and EMBL, and has been continuously improved ever since. The second article presents a strategy for exploiting radiation damage, recognised as a major issue in macromolecular crystallography experiments at synchrotron sources, to solve 3D structures.

The following two articles highlight two technical developments made by the ESRF. The first examines white beam mirror systems, which were designed and developed to meet the performance required by the new, upgraded beamlines. Based on generic technologies, several systems associating thermal and mechanical stability and high positioning accuracy have been produced. The second introduces a high-frame-rate detector based on the FReLoN design. This detector was developed specifically for kHz-time-resolved energy EXAFS and features a linear image sensor coupled with an electronic shutter.

The final two articles describe the development of tools for interacting with large datasets. Harvesting metadata and the Umbrella portal for authenticating users are both essential building blocks developed through European partnerships between neutron and photon facilities. Together with high-speed detector readout systems, they complement the full data acquisition chain and will allow well-structured data to be accessed remotely, such that particularly large datasets can remain on-site instead of tedious copying to USB disks.

J. SUSINI and R. DIMPER

X-RAY PHASE CONTRAST IMAGING WITH NANORADIAN ANGULAR RESOLUTION

Edge-illumination (EI) X-ray phase contrast imaging (XPCI) was developed in the late nineties at Elettra [1]. The goal was to devise an alternative to analyser-based imaging (ABI, [2]) that would not require the use of a crystal analyser. The idea underpinning this method is that illuminating only the physical edge of the detector pixels enables a fine angular selection on photon direction (**Figure 139a**), analogous to that obtained through the crystal reflectivity curve in ABI. This analogy, already observed in the

Principal publication and authors
P.C. Diemoz (a,b), M. Endrizzi (a), C.E. Zapata (a,b), Z.D. Pešić (c), C. Rau (c), A. Bravin (d), I.K. Robinson (b,e) and A. Olivo (a,b), *PRL* **110**, 138105 (2013).
(a) Department of Medical Physics and Bioengineering, UCL, London (UK)
(b) Research Complex at Harwell, Didcot (UK)
(c) Diamond Light Source, Didcot (UK)
(d) ESRF
(e) London Centre for Nanotechnology, London (UK)

original EI paper [1], was later formally demonstrated [3].

Eliminating the crystal means that the radiation does not need to be monochromatic or tightly collimated. This enabled the method to be adapted to polychromatic and divergent beams generated by conventional X-ray sources through a pair of apertured masks [4], which repeat the EI configuration over the entire area of a 2D detector. The plurality of beams simultaneously "edge-illuminating" many detector lines replaces the sample scanning used at synchrotrons. Although this setup might superficially resemble that of Talbot interferometry [2], the underlying physical principle is very different. In EI, the aperture pitch is between one and two orders of magnitude larger, and as said its only aim is to repeat the EI condition for each pixel row of a 2D detector. The beamlets are physically separated and do not interfere: the phase sensitivity is created by each beamlet impinging on an absorbing edge. Indeed, the lab implementation of EI is a completely incoherent method: source sizes of up to 100 µm have been used, which lead to a coherence length at least two orders of magnitude smaller than the mask pitch.

Despite this negligible degree of spatial coherence, EI enables quantitative phase retrieval [5]. The spatial incoherence is modelled as a "spread" of each beamlet; however, as long as the edge cuts the "spread" beamlet in half, minimal refraction-induced movements of the beamlet can still be detected, and related back to the phase shift gradient that caused them.

The EI method provides intense phase signals with incoherent sources. We wanted to discover whether use of a coherent source could be of benefit. In this work, we found that EI sets a new record for phase sensitivity, as it reduces the detectability threshold for refraction angles by about one order of magnitude compared to previous methods. EI XPCI setups were installed both at ESRF ID17 and on the "coherence branch" of Diamond I13. In both cases, a long sample-to-detector distance (5-15 m) was used to maximise angular sensitivity. We deliberately spanned a wide energy range (12 to 85 keV) to demonstrate the concept's validity under varying experimental conditions. The data analysis required the development of a new phase retrieval method. In EI, scanning the edge over the detector yields an "integral" sensitivity curve (Figure 139b), which plays the same role as the rocking curve in ABI [3]. Its derivative is equal to the beam shape: with incoherent radiation, this is a bell-shaped curve, normally well approximated by a Gaussian. In the coherent case, diffraction effects make this curve significantly irregular (Figure 139c), and it proved necessary to take these irregularities into account to perform an accurate phase retrieval. Sensitivity curves were simulated by means of Fresnel-Kirchhoff diffraction integrals and successfully compared to the experimental ones, which provided the basis for the modified phase-retrieval method. This was then applied to samples of known optical properties, demonstrating retrieval of the correct refractive indices, *i.e.* quantitative reliability. Error analysis

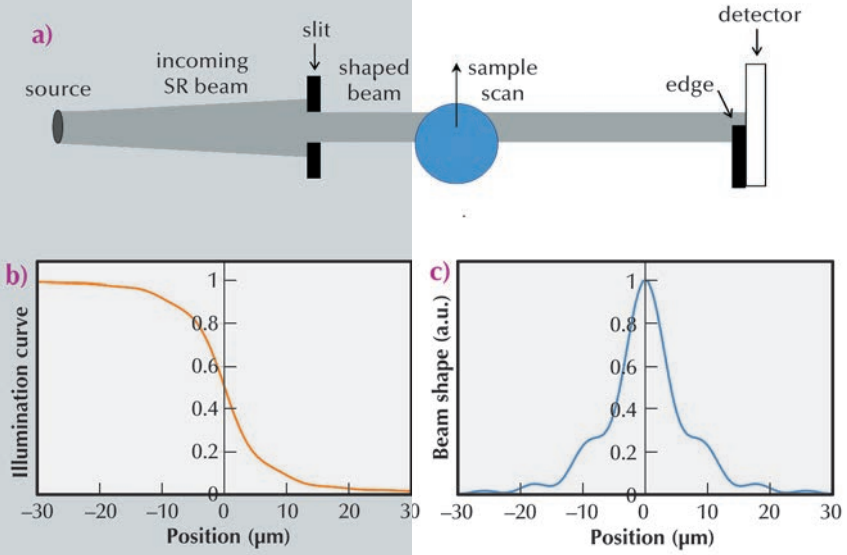

Fig. 139: Experimental set up (a), "integral" sensitivity curve (b), and derivative of the same, yielding the beam shape (c).

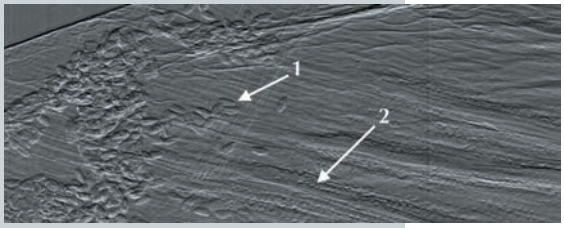

Fig. 140: Differential phase image of a flower petal, with arrows indicating: 1 pollen grains; 2 individual cells aligned in the petal veins.

on the retrieved refraction angle maps enabled determination of the sensitivity threshold, which was ~2 nrad for the data acquired at the ESRF. Finally, to further demonstrate the extremely high angular resolution, we imaged very weakly refracting samples (*e.g.* a 10 µm thick polypropylene foil in water, which has an almost identical refractive index) and still obtained strong phase signals. The level of angular resolution achieved enables the detection of density gradients of the order of 10^{-4} g/cm^3 mm^{-1}, or thickness gradients of micrometres over millimetres. As an example, **Figure 140** shows an image of a flower petal where pollen grains and rows of cells in the petal veins can be clearly distinguished. This new technique is expected to allow previously inaccessible scientific applications to be tackled.

References
[1] A. Olivo *et al, Med. Phys.* **28**, 1610-19 (2001).
[2] A. Bravin, P. Coan and P. Suortti, *Phys. Med. Biol.* **58**, R1-R35 (2013).
[3] P.R.T. Munro, C.K. Hagen, M. Szafraniec and A. Olivo, *Opt. Exp.* **21**, 11187-201 (2013).
[4] A. Olivo and R. Speller, *Appl. Phys. Lett.* **91**, 074106 (2007).
[5] P.R.T. Munro, K. Ignatyev, R.D. Speller and A. Olivo, *PNAS* **109**, 13922-27 (2012).

BETTER PHASE IMAGES WITH "messy" X-RAY BEAMS

Principal publication and authors
M. Stockmar (a), P. Cloetens (b), I. Zanette (a), B. Enders (a), M. Dierolf (a), F. Pfeiffer (a) and P. Thibault (a,c), *Scientific Reports* **3**, 1927 (2013).
(a) Physics Department, Technische Universität München, Garching (Germany)
(b) ESRF, Grenoble (France)
(c) Current address: Physics & Astronomy Department, University College London (UK)

Although the development of X-ray optics has seen remarkable progress, technological constraints of fabrication processes are still limiting the quality and resolution of images obtained with X-ray lenses. In addition, traditional microscopy techniques based on these lenses are generally limited to absorption contrast and do not provide a means to extract valuable quantitative phase images of a sample. Lensless techniques overcome these limitations by replacing X-ray optics with a computer algorithm that reconstructs both the absorption and the phase shift produced by a sample. One of these techniques, ptychography **[1]**, is used today with great success as a high-resolution extension to traditional scanning microscopy techniques. However, it may suffer from long acquisition times related to the scanning procedure, where only a small part of the sample is illuminated and the huge dynamic range required in the far-field diffraction patterns. Lensless full-field techniques such as inline holography are typically much faster since they illuminate the whole sample at once and can operate with detectors with a reduced dynamic range. However, such near-field propagation techniques can succeed only if the phase and intensity of the incoming beam are relatively uniform, since inhomogeneities in the incident wavefront mix with the sample in a non-trivial way.

A hybrid between ptychography and holography, near-field ptychography overcomes those limitations by intrinsically taking the distortions in the wavefront into account. To achieve this, a series of images is recorded where the object is moved to different lateral positions while the illumination with its distortions stays fixed. Besides the experimental parameters like energy and the setup geometry, the ptychographic phase-retrieval algorithm does not require any prior knowledge about the sample. It uses knowledge about the lateral positions to separate the sample cleanly from the (distorted) illumination in an iterative manner. The result is a quantitative image of the sample and also a quantitative image of the illumination.

A first experimental demonstration of the technique was carried out at the nano imaging endstation of **ID22** with the standard configuration for (magnified) holotomography **[2]**, which is depicted in **Figure 141**. The sample consisted of a well-known test structure, a so-called "Siemens star". The reconstructed images are shown in **Figures 142a-c**. Further, it was demonstrated that the quality of the image could be greatly improved when additional distortions are introduced in the illumination. **Figures 142e-g** show the reconstructed images obtained from a dataset recorded after a piece of cardboard, the so-called diffuser, was added in the beam path. The results

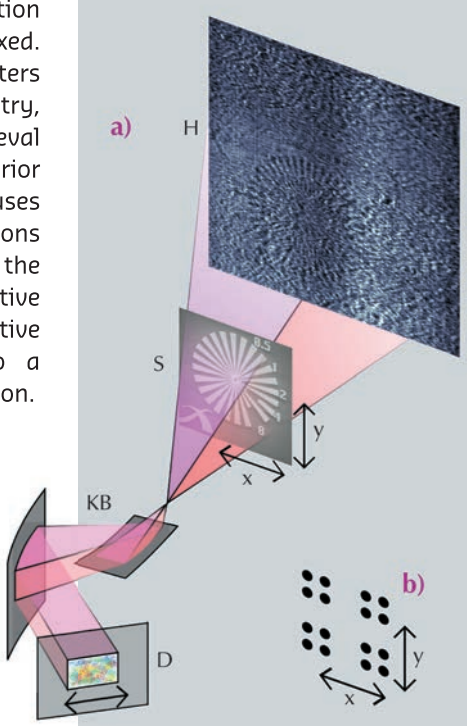

Fig. 141: Schematic of the experimental setup used for X-ray near-field ptychography. (a) X-rays from an undulator source (not depicted) are focussed by Kirkpatrick-Baez mirrors (KB) to record a magnified hologram (H) of the sample (S). A piece of cardboard, the so-called diffuser (D), can be placed into the beam to distort the wavefront. The sample mounted on a high-precision stage is moved as depicted in (b) transversally, where at each of the 16 positions a raw image is recorded.

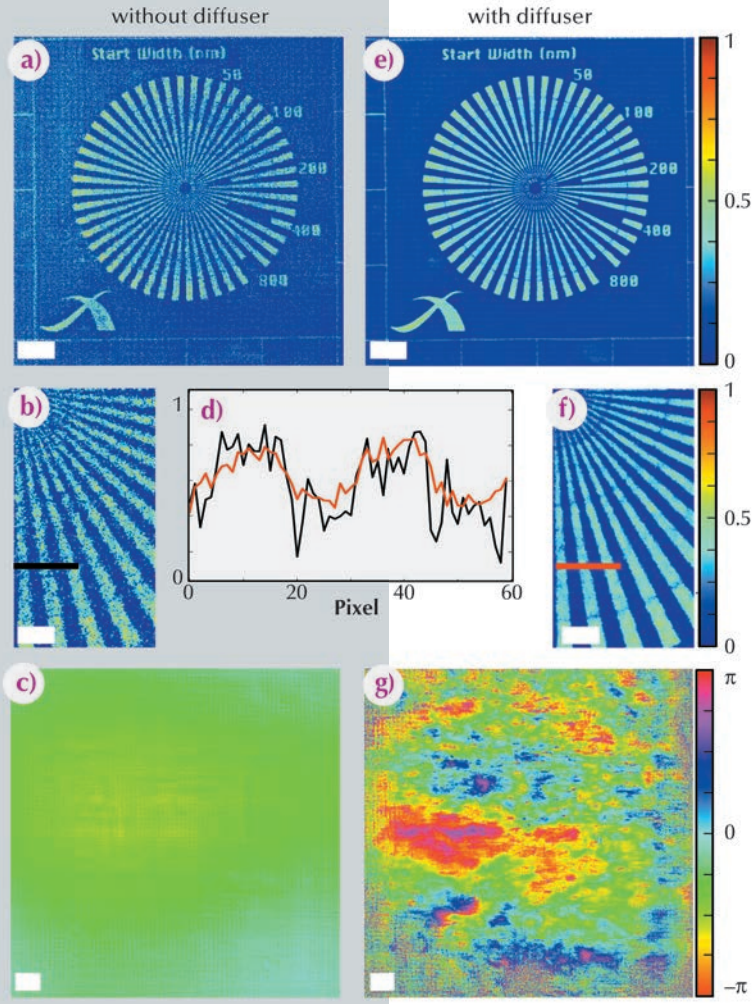

are shown in **Figures 142e-g**. Near-field ptychography is a quantitative technique: the reconstructed phase shift of the X-ray wave caused by the test structure is in good agreement with theoretical expectations and other measurements.

In combination with computed tomography, this approach has great potential for a quantitative visualisation at the nano scale, *e.g.* of samples from materials science research. Besides imaging applications, this approach can also be used to characterise optical elements. Moreover, it can also be transferred to optical light microscopy or electron microscopy.

Fig. 142: Reconstructed images of the sample and the illumination. (a) the phase of the reconstructed image of the sample without the additional distortions. (b) a magnified region. (c) the phase of the illumination. (e) the sample with diffuser in the beam path. The illumination (g) now looks rather "messy", however, the image quality has significantly increased (f), a comparison with (b) is shown in (d). The scale bars indicate 5 µm and 2 µm for the magnified regions of interest. Note that surrounding empty areas of the object were cropped.

References

[1] M. Dierolf, A. Menzel, P. Thibault, P. Schneider, C.M. Kewish, R. Wepf and F. Pfeiffer, *Nature* **467**, 436–439 (2010).

[2] R. Mokso, P. Cloetens, E. Maire, W. Ludwig and J.-Y. Buffière, *Applied Physics Letters* **90**, 144104 (2007).

Authors

T.-N. Tran Thi (a), S. Dubois (b), J. Baruchel (a), N. Enjalbert (b), M. Tsoutsouva (a), T. Schülli (a) and T. Lafford (a).

(a) ESRF

(b) CEA-INES, Savoie Technolac, Bourget du Lac (France)

CORRELATION BETWEEN THE LATTICE DISTORTION INDUCED BY THE ALUMINIUM BACK CONTACT AND THE PHOTOVOLTAIC EFFICIENCY IN SILICON SOLAR CELLS

For high efficiency in silicon solar cells, the aluminium back contact is required to have low carrier recombination velocities and low series resistances. The aluminium paste for the back contact is typically screen-printed, followed by annealing and cooling, which creates eutectic and doped layers at the back surface of the silicon. Even though this technique is now used in industrial

silicon solar cell manufacture, the various aluminium pastes available on the market give different photovoltaic (PV) performances. To explore this issue, the distortion and strain of the Si in contact with the Al back layer have been characterised by coupling X-ray section topography (**Figure 143**) at BM05 and X-ray nanodiffraction measurements at ID01. Rocking curve imaging section topography (RCIST) software was developed in order to analyse the ensemble of rocking curves and generate maps of the integrated intensity, the full width at half maximum and the peak position.

The results obtained at both BM05 and ID01 strongly suggest a correlation between the lattice distortion of the Si in contact with the eutectic and Al layers, and the photovoltaic efficiency. This distortion varies depending on the Al paste used, giving "good" and "less good" PV performance (**Figure 144**). The eutectic layer in the Al back contact is directly associated with the distortion and strain of the Si back surface region. The higher PV efficiency of the "good" paste appears to be related to the better homogeneity of the eutectic layer, associated with smaller distortion and strain of the Si back surface. This is directly linked to the amount of Al, Al grain size, and the precise composition of Al and other components in the different pastes. For the manufacturing process, choosing a good Al paste is therefore crucial for producing good solar cell products.

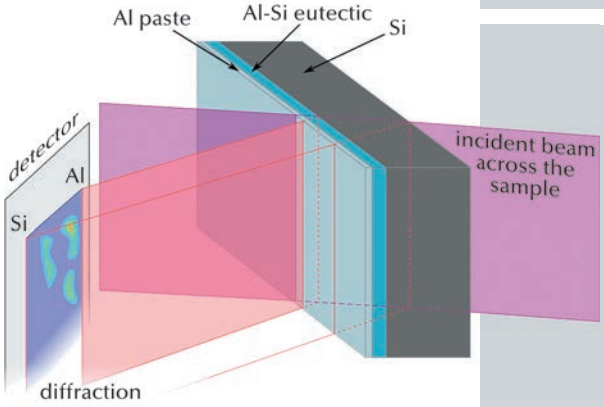

Fig. 143: Diagram of diffraction section topography for a solar cell with Al back plane.

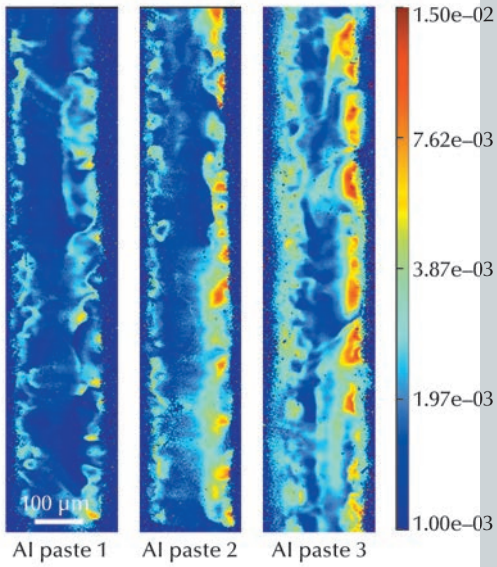

Fig. 144: Si 220 FWHM maps (in degree) from section topography rocking curve imaging of solar cells based on mono-like Si, with Al back-planes made from the three different Al pastes.
The face with the Al back plane is on the right of the virtual section image and the front side is on the left. There is clearly more distortion induced on the side with the Al back plane. Even though the mono-like Si contains many lattice defects formed during the growth, the different Al pastes clearly produce different effects - the Si 220 FWHM values vary significantly. Al paste 1 ("good" photovoltaic efficiency) causes less distortion of the Si wafer, with FWHM values as low as 2 x 10^{-3} degrees, while Al paste 3 ("less good") induces misorientations up to 8 x 10^{-3} degrees.

The results clearly demonstrate that synchrotron methodologies are valuable techniques for studying, not only the structure and crystalline perfection of Si, but also features associated with electrical efficiency.

AUTOMATIC PROCESSING OF MX DIFFRACTION DATA

In the last decade of synchrotron macromolecular crystallography (MX) experiments, remarkable advances have been made in almost every aspect of the process. Automatic sample changing, high-brilliance beams and high-speed detectors have all contributed to a dramatic reduction in the amount of time required for even the most complex MX experiments. However, the ability to collect at extremely high rates does not come without problems: users have less "idle" time to prepare their experiment and analyse their results. Thus, it has become necessary for new advanced tools to be developed, to quickly and accurately plan diffraction experiments **[1]**, and to provide rapid feedback to the user on the quality of the data that

Principal publication and authors
S. Monaco (a), E. Gordon (a), M.W. Bowler (b,c), S. Delagenière (a), M. Guijarro (a), D. Spruce (a), O. Svensson (a), S.M. McSweeney (a), A.A. McCarthy (b,c), G. Leonard (a) and M.H. Nanao (b,c), *J. Appl. Cryst.* **46**, 804-810 (2013).
(a) ESRF
(b) European Molecular Biology Laboratory, Grenoble (France)
(c) Unit of Virus Host–Cell Interactions, UJF-EMBL-CNRS, UMI 3265, Grenoble (France)

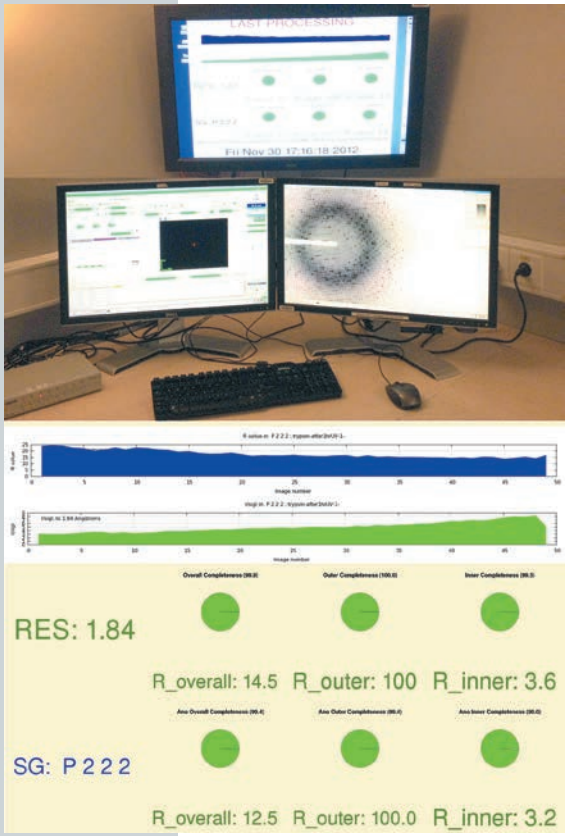

Fig. 145: Data collection feedback at beamline ID23-2.

has been collected. This work focuses on the latter of the two tools, feedback on data quality.

In the Spring of 2010, after work from various ESRF and EMBL groups and initial testing on ID23-EH2, a system for the automatic processing of data was deployed on all MX insertion device beamlines. While this initial version was quite successful, it has been continuously improved to reach the current system, which now offers state of the art feedback to all MX users.

Since the very beginning, a double-headed approach has been employed towards data processing that analyses the same data in multiple ways, using multiple subsystems. The first subsystem is engineered to produce a rough but very high-speed processing of the data for the user, without using many of the known techniques to incrementally improve data quality. The processed data is available to the user shortly after the data collection has ended (currently 10 seconds to 2 minutes after the end of the data collection) both on the file system, the ISPyB database [2], and *via* a dedicated monitor (**Figure 145**).

The second subsystem attempts to emulate the steps that would be taken by an experienced crystallographer, to produce the highest quality data processing, albeit at the expense of run time. Data from this subsystem is indeed of sufficient quality to often facilitate the determination of experimental phases automatically, and without any user intervention. A selection of the structures that have been determined automatically is presented in **Figure 146**.

Without an intuitive mechanism for the user to browse the results of these data reductions, all of this effort would be of limited use. Therefore, significant effort has gone into expanding the data model of ISPyB to handle different data collection types, the auto-processing data, and even the auto-structure

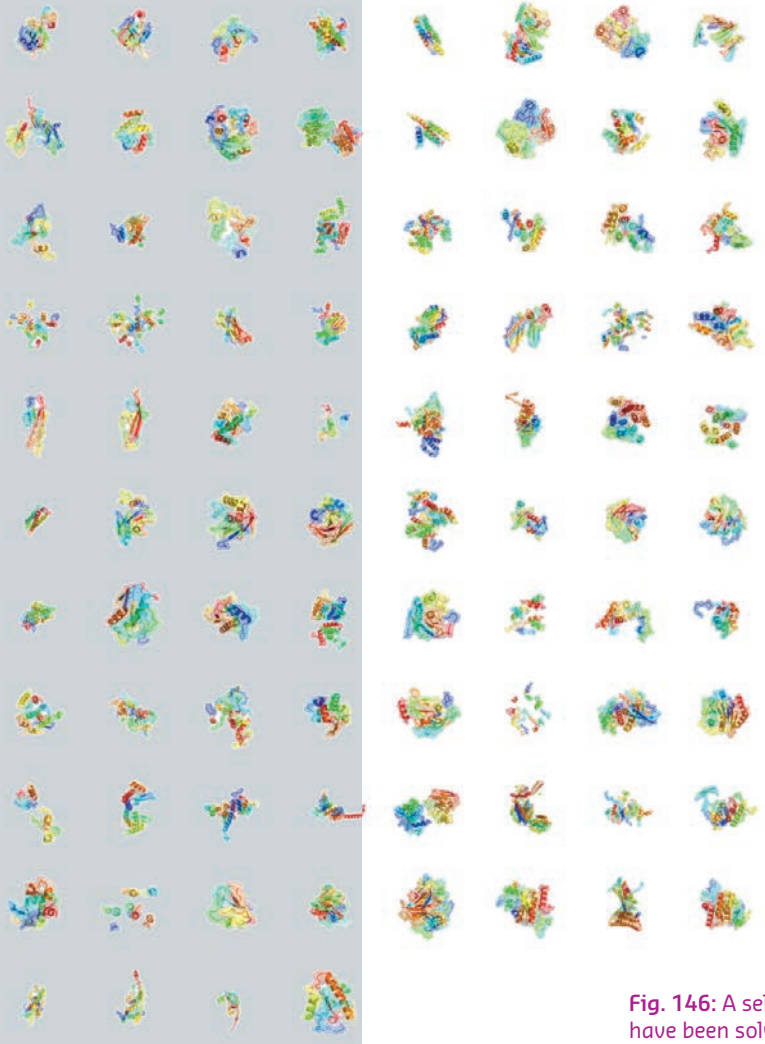

Fig. 146: A selection of structures that have been solved automatically.

determination data. The result of this is a clean and user-friendly interface that allows the user to rapidly compare the data quality from different datasets, view inline graphs of data quality and download the processed files.

These two systems have evolved significantly in their speed and robustness over the last three years, to the point now that they are simply part of the portfolio of ESRF services that users expect.

References
[1] G.P. Bourenkov and A.N. Popov, *Acta Crystallogr D Biol Crystallogr.* **66**, 409-19 (2010).
[2] S. Delagenière, P. Brenchereau, L. Launer, A.W. Ashton, R. Leal, S. Veyrier, J. Gabadinho, E.J. Gordon, S.D. Jones, K.E. Levik, S.M. McSweeney, S. Monaco, M. Nanao, D. Spruce, O. Svensson, M.A. Walsh and G.A. Leonard, *Bioinformatics* **27**, 3186-92 (2011).

SEGMENTING DATASETS FOR RADIATION DAMAGE INDUCED PHASING

Principal publication and authors
D. de Sanctis (a) and M.H. Nanao (b,c), *Acta Cryst.* **D68**, 1152–1162 (2012).
(a) ESRF
(b) European Molecular Biology Laboratory, Grenoble (France)
(c) Unit of Virus Host–Cell Interactions, UJF-EMBL-CNRS, UMI 3265, Grenoble (France)

Radiation damage of biological material is a major problem in macromolecular crystallography experiments at synchrotron sources. Ionising radiation produces free radicals that destroy the crystalline order of the sample and damage, on a faster time scale, highly reactive centres. Data collection at cryogenic temperature extends the lifetime of measured samples, but intense and highly-focused beams still produce damage that cannot be ignored. Specific sites that exhibit higher radiation sensitivity can be damaged very quickly, making the interpretation of the electron density map more difficult, and weaken the anomalous signal in a dataset by depleting the electron density of heavier atoms (because of their bigger photoelectric cross-section). Some experiments have shown that specific radiation damage can be used to solve the three dimensional structure of novel macromolecules. These experiments are commonly known as radiation damage induced phasing (RIP) experiments.

Differences in intensities between two datasets collected at low X-ray dose, on the same crystal, interleaved by a high dose exposure, permit the location of the positions of the damaged sites that can eventually be used as "fake" heavy atoms to calculate *ab initio* experimental phases, as in an isomorphous replacement experiment. The damaged sites are usually heavy atoms and/or disulfide bonds **[1-4]**. Practical applications of this method are limited mainly by the difficulties of choosing the right X-ray dose: too high a dose can destroy the crystalline order and the diffracting power and too low a dose might not induce enough to damage the sites, and make their positions harder to find. Furthermore, the optimal dose varies from protein to protein and not every macromolecule is solvable by these means, as not all molecules present sites that can be used for RIP. In this work, we have further extended the way in which the experiment is conceived, by doing away with the collect-burn-collect protocol, and instead segmenting a large dataset into multiple subsets (**Figure 147**). The differences between two subsets, the first one beginning at frame 1, and the second one beginning with the last image in the dataset and extending

Fig. 147: Schematic diagram of the segmented RIP method. Images from a normally collected oscillation dataset are used to create two subsets, the 'before' (orange) and 'after' (red) datasets, which are then subjected to RIP analysis (green).

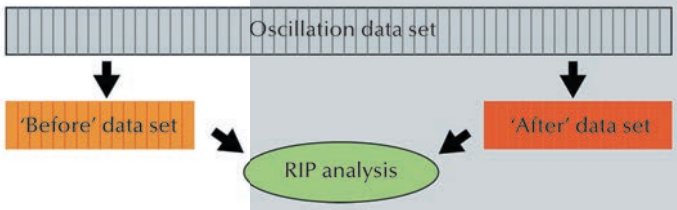

Fig. 148: Example of experimental electron density map calculated after Segmenting RIP, with a partial model built automatically.

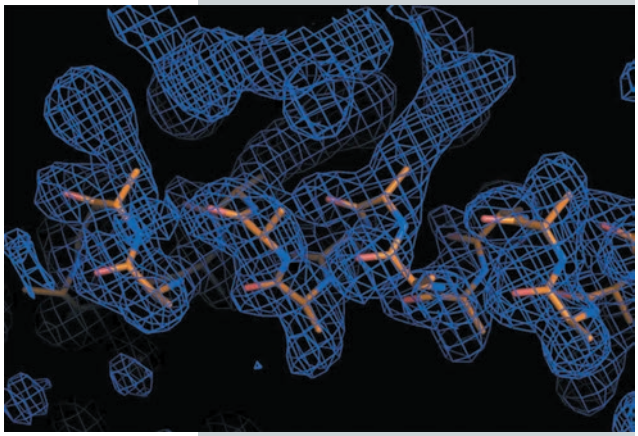

References
[1] G. Evans, M. Polentarutti, K. Djinovic Carugo and G. Bricogne, *Acta Cryst.* **D59**, 1429–1434 (2003).
[2] M.H. Nanao, G.M. Sheldrick and R.B.G. Ravelli, *Acta Cryst.* **D61**, 1227–1237 (2005).
[3] U.A. Ramagopal, Z. Dauter, R. Thirumuruhan, E. Fedorov and S.C. Almo, *Acta Cryst.* **D61**, 1289–1298 (2005).
[4] K. Futterer, R.G.B. Ravelli, S.A. White, A.J. Nicoll and R.K. Allemann, *Acta Cryst.* **D64**, 264–272 (2008).
[5] S. Monaco, E. Gordon, M.W. Bowler, S. Delagenière, M. Guijarro, D. Spruce, O. Svensson, S.M. McSweeney, A.A. McCarthy, G. Leonard and M.H. Nanao, *J Appl Crystallogr.* **46**, 804–810 (2013).

as many images towards the first one, are then used to determine the position of damaged sites and to calculate experimental phases (**Figure 148**). Different subsets of images are automatically selected to constitute the second dataset, in an attempt to identify the optimal X-ray dose. In contrast to normal radiation damage induced phasing, no optimisation is required for the data collection protocol and no preliminary knowledge of the crystal composition is necessary.

Segmenting RIP is started from the output of GrenADeS autoprocessing [5] and can be triggered automatically for each dataset collected on an ESRF MX beamline. The method is well suited to the trend towards faster detectors that result in datasets containing extremely large numbers of images, collected in a few minutes.

The implementation of Segmenting RIP at the ESRF extends further the concept of software automation that is provided to the user community and represents an excellent example of the synergistic interaction of the development of new tools and automation that takes place at the Structural Biology beamlines.

NEW GENERATION MIRROR SYSTEMS FOR ESRF UPGRADE BEAMLINES

Authors
R. Baker (a), R. Barrett (a), C. Clavel (a), Y. Dabin (a), L. Eybert (a), T. Mairs (a), M. Mattenet (a) and J. Guillemin (b).
(a) ESRF
(b) SPRETEC, Seyssins (France)

Many new or refurbished beamlines constructed during the ESRF Upgrade Programme (2009 – 2015) will be equipped with white beam mirror systems. The performance objectives of these new beamlines are extremely challenging in terms of beam stability and focal spot size, leading to equally challenging specifications on opto mechanical beam delivery systems, not least the first or "white beam" mirror assembly.

High heatloads of several hundred watts coupled with extremely tight tolerances on mechanical stability and positioning mean that particularly stable supports and ultra high-precision positioning systems are mandatory to guarantee optimal performance. As white beam mirrors are the first reflective element on the beamline, any form of instability or alignment error on the mirror can be vastly magnified at the sample position, often situated more than 100 metres further downstream.

A working group was created in 2009 to address the above issues, to develop an entirely new mirror support system and to streamline design by defining generic solutions wherever possible.

At each stage, from the EXPH floor to the X ray beam axis, we have attempted to solve the conflicting engineering problem of ensuring optimal thermal and mechanical stability whilst maintaining the highest possible accuracy and sensitivity of the various positioning elements.

From the ground up, this has lead to the development of novel granite-based supports integrating motorised "air side" alignment stages in a parallel configuration (as opposed to more classical series arrangement) ensuring superior compactness and rigidity. These are grouted directly to the EXPH floor to guarantee the stiffest possible mirror support and zero vibration amplification (**Figure 149**).

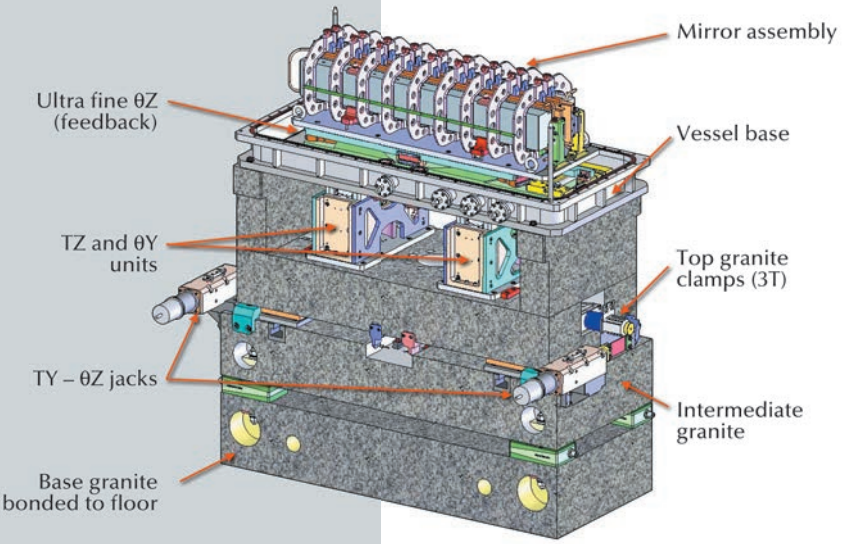

Fig. 149: Generic white beam mirror assembly showing high stiffness multi axis support, precision elevators. UHV fine tune mechanics and cooled optics.

Specific ex – vacuum mirror elevators have been developed to ensure precise vertical positioning. The stiffest commercially available linear bearing stages - purchased and modified to meet our stringent requirements - are integrated into ESRF-designed "over constrained" mechanics. They show an excellent compromise between travel range, load capacity, precision, resolution and rigidity, and are now a generic subassembly manufactured and assembled in batches of 5 to 10 units.

Special attention has been paid to the management of instability caused by thermal load. Difficulties in this domain are twofold:

Firstly, protection of the mirror block from overheating and thermally induced deformation, caused by the power density of the incoming white beam. Although this problem has been largely addressed in the past and has lead to the so called "smart cut profile" optimisation of the mirror itself, additional improvements have been made to the cooling system. Careful dimensioning and pipe routing prevent vibrations from the cooling circuit reaching the mirror, while calibrated clamps ensure uniform pressure and therefore improved thermal contact between the side cooling blocks and the optics.

Secondly, thermal drift of surrounding mechanics and adjustment mechanisms due to Compton scattering. This can represent up to 20% of the total incoming beam power and, due to its diffuse nature, is extremely difficult to predict. Our proposed solutions are to carefully choose and match materials according to their coefficient of thermal expansion, to control the temperature of critical mechanical parts (independent water cooling circuits) and to implement cooled copper shielding as close as possible to the optical face.

For ultra-fine UHV beam incidence tuning and thermal expansion compensation during bakeout, high stiffness subsystems based on piezo-driven flexural elements combined with closed loop position feedback ensured by capacitive sensors have also been developed. Extensive finite element analysis, prototyping and evaluation testing were required, but angular positioning with a resolution down to 50 nanoradians is now possible.

To date, 10 generic mirror systems have been or are being installed. Results obtained from first tests are encouraging: beam quality and stability when compared to existing systems have been significantly improved, thermal drift has been controlled and, perhaps more importantly, thermal stabilisation time (time required to reach thermal equilibrium following exposure to the white beam) has been considerably reduced (**Figure 150**). Manufacture is often performed in batches and the assembly and installation procedures have been standardised as much as possible.

Finally, in cases where more than 4 precise motorised degrees of freedom are required to position optics (*e.g.* for toroidal mirrors), hexapods become an interesting option. Collaboration between the ESRF and a hexapod manufacturer (Symetrie, France) has lead to the development of a new hexapod with improved stiffness and resolution. It may be used in association with generic flexure-based "in vacuum" angular positioning units when extremely high-resolution adjustment of beam incidence or rapid angular correction are required. Such a hexapod has been installed and tested on ID20. First results are impressive: linear and angular resolution, stiffness and long term thermal stability have all been vastly improved over existing hexapods.

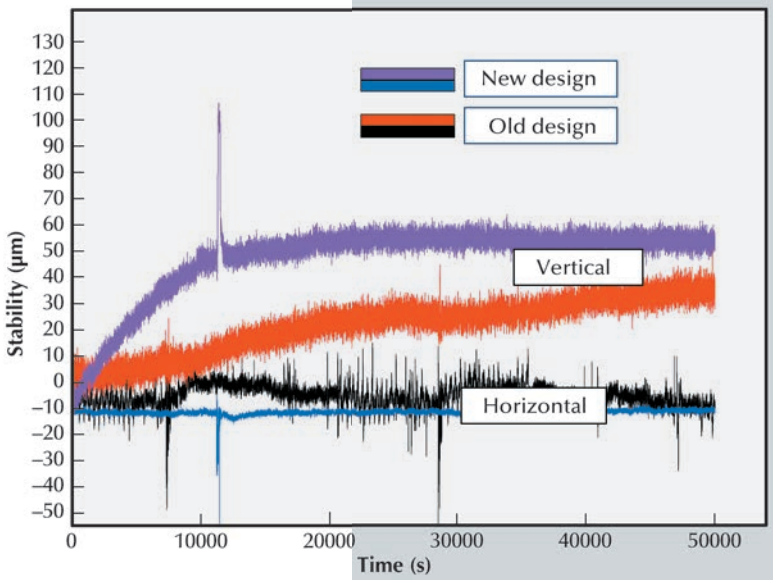

Fig. 150: Horizontal and vertical beam position evolution following exposure to the white beam (thermal stabilisation time) - comparison between old and new designs.

Authors
J.-C. Labiche, E. Collet, L. Siron, J.J. Thevenin, C Ponchut, A. Homs, M.C. Dominguez, J. Borrel, C. Jarnias, C. Strohm, I. Kantor, O. Mathon and S. Pascarelli.
ESRF

NEW KHz FRAME-RATE DETECTOR APPLIED TO TIME-RESOLVED EXAFS

We have developed a new high frame rate detector based on the FReLoN design and featuring a linear image sensor coupled to an electronic shutter. This new detector has been developed specifically for fast time-resolved energy dispersive EXAFS at beamline ID24 [1].

ID24 is an energy-dispersive X-ray absorption beamline (XAS) that has recently been rebuilt through the ESRF Upgrade Programme. It offers the user community new opportunities for investigating matter at extreme conditions of pressure, temperature and magnetic field. These experiments combine very stringent time resolution (usually below the millisecond) coupled to a small focal spot (few micrometres). Detector readout speed is the limiting factor for time resolution.

The new EXAFS detector is based on the layout of the previous model, with a phosphor screen X-ray converter coupled to a CCD camera by a tandem lens system. The optical front-end was totally redesigned in order to fit the horizontal beamsize that increases from 50 mm to 100 mm and now includes a custom high-resolution front lens. The lens assembly was designed so as to enable spatial resolutions up to 4 k pixels, if needed. The system includes a motorised focusing and a motorised iris diaphragm for fine resolution and sensitivity adjustments.

The workhorse detector during the past 10 years has been the ESRF FReLoN camera, equipped with a conventional 2D CCD area image sensor used as a linear image sensor via line binning [2]. For the upgraded ID24, the number of photons transmitted by the sample is close to ~ 10^{14} ph/s. However, the 1 KHz acquisition frequency was a limitation of the present FReLoN camera [2], which did not allow efficient detection for such a high photon count. To go beyond the KHz frame-rate while maintaining a high dynamic range, linearity and spatial (or equivalently, energy) resolution, a new system had to be designed that would allow single images to be recorded without lag or aliasing of images. These features were considered essential for sub-ms EXAFS.

A new camera was developed, based on the linear CCD image sensor 11156 from Hamamatsu, consisting of an array of 2048 pixels of dimensions 14 x 1000 μm^2 (**Figure 151**). The S11156-2048 chip utilises a resistive gate structure that allows high-speed transfer, with "on chip" electronic shutter function, offering significantly reduced image lag (less than 0.1%). Its minimum exposure time is 30 µs, and it has a true dynamic range of 14 bit. With its back-thinned structure, this CCD also offers high sensitivity (> 80% quantum efficiency) from the UV to the NIR region of the spectrum. **Figure 152** illustrates the quality of data collected on pure Cu foil on ID24.

To demonstrate the potential of the new "Hamamatsu sensor" FReLoN camera, a time-resolved XAS study of iron oxidation at high temperature was performed at beamline ID24. A pure Fe foil of 5 µm thickness exposed to normal atmosphere (oxygen fugacity = –0.7) was heated with a highly

Fig. 151: The S11156 Hamamatsu sensor integrated in the FReLoN camera.

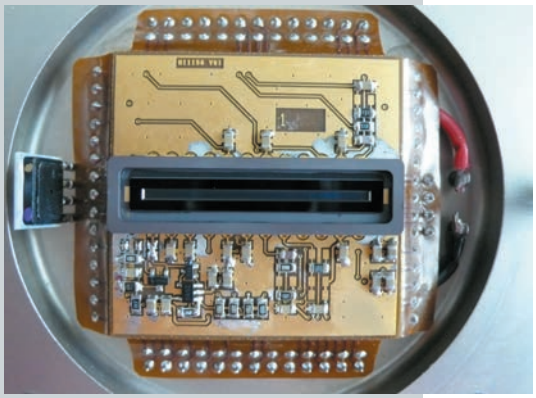

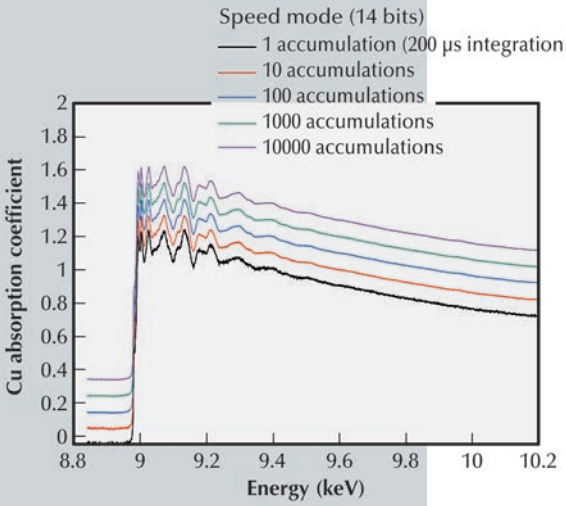

Fig. 152: Cu K –edge EXAFS recorded at ID24 by averaging an increasing number of accumulations of 200 µs each. The EXAFS features are already clearly visible in the single shot spectrum (black).

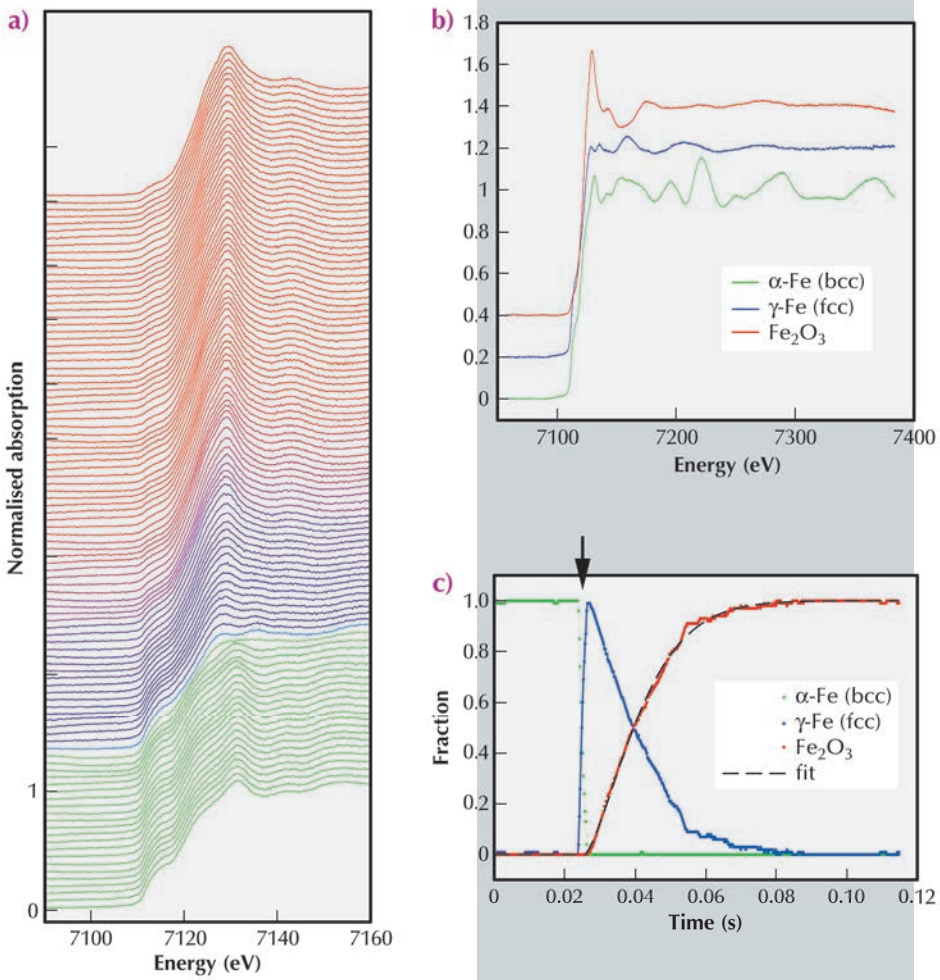

Fig. 153: a) Sequence of Fe K-edge XAS, acquired every 200 µs. b) Principal components of the dataset: α-Fe, γ-Fe and Fe_2O_3. c) Time evolution of relative fractions. The black arrow indicates the onset of laser heating. Courtesy of I. Kantor.

defocused 5 W IR laser. A polychromatic X-ray beam was focused down to about 5 x 4 µm² on the sample in order to minimise probed thermal gradients. The foils temperature was raised from room temperature to about 1200 K within a few ms. **Figure 153a** shows a sequence of Fe K-edge (7.1 keV) XAS spectra, recorded every 200 µs allowing the kinetics of the chemical reaction to be followed *in situ*. Spectral features change as the reaction evolves from ambient temperature (data in green) to the highest temperatures (data in red). The EXAFS spectra were processed with a standard linear combination fit technique to determine the relative fractions of the principal components (**Figure 153b**) – namely, α-Fe (body-centred cubic structure), γ-Fe (face-centred cubic polymorph of iron) and Fe_2O_3 hematite. The evolution with time of the relative fractions of the three phases is shown in **Figure 153c**.

The performance of the new detector appears to be very attractive for a number of applications beyond EXAFS, for example, for computed tomography imaging of fast-moving samples that are particularly important for *in vivo* physiological studies.

References
[1] S. Pascarelli *et al.*, *J. Synch. Rad.* **13**, 351 (2006).
[2] J.C. Labiche *et al.*, *Rev. Sci. Instrum.* **78**, 091301 (2007).

THE META-WORLD OF METADATA MANAGEMENT AT THE ESRF

Meta is derived from the Greek preposition μετ'α meaning "after", "beyond", "adjacent", "self" [1]. In the scientific context it is often used to mean adjacent or about. In the case of metadata it is used to mean data about data. Typical examples of metadata are file name, owner and date created. In the case of the ESRF, metadata includes the experimental context under which the data were collected such as X-ray energy, sample, experiment parameters.

Data is one of the main products produced at the ESRF. Scientific results depend on the contents of the data produced. The ESRF is a big producer of data but often without metadata. With the exception of macromolecular crystallography (MX) and certain tomography experiments, most of the data produced at the ESRF does not have a standard set of metadata describing it. This means a large number of experiments rely entirely on the users manually collecting metadata

Principal publication and authors
A. Götz (a), N. Bessone (a), C. Cleva (a), D. Porte (a), J. Meyer (a) and A. Mills (b).
(a) ESRF
(b) STFC (UK)

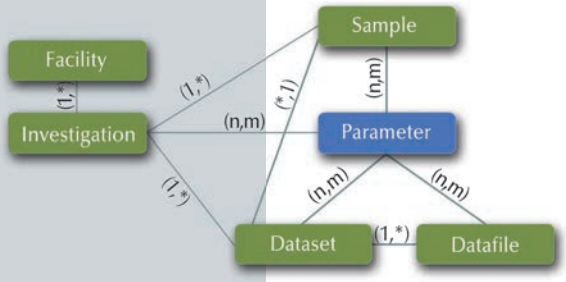

Fig. 154: Flexible ICAT metadata model.

in their notebooks. Although this does not prevent scientific publications it ultimately does influence the ease with which users can analyse their data. It also seriously hampers or even prevents online data analysis from being done because data cannot be analysed automatically.

Experiments which are collecting metadata in a systematic fashion already, MX and tomography, have developed specific metadata solutions. These consist of a dedicated metadata database and macros which collect the metadata during the data acquisition process. The databases are called IspyB and TomoDB respectively. The database table structures have been designed to take into account the specific needs of the experiments involved, *i.e.* crystallography and tomography. The IspyB database [2] has shown the advantages of metadata by becoming a central part of the MX experiments both before and after beam time. These database tables structures are however too specific to be applied to other kinds of experiments without major modifications. IspyB is used at two sites currently (ESRF and DLS) and there is interest from other sites for MX experiments.

Fig. 155: Software architecture for TomoDB ICAT metadata ingester developed for ID19.

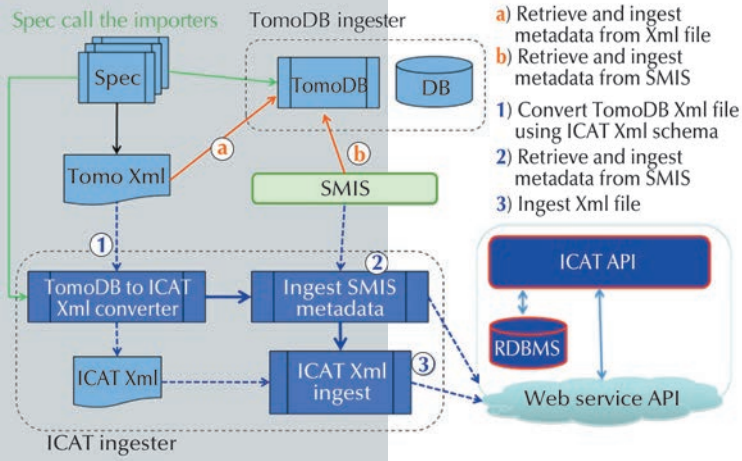

PaNdata [3] is a consortium of all photon and neutron sources in Europe dedicated to sharing good practices of data management. One good practice is the collecting, storing and searching of metadata. PaNdata provides a generic database for storing and searching metadata called ICAT. ICAT [4] is an open source metadata management system designed for large facilities, which has been developed by ISIS and the Scientific Computing Department of STFC. ICAT is in production at ISIS and DLS, and several laboratories (*e.g.* ALBA, DESY, ELETTRA and ESRF) have deployed ICAT prototype instances, which have been tested during service verification runs. ICAT can be searched across facilities.

The ICAT database schema (**Figure 154**) is closely related to the standardised metadata schema implemented in NeXus. NeXus provides a complete description of the experimental conditions during an experiment, and covers essentially all of the data required for meaningful searches in a metadata catalogue. ICAT has many attractive features, such as a programmable web service interface, user authentication and authorisation, the integration of provenance information and the registration of data object identifiers. Developments at the moment include the ICAT data service (IDS) and using the Umbrella user authentication mechanisms.

The European funded projects Pandata-ODI and CRISP have financed resources for the ESRF to install and adapt ICAT to the ESRF beamlines. This project has been going on for 12 months and will continue to be financed for another 12 months. ICAT has been installed and an ingester for TomoDB has been written (**Figure 155**). Over the next 12 months an ingester will be written that can be used for all experiments to store generic and specific metadata in the database.

The goal of the metadata project at the ESRF is to collect metadata for all kinds of experiments on all beamlines automatically. Achieving this will allow metadata that is collected at the same time as the raw data to be fully exploited. Online data analysis will be facilitated and in some case made

possible. With increasing data volumes online data analysis is essential for providing users with feedback on the data quality during the experiment. Another important issue addressed using metadata is data management including data archiving, exporting and searching. These issues are not managed systematically nor automatically at the ESRF today. A generalised solution for metadata will make this possible in the future.

References
[1] http://en.wikipedia.org/wiki/Meta
[2] S.Delangere *et al.*, *Bioinformatics* **27**, 3186-92 (2011).
[3] http://pan-data.eu/
[4] https://code.google.com/p/icatproject/

THE UMBRELLA FEDERATED IDENTITY MANAGEMENT SYSTEM – A FOUNDATION FOR FUTURE IT APPLICATIONS

Authors
D. Porte (a), F. Schlünzen (b), J. Savoyet (a) and R. Dimper (a).
(a) ESRF
(b) DESY

Before authorisation is granted to use information technology (IT) services, users need to be authenticated. This may sound trivial, but it is not if one considers that in an ideal world every user should have only one username and one (very secure) password. We are far from such an ideal world because we are all using a multitude of accounts with different credentials (username and password). Identity management, or the lack of, has a real impact when it comes to accessing IT services that are decentralised or when persistent identification is required to be able to access resources over a very long period of time. This is why federated identity management was identified several years ago as a stepping stone for future decentralised IT applications between large scale research infrastructures, leading to the development of the Umbrella system.

Umbrella is a federated identity system designed by the European photon and neutron source facilities (PaNs) supported by the FP7 projects EuroFEL, PaNdata, and CRISP. It aims at making life easier and science more productive for the facilities and their users. First of all Umbrella provides any PaN user –and effectively anyone interested in scientific discovery- with a unique identity, the Umbrella ID. Equipped with such an ID, a user can visit facilities with a single sign-on. Since the same identity is known at each of the facilities, users can access distributed data more easily, manage administrative processes or make use of the services and resources provided by the facilities (**Figure 156**).

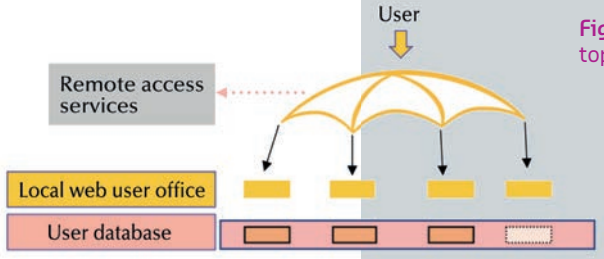

Fig. 156: Umbrella topology.

An UmbrellaID can easily be obtained by registering at https://umbrellaid.org. The only requirement is a valid e-mail address to confirm the registration. In the registration process one chooses a unique username and a secure password. Behind the scenes Umbrella creates a unique and persistent ID which will never change. A user can use the same UmbrellaID throughout their entire scientific career (and beyond).

Umbrella is based on a fairly complex and federated infrastructure. Several facilities operate an instance of the Identity Provider (IdP) and an instance of a Directory Service (DS). The DS holds the user database. The individual DS instances are synchronised through a mechanism called master-master replication. Each IdP is continuously monitored for availability, and all available IdP's are registered at a GeoDNS location service. The system is designed for the highest availability and stability.

A user creating an account on one of the Service Providers (SP) is redirected to the nearest available IdP through the GeoDNS. The IdP validates the account information and returns a set

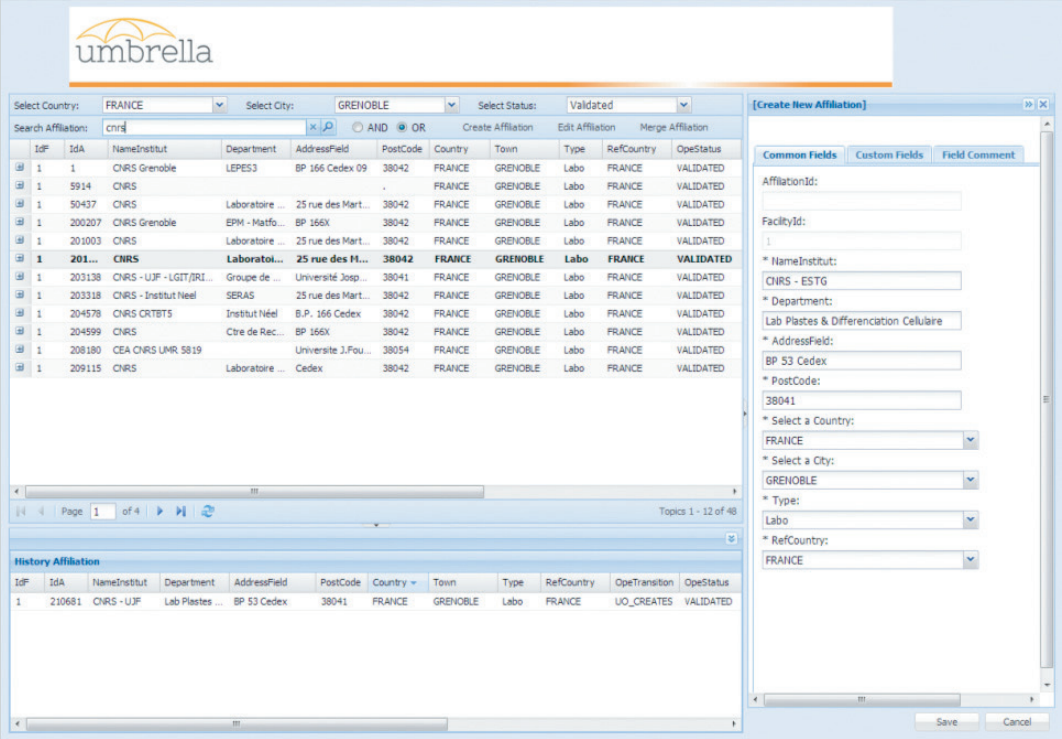

Fig. 157: Graphical user interface - affiliation database.

of credentials which are stored in the web-browser. These credentials then allow access to all Web-based User Offices in the Umbrella Federation and to a rapidly increasing set of IT services of the facilities.

The Umbrella system is based on Shibboleth, a well established and widely used open-source implementation of federated identity standards, namely the OASIS Security Assertion Markup Language (SAML). This guarantees that not only the personal data stored at UmbrellaID.org or at the facilities but the entire communication process is conform to the highest standards. The complexity of the process is entirely invisible to the user who will just see a single window asking for a username and password – once.

Users of our facilities are affiliated to a company or public institution. The affiliation corresponds to the professional address of a user and is important information for user offices in the workflow of processing research proposals - usage statistics are based on the affiliation. At present each facility maintains a local affiliation database. Sharing the same affiliation database will avoid users having to provide identical information several times, and user offices having to invest time and effort in the maintenance of individual and largely overlapping databases. ESRF has developed an affiliation management application for a federated central database as an integral component of the Umbrella system (**Figure 157**). The system has been presented to User Office representatives in an ESRF-hosted workshop in November during which implementation and operational issues were addressed.

The deployment of Umbrella and the implementation of new services are work in progress. The User Offices of PSI, ILL, and ESRF are already accepting the UmbrellaIDs and others will follow in the months ahead. "Umbrella enabled" data catalogues to access, share, manage or cite scientific data are currently under development. Another goal of the collaboration is to enable remote login to actual compute resources – which could be seen as a single virtual machine or a powerful high-performance cluster. In the long-run it is expected that Umbrella will become the entry point for the user community of the European Photon and Neutron facilities for authentication in view of a rich ecosystem of decentralised services.

ACCELERATOR AND X-RAY SOURCE

Throughout 2013, the Accelerator and Source Division has continued its efforts to ensure reliable operation, as well as implementing major upgrades to all subsystems of the accelerator complex. Many of these new developments are described hereafter.

BEAM PARAMETERS OF THE STORAGE RING

Table 1 presents a summary of the characteristics of the storage ring electron beam.

Energy	[GeV]	6.04
Maximum current	[mA]	200
Horizontal emittance	[nm]	4
Vertical emittance	[pm]	4
Revolution frequency	[kHz]	355
Number of bunches		1 to 992
Time between bunches	[ns]	2.82 to 2816

Table 1: Principal characteristics of the electron beam.

Table 2 gives the main optic functions, electron beam sizes and divergences at various source points. For insertion device source points, the beta functions, dispersion, sizes and divergences are calculated in the middle of the straight section. For bending magnets, two representative source points have been selected for each type of magnet (even or odd cell number), corresponding to magnetic fields of 0.4 T and 0.85 T. These points differ by the observation angles, of respectively 3 and 9 mrad from the entrance of the magnet.

Electron beam profiles are Gaussian and the size and divergence are presented in terms of rms values. The associated full width at half maximum sizes and divergences are 2.35 times higher. Horizontal electron beam sizes and divergences are given for the multibunch filling modes and apply to almost all filling patterns, except when the current per bunch is larger than 4.5 mA, for which a slightly larger size and divergence are attained because of the increased energy spread of the electron beam.

Vertical electron beam sizes and divergences are given for a vertical emittance of 4 pm, which is now the standard for 2 x 1/3 and 7/8+1 filling modes. The vertical sizes and divergences are about 1.4 times larger in uniform filling mode (due to ion effects, which are partially corrected by the use of a vertical bunch-by-bunch feedback). To increase the lifetime of the stored beam, the vertical beam sizes and divergences are deliberately increased by about a factor of 4 in the 16-bunch, 4-bunch and hybrid filling patterns.

The lifetime, bunch length and energy spread mainly depend on the filling

		Even ID (ID2, ID6...)	Odd ID (ID1, ID3...)	Even BM (ID2, ID6...) 3 mrad	Even BM (ID2, ID6...) 9 mrad	Odd BM (ID1, ID3...) 3 mrad	Odd BM (ID1, ID3...) 9 mrad
Magnetic field	[T]	Variable	Variable	0.4	0.85	0.4	0.85
Horiz. Beta function	[m]	37.6	0.35	1.33	1.06	2.12	1.61
Horiz. Dispersion	[m]	0.134	0.031	0.062	0.051	0.089	0.075
Horiz. rms e- beam size	[µm]	413	50	99	85	132	113
Horiz. rms e- divergence	[µrad]	10	107	116	114	104	99
Vert. Beta function	[m]	2.95	2.97	41.7	42.0	32.1	32.2
Vert. rms e- beam size	[µm]	3.4	3.4	12.9	13.0	11.3	11.4
Vert. rms e- divergence	[µrad]	1.17	1.16	0.50	0.50	0.36	0.36

Table 2: Beta functions, dispersion, rms beam size and divergence at the various source points (ID = insertion device; BM = bending magnet).

Filling pattern		Uniform	7/8 + 1	Hybrid	16-bunch	4-bunch
Number of bunches		992	870+1	24x8+1	16	4
Maximum current	[mA]	200	200	200	90	40
Lifetime	[h]	50	45	30	16	9
Rms energy spread	[%]	0.11	0.11	0.11	0.12	0.16
Rms bunch length	[ps]	20	20	25	48	55

Table 3: Current, lifetime, bunch length and energy spread for a selection of filling modes.

pattern. These are given in **Table 3** for a few representative patterns. Note that in both 16-bunch and 4-bunch filling patterns, the energy spread and bunch length decay with the current (the value indicated in the table corresponds to the maximum current). The bunch lengths are given for the usual radio-frequency accelerating voltage of 9 MV (8 MV for 16-bunch and 4-bunch).

SUMMARY OF ACCELERATOR OPERATION

The exceptional five-month shutdown in 2012 made it an unusual year, with only 3540 hours of scheduled beamtime. Operation returned to normal for 2013, with 5502 hours of scheduled beam delivery for the Users (plus additional shifts for Radiation and Personal Safety System tests).

Fig. 158: Uninterrupted beam delivery for 168 hours in 4 * 10 mA filling mode during May (Run 2013-02; week 8 [4 * 10 mA]).

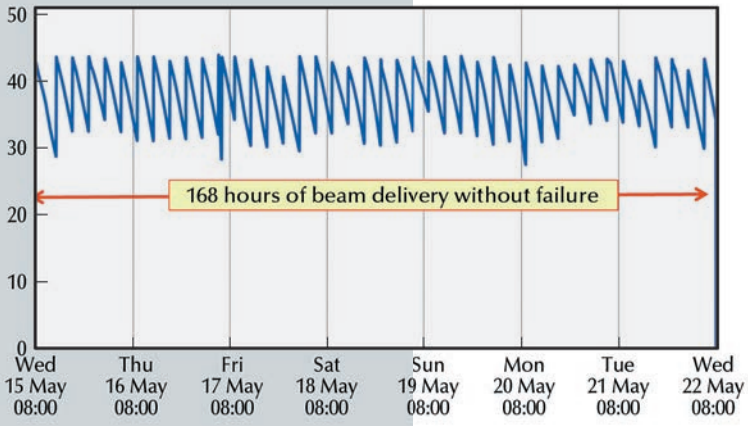

Out of these scheduled 5502 hours, 5396.65 hours were delivered, which represents an accelerator availability of 98.93% This excellent figure is very close to the all-time ESRF record of 99.04% in 2009. That this was achieved was thanks to the absence of any significant failures in 2013. Indeed, the longest failure lasted less than 3 hours and can be described as a tricky diagnostic event, during a weekend, that required the intervention of several experts, with the eventual discovery of abnormal behaviour on the limit switch of a manual valve.

Similarly, the mean time between failures (MTBF) of 79.7 hours is the second best MTBF ever obtained at the ESRF (the record is 107.8 hours in 2011). In April, during the second run of the year, a series of beam position

RUN NUMBER	TOTAL 2012	2013-01	2013-02	2013-03	2013-04	2013-05	TOTAL 2013
Start		22/01/2013	22/03/2013	31/05/2013	23/08/2013	18/10/2013	
End		13/03/2013	22/05/2013	31/07/2013	09/10/2013	18/12/2013	
Total number of shifts	**528**	150	183	183	141	183	**840**
Number of USM shifts	**442.5**	128.13	147.88	149.13	113.38	149.25	**687.75**
Beam available for users (h)	**3458.64**	999.9	1154.8	1174.8	888.65	1178.50	**5396.65**
Availability	**98.58%**	**98.38%**	**98.5%**	**99.22%**	**99.11%**	**99.45%**	**98.93%**
Dead time for failures	**1.42%**	1.6%	1.5%	0.8%	0.9%	0.6%	**1.07%**
Dead time for refills	**0.88%**	0.8%	0.9%	0.7%	1.1%	0.7%	**0.84%**
Average intensity (mA)	**138.2**	157	118	174	100	150	**92.2**
Number of failures	**59**	17	23	9	10	10	**69**
Mean time between failures (h)	**60**	60.3	51.4	132.6	90.7	119.4	**79.7**
Mean duration of a failure (h)	**0.85**	1	0.8	1	0.8	0.7	**0.86**

Table 4: Overview of storage ring operation in 2013.

interlocks (BPIs) spoilt the MTBF. Due to the random aspects of these interlocks, it took about 2 weeks and some effort to locate the origin, which was a corrector power supply oscillating for a short period at random moments. This abnormal behaviour was tracked down to a design flaw in a newly installed corrector-family power supply.

The noticeable absence of repetitive events (especially during Run 3 and 5 when the MTBF largely exceeded 100 hours) resulted in many weeks in which the beam was delivered without any interruption. As an example, there were 21 periods with more than 100 hours of beam delivery without a single interruption, including 2 periods of 168 hours (see **Figure 158**) and one of 167 hours. An overview of the year is presented in **Table 4**.

In 2013, three major upgrades took place in the storage ring: the commissioning of the first 7 m straight section in cell 23 (winter 2012/2013 shutdown), the installation of two prototypes of higher order mode (HOM)-damped RF cavities in the same cell (summer 2013 shutdown) and the successful installation of a 2.5 m-long in-vacuum undulator upstream of the ID16 straight section. Two newly-installed RF cavities, which have been running in both passive and active modes, have had no negative effects on the operation of the accelerators.

FILLING PATTERNS

Figure 159 presents the distribution of filling modes delivered in 2013. This distribution of modes has not drastically evolved over the last four years, when the 7/8+1 filling mode was introduced. This mode remains the best compromise for Users who need intensity and/or time-structure. The uniform mode remains mainly for the need of specific experiments on one beamline.

It is worth noting that during machine dedicated time (MDT), several shifts were used with the beamlines to assess the top-up mode in 16-bunch with refills every 10, 20 and 30 minutes. Many scientists expressed their enthusiasm thanks to the excellent results obtained. Details are given later in the article on this subject.

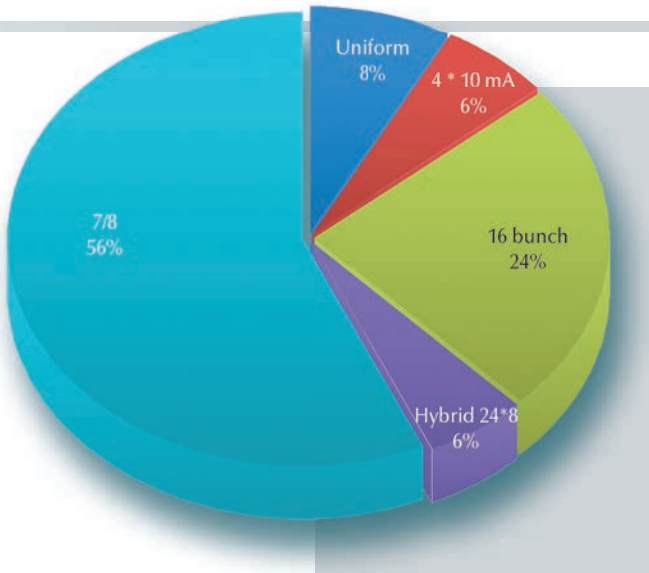

Fig. 159: Distribution of the various filling modes in 2013.

TECHNICAL DESIGN STUDY FOR THE NEW STORAGE RING

The ASD is progressing with the technical design study (TDS) for the Accelerator Phase II Upgrade, which is focused on greatly improving the brightness of the source by decreasing the horizontal equilibrium emittance of the storage ring from the current 4 nm to 150 pm. This will be possible by replacing the present 32-double bend achromat arcs with a much more compact lattice based on a hybrid 7-bend achromat (see **Figure 160**). The smaller emittance, together with shorter-period, smaller-gap undulators and new beamline optics optimised to take full advantage of the new source,

will allow a general improvement in performance by about a factor of 100.

There are several design restrictions, including maintaining the present injection complex and injection scheme, as well as the existing straight sections and beamlines, in an almost unchanged state. The existing arc hardware, such as some power supplies, vacuum system components and diagnostics must also be reused as much as possible. Another design goal is to reduce operation costs, specifically wall-plug power.

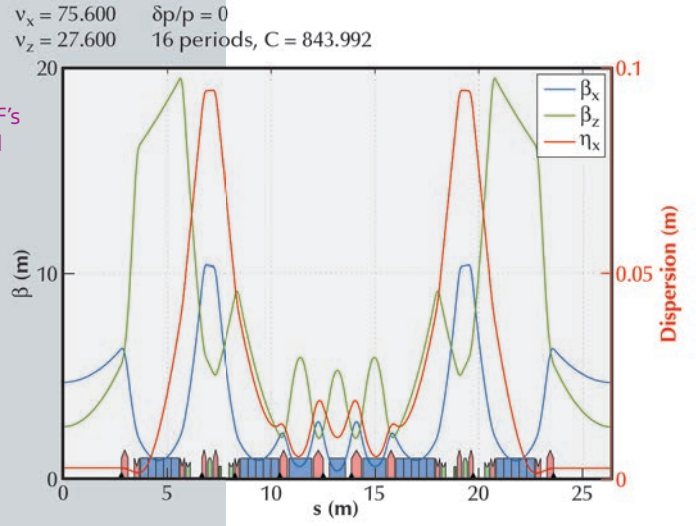

Fig. 160: The S28 design for the ESRF's new hybrid 7-bend achromat lattice.

On 5th and 6th September 2013, the newly formed Accelerator Project Advisory Committee (APAC), nominated by the ESRF Council, reviewed the project and current progress in the development of the TDS. A status report of all the main activities, grouped in working packages (Beam Dynamics, Magnets, Electron and Photon Beam Transport, Power Supplies, Radiofrequency, Implementation, Diagnostics and Beam Control, Photon Source and User Interface, Injector Upgrade), was presented to the Committee. The APAC report was very positive and the Committee strongly supports the effort of the ASD towards the completion of the TDS. Three more meetings are planned before the end of 2014, with a detailed report given from the APAC to the Management and the Council each time. The project team is now preparing the TDS report to be presented to the committees in spring 2014.

7-METRE STRAIGHT SECTION

As part of the ongoing upgrade of the accelerator complex, the ID23 straight section has been lengthened from 5 m to 7 m, with no disruption to the operation of beamline ID23. The magnets at both ends of the straight section have been replaced by shorter and stronger ones. The two undulators presently in operation have been moved to either end of the straight section, leaving free space in the centre for installation of the new RF HOM-damped cavities (**Figure 161**). The 7 m straight section, which broke the symmetry of the storage ring, has not caused any deterioration of the beam parameters – in fact they are now even better thanks to improved optic tuning techniques.

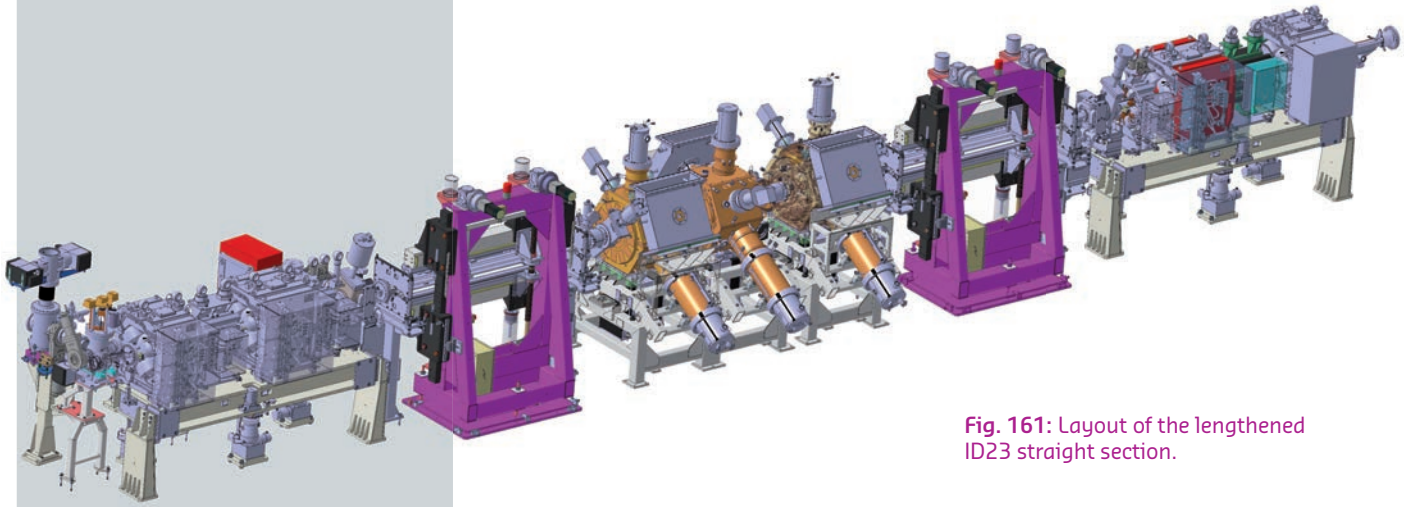

Fig. 161: Layout of the lengthened ID23 straight section.

In addition to the new magnets and corresponding power supplies installed in the straight section, the modification required a change of magnet coils and new power supplies, providing individual control of the quadrupoles over a full cell, rather than over a whole magnet family, as in the past. These modifications were completed with the installation of the new straight section girders and new magnets during the winter 2012-2013 shutdown.

During the first half of 2013, before the installation of the RF cavities, an additional quadrupole was installed at their location and powered during machine dedicated studies only. The aim was to test the possibility of splitting a long straight section into two halves with a small vertical β of 1.5 m in the middle of each half. This configuration could allow a further reduction of the undulator gaps, possibly down to 4 mm. The tests provided the opportunity to check the impact on the machine performance of such a significant modification to the optics, in particular on injection efficiency and lifetime. The experiments have indicated that the effects are rather limited. This extensive project, which included the reconstruction of part of a cell arc, as well as the whole straight section, was also an excellent exercise in view of future works towards a new storage ring lattice (**Figure 162**).

Fig. 162: The first 7 m straight section during installation at ID23 in January 2013.

TOP-UP OPERATION

In order to reduce the heat load variation on the beamline optics, top-up filling of the storage ring is under evaluation. This mode of operation will be beneficial to the 16-bunch mode by reducing the current variation, but also by allowing delivery at low vertical emittance. Today, the vertical beam size is increased (blown-up) in order to increase the lifetime. For multibunch mode, in comparison to the smooth stability induced by the long lifetime, the frequent injection perturbations induced by the top-up have been evaluated in depth in collaboration with beamline scientists in order to establish the benefits, if any, for this filling pattern.

A new cleaning technique has been developed for this project and is now routinely used during user service mode (USM) for the 16-bunch and hybrid modes. It reduces the strong vertical blow-up just after injection from 2 nm to only a few pm. The development of bunch cleaning in the booster will continue and will benefit from the upgrade of the injector. In particular, a new booster power supply system (BPSS) operating at 4 Hz is under development for the dipole and quadrupole magnets of the booster.

Top-up in 16-bunch has been developed and tested during MDT. The reliability of the storage ring has been validated with 90 mA average current in 16-bunch, refilled every 10 minutes, lasting for hours without disturbance, all parameters being even more stable in this configuration. The radioprotection aspects are satisfactory (injection has already been performed with the front end open) but a formal agreement from the authorities for operation in USM is needed. Large horizontal stability perturbations are still induced during injection for a few seconds due to the presence of sextupoles in the injection

bump – solutions using the feedback are under development. An injection sequencer has been developed in order to automatically manage the equipment and to optimise the electrical consumption. Using this tool, top-up injection is now completed in less than 30 seconds.

The injector upgrade has already been initiated with the renewal of the booster RF, which allows a drastic reduction in electrical consumption. In addition to the renewal of the BPSS, a number of parameters still remain to be finalised before implementation.

Fig. 163: Synopsis of eight hours of top-up tests in 16-bunch mode with beamlines.

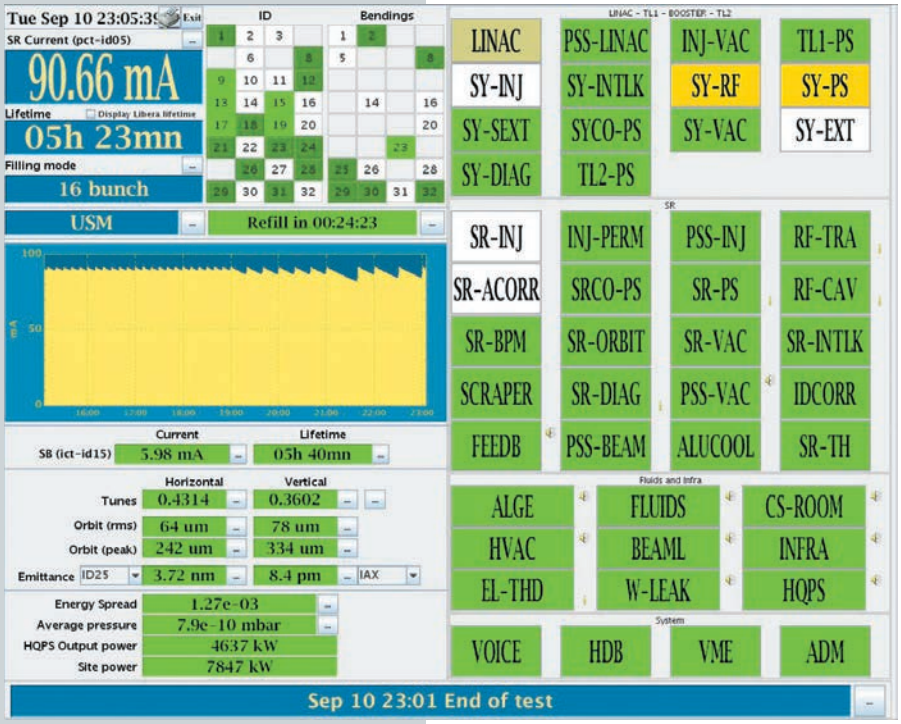

The top-up frequency is a crucial parameter for this project. A survey of the top-up operational aspects has been done for most light sources, showing large discrepancies between them. For the ESRF, the frequency will be determined following consultation with the users and could be between 10 and 30 minutes. Top-up tests with beamlines took place on Tuesday 10 September (see **Figure 163**) for 8 hours (2 hours with a refill every 10 minutes for preparation of the beamlines, then 2 hours with a refill every 10 minutes, 2 hours with a refill every 20 minutes and 2 hours with a refill every 30 minutes). Beam was delivered for 8 hours without any beam losses or major disturbances. Reports sent from each participating beamline are now being analysed. A preliminary result provided by ID18 indicates that a refill every 30 minutes is the extreme limit at which one can benefit from the stability of the optics.

Beamlines ID13 and ID15, which use in-vacuum undulators that are normally incompatible with top-up injection, could be made to work in this new mode thanks to the inhibition of an interlock. Today during injection, the in-vacuum undulators are left slightly open, to avoid beam losses, but during top-up operation the in-vacuum undulators will need to remain closed. Normally an interlock prevents injection with a closed gap, but inhibiting this limitation allows the injection to take place with the gap closed. This produces higher beam losses at this location but preliminary results indicate that it is manageable.

NEW BUNCH CLEANING

The cleaning required for the time-structured modes of operation is now performed for the 16-bunch and 24 x 8 bunch hybrid modes using a new system. This system is implemented on the bunch-by-bunch feedback system, using the bunch-by-bunch Libera beam position monitor electronics and the wide-bandwidth stripline kicker to perform time-gated cleaning. With this new method, the tuning of the cleaning is much easier, which is particularly beneficial for the 24 x 8 hybrid mode. It also avoids blowing up of the main bunches, which caused an apparent emittance increase during cleaning when the previous system was used.

However, since this cleaning is performed after injection in the storage

ring, it is not compatible with the future top-up mode of operation as during the time interval between the injection and the cleaning, parasitic electrons are stored outside the main bunch buckets. This is not a problem when the injections are separated by hours, but will not be acceptable if the interval between the injections becomes much smaller.

A new cleaning system is now being implemented to perform the cleaning 5 to 10 milliseconds after injection in the booster. This system will be based on a system tested a few years ago. The prototype system was not working reliably enough due to the lack of injection-to-injection stability of the tune. To overcome this problem, a fast and accurate measurement system of the dipole and quadrupole currents is being added to the system. From this measurement, the precise value of the frequency of the beam excitation signal, which will kill the parasitic bunches, will be derived for each injection.

NEW HOM-DAMPED CAVITIES IN THE STORAGE RING POWERED BY 150 kW RF SOLID-STATE AMPLIFIERS

Following on from the installation of four solid state amplifiers (SSAs) in the booster in 2012, the first two out of three 150 kW SSAs for the storage ring were delivered by ELTA and installed in cell 23 in June and September 2013, respectively (see **Figure 164**). They have passed the site acceptance tests and were connected to the first two HOM-damped cavities, which had been installed in August in the middle of the 7 m straight section of cell 23. Since October 2013, these two cavities have been in operation in USM and provide 0.5 MV accelerating voltage each. The third HOM-damped cavity was installed in cell 23 during the winter shutdown (**Figure 165**). The last SSA was delivered and had its preliminary site acceptance test with a dummy load in December. From January 2014 it will power the third cavity.

An important milestone has also been achieved with the in-house development of SSAs using cavity combiners. In July, the first 10 kW prototype combining 18 RF modules was successfully tested. It delivered as much as 12 kW with a global efficiency above 62%. The next step will be to manufacture and connect 114 further RF modules to the cavity combiner in order to reach the design goal of 75 kW with 132 connected RF modules.

Fig. 164: Three new HOM-damped cavities (undergoing vacuum conditioning) in the 7 m straight section of cell 23.

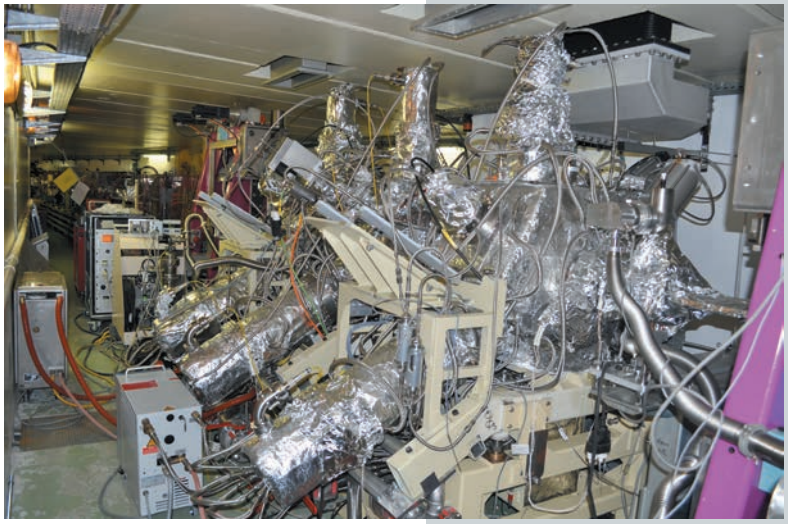

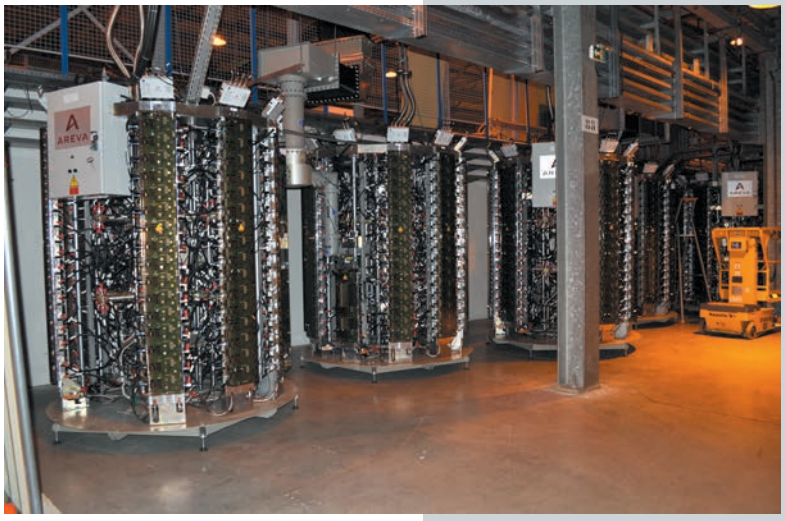

Fig. 165: Three 150 kW SSAs powering the HOM-damped cavities in cell 23.

STATUS OF THE DEVELOPMENT OF NEW ELECTRONICS FOR BOOSTER BEAM POSITION MONITORS

Modernisation of the 25-year-old electronics for RF signal acquisition and processing of the booster beam position monitor system is now in progress, with a complete design study for new electronics followed by the realisation of two fully operational prototypes. The specifications have been defined at the ESRF and the design work and production has been out-sourced to the same company that produces the beam position monitor electronics for the storage ring (Libera). The design reports have recently been approved and the prototypes are being tested by the manufacturer and are expected at the ESRF for further tests at the end of this year.

MOVEABLE QUADRUPOLES IN THE BOOSTER

In order to have better control of the orbit deviations of the beam in the booster, a mechanical system that allows a quadrupole to be moved transversely has been conceived and implemented. This mechanical system and the motorisation for the remote control of the translation was conceived so that it could be installed underneath a quadrupole magnet without dismounting the magnet and without stopping the vacuum system in the booster chamber. A total of three quadrupoles were equipped during the summer shutdown (see **Figure 166**) and their subsequent use has allowed a reduction of the rms orbit deviation by nearly 50%. It is planned to install motorisation systems on other quadrupoles in order to reduce the orbit distortions in the booster by about a factor of 5 overall.

Fig. 166: Motorisation enabling a quadrupole in the booster to be displaced.

MEMBERS AND ASSOCIATE COUNTRIES

(AS OF FEBRUARY 2014)

Members' shares:

27.5%	France
25.5%	Germany
15%	Italy
14%	United Kingdom
4%	Spain
4%	Switzerland
6%	Benesync (Belgium, The Netherlands)
4%	Nordsync (Denmark, Finland, Norway, Sweden)

Additional contributions

1%	Portugal
1.5%	Israel
1.3%	Austria
1%	Poland
1,05%	Centralsync (Czech Republic 0,55%, Hungary 0,25%, Slovakia 0,25%)
0.3%	South Africa

THE BEAMLINES

Details of the public ESRF beamlines as well as those operated by Collaborating Research Groups (CRG) are given in **Tables 5** and **6**. **Figure 167** shows the location of the beamlines in the experimental hall.

- Public beamlines
- CRG beamlines
- Instrumentation test and development beamlines
- Free bending magnet ports

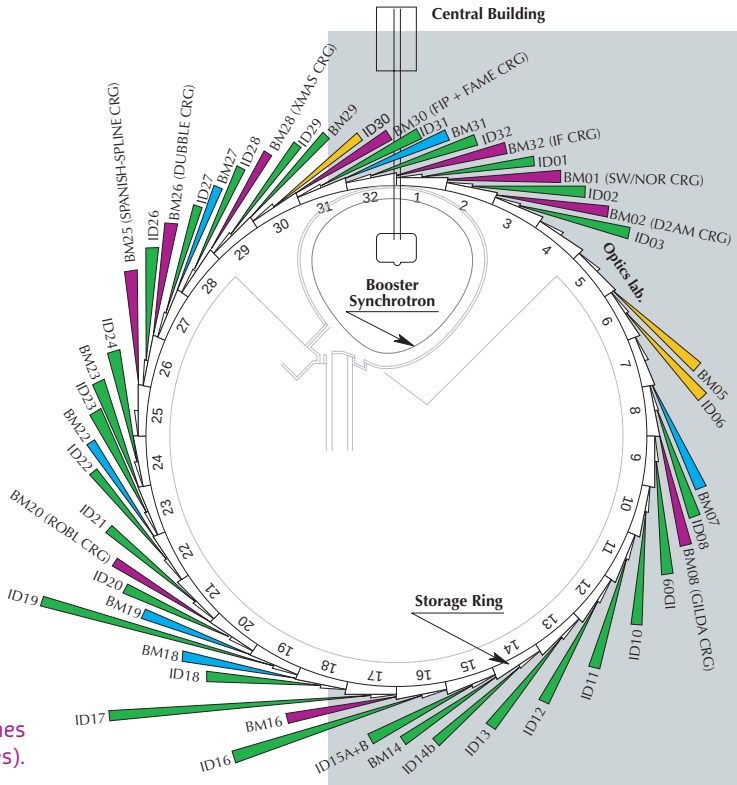

Fig. 167: Experimental hall showing location of the beamlines (public and CRG beamlines).

SOURCE POSITION	NUMBER OF INDEPENDENT END-STATIONS	BEAMLINE NAME	STATUS	
ID01	1	Microdiffraction imaging	Closed	since 01/14
ID02	1	High brilliance	Closed	since 07/13
ID03	1	Surface diffraction	Operational	since 09/94
ID08	1	Dragon	Closed	since 10/13
ID09	1	White beam	Operational	since 09/94
ID10	1	Soft interfaces and coherent scattering	Operational	since 06/12
ID11	1	Materials science	Operational	since 09/94
ID12	1	Circular polarisation	Operational	since 01/95
ID13	1	Microfocus	Operational	since 09/94
ID14B	1	Protein crystallography	Closed	since 12/13
ID15A	1	High energy diffraction	Operational	since 09/94
ID15B	1	High energy inelastic scattering	Operational	since 09/94
ID17	1	Medical	Operational	since 05/97
ID18	1	Nuclear scattering	Operational	since 01/96
ID19	1	Topography and tomography	Operational	since 06/96
ID20	1	Inelastic X-ray Scattering	Operational	since 06/13
ID21	1	X-ray microscopy / IR Spectroscopy	Operational	since 12/97
ID22	1	Microfluorescence	Closed	since 04/13
ID23	2	Macromolecular crystallography MAD	Operational	since 06/04
		Macromolecular crystallography microfocus	Operational	since 09/05
ID24	1	Dispersive EXAFS	Operational	since 02/96
ID26	1	X-ray absorption and emission	Operational	since 11/97
ID27	1	High pressure	Operational	since 02/05
ID28	1	Inelastic scattering II	Operational	since 12/98
ID29	1	Multiwavelength anomalous diffraction	Operational	since 01/00
ID31	1	Powder diffraction	Closed	since 01/14
BM14	1	Macromolecular crystallography (MAD)	Operational	since 01/10
BM23	1	X-ray absorption spectroscopy	Operational	since 03/11
BM29	1	Bio SAXS	Operational	since 06/12
Operational in 2014 :				
ID16A	1	Nano-imaging	Operational	from 05/14
ID16B	1	Nano-analysis	Operational	from 04/14
ID22	1	High-resolution powder-diffraction	Operational	from 05/14
ID32	1	Soft X-ray spectroscopy	Operational	from 07/14

Table 5: List of the ESRF public beamlines.

SOURCE POSITION	NUMBER OF INDEPENDENT END-STATIONS	BEAMLINE NAME	FIELD OF RESEARCH	STATUS
BM01	2	Swiss-Norwegian BL	X-ray absorption & diffraction	Operational since 01/95
BM02	1	D2AM (French)	Materials science	Operational since 09/94
BM08	1	Gilda (Italian)	X-ray absorption & diffraction	Operational since 09/94
BM20	1	ROBL (German)	Radiochemistry & ion beam physics	Operational since 09/98
BM25	2	SPLINE (Spanish)	X-ray absorption & diffraction	Operational since 04/05
BM26	2	DUBBLE (Dutch/Belgian)	Small-angle scattering	Operational since 12/98
			EXAFS	Operational since 06/01
BM28	1	XMAS (British)	Magnetic scattering	Operational since 04/98
BM30	2	FIP (French)	Protein crystallography	Operational since 02/99
		FAME (French)	EXAFS	Operational since 08/02
BM32	1	IF (French)	Interfaces	Operational since 09/94

Table 6: List of the Collaborating Research Group beamlines.

USER OPERATION

In our 19th year of successful operation for scientific users, we look back on user operation at the facility over the past year, 2013. Following the first ever "long shutdown" from December 2011 to May 2012, 2013 saw the return to full user operation for the majority of users. The new EX2 experimental hall extension was completed and construction work began on the long beamlines which will inhabit this extension building. Phase I of the Upgrade Programme continued its steady course: the new inelastic scattering upgrade beamline ID20 was opened and beamlines ID01, ID02, ID08, ID14-1, ID14-4, ID22 and ID31 were all closed for upgrade at various points during the year to be rebuilt as upgrade beamlines on ID01, ID02, ID32, ID30A-3, ID30B, ID16 (NINA) and ID22 respectively. In total, the equivalent of around 27 ESRF publicly funded beamlines and 9 CRG beamlines were available for users in 2013. **Figure 168** shows the number of applications for beamtime received since 2007. The number of applications received is heading back up towards the pre-shutdown level and, taking into account the unavailability of the beamlines undergoing upgrade and the permanent closure of others, the number of proposals received per operating beamline continues to increase.

Proposals for experiments are selected and beamtime allocations are made through peer review. As in previous years, beamtime for 2013 was allocated based on recommendations made by review committees of specialists, for the most part from European countries and Israel. For 2013 a new structure was put into place for the proposal review process with the aim of allowing all proposals received for a particular beamline to be assessed by the same review committee. This gives the committees a better overall view of all the projects proposed for a single beamline, and allows them greater flexibility to optimise the selection of proposals awarded beamtime on each beamline. Beamlines of similar techniques or activities were grouped together to form 10 new review committees:

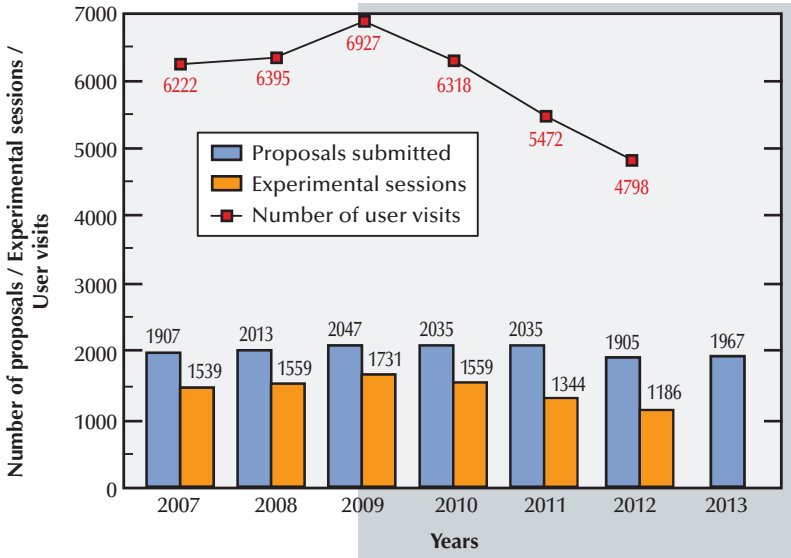

Fig. 168: Applications for beamtime, experimental sessions and user visits, 2007 to 2013. The final number of experimental sessions and user visits for 2013 were not available at the time of going to press.

- C01 (ID01, ID03, BM25B, BM32)
- C02 (ID11, ID15A, ID15B, ID31)
- C03 (ID08, ID12, ID20, ID26, ID32, BM28)
- C04 (ID24, BM01B, BM08, BM20, BM23, BM25A, BM26A, BM30B)
- C05 (ID06-LVP, ID09A, ID18, ID27, ID28, BM01A)
- C06 (ID17, ID19)
- C07 (ID13, ID16A&B, ID21, ID22)
- C08 (ID02, BM26B)
- C09 (ID09B, ID10, BM02)
- C10 (Structural Biology Beamlines).

At the same time, the scientific areas of ESRF research activities were redefined, since these no longer dictate the review committee structure and size. The new scientific areas are shown in **Table 7**. In addition a societal theme classification was implemented with the aim of monitoring the societal relevance of the research carried out at the ESRF, based on the following themes:

- Earth and Environment
- Health
- Information and Communication Technology
- Energy
- Other Functional Materials
- Fundamental Science
- Other

Table 7: Number of shifts of beamtime requested and allocated for user experiments, in 2013. Note: Methods and Instrumentation figures are for half a year only.

Scientific field	Total shifts requested	Total shifts allocated
Chemistry	4 398	1 668
Earth Sciences	1 659	702
Environment	915	366
Hard Condensed Matter Science	8 372	3 173
Cultural Heritage	337	96
Life Sciences	847	312
Applied Materials Science	5 151	1 927
Medicine	1 135	535
Engineering	282	75
Methods & Instrumentation	155	72
Structural Biology	3 106	2 121
Soft Condensed Matter	2 747	1 045
Totals	**29 104**	**12 092**

The newly structured review committees met twice during the year, around six weeks after the deadlines for submission of proposals (1 September 2012 and 1 March 2013). They reviewed 1967 applications for beamtime, and selected 845 (43%), which were then scheduled for experiments.

Requests for beamtime in 2013, which is scheduled in shifts of 8 hours, totalled 29,104 shifts or 232,832 hours, of which 12,092 shifts or 96,736 hours (41.6%) were allocated. The distribution of shifts requested and allocated, by scientific area, is shown in **Table 7**.

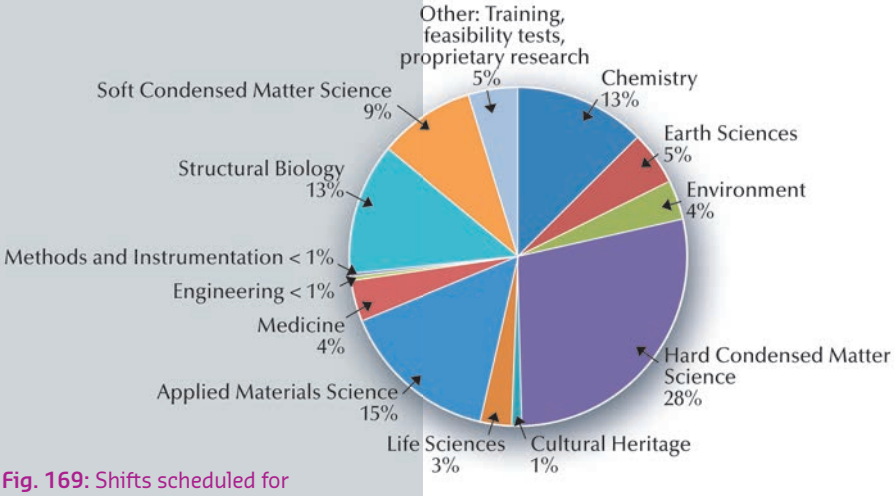

Fig. 169: Shifts scheduled for experiments, March to July 2013, by scientific area.

The breakdown of shifts scheduled for experiments by scientific area in the first half of 2013 is shown in **Figure 169**. This same period saw 2764 visits by scientists to the ESRF under the user programme, to carry out 683 experiments. Overall, the number of users in each experimental team averaged just over 4 persons, as in all previous years, and the average duration of an experimental session was 9 shifts, as in 2012. This can be further broken down to show an average duration of 3 shifts for MX experiments and 13 shifts for non-MX experiments. The annual number of experimental sessions and user visits since 2007 is shown in **Figure 168**. The effect of the reduction in beamtime available in 2011 and 2012 due to the long shutdown is clearly visible in the lower-than-normal numbers of experimental sessions and user visits. With the return to normal user operation in 2013, we will see these figures rise significantly again once the 2013/II scheduling period finishes at the end of February 2014, although they are not expected to reach pre-shutdown levels due to the lower amount of overall beamtime available.

One of the principle measurable output parameters of the ESRF is the number and quality of publications accepted in peer-reviewed journals. **Figure 170** shows how this number has been rising continuously over the past years to reach a plateau of just under 1900 publications per year, corresponding to the maximum operation level of the ESRF. These are excellent figures, with a publication output systematically on a level of well over one publication per experimental session. The year 2013 promises to be highly fruitful, with 1785 publications already registered in the ILL/ESRF Library database, though publication levels are expected to drop slightly as a result of the reduced numbers of experiments carried out during 2011 and 2012. Since the ESRF began user operation back in 1994, a total of 23,297 publications have been accepted in peer-reviewed journals. Of these, nearly 300 every year are published in high impact factor journals.

User responses to questionnaires show once again that the ESRF continues to maintain its excellent reputation concerning the assistance and service given by scientists and support staff on beamlines, and travel and administrative arrangements, in addition to the quality both of the beam and of the experimental stations. Facilities on site, such as preparation laboratories, the Guesthouse and a canteen open 7 days a week, also make an important contribution to the quality of user support.

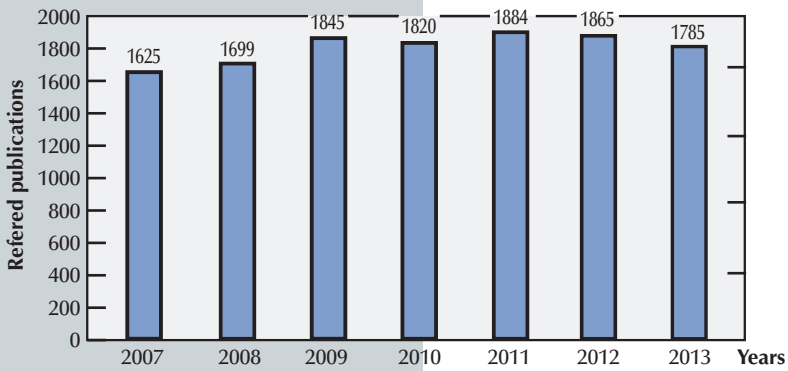

Fig. 170: Numbers of publications appearing in refereed journals reporting on data collected either partially or totally at the ESRF, 2007 to 2013.

ADMINISTRATION AND FINANCE

Expenditure and income 2012

Expenditure		kEuro
Accelerator and Source		
Personnel		5 448.7
Recurrent		1 112.2
Operating costs	*1 046.2*	
Other recurrent costs	*66.0*	
Capital		4 180.5
Accelerator and Source developments	*4 180.5*	
Beamlines, experiments and in-house research		
Personnel		17 852.7
Recurrent		4 796.2
Operating costs	*1 494.3*	
Other Recurrent costs	*3 301.9*	
Capital		11 142.4
Beamline developments	*10 438.6*	
Beamline refurbishment	*703.8*	
Technical and administrative supports		
Personnel		26 925.3
Recurrent		10 929.3
Capital		17 487.1
Industrial and commercial activity		
Personnel		336.6
Recurrent		62.0
Unexpended committed funds		
Funds carried forward to 2013		5 960.0
Total		**106 233.0**

Income	kEuro
2012 Members' contributions	83 666.0
Funds carried forward from 2011	4 076.3
Other income	
Scientific Associates	5 111.0
Sale of beamtime	1 087.0
Compensatory funds	2 650.0
Scientific collaboration and Special projects	3 681.2
Excess income	–263.5
Pre-financing	845.0
Pre-financing carried forward to 2013	5 380.0
Total	**106 233.0**

Revised expenditure and income budget for 2013

Expenditure		kEuro
Accelerator and Source		
Personnel		5 915
Recurrent		1 770
Operating costs	*1 690*	
Other recurrent costs	*80*	
Capital		6 772
Accelerator and Source developments	*6 772*	
Beamlines, experiments and in-house research		
Personnel		18 787
Recurrent		5 163
Operating costs	*1 318*	
Other Recurrent costs	*3 845*	
Capital		18 206
Beamline developments	*18 206*	
Beamline refurbishment	*0*	
Technical and administrative supports		
Personnel		26 164
Recurrent		12 573
Capital		16 435
Industrial and commercial activity		
Personnel		470
Recurrent		105
Total		**114 360**

Income	kEuro
2013 Members' contributions	84 981
Funds carried forward from 2012	843
Building costs provision	1 000
Other income	
Scientific Associates	5 408
Sale of beamtime	1 670
Compensatory funds	2 005
Scientific collaboration and Special projects	8 032
Pre-financing	10 421
(including 5 380 from 2012)	
Total	**114 360**

The budget for 2013 includes additional contributions from Members and Scientific Associates of 13 347 kEUR dedicated to the Upgrade Programme. The Upgrade expenditure budget amounts to a total of 37 580 kEUR including 12 812 kEUR of ESRF operating budget.

Expenditure 2012 by nature of expenditure

	kEuro
PERSONNEL	
ESRF staff	48 688.0
External temporary staff	82.4
Other personnel costs	1 792.7
RECURRENT	
Consumables	6 122.7
Services	8 960.9
Other recurrent costs	1 816.3
CAPITAL	
Buildings, infrastructure	13 753.1
Lab. and Workshops	1 592.5
Accelator and Source incl. ID's and FEs	4 180.5
Beamlines, Experiments	11 142.3
Computing Infrastructure	2 126.8
Other Capital costs	14.8
Unexpended committed funds	
Funds carried forward to 2013	5 960.0
Total	**106 233.0**

Revised budget for 2013 by nature of expenditure

	kEuro
PERSONNEL	
ESRF staff	51 330
External temporary staff	61
Other personnel costs	1 945
RECURRENT	
Consumables	7 238
Services	9 968
Other recurrent costs	2 405
CAPITAL	
Buildings, infrastructure	12 314
Lab. and Workshops	2 891
Accelator and Source incl. ID's and FEs	6 772
Beamlines, Experiments	18 206
Computing Infrastructure	1 125
Other Capital costs	105
Total	**114 360**

2013 manpower *(posts filled on 31/12/2013)*

	Scientists, Engineers, Senior Administrators	Technicians and Administrative Staff	PhD Students	Total
Staff on regular positions				
Accelerator and Source	29	38.1	1.5	68.6
Beamlines, instruments and experiments*	222	84.7	21.5	328.2
General technical services	28.6	53		81.6
Directorate, administration and central services	38.7	50.4		89.1
Sub-total	*318.3*	*226.2*	*23*	*567.5*
Other positions				
Short term contracts	17.3	13		30.3
Staff under "contrats de professionnalisation"		30		30
European Union grants			1	1
Temporary workers				0
Total	**335.6**	**269.2**	**24**	**628.8**
Scientific collaborators and consultants	*6*			*6*
External funded research fellows	*12*		*9*	*21*

** Including scientific staff on time limited contracts.*

Financial resources in 2011, 2012, 2013 and 2014, by major programme

(current prices in MEuro for the respective years)

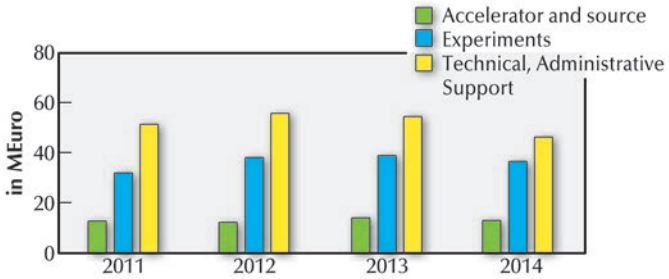

Financial resources in 2011, 2012, 2013 and 2014, by nature of expenditure

(current prices in MEuro for the respective years)

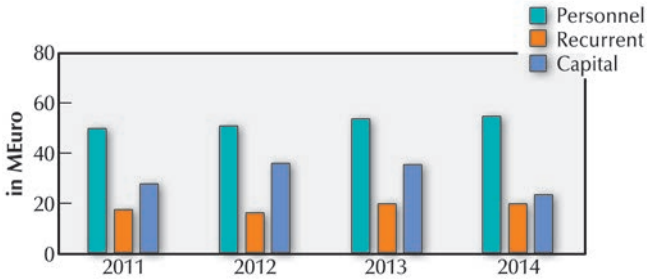

ORGANISATION CHART OF THE ESRF

(AS OF JANUARY 2014)

Administrative and Finance Committee
Chairperson: A-M. Hundere

Council
Chairperson:
B. Girard
up to 3 delegates per Contracting Party

Science Advisory Committee
Chairperson: K. Hämäläinen

Director General
F. Sette

DG's Services:
- Head of DG's Office/Secretary of Council: I. Echeverria
- Communication Unit
- Business Development Office
- Internal Auditor
- Safety Group

Beam Time Allocation Panels
C01 (ID01, ID03, BM25B, BM32) Chairperson: A. Stierle
C02 (ID11, ID15A, ID15B, ID22) Chairperson: A. Beale
C03 (ID12, ID20, ID26, ID32, BM28) Chairperson: H. Tjeng
C04 (ID24, BM23, BM01B, BM08, BM20, BM25A, BM26A, BM30B) Chairperson: C. Lamberti
C05 (ID06-LVP, ID09A, ID18, ID27, ID28, BM01A) Chairperson: U. Schwarz
C06 (ID17, ID19) Chairperson: A. Olivo
C07 (ID16A, ID16B, ID21) Chairperson: I. Fairchild
C08 (ID02, ID13, BM26B) Chairperson: P. Stepanek
C09 (ID09B, ID10, BM02) Chairperson: A. Plech
C10 (Structural Biology Beamlines) Chairperson: M. Czjzek

ACCELERATOR AND SOURCE
Director: P. Raimondi

- Beam dynamics and applications
- Power supplies
- Insertion devices
- Front-ends
- Radio frequency and linac
- Diagnostics
- Operation
- Secretariat

ADMINISTRATION
Director: L-J. Sánchez Ortiz

- Personnel
- Finance
- Purchasing

- Joint ILL/ESRF
- Medical service
- Joint ILL/ESRF
- Library

EXPERIMENTS

Director: B-W. Dijkstra

Beamline groups:
- Structural biology
- Structure of soft matter
- X-ray imaging

Director: H. Reichert

Beamline groups:
- Dynamics and extreme conditions
- Electronic structure and magnetism
- Structure of materials

Scientific infrastructure
- Theory
- User office
- CRG liaison
- Secretariat

INSTRUMENTATION SERVICES AND DEVELOPMENT DIVISION
Head: J. Susini

- Advanced analysis and modeling
- Detector and electronics
- Software
- X-ray optics
- Mechanical engineering

TECHNICAL INFRASTRUCTURE DIVISION
Head: R. Dimper

- Management information systems and web
- Systems and communication
- Buildings and infrastructure
- EX2/CPER project team
- Survey and alignment
- Vacuum

Cover
Cover design by M. Scandella based on the figure of phonon dispersion of $Na_{0.8}CoO_2$ from the article Rattling modes in thermoelectric sodium cobaltate by D.J. Voneshen *et al.*, p 29.

We gratefully acknowledge the help of:

C. Argoud, B. Boulanger, K. Clugnet, K. Colvin, M. Cotte, E. Dancer, B. Dijkstra, R. Dimper, I. Echeverría, R. Felici, A. Fitch, K. Fletcher, P. Gaget, S. Gerlier, C. Habfast, E.S. Jean-Baptiste, A. Joly, A. Kaprolat, M. Krisch, G. Leonard, J. McCarthy, S. McSweeney, T. Narayanan, S. Pascarelli, P. Raimondi, H. Reichert, S. Rio, M. Scandella, F. Sette, J. Susini and all the users and staff who have contributed to this edition of the Highlights.

Editor
G. Admans
Layout
Pixel Project
Printing
Imprimerie du Pont de Claix

Communication Group
ESRF
BP220 • 38043 Grenoble • France
Tel. +33 (0)4 76 88 20 56
Fax. +33 (0)4 76 88 25 42
http://www.esrf.eu